
Quantum/Classical Simulation of Molecular Excited State Dynamics and Spectroscopy

**From Iodine in Krypton to Enone-Lewis Acid
Complexes in an Explicit Solvent**

Martin Thomas Peschel

2023

Dissertation zur Erlangung des Doktorgrades
der Fakultät für Chemie und Pharmazie
der Ludwig-Maximilians-Universität München

**Quantum/Classical Simulation of Molecular
Excited State Dynamics and Spectroscopy**
**From Iodine in Krypton to Enone-Lewis Acid Complexes
in an Explicit Solvent**

Martin Thomas Peschel

aus

Jena, Deutschland

2023

Erklärung

Diese Dissertation wurde im Sinne von §7 der Promotionsordnung vom 28. November 2011 von Frau Prof. Dr. Regina de Vivie-Riedle betreut.

Eidesstattliche Versicherung

Diese Dissertation wurde eigenständig und ohne unerlaubte Hilfe erarbeitet.

München, November 3, 2023

Martin Thomas Peschel

Dissertation eingereicht am: 09.08.2023
1. Gutachterin/Gutachter: Prof. Dr. Regina de Vivie-Riedle
2. Gutachterin/Gutachter: Prof. Dr. Christian Ochsenfeld
Mündliche Prüfung am: 20.10.2023

Contents

| | |
|--|-------------|
| Abstract | vi |
| List of Publications | viii |
| Introduction | 1 |
| 1. Method Development and Theoretical Background | 5 |
| 1.1. Ehrenfest Dynamics | 5 |
| 1.2. Multi-Configurational Ehrenfest | 18 |
| 1.3. Trajectory Surface Hopping | 29 |
| 2. Energy Transfer in Linear Spectroscopy | 33 |
| 3. Excited State Properties and Reactivities of Cyclic 2-Enones | 45 |
| 3.1. <i>Z/E</i> Isomerization and Diels-Alder Reaction of Cyclohept-2-enones | 50 |
| 3.2. α -Cleavage and Ring Contraction of 5,5-Dialkylcyclopent-2-enones | 67 |
| 4. Excited State Dynamics and Spectroscopy of Lewis-Acid-Enone Complexes | 79 |
| 4.1. Relaxation to the Triplet States in Cyclohex-2-enone-BF ₃ | 83 |
| 4.2. Excited State Dynamics of Cyclohex-2-enone-BF ₃ in Solution | 95 |
| 4.3. A Complex Excited State Electronic Structure Leads to Unexpected Reactivity: B-Cl Bond Fission in Benzaldehyde-BCl ₃ | 103 |
| 5. Summary | 119 |
| A. The Semi-Classical Wigner Sampling Approach to Calculate Optical Spectra | 121 |
| B. Supporting Information for Chapter 2 | 123 |
| B.1. Susceptibility and Absorbance | 123 |
| B.2. Sub-Cycle Dynamics and Coherent Transients Explained in Terms of the Evolution of the Coherence | 124 |
| C. Supporting Information for Section 4.2 | 126 |
| C.1. Details of CASPT2 Calculations on Cyclohex-2-enone-BF ₃ | 126 |
| C.2. Results of the TDDFT Benchmark | 127 |
| Bibliography | 131 |
| Acronyms | 148 |
| Danksagung | 150 |

Abstract

The ability of modern quantum chemistry to answer ever more complex questions rises steadily. In this thesis, a comprehensive exploration of molecular photochemistry using high-level electronic structure methods for quantum-classical dynamics is presented.

The first chapter introduces theoretical methods for simulating photodynamical processes, focussing on the relaxation of molecules in explicit atomistic environments. These approaches include nuclear wavepacket dynamics embedded within classical molecular dynamics. The presented Ehrenfest and multi-configurational Ehrenfest approaches are applied to small molecules surrounded by noble gas atoms. Furthermore, trajectory surface hopping is discussed, as, in later chapters, the program SHARC is used to perform such simulations. During this thesis, adaptive time-stepping and two new interfaces to electronic structure codes were implemented. These methods facilitate efficient and accurate dynamics calculations on a variety of photochemically relevant systems ranging from simulations in the gas phase with high-level XMS-CASPT2 electronic structure (including spin-orbit couplings) to QM/MM simulations in the condensed phase.

The second chapter focuses on the energy transfer between an infrared laser and solvated molecules, combining the traditional harmonic approximation to calculate infrared spectra with methods based on *ab initio* molecular dynamics. This methodology is used to elucidate the coherent energy transfer dynamics from the field to the molecule in field-resolved spectroscopic measurements.

The third chapter of this thesis surveys the intricate world of 2-enone photochemistry. By exploring $\pi\pi^*$ and $n\pi^*$ reactivity using high-level electronic structure methods, insights are gained into the *Z/E* isomerization of cyclohept-2-enone and the photoinduced rearrangement of 5,5-dimethylcyclopent-2-enone to a ketene.

In the final chapter, mechanistic investigations are extended to Lewis acid-coordinated enones, uncovering the impact of coordination on the electronic states, UV-Vis spectra, and reactivity. Trajectory surface hopping calculations are used in combination with ultrafast transient absorption spectroscopy to uncover the dynamics of the relaxation of cyclohex-2-enone-BF₃ to the reactive triplet states and the photo-induced B-Cl bond dissociation in benzaldehyde-BCl₃.

Collectively, this work exemplifies the potent synergy of computational and spectroscopic techniques in unraveling photochemical mechanisms. From explicit solvent relaxation to multi-step organic reactions and from spectroscopic signatures to intricate electronic transitions, this thesis advances our understanding of photochemical processes across a spectrum of molecular examples. The findings have implications for the design and understanding of photochemical reactions and spectroscopic studies in complex environments.

List of Publications

This thesis is based on the following six publications listed in chronological order. They are reprinted in the chapter 1 (**I**), chapter 2 (**IV**), chapter 3 (**III**, **VI**) and chapter 4 (**II**, **V**).

- I** J. P. P. Zauleck, M. T. Peschel, F. Rott, S. Thallmair, and R. de Vivie-Riedle, “Ultrafast Reactive Quantum Dynamics Coupled to Classical Solvent Dynamics Using an Ehrenfest Approach”, *Journal of Physical Chemistry A* **122**, 2849–2857 (2018).
- II** M. T. Peschel, P. Kabaciński, D. P. Schwinger, E. Thyryhaug, G. Cerullo, T. Bach, J. Hauer, and R. de Vivie-Riedle, “Activation of 2-Cyclohexenone by BF_3 Coordination: Mechanistic Insights from Theory and Experiment”, *Angewandte Chemie International Edition* **60**, 10155–10163 (2021).
- III** D. P. Schwinger, M. T. Peschel, C. Jaschke, C. Jandl, R. de Vivie-Riedle, and T. Bach, “Diels-Alder Reaction of Photochemically Generated (*E*)-Cyclohept-2-enones: Diene Scope, Reaction Pathway, and Synthetic Application”, *Journal of Organic Chemistry* **87**, 4838–4851 (2022).
- IV** M. T. Peschel, T. Buberl, M. Högner, R. de Vivie-Riedle, and I. Pupeza, “Sub-optical-cycle light-matter energy transfer in molecular vibrational spectroscopy”, *Nature Communications* **13:5897**, 1–8 (2022).
- V** D. P. Schwinger, M. T. Peschel, T. Rigotti, P. Kabaciński, T. Knoll, E. Thyryhaug, G. Cerullo, J. Hauer, R. de Vivie-Riedle, and T. Bach, “Photoinduced B–Cl Bond Fission in Aldehyde- BCl_3 Complexes as a Mechanistic Scenario for C–H Bond Activation”, *Journal of the American Chemical Society* **144**, 18927–18937 (2022).
- VI** N. Jeremias, M. T. Peschel, C. Jaschke, R. de Vivie-Riedle, and T. Bach, “Photochemical Ring Contraction of 5,5-Dialkylcyclopent-2-enones and *in situ* Trapping by Primary Amines”, *Journal of Organic Chemistry* **88**, 6294–6303 (2023).

Additional publications listed in chronological order:

- VII** R. Mundil, S. Hermanová, M. Peschel, A. Lederer, and J. Merna, “On the topology of highly branched polyethylenes prepared by amine-imine nickel and palladium complexes: the effect of *ortho*-aryl substituents”, *Polymer International* **67**, 946–956 (2018).
- VIII** T. Buberl, M. Peschel, M. Högner, R. de Vivie-Riedle, and I. Pupeza, “Sub-Optical-Cycle Light-Matter Energy Transfer Dynamics in Molecular Vibrational Spectroscopy”, in 2021 Conference on Lasers and Electro-Optics Europe & European Quantum Electronics Conference (CLEO/Europe-EQEC) (June 2021).

Introduction

Photochemical reactions offer numerous advantages in various scientific and industrial applications. They enable selective and precise transformations of molecules, allowing for the creation of specific products with high efficiency. Photochemistry also provides access to unique reaction pathways, often resulting in novel and complex compounds that might be challenging to synthesize otherwise. Additionally, photochemical processes are environmentally friendly, as they often utilize light as the primary energy source, eliminating the need for hazardous reagents and reducing waste generation.[9–12] These advantages make photochemical reactions invaluable in fields such as organic synthesis and materials science, paving the way for new, sustainable, and innovative solutions to complex chemical problems. A deep understanding of the primary processes and mechanisms of photochemical reactions is required to aid any future discovery process. Obtaining this knowledge can be challenging and requires input from theoretical and computational chemistry, physical chemistry, spectroscopy, and synthetic organic or inorganic chemistry. The goal is the prediction and most effective utilization of yet unknown photoreactivity. In this work, we will approach this task from the computational point of view. This includes predicting the states involved in a photochemical process, calculating their dynamics and spectral properties, and finding out how they are altered by interactions with their environment (the catalysts or solvents) such that reactions are steered toward a particular outcome.

When a molecule is excited by light, it absorbs photons of specific wavelengths, corresponding to the energy gaps between its electronic energy levels. In the Born-Oppenheimer (BO) picture,[13–15] the energy of the absorbed photons excites the molecule from its ground state potential energy surface (PES) to an excited state PES, causing a sudden change in its electronic structure. This change drives the molecule far away from its original equilibrium structure and the thermal equilibrium with the surrounding environment.[16] Due to the non-equilibrium nature of the processes involved, photochemical reactions can not easily be described by statistical theories such as transition state theory. That means that static calculations of free energies at critical points of the PES, which are (with few exceptions) sufficient to understand ground state reactivity, only give a (valuable) first impression of the processes involved in an excited state reaction. Thus, when investigating photochemistry, it is often necessary to explicitly simulate the dynamics of the molecular system to obtain, for example, the branching ratios into different relaxation channels.[17] In solution, these dynamics can also be affected by the solvation environment of the molecule in non-trivial ways.[18, 19] The large amplitude motions of the atoms during the relaxation process can, for example, lead to collisions with the solvent cage, a process that leads to a strong correlation between the motion of the system and its surroundings. The first chapter of this work will deal with methods to simulate dynamics, including such environmental effects. Treating the whole molecule and the environment with its many (electronic and nuclear) degrees of freedom using a fully quantum description is computationally intractable. Thus, we will focus on semi-classical approaches that treat the nuclear motion (of the

environment or the whole system) classically. Chapter 1 will start with a discussion of Ehrenfest dynamics[20–23] applied to system-bath dynamics, a mean-field approach for nuclear motion that is accurate on short timescales. Afterward, multi-configurational Ehrenfest (MCE) theory will be presented,[24–28], which can be used to extend the timeframe for which Ehrenfest dynamics is valid. As an application, the dynamics of an iodine-krypton cluster will be investigated. Finally, trajectory surface hopping (TSH) will be reviewed,[29, 30] where the line of separation between the quantum and the classical description will not be drawn between the solvated molecule and the environment but between the electronic and nuclear systems. In TSH, the motion of the nuclei is guided by a single adiabatic PES at any time, with stochastic jumps between different adiabatic states modeling relaxation and branching processes. This method will be the workhorse for simulations in chapter 4, where it is applied to an Enone-Lewis Acid complex in an explicit solvation environment (section 4.2).

In addition to the theoretical investigation of these ultrafast dynamics, spectroscopic detection of the same processes is possible. The dialogue with experimentalists is a theoretician’s reality check. Otherwise, the many parameters of a simulation can easily lead to an unphysical model. Furthermore, the constraints on experimental observations are quite different from the ones in simulations. Simulations of excited state dynamics are usually limited in the size of the simulated system and the time span that can be simulated. Furthermore, a constant cost vs. accuracy tradeoff has to be made. Experimental observations are more often limited by the stability and purity of the available materials and the intricacies of the experimental setup (time resolution, available pump/probe wavelengths, etc.). Thus, spectroscopic techniques and simulations complement each other when studying the mechanisms of photochemical reactions. One powerful technique for investigating excited molecules on ultrafast time scales and directly observing the predicted transient species is ultrafast transient absorption (TA) spectroscopy. This pump-probe technique, pioneered by Zewail and co-workers,[31, 32] works by first exciting the molecule using a femtosecond pump pulse, which triggers the excited state dynamics. Then, after a variable time delay, the changes in the molecule are interrogated by a second pulse, the probe. This pulse should be as spectrally broad as possible to follow the excited state nuclear motion over the entire excited state PES and obtain as much spectral information as possible about the transient species. However, the transient spectra are often hard to interpret due to broad and often featureless excited state absorption (ESA) bands that might even overlap with contributions from stimulated emission. Here, quantum chemical calculations can be helpful. By using high-level electronic structure methods and an appropriate sampling of nuclear configurations,[33] it is possible to reproduce the bands, disentangle different contributions to the absorption, and ensure the correct assignment of signals to certain transient species.[34] Examples of this methodology will be given in chapter 4 of this work.

There is also constant development of new spectroscopic methods. A recent example is field-resolved spectroscopy, where the coherent part of the electric field of a laser pulse passing through a sample is detected using electro-optic sampling.[35] With this technique, the electric field can be recorded with sub-fs time resolution, and the molecular sample’s signatures imprinted onto the field can be studied. The intricacies of the energy transfer between the laser field and the molecule in its solvation environment are discussed in chapter 2.

Which processes do we wish to study using the above-described computational and spectroscopic methods? 2-Enones, sometimes called α,β -enones, are one of the most prolific classes of compounds when it comes to their photoreactivity.[36] Depending on the structure of the specific 2-enone, specific reaction conditions (solvent, irradiation wavelength, concentration of the enone), and differing reaction partners, a large variety of photochemical pathways can be explored, ranging from photorearrangements[6, 37] over photoreductions[38] and dimerizations[39, 40] to crossed [2+2] photocyclizations[41, 42] or photo-initiated Diels-Alder reactions.[3, 43, 44] This wealth of different accessible pathways is due to the tight interplay between the $n\pi^*$ and $\pi\pi^*$ states of the 2-enone,[45, 46] which are the topic of chapter 3 of this work. Because of the many different possible products, there is considerable interest in altering the excited state energy landscape of the 2-enone to enable new and more selective transformations. Here, the recently emerging field of organo-photocatalysis can be explored.

In the last years, organo-photocatalysis has experienced an explosion in terms of applications, redesign of well-established systems, and identification of novel scaffolds.[47, 48] These novel photocatalysts hold great promise for a wide variety of synthetic applications. A photocatalyst's most straightforward mode of action is just to be excited and then transfer the excitation energy to the reactive substrate (either through triplet or singlet sensitization).[49] The photocatalyst might also act as a redox reagent,[50–52] with excited state species often having strong oxidating (or reducing) properties, especially if charge separation occurs. In this way, the catalyst can enable a reaction by electron transfer from (to) the substrate. The catalyst is then regenerated through a sacrificial electron acceptor (electron donor), which, by itself, has much less extreme redox potential. Finally, photocatalysts can alter the absorption properties of the substrate in a way that it can be excited more readily. In this way, the complex of the substrate and the catalyst can be excited selectively, and the catalyst can change the course of the reaction via its electronic or steric influence without directly carrying the excitation. An example of photocatalysis of the latter kind is the photo-activation of 2-enones by Lewis acid catalysts,[53–55] which will be studied in chapter 4 of this work.

This thesis presents significant advancements in understanding the photochemical processes of molecular systems through the development of innovative computational techniques and their application to a broad spectrum of chemical systems. In all of these applications, the separation between a molecular system's quantum and classical parts features prominently. The first chapter models cyanogen iodide (ICN) in liquid argon (section 1.1) and iodine embedded in a krypton cluster (section 1.2) with quantum dynamics (QD) approaches based on Ehrenfest dynamics. Thus, we discuss the coupling between the nuclear motion of a solvated molecule (treated quantum mechanically) and the motion of the surrounding environment (treated classically). The second chapter treats the interaction of methylsulfonylmethane (DMSO₂) with an explicitly time-dependent electric field, an infrared (IR) laser pulse. This is done in two different ways, via a separation between the electric field (treated classically) and the vibrational states of the molecule (treated quantum mechanically) or via a classical dipole autocorrelation function calculated from *ab initio* molecular dynamics (MD),[56, 57] which implies a separation between the electrons (treated quantum mechanically) and the vibrations (treated classically). The separation between electronic and nuclear degrees of freedom will also be discussed in the context of the TSH approach (section 1.3). Some new developments are presented here, particularly a new interface between the fast and

low-scaling electronic structure code FermiONs++[58–60] and the SHARC package for excited state dynamics. We will apply this interface to quantum mechanics/molecular mechanics (QM/MM) simulations of the complex of cyclohex-2-enone and BF_3 in dichloromethane (DCM) solution (section 4.2). This is put into context by a treatise on the electronic structure and reactivity of small, cyclic 2-enones (chapter 3) and the excited state dynamics and spectroscopy of their Lewis acid complexes (chapter 4). Both of these chapters feature close collaboration with experimentalists. In chapter 3, the focus is on high-level static extended multi-state complete active space perturbation theory (CASPT2) (XMS-CASPT2) calculations[61, 62] to explain mechanistic observations made in synthetic experiments.[3, 6] In contrast, in chapter 4, dynamical calculations lead the way for ultrafast TA experiments and the discovery of new reactions.[2, 5] In summary, the findings presented in this work demonstrate the considerable impact of *ab initio* simulations on the design and understanding of photochemical reactions and spectroscopic studies in complex environments.

1. Method Development and Theoretical Background

Spectroscopic properties of a molecular system can be accurately calculated from the wavefunction Ψ , given by the time-dependent Schrödinger equation (TDSE)[63, 64]

$$i\hbar \frac{\partial}{\partial t} \Psi(t) = (\hat{H}_{mol} + \hat{V}_{ext}(t)) \Psi(t), \quad (1.1)$$

in which \hat{H}_{mol} , the molecular Hamiltonian, contains the kinetic operators and all interactions between the constituents of the system, and $\hat{V}_{ext}(t)$ describes the time-dependent interaction with the external fields. In the (electric) dipole approximation, $\hat{V}_{ext}(t)$ takes the form

$$\hat{V}_{ext}(t) = \hat{\mu}_{mol} \cdot \mathcal{E}(t), \quad (1.2)$$

where $\hat{\mu}_{mol}$ is the dipole operator of the molecular system and $\mathcal{E}(t)$ is the electric field.

In this first chapter, we describe several approaches that can be used to simulate the dynamics of a molecular system that evolves under the TDSE. Suppose the molecular system is not isolated but instead embedded in a complex environment. In that case, it is not feasible to include the environment and its interactions with the system of interest in \hat{H}_{mol} and solve the TDSE due to the many degrees of freedom present in the environment. Thus, a variety of approximations exist. In the first section, Ehrenfest dynamics will be discussed, where the system and environment are treated based on a simple product ansatz, followed by a classical approximation for the environment's degrees of freedom. Due to this classical treatment, the number of degrees of freedom is not a limiting factor in most cases. It can accurately treat short-time dynamics within the so-called Ehrenfest time and is a starting point for deriving more detailed approximations. Accordingly, in the second section, MCE will be discussed, which expands on the Ehrenfest approach by adding some quantum character back into the description of the environment. Hence, it extends the time frame for which the dynamics are accurate and can, in principle, treat some quantum effects in the environment. Ehrenfest dynamics and MCE can be applied to either the separation between the electrons and nuclei in the same molecule or the separation between the nuclear degrees of freedom of a system molecule and the nuclear degrees of freedom of a bath. In a third section, we will discuss TSH which, in addition to the short-time limit, is also approximately correct in the long-time limit. However, it fails for dense sets of states with delocalized couplings between them and can not capture quantum effects in the environment. It is best applied to the separation between the electronic system and the nuclei of a molecule.

1.1. Ehrenfest Dynamics

Ehrenfest dynamics was one of the earliest approaches to describe the coupling between a quantum and a classical system. Ehrenfest Dynamics[20–23] is often applied to a single

molecule where the electronic degrees of freedom are separated from the nuclear degrees of freedom and the latter are treated as the environment. In this section, we will apply the approach to the separation of a molecular system S , described quantum mechanically, and a condensed phase environment E , described classically. In this context, we use Ehrenfest dynamics to draw the line for the quantum-to-classical transition between the nuclear degrees of freedom of the embedded system and the nuclear degrees of the environment. Electronic degrees of freedom of the embedded system are treated by the BO approximation.

Any Hamiltonian describing a system embedded in an environment can be expressed as

$$\hat{H} = \hat{H}^S + \hat{H}^E + \hat{V}^{ES} \quad (1.3)$$

with a part \hat{H}^S depending only on the system degrees of freedom, a part \hat{H}^E depending on the environmental degrees of freedom, and a coupling potential \hat{V}^{ES} that depends on both, the system and the environment.

The simplest possible approach for the wavefunction that separates the environmental degrees of freedom from the system degrees is a product of a system wavefunction Ψ^S and an environment wavefunction Ψ^E ;

$$\Psi = \Psi^S \Psi^E. \quad (1.4)$$

Inserting this approach into the TDSE (eq. (1.1)) and forming appropriate inner products, a coupled set of differential equations is obtained. These equations have the same structure as the TDSE. The coupling between the system and the environment appears in both as a time-dependent mean-field potential. For example, the system experiences a potential $\langle \Psi^E(t) | \hat{V}^{ES} | \Psi^E(t) \rangle$ where the time dependence originates from the motion of the wavepacket associated with the environment.

$$i\hbar \frac{\partial}{\partial t} \Psi^S(t) = (\hat{H}^S + \langle \Psi^E(t) | \hat{V}^{ES} | \Psi^E(t) \rangle) \Psi^S(t) \quad (1.5)$$

$$i\hbar \frac{\partial}{\partial t} \Psi^E(t) = (\hat{H}^E + \langle \Psi^S(t) | \hat{V}^{ES} | \Psi^S(t) \rangle) \Psi^E(t) \quad (1.6)$$

This is known as the time-dependent self-consistent field (TDSCF) or time-dependent Hartree (TDH) method[65–67], which serves as a starting point for the derivation of Ehrenfest dynamics. Ehrenfest dynamics is the classical analog to TDSCF, where a classical trajectory has replaced the wavepacket of the environment. Thus, the Ehrenfest approach is also known as quantum/classical TDSCF.[68, 69] A detailed derivation of the Ehrenfest equations of motion can, for example, be found in [21, 23, 70, 71]. The working equations of the Ehrenfest method are

$$i\hbar \frac{\partial \Psi^S}{\partial t} = (\hat{H}^S + \hat{V}^{ES}(q^E)) \Psi^S \quad (1.7)$$

and

$$m^E \frac{\partial^2 q^E}{\partial t^2} = -\nabla (V^E + \langle \Psi^S | V^{ES} | \Psi^S \rangle). \quad (1.8)$$

The motion of the environment is no longer described by the TDSE but by a trajectory following Newton's second law, with a well-defined position $q^E(t)$. It experiences a mean-field force $-\nabla \langle \Psi^S | V^{ES} | \Psi^S \rangle$ evaluated as an integral over the entire quantum system's

wavepacket. This is in contrast to the TSH method that will be presented in section 1.3. Because of this, Ehrenfest dynamics is independent of the basis which is used to express the wavepacket. In the equation for the quantum system, the expectation value over the environment wavepacket has been replaced by a simple evaluation of the coupling potential \hat{V}^{ES} at the classical position of the environment $q^E(t)$.

As part of this thesis, a previous implementation[72] of an Ehrenfest approach coupling the internal degrees of freedom of a solute molecule to a bath made up of explicit classical atoms/molecules was tested and refined. It combines a pre-calculated PES for the quantum system's H_S with classical force-fields for the environment V_E and the interaction V_{ES} that are evaluated *on the fly*. The quantum dynamics calculations on the potential energy surface were performed by our in-house QD program, which was coupled to the MD program GROMACS[73] to calculate the system-environment interaction and to propagate the classical environment. Simulations were carried out on the photo-dissociation of ICN in liquid argon and on the $S_2 \rightarrow S_1$ relaxation of Uracil in an aqueous solution.[74–77]

The article “Ultrafast Reactive Quantum Dynamics Coupled to Classical Solvent Dynamics Using an Ehrenfest Approach” was published in *Journal of Physical Chemistry A*. Key points are:

- The approach for mixed quantum/classical dynamics can be implemented in a stable manner using fixed time-steps of 0.1 fs with a velocity Verlet integrator for the classical environment and a Chebychev or a split-operator propagator for the quantum system. Errors in energy conservation are lower than $10^{-5} E_H$ for the ICN system.
- A new algorithm is developed that properly includes the rotation and translation of the solute molecule in the classical system while only including the vibrational degrees of freedom described by the potential energy surface in the quantum description.
- The dissociation of ICN is severely hindered by collisions with the argon atoms. Forty-nine independent Ehrenfest trajectories are sufficient to converge the percentage of un-dissociated ICN to within 2%. While almost the whole wavepacket dissociates in the gas phase, in solution, 55% of the total probability density is trapped by the solvent cage. Whether trapping occurs or not depends on the specific arrangement of the solvent atoms.
- Decoherence can be observed when averaging over all trajectories since the fixed phase relationship is lost due to the differently fluctuating interaction energy in each solvent environment. It is clearly visible as a reduction in interference patterns in the Wigner distribution.
- The speed of the $S_2 \rightarrow S_1$ relaxation of Uracil is not directly affected by the solvation in water. Periodic increases and decreases in the S_1 barrier are observed. Individual Ehrenfest configurations, consisting of a vibronic Uracil wavepacket and the associated trajectory of bulk water, are found to relax slightly slower or faster. However, with 35 initial conditions for the solvent environment, these effects average out such that, in the final statistical ensemble of all Ehrenfest configurations, no significant difference to the gas phase simulation is observed. This is in line


with experiments where the fastest relaxation constant is largely independent of solvation and similar to the one observed in the gas phase.[78, 79]

Hereafter, the article “Ultrafast Reactive Quantum Dynamics Coupled to Classical Solvent Dynamics Using an Ehrenfest Approach” published in *Journal of Physical Chemistry A* is reprinted with permission from *Journal of Physical Chemistry A*, **122**, 2849–2857 (2018). Copyright 2018 American Chemical Society. Supplementary information is available online.

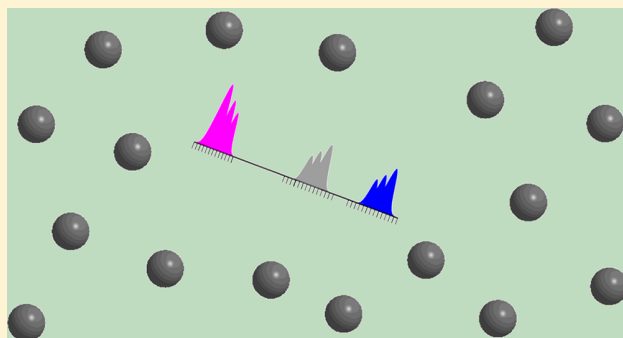
Ultrafast Reactive Quantum Dynamics Coupled to Classical Solvent Dynamics Using an Ehrenfest Approach

Julius P. P. Zauleck, Martin T. Peschel, Florian Rott, Sebastian Thallmair,[†] and Regina de Vivie-Riedle^{*†}

Department of Chemistry, Ludwig-Maximilians-Universität München, D-81377 München, Germany

 Supporting Information

ABSTRACT: The inclusion of solvent effects in the theoretical analysis of molecular processes becomes increasingly important. Currently, it is not feasible to directly include the solvent on the quantum level. We use an Ehrenfest approach to study the coupled time evolution of quantum dynamically treated solutes and classical solvents system. The classical dynamics of the solvent is coupled to the wavepacket dynamics of the solute and rotational and translational degrees of freedom of the solute are included classically. This allows quantum dynamics simulations for ultrafast processes that are decided by environment interactions without explicit separation of time scales. We show the application to the dissociation of ICN in liquid Ar as a proof of principal system and to the more applied example of uracil in water.



INTRODUCTION

Solvents play an important role in molecular processes. They are the medium in which a majority of reactions take place and influence the course of reactions directly or indirectly. While most catalytic effects of the solvent can be qualitatively described very well and then be modeled accordingly,¹ the more subtle influences like viscosity or electrostatic interaction are often more difficult to include.^{2,3} However, they sometimes are decisive to the outcome of a reaction.^{4–9} One way this can happen is by electrostatic stabilization of certain reaction pathways, thereby favoring their respective products.^{5,6} Other possibilities are dynamic solvent effects^{7,8,10} that can for example deflect dissociative motions, because solvent molecules have to be pushed away. This can favor one of several competing pathways as well. Further complexity is added if quantum effects such as tunneling and passing through conical intersections (CoIn)^{11,12} occur. Then, quantum dynamics (QD) simulations are most suited.

There exist a number of strategies to describe a mixed quantum-classical interaction for different systems or to partly introduce quantum behavior to classical systems. Examples are the polarizable continuum models^{13–15} that allow to approximate solvent effects in quantum chemical calculations using an implicit description, the linearized semiclassical initial value representation,^{16–19} which describes all particles of a system with increasing quantum behavior until convergence is reached, Ehrenfest dynamics,^{20–22} which separates the system into a quantum and a classical subsystem that interact, fewest-switches surface hopping,^{20,23} in which some quantum behavior is introduced to classical nuclear trajectories by allowing transitions between electronic states and the use of the

Liouville–von Neumann equation^{24–27} for different quantum-classically coupled approaches^{28–35} which introduces the environment as a classically treated bath and can with approximations be applied to systems with environments of realistic sizes.³⁵ We are interested in a description suited for ultrafast reaction dynamics where the focus lies on the solute that has to be treated quantum dynamically. In this direction we developed two methods for modeling solvent effects in QD simulations, either implicitly in a continuum model by the use of a friction force⁷ or explicitly by using molecular dynamics (MD) snapshots of the solvent.⁸ Both approaches cover many scenarios involving solute–solvent interaction, but not all. As the former calculates the interaction as Stokes' friction caused by viscosity, cases where collisions between solute and solvent atoms deflect the internal momentum of the solute are not taken into account. Those collisions are included in the latter method, but as it relies on frozen snapshots, the response of the solvent to the motion of the solute is not included. For some systems this is sufficient as basic repulsion by the solvent cage can introduce the required deceleration. In the case of more complex reactions a response of the solvent cage is desirable. For example, if the shape of the solute changes considerably due to the formation of a new bond, the solvent environment has to rearrange accordingly. In case of a frozen snapshot, the solute will prevent the reaction and additional information about the system is necessary for a meaningful interpretation. If the solvent is allowed to respond, the solvent cage can make

Received: October 19, 2017

Revised: February 16, 2018

Published: March 2, 2018



space for the expanding solute in real time. Thus, the natural next step is to explicitly include the solvent dynamics to enable a fully coupled QD/MD (cQDMD) description.

The time-dependent self-consistent field (TDSCF)^{36,37} method we use here accomplishes this. It treats selected nuclear degrees of freedom of the solute using quantum mechanical wavepackets while the nuclei of the solvent are represented classically. In doing so, it propagates a grid-based QD solute system on its intrinsic potential energy surface and simultaneously propagates the solvent classically by extending the TDSCF approach to larger, reactive environments and a multidimensional description of the solute using selected active degrees of freedom. It should be noted that the TDSCF method is closely related to a grid-based implementation of the molecular dynamics with quantum transitions (MDQT) approach when part of the nuclear degrees of freedom are included in the quantum system.³⁸ In MDQT, the difference is that the classical degrees of freedom interact only with one electronic state of the wave packet at any given time. The TDSCF approach was previously applied to the much smaller or less reactive systems, such as the dissociation of the clusters I₂Ne,³⁹ I₂He,⁴⁰ XeHI,⁴¹ and ArHCl⁴² in gas phase or the vibrational relaxation of a cyanide ion in water.^{43,44} Our method is to some extent related to an approach by Yamada et al.,⁴⁵ which propagates a solute quantum dynamically in its eigenstate representation and couples it to a semiclassical solvent using a fewest switches algorithm but is restricted to a single degree of freedom for the solute. The grid-based character of the approach we are presenting allows for more general applications within the field of ultrafast dynamics, including molecular processes like chemical reactions that move far away from equilibrium structures and for more degrees of freedom for the quantum system. While one could in principle include multiple solvent configurations for systems that simultaneously explore different reactive channels, this is in ultrafast processes usually not the case and at this point our focus remains on single solvent configurations. To our knowledge, we are the first to apply this approach in this general extent to grid-based QD with all its advantages. It also allows the inclusion of translational and rotational motion of the solute and offers an approach toward describing decoherence. In each step, the interaction between solvent and solute is treated using a quantum-classical TDSCF,^{36,37} also known as Ehrenfest dynamics.^{20,21} While first physical interpretations can be made, the main focus of this work lies on presenting a method that allows a straightforward way to simulate solvated systems whenever force fields are available for the solvent and solute–solvent interactions and to present the study of first applications.

In the following section we present the theoretical background of our approach and introduce an extension of quantum-classical TDSCF allowing for translation and rotation of the solute. We then present the application to two example systems. One is the dissociation of electronically excited ICN in liquid argon where the QD can be reduced to a one-dimensional grid along the carbon–iodine bond. As a second example we discuss the ultrafast relaxation of uracil in liquid water after photoexcitation during its first few hundred femtoseconds which can be well described by the dynamics on a two-dimensional PES⁴⁶ before we conclude.

TDSCF FORMULATION TO COUPLE A NUCLEAR WAVEPACKET TO CLASSICAL NUCLEI

As a first step, the nuclear and electronic degrees of freedom of the solute are separated by means of the Born–Oppenheimer approximation or a post-Born–Oppenheimer approach. Next, the nuclear degrees of freedom to be used in the QD are chosen and the corresponding grid-based potential energy surface (PES) of the solute in the gas phase is calculated. This can be done with any number of electronic states. The expected initial structure of the solute is then placed in a random orientation of the classically treated solvent environment, followed by an equilibration of the solvent while keeping the solute frozen using a constraint algorithm. Equilibration of the solvent can be achieved with a gradient descent algorithm, ensuring the absence of unphysically small distances.

As a result, we obtain a possible initial condition for the full system, once the solvent arrangement reaches a relative minimum. There are several choices for the constraint algorithm, we chose to use RATTLE⁴⁷ throughout our work. As a last step, before initiating the cQDMD approach, the solvent system is brought to the desired temperature using a thermostat.

The initial wavepacket on the solute PES has now to be coupled to the MD of the solvent to be propagated. This can be accomplished by the use of quantum-classical TDSCF also known as Ehrenfest dynamics. It starts by treating the total wave function Ψ of a system as the product of the wave functions of two subsystems. This results in the quantum–quantum TDSCF method,⁴⁸ yielding coupled equations to propagate both systems using QD:

$$i\hbar \frac{\partial \Psi^E}{\partial t} = (T^E + V^E + \langle \Psi^S | V^{ES} | \Psi^S \rangle) \Psi^E \quad (1)$$

$$i\hbar \frac{\partial \Psi^S}{\partial t} = (T^S + V^S + \langle \Psi^E | V^{ES} | \Psi^E \rangle) \Psi^S \quad (2)$$

T and V are kinetic and potential energy operators, respectively, the superscripts E and S indicate that a quantity belongs to the environment or the solute, and ES means it belongs to both. At this point the subsystems are usually separated based on their mass in a system of light and a system of heavy particles. The light subsystem then continues to be treated using QD while the heavier one is approximated using MD.²¹

We do not distinguish light from heavy subsystems but realize that we are mainly interested in a highly precise description of the dynamics of the solute whereas the dynamics of the solvent are of minor interest. The major purpose of the inclusion of the solvent environment is rather to cover its effect on the solute behavior. Hence, we approximate the solvent as classical particles. While this misses quantum effects in the solvent and correlational interaction between the solute and the solvent, those effects cannot be included explicitly due to the size of such a system. The resulting working equations²⁰ are given by

$$M_I \ddot{R}_I = -\nabla_I \sum_J V_{IJ}^E - \nabla_I \langle \Psi^S | V_I^{ES} | \Psi^S \rangle \quad (3)$$

as the equations of motion for the solvent and by

$$i\hbar \frac{\partial \Psi^S}{\partial t} = \left(T^S + V_{\text{PES}}^S + \sum_I V_I^{ES} \right) \Psi^S \quad (4)$$

as the Schrödinger equation for the solute. The form of the potential operator V_I^{ES} in eq 3 and 4 results from the wave function of the solvent being a Dirac delta function in the classical limit. The indices I and J refer to the I th atom and J th atom of the solvent, respectively, M_I is the mass of the I th atom, and R_I is its position vector. $V_{IJ}^{\text{E}}(R_I, R_J)$ is the interaction potential between the particles of the solvent environment and $V_I^{\text{ES}}(R_I, r)$ is the interaction potential between the solvent particles and the solute which together with $\Psi^{\text{S}}(r)$ results in a mean field in eq 3. The mean field is a function of the degrees of freedom r of the solute. eq 4 uses the kinetic energy operator $T^{\text{S}}(r)$ and the PES $V_{\text{PES}}^{\text{S}}(r)$ of the solute as well as $V_I^{\text{ES}}(R_I, r)$. The potentials V_{IJ}^{E} and V_I^{ES} can for example be calculated using force fields or to some extent using quantum chemistry.⁷ Figure 1 illustrates the construction of V_I^{ES} . Note that for each point of

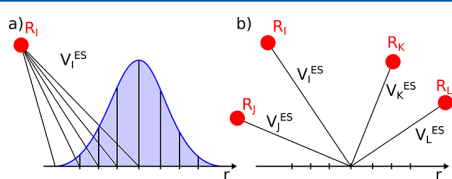


Figure 1. Schematic representation of the interaction potential V_I^{ES} construction from two perspectives. (a) Solute acting on solvent particle I . Using the example of a Gaussian wavepacket, every interaction potential between the solute at grid coordinate r and the solvent is calculated and weighed according to the population density $|\Psi^{\text{S}}|^2$ shown. (b) Four solvent particles acting on the solute. This interaction is shown for one exemplary grid point, corresponding to a point in the configuration space of the solute. The interaction potentials from the solvent particles are summed and such a sum has to be calculated for every grid point, resulting in an energy surface for the interaction potential on the grid.

the PES represented on a spatial grid the corresponding geometry of the solute has to be used to calculate V_I^{ES} . To calculate the force acting on a solvent particle, every interaction potential between the solute at grid coordinate r and the solvent is calculated and weighed according to its population density. For the solute, the interaction potentials from the solvent particles are summed at every grid point, resulting in the sum of the interaction potentials $\sum_I V_I^{\text{ES}}$. It is also worth pointing out that the interaction potential between the solvent and the solute in the QD calculation has the form of a changing external potential.^{7,8} Equations 3 and 4 can be solved using the standard propagation tools of QD and MD. We used the split-operator method⁴⁹ for the QD of ICN, the Chebychev propagation scheme⁵⁰ for the QD of uracil and the velocity Verlet integrator⁵¹ for the MD throughout this work.

Thus, far, the time evolution of the solute is restricted to the QD of the selected degrees of freedom. In addition, rotation and translation can easily be included using a classical approach. The main motivation for this is the difference in the distributions of collisions that are experienced by the solute with and without these external degrees of freedom. This is especially relevant for light solutes as they, according to the Maxwell–Boltzmann distribution, have larger velocities. Ideally, one would like to have the same interaction potential in both directions between the solute and the solvent system. Thus, since a force weighted according to the population on a grid point corresponding to a certain solute geometry acts on the solvent, the identically weighted counter force should act on exactly this geometry. While this could be realized by adding

the rotational and translational degrees of freedom to the QD simulation, the computational cost of this gain in accuracy is unreasonably large. Instead, as an approximation we use a single geometry on which the counter force is acting, corresponding to the classical treatment of these degrees of freedom. To achieve this, we include an additional step while discretizing the time. As we progress one time step according to eqs 3 and 4, we also propagate a virtual rigid classical solute (VRCS) system where all internal degrees of freedom are frozen using a constraint algorithm. It replaces the quantum system for the MD step and is propagated classically using the aforementioned counter forces. Afterward, the rotation and translation of the VRCS is transferred to the quantum system by means of changing the location and orientation of the spatial grid with respect to the solvent box. The VRCS could also be used to treat the rotational influence on the vibrational degrees of freedom. However, we chose to not include this interaction due to its small impact on our systems.

To construct the VRCS, a single solute structure has to be found that approximates the relevant dynamical properties best. One way is by simply using the geometry corresponding to the position expectation values of the wavepacket given by $r_i^{\text{VRCS}} = \langle \Psi^{\text{S}} | r_i^{\text{S}} | \Psi^{\text{S}} \rangle$ for the i th internal coordinate r_i . Another way to do this is by enforcing that the VRCS system has the same center of mass and most similar moment of inertia ($I = \sum_i m_i x_i^2$ along a principal axis) as the respective expectation values of the quantum system. After testing both, we found that the error in energy conservation resulting from the former way is an order of magnitude smaller and decided to use this one. Since finding a structure with a moment of inertia that is most similar to the expectation value of the moment of inertia introduces additional complications, such as the ambiguity of these structures in higher-dimensional internal coordinate spaces, the use of the position expectation value is a justified simplification. Note that the latter approximation might result in a slightly better conservation of angular momentum. After the propagation of this VRCS system, the space grid of the QD system is translated by the same distance and rotated by the same angles within the classical solvent environment.

These considerations allow us to formulate a propagation step using the same time increment for all systems. The QD of the solute require the interaction potential V_I^{ES} and the PES. The solvent atoms require forces between themselves and between themselves and the solute. Again, the solvent–solute forces have to be calculated for every geometry corresponding to a grid point and weighed according to the population on that grid point before being summed up. The VRCS gets its forces on the individual atoms as population weighted forces over all geometries, summed over all solvent atoms:

$$\mathbf{F}_i^{\text{VRCS}} = \sum_I \int |\Psi^{\text{S}}(r)|^2 \mathbf{F}_i(r) dr \quad (5)$$

Both QD and MD systems are then propagated using these interactions and their previous positions, velocities, or wave functions depending on the propagation algorithm. For the solvent this finalizes the step. The QD solute system in addition has to be updated according to the changes in center of mass and angular orientation in the VRCS system. An illustration of this algorithm can be found in Figure S1 in the Supporting Information.

Note that at each time step, it is necessary to calculate all the interaction forces and energies between the solute which is

represented in internal coordinates and the solvent in Cartesian coordinates. This can be done with a procedure that constructs a geometry in Cartesian coordinates for each point of the solute grid. Using the three translational and three rotational degrees of freedom contained in the VRCS, the M internal coordinates and the $3N-6-M$ constraints for a nonlinear system of N atoms, there is always a unique geometry for each grid point. The same is true for linear systems, having one more constraint and one less rotational degree of freedom. There are several ways to construct this mapping, as reference points within the studied systems have to be used. For the example of ICN, where only the distance between I and C is unconstrained, one may start by aligning the molecule along the x -axis and setting the position of the I atom to $x_I = -R_{IC}$ using the IC distance R_{IC} , the C atom to $x_C = 0$ and the N atom to $x_N = R_{CN}$ using the constrained CN distance R_{CN} . In the second step the center of mass of the molecule can be shifted to the center of mass of the VRCS and using Euler angles, the molecule can be rotated to align its axis with the axis of the VRCS.

RESULTS AND DISCUSSION

A Simple Test Case: ICN in Liquid Ar. We implemented this cQDMD approach using a QD program of our own design coupled to Gromacs⁵² performing the calculation of the interaction energies and forces and the MD of the solvent. The time evolution after electronic excitation of ICN in liquid argon at 84 K and 1 bar was chosen as example system. The dissociation of ICN in an argon environment is a well-studied test case.^{38,53–55} The system was simulated using the one-dimensional excited spin-orbit state S_1 as described by Goldfield et al.⁵⁶ as the internal PES for the solute. It was placed in a periodic box with side lengths of 21.17 Å, 200 Ar atoms and a van der Waals cutoff of 10 Å. The initial wavepacket is given by a stationary Gaussian with its center at a distance of 2.12 Å and a standard deviation of 0.121 Å unless stated otherwise. This corresponds to the vibrational ground state of the S_0 state and can therefore be considered as a first approximation of a laser excitation from the electronic ground state. The potentials for the solvent-solvent and solvent-solute interaction have been used as given by Benjamin et al.⁵⁷ The initial conditions of the QD system are also illustrated in Figures S2 and S3 in the Supporting Information. For each simulation the initial condition of the solvent was created by equilibrating a random orientation of the argon atoms. The system was propagated with the split-operator method⁴⁹ using time steps of 0.1 fs.

Given that the energy expectation value of the initial wavepacket lies well above the dissociation energy (7.3 times as much), dissociation is expected when no environment is present. This is also the result of a QD simulation in vacuum shown in the upper panel of Figure 2 (black line) with an undissociated fraction of only 3% after 700 fs. We define parts of the wavepacket with an iodine-carbon distance $r_{IC} > 6.5$ Å as dissociated and remove them using a negative imaginary potential, since after this distance the chance of recombination is negligible. What happens in the solvent environment? The averages of 49 cQDMD simulations with random solvent arrangements are shown in the upper panel of Figure 2 (red line) together with the results of two exemplary simulations (green and blue lines). Note that a small number of initial conditions for the solvent environment is sufficient to reach convergence in the observables of the quantum system, as can be seen in the lower panel of Figure 2. The reason is that the

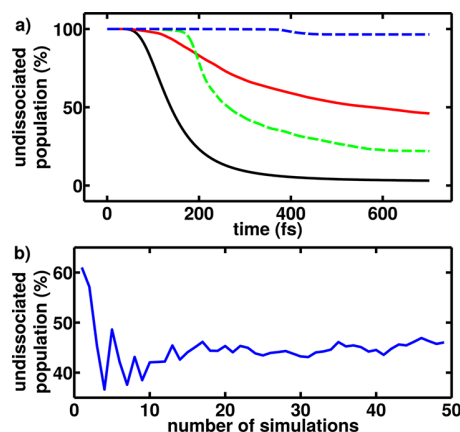


Figure 2. Percentage of undissociated ICN after time t and convergence behavior of dissociation percentage. (a) Reference system without solvent (black solid), two sample simulations with different initial solvent arrangements (green and blue dashed), and the averaged result over 49 simulations using different initial solvent arrangements (red solid). (b) Percentage of the undissociated population at 700 fs as a function of the number simulations with different initial conditions. Convergence is achieved after about 20 simulations.

interaction potential with the solvent environment is essentially projected on the low-dimensional space of the quantum system and then further reduced to a single scalar value. The results of the simulations suggest that the dissociation pathway is still accessible in a liquid argon environment, however, the dissociation is delayed and a significant part of the wavepacket gets trapped inside the solvent cage. Hence, the percentage of undissociated ICN raises to 45% in liquid argon, which is about 15 times higher than in vacuum.

The energy of the two subsystems including rotation and translation of the QD system is shown in Figure 3. Here we used another set of starting conditions with a lower, non dissociative energy of the initial wavepacket, a stationary Gaussian with its center at a distance of 2.74 Å and a standard deviation of 0.079 Å (see Figure 3 in the Supporting

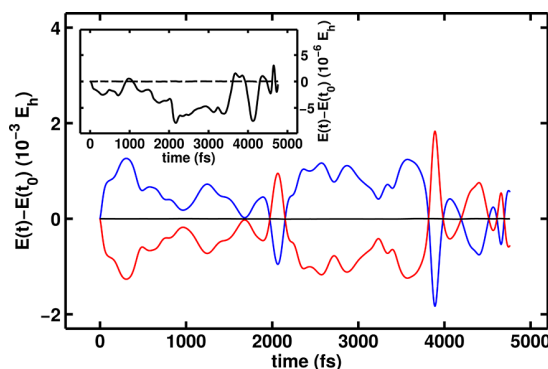


Figure 3. Change in energy for the QD (red solid) and the MD (blue solid) system during a single simulation for the low energy initial conditions. The errors in energy conservation introduced together with translational and rotational degrees of freedom (black solid) are negligible in comparison to the exchanged energy. The interaction potential energy is included in the quantum system. The subplot compares the error in total energy conservation over time without (black dashed) and with (black solid) translational and rotational degrees of freedom of the QD system.

Information). It can be seen that the energy exchange between the QD (red line) and the MD system (blue line) has a very small relative error (black line). The error in energy conservation is depicted magnified in the subplot of Figure 3. In the case of the full system without rotational and translational degrees of freedom of the solute the fluctuations are on the order of $10^{-8} E_h$ which can be attributed to numerical errors. This is to be expected since the TDSCF approach by itself is energy conserving.⁵⁸ As we include the translational and rotational degrees of freedom of the solute, the fluctuations increase up to the order of $10^{-6} E_h$. This is consistent with our expectations of the introduction of small errors due to the use of the position expectation values used for the propagation of the VRCS.

For the computation time we expect the typical algorithm-dependent scaling behavior for the subsystems.⁵⁹ In our case, having no Coulomb interactions and using a cutoff, this is $O(m)$ for the MD with the number of solvent atoms m and $O(n \log n)$ for the QD due to the use of the fast Fourier transform with n being the number of grid points used for the solute. Calculating the interaction between the subsystems is $O(n)$ as the interaction potential is calculated for every grid point. For our calculations, we observed linear scaling with the number of grid points used, up to a maximum of $n = 2048$. This means that the higher scaling of the QD algorithms has not taken over yet, which is explained by the large number of potential calculations between the n solute structures and the solvent atoms closer than the cutoff radius.

Another phenomenon that should be observable in this scenario is decoherence. Since we performed simulations starting from an ensemble of different initial conditions, we are able to make physical predictions, e.g., estimate decoherence times. We chose to calculate the decrease of the coherence $\gamma = \sum_{i \neq j} |\rho_{ij}|$. Here $\rho = \frac{1}{N} \sum_{i=1}^N \rho^i$ where ρ^i is the density matrix of the i th initial condition of the solvent taking into account $N = 21$ initial conditions. ρ^i was constructed using the first 50 vibrational eigenstates of the gas phase molecule in its S_1 state as basis. An exponential decrease with a time constant $\tau = 380$ fs is observed. This is comparable to decoherence times in similar systems.^{60,61} Figure 4a shows the evolution of the coherence $\gamma(t)$ together with the exponential fit. There might be decoherence on a substantially longer time scale leading to a better description by a multiexponential fit. However, a monoexponential fit describes the decay well on the studied time scale. Another way to observe decoherence is to compare the density matrix ρ for the low energy initial conditions for the wavepacket. The Wigner function of a wavepacket propagated in the gas phase and the Wigner function of the sum of the wavepackets propagated in the environment which are shown in Figure 4, parts b and c, respectively. It can be seen that the interference pattern simplifies in the solvent environment with the loss of phase relation due to the varying impact of the different environment arrangements. The convergence behavior for all shown quantities as well as the decrease of purity over time is shown in the Supporting Information.

A Real Life Example: Uracil in Water. The photo-relaxation of uracil is key to understanding the photostability of RNA, since it can provide insight into the main mechanism by which photodamage is prevented. As a range of pump–probe experiments have shown, it is a complex multistep process in the gas phase^{62–64} as well as in solution.^{65–67} In general, these

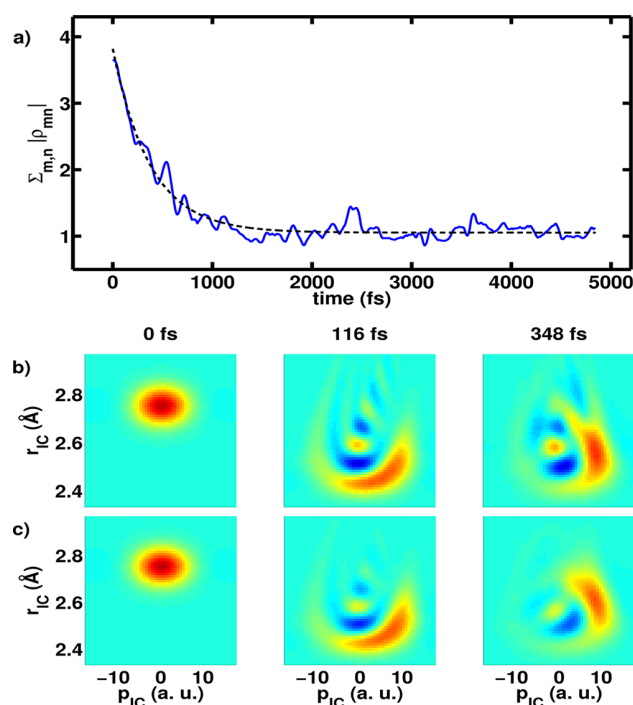


Figure 4. Decrease of coherence of the system with the low energy initial conditions. (a) Coherence traced over 21 randomly chosen starting conditions as a function of time (blue solid) together with the monoexponential fit (black dotted). (b) Wigner function of a simulation in the gas phase at 0, 116, and 348 fs. (c) Wigner function for the sum of all 21 simulations in the liquid argon environment at the same times. The red areas indicate a positive sign and the blue areas a negative sign.

studies have identified a biexponential decay from which two lifetimes can be extracted. The first short one τ_1 is around 105 fs in the gas phase⁶⁴ and 120 fs in solution for the related 1-cyclohexyluracil⁶⁵ while the second one τ_2 longer than 1 ps in the gas phase as well as in solution. Here, we are focusing on the first step, which has been attributed to an ultrafast decay from the bright S_2 state with $\pi\pi^*$ character to the dark S_1 state with $n\pi^*$ character via a CoIn.^{68,69}

Our system consists of a central uracil molecule and 217 water molecules embedded in a periodic box with side lengths of 19 Å. We use the AMBER14SB^{70,71} force field for the VRCS of uracil and the interaction potential and TIP3P⁷² for the MD of water. For the van der Waals and Coulomb interactions a cutoff of 7 Å was used. Long-range Coulomb interactions were taken into account by the reaction-field mechanism implemented in Gromacs. The system was equilibrated at 298.15 K and 1 bar while keeping the uracil molecule frozen in its ground state geometry. Then, during a time evolution of 200 ps frames were extracted every 5 ps as starting points for the cQDMD simulations. Out of the resulting 40 arrangements, 35 were randomly chosen as initial conditions. For the internal degrees of freedom of uracil we used a two-dimensional two state model. Uracil is represented in a configuration space spanned by the vector connecting the Franck–Condon point with the small S_2 minimum ($q_{FC \rightarrow S_2min}$) and the vector, connecting the Franck–Condon point with the S_2/S_1 CoIn ($q_{FC \rightarrow CoIn}$). The optimization of the corresponding structures, the construction of the gas phase S_2 PES and the construction of the nonadiabatic coupling matrix elements in these coordinates

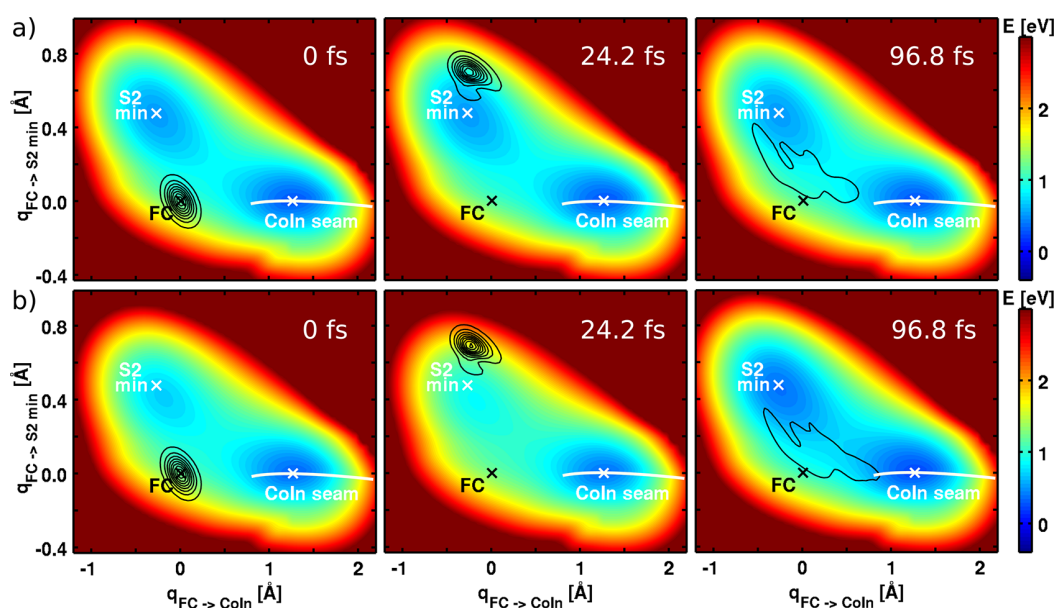


Figure 5. Wavepacket propagation on the S_2 surface of uracil. The surface is spanned by the Franck–Condon point, the local S_2 minimum and the S_2/S_1 CoIn. Nonadiabatic coupling takes place along the CoIn seam indicated by the curved white line. (a) Propagation in the gas phase. (b) Sample calculation in water, where the relaxation speed is slightly increased due to a collision solvent molecules at around 24.2 fs.

on the MRCI(12,9) level of theory is described elsewhere.^{46,68,73} A negative imaginary potential represents the S_1 PES and we approximate the nonadiabatic coupling as being solvent independent. As the starting wavepacket, the lowest vibrational eigenstate of the ground state was transferred to the S_2 state. The dynamics in the gas phase that result from this starting condition are comparable to an excitation by a simple probe pulse.⁴⁶ 35 cQMD trajectories were propagated with a time step of 0.1 fs using the Chebychev propagator.⁵⁰

In the gas phase, the wavepacket oscillates twice in the S_2 minimum before parts of it cross the barrier between the S_2 minimum and the CoIn at around 100 fs leading to relaxation to the S_1 state (Figure 5a). In all 35 simulations in water, a similar behavior is observed, with an example shown in Figure 5b. The influence of the water environment clearly shows in the time dependence of the potential energy surface. These effects lead to slightly different relaxation behaviors in the individual trajectories, but no deviation from the general scheme. A process that influences relaxation is the collision of the wavepacket with solvent molecules during its oscillations in the S_2 minimum. We also observe periodic increases or decreases in the height of the barrier due to the interaction with the water molecules. However, within this theoretical description using the AMBER14SB force field the influence of these two factors is rather minute and over different trajectories, they accelerate as well as decelerate the relaxation. Hence, in the mean of all 35 simulations, no significant deviation from the gas phase relaxation is observed (Figure 6). Overall, this means that the cavity of the uracil molecule does not need to change much to allow for the motions associated with the relaxation process.

These findings are in line with experiments⁶⁵ that show only little solvent dependence of τ_1 and only a small difference to the gas phase. They also compare well with previous theoretical studies by Doltsinis et al. using nonadiabatic ab initio dynamics on TDDFT level⁷⁴ that focus on the S_1 state in solution and show no qualitative difference governing nonradiative decay in

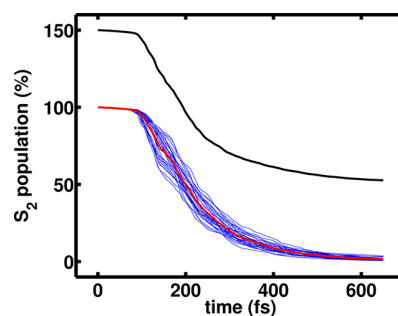


Figure 6. Decrease of S_2 population in the gas phase (black line, shifted by 50%) and of 35 cQMD simulations in water (blue lines). The red line marks the average of the simulations in water.

the gas phase and in aqueous solution. On a longer time scale, associated with S_1/S_0 relaxation, transient UV absorption spectra have shown characteristics of vibrational cooling in the aqueous environment.⁶⁷ With the approach presented here, we might be able to investigate these in the future.

CONCLUSIONS

We presented an approach that is an extension of our recently presented QD/MD approach⁸ and builds on the quantum-classical TDSCF scheme. It captures environmental effects onto reactive systems for ultrafast processes by simultaneously propagating a quantum solute system coupled to a classical solvent system using a TDSCF. As the quantum system is propagated on a spatial grid, this method is generally applicable to most PES, which makes it especially suited for reactive scenarios where the solvent has an important influence on the outcome. Additionally, it is easily transferable to other systems, as long as force fields are available for the solvent and a suited grid representation is found for the solute in reduced dimensionality. It also allows the inclusion of classical rotational and translational degrees of freedom of the solute, leading to a more accurate simulation of collisions. We presented the

dissociation of ICN in liquid argon and the photorelaxation of uracil in water as a example systems and examined the decoherence in our simulations of the ICN system. While our approach is fairly general with respect to the solvation scenario, it is limited in the extreme by cases where significant parts of the wave function are widely separated during the propagation. In these cases and in scenarios with a stronger focus on correct energy transfer between the subsystems, MDQT or multi-configurational methods may be beneficial.

There are a few directions for further development. One is the possible decoupling of the time step size of the two subsystems. In principle, each subsystem could use its own appropriate step size and usually the step size of the MD system could be increased relative to the QD system. It might also be worth to explore the use of MCTDH instead of a grid-based approach for scenarios where the MCTDH excels. Additionally, it is straightforward to move to a larger test system that will allow us to challenge our approach.

■ ASSOCIATED CONTENT

📄 Supporting Information

The Supporting Information is available free of charge on the ACS Publications website at DOI: 10.1021/acs.jpca.7b10372.

Flowchart illustrating our algorithm and plots of the different initial conditions for the QD calculations of ICN presented and the time evolution of the purity of the ICN system together with the convergence behavior of the other decoherence measures studied (PDF)

■ AUTHOR INFORMATION

Corresponding Author

*(R.d.V.-R.) E-mail: regina.de_vivie@cup.uni-muenchen.de.

ORCID

Sebastian Thallmair: 0000-0002-3396-5840

Regina de Vivie-Riedle: 0000-0002-7877-5979

Present Address

†(S.T.) Groningen Biomolecular Sciences and Biotechnology Institute and The Zernike Institute for Advanced Material, University of Groningen, 9747 AG Groningen, The Netherlands.

Notes

The authors declare no competing financial interest.

■ ACKNOWLEDGMENTS

We gratefully acknowledge support by the DFG via the Cluster of Excellence: The SFB749 and Munich Centre for Advanced Photonics.

■ REFERENCES

- (1) Kohen, A.; Klinman, J. P. Enzyme Catalysis: Beyond Classical Paradigms. *Acc. Chem. Res.* **1998**, *31*, 397–404.
- (2) Stratt, R. M.; Maroncelli, M. Nonreactive Dynamics in Solution: The Emerging Molecular View of Solvation Dynamics and Vibrational Relaxation. *J. Phys. Chem.* **1996**, *100*, 12981–12996.
- (3) Moskun, A. C.; Jailaubekov, A. E.; Bradforth, S. E.; Tao, G.; Stratt, R. M. Rotational Coherence and a Sudden Breakdown in Linear Response Seen in Room-Temperature Liquids. *Science* **2006**, *311*, 1907–1911.
- (4) Li, X.; Maroncelli, M. Solvent-Controlled Electron Transfer in Crystal Violet Lactone. *J. Phys. Chem. A* **2011**, *115*, 3746–3754.
- (5) Sailer, C. F.; Thallmair, S.; Fingerhut, B. P.; Nolte, C.; Ammer, J.; Mayr, H.; de Vivie-Riedle, R.; Pugliesi, I.; Riedle, E. A Comprehensive

Microscopic Picture of the Benzhydryl Radical and Cation Photo-Generation and Interconversion through Electron Transfer. *ChemPhysChem* **2013**, *14*, 1423–1437.

(6) Struebing, H.; Ganase, Z.; Karamertzanis, P. G.; Sioumkrou, E.; Haycock, P.; Piccione, P. M.; Armstrong, A.; Galindo, A.; Adjiman, C. S. Computer-Aided Molecular Design of Solvents for Accelerated Reaction Kinetics. *Nat. Chem.* **2013**, *5*, 952–957.

(7) Thallmair, S.; Kowalewski, M.; Zauleck, J. P. P.; Roos, M. K.; de Vivie-Riedle, R. Quantum Dynamics of a Photochemical Bond Cleavage Influenced by the Solvent Environment: A Dynamic Continuum Approach. *J. Phys. Chem. Lett.* **2014**, *5*, 3480–3485.

(8) Thallmair, S.; Zauleck, J. P. P.; de Vivie-Riedle, R. Quantum Dynamics in an Explicit Solvent Environment: A Photochemical Bond Cleavage Treated with a Combined QD/MD Approach. *J. Chem. Theory Comput.* **2015**, *11*, 1987–1995.

(9) Kumpulainen, T.; Lang, B.; Rosspeintner, A.; Vauthey, E. Ultrafast Elementary Photochemical Processes of Organic Molecules in Liquid Solution. *Chem. Rev.* **2017**, *117*, 10826.

(10) Bondar, D. I.; Cabrera, R.; Campos, A.; Mukamel, S.; Rabitz, H. A. Wigner-Lindblad Equations for Quantum Friction. *J. Phys. Chem. Lett.* **2016**, *7*, 1632–1637.

(11) Burghardt, I.; Cederbaum, L. S.; Hynes, J. T. Environmental effects on a conical intersection: A model study. *Faraday Discuss.* **2004**, *127*, 395–411.

(12) Cederbaum, L. S.; Gindensperger, E.; Burghardt, I. Short-Time Dynamics Through Conical Intersections in Macrosystems. *Phys. Rev. Lett.* **2005**, *94*, 113003.

(13) Cossi, M.; Rega, N.; Scalmani, G.; Barone, V. Energies, structures, and electronic properties of molecules in solution with the C-PCM solvation model. *J. Comput. Chem.* **2003**, *24*, 669–681.

(14) Tomasi, J.; Mennucci, B.; Cammi, R. Quantum Mechanical Continuum Solvation Models. *Chem. Rev.* **2005**, *105*, 2999–3094.

(15) Caricato, M. A corrected-linear response formalism for the calculation of electronic excitation energies of solvated molecules with the CCSD-PCM method. *Comput. Theor. Chem.* **2014**, *1040-1041*, 99–105.

(16) Shi, Q.; Geva, E. Semiclassical Theory of Vibrational Energy Relaxation in the Condensed Phase. *J. Phys. Chem. A* **2003**, *107*, 9059–9069.

(17) Ka, B. J.; Geva, E. Classical vs Quantum Vibrational Energy Relaxation Pathways in Solvated Polyatomic Molecules. *J. Phys. Chem. A* **2006**, *110*, 13131–13138.

(18) Liu, J.; Miller, W. H. Linearized semiclassical initial value time correlation functions using the thermal Gaussian approximation: Applications to condensed phase systems. *J. Chem. Phys.* **2007**, *127*, 114506.

(19) Liu, J.; Miller, W. H.; Paesani, F.; Zhang, W.; Case, D. A. Quantum dynamical effects in liquid water: A semiclassical study on the diffusion and the infrared absorption spectrum. *J. Chem. Phys.* **2009**, *131*, 164509.

(20) Tully, J. C. Mixed quantum-classical dynamics. *Faraday Discuss.* **1998**, *110*, 407.

(21) Marx, D.; Hutter, J. In *Modern Methods and Algorithms of Quantum Chemistry*, 2nd ed.; Grotendorst, J., Ed., John von Neumann Institute for Computing: Jülich, Germany, 2000; Vol. 3, pp 301–449.

(22) Li, X.; Tully, J. C.; Schlegel, H. B.; Frisch, M. J. Ab initio Ehrenfest dynamics. *J. Chem. Phys.* **2005**, *123*, 084106.

(23) Tully, J. C. Molecular dynamics with electronic transitions. *J. Chem. Phys.* **1990**, *93*, 1061–1071.

(24) Fano, U. Description of States in Quantum Mechanics by Density Matrix and Operator Techniques. *Rev. Mod. Phys.* **1957**, *29*, 74–93.

(25) Lindblad, G. Entropy, information and quantum measurements. *Commun. Math. Phys.* **1973**, *33*, 305–322.

(26) Lindblad, G. Expectations and entropy inequalities for finite quantum systems. *Commun. Math. Phys.* **1974**, *39*, 111–119.

(27) Lindblad, G. On the generators of quantum dynamical semigroups. *Commun. Math. Phys.* **1976**, *48*, 119–130.

- (28) Donoso, A.; Martens, C. C. Semiclassical multistate Liouville dynamics in the adiabatic representation. *J. Chem. Phys.* **2000**, *112*, 3980–3989.
- (29) Wong, K. F.; Rossky, P. J. Dissipative mixed quantum-classical simulation of the aqueous solvated electron system. *J. Chem. Phys.* **2002**, *116*, 8418–8428.
- (30) Hanna, G.; Kapral, R. Quantum-classical Liouville dynamics of nonadiabatic proton transfer. *J. Chem. Phys.* **2005**, *122*, 244505.
- (31) Hanna, G.; Kapral, R. Quantum-classical Liouville dynamics of proton and deuteron transfer rates in a solvated hydrogen-bonded complex. *J. Chem. Phys.* **2008**, *128*, 164520.
- (32) Kim, H.; Nassimi, A.; Kapral, R. Quantum-classical Liouville dynamics in the mapping basis. *J. Chem. Phys.* **2008**, *129*, 084102.
- (33) Rezik, N.; Hsieh, C.-Y.; Freedman, H.; Hanna, G. A mixed quantum-classical Liouville study of the population dynamics in a model photo-induced condensed phase electron transfer reaction. *J. Chem. Phys.* **2013**, *138*, 144106.
- (34) Hsieh, C.-Y.; Kapral, R. Analysis of the forward-backward trajectory solution for the mixed quantum-classical Liouville equation. *J. Chem. Phys.* **2013**, *138*, 134110.
- (35) Martinez, F.; Hanna, G. Assessment of approximate solutions of the quantum-classical Liouville equation for dynamics simulations of quantum subsystems embedded in classical environments. *Mol. Simul.* **2015**, *41*, 107–122.
- (36) Wang, L.; McCoy, A. B. Time-dependent studies of reaction dynamics: a test of mixed quantum/classical time-dependent self-consistent field approximations. *Phys. Chem. Chem. Phys.* **1999**, *1*, 1227–1235.
- (37) Whittier, G. S.; Light, J. C. Quantum/classical time-dependent self-consistent field treatment of Ar+HCO inelastic and dissociative scattering. *J. Chem. Phys.* **1999**, *110*, 4280–4290.
- (38) Fernandez Alberti, S.; Echave, J.; Engel, V.; Halberstadt, N.; Beswick, J. A. Hybrid quantum/classical study of ICN in an Ar matrix: Photofragmentation and cage exit. *J. Chem. Phys.* **2000**, *113*, 1027–1034.
- (39) Gerber, R. B.; Buch, V.; Ratner, M. A. Time-dependent self-consistent field approximation for intramolecular energy transfer. I. Formulation and application to dissociation of van der Waals molecules. *J. Chem. Phys.* **1982**, *77*, 3022–3030.
- (40) Bisseling, R. H.; Kosloff, R.; Gerber, R. B.; Ratner, M. A.; Gibson, L.; Cerjan, C. Exact time-dependent quantum mechanical dissociation dynamics of I₂He: Comparison of exact time-dependent quantum calculation with the quantum time-dependent self-consistent field (TDSCF) approximation. *J. Chem. Phys.* **1987**, *87*, 2760–2765.
- (41) Alimi, R.; Gerber, R. B.; Hammerich, A. D.; Kosloff, R.; Ratner, M. A. Validity of time-dependent self-consistent-field (TDSCF) approximations for unimolecular dynamics: A test for photodissociation of the Xe-HI cluster. *J. Chem. Phys.* **1990**, *93*, 6484–6490.
- (42) Garcia-Vela, A.; Gerber, R. B.; Valentini, J. J. Effects of solvation by a single atom on photodissociation: Classical and quantum/classical studies of HCl photolysis in ArHCl. *J. Chem. Phys.* **1992**, *97*, 3297–3306.
- (43) Bastida, A.; Cruz, C.; Zúñiga, J.; Requena, A.; Miguel, B. The Ehrenfest method with quantum corrections to simulate the relaxation of molecules in solution: Equilibrium and dynamics. *J. Chem. Phys.* **2007**, *126*, 014503.
- (44) Bastida, A.; Zúñiga, J.; Requena, A.; Miguel, B. Full quantum vibrational simulation of the relaxation of the cyanide ion in water using the Ehrenfest method with quantum corrections. *J. Chem. Phys.* **2008**, *129*, 154501.
- (45) Yamada, A.; Kojima, H.; Okazaki, S. A molecular dynamics study of intramolecular proton transfer reaction of malonaldehyde in solutions based upon mixed quantum-classical approximation. I. Proton transfer reaction in water. *J. Chem. Phys.* **2014**, *141*, 084509.
- (46) Keefer, D.; Thallmair, S.; Matsika, S.; de Vivie-Riedle, R. Controlling Photorelaxation in Uracil with Shaped Laser Pulses: A Theoretical Assessment. *J. Am. Chem. Soc.* **2017**, *139*, 5061–5066.
- (47) Andersen, H. C. Rattle: A “Velocity” Version of the Shake Algorithm for Molecular Dynamics Calculations. *J. Comput. Phys.* **1983**, *52*, 24–34.
- (48) Dirac, P. A. M. Note on Exchange Phenomena in the Thomas Atom. *Math. Proc. Cambridge Philos. Soc.* **1930**, *26*, 376–385.
- (49) Feit, M. D.; Fleck, J. A., Jr.; Steiger, A. Solution of the Schrödinger Equation by a Spectral Method. *J. Comput. Phys.* **1982**, *47*, 412.
- (50) Tal-Ezer, H.; Kosloff, R. An Accurate and Efficient Scheme for Propagating the Time Dependent Schrödinger Equation. *J. Chem. Phys.* **1984**, *81*, 3967–3971.
- (51) Swope, W. C.; Andersen, H. C.; Berens, P. H.; Wilson, K. R. A computer simulation method for the calculation of equilibrium constants for the formation of physical clusters of molecules: Application to small water clusters. *J. Chem. Phys.* **1982**, *76*, 637.
- (52) Hess, B.; Kutzner, C.; Van Der Spoel, D.; Lindahl, E. GROMACS 4: Algorithms for Highly Efficient, Load-Balanced, and Scalable Molecular Simulation. *J. Chem. Theory Comput.* **2008**, *4*, 435–447.
- (53) Krylov, A. I.; Gerber, R. B. Photodissociation of ICN in solid and in liquid Ar: Dynamics of the cage effect and of excited-state isomerization. *J. Chem. Phys.* **1994**, *100*, 4242–4252.
- (54) Fernandez Alberti, S.; Halberstadt, N.; Beswick, J. A.; Echave, J. A theoretical study of photofragmentation and geminate recombination of ICN in solid Ar. *J. Chem. Phys.* **1998**, *109*, 2844–2850.
- (55) Helbing, J.; Chergui, M.; Fernandez-Alberti, S.; Echave, J.; Halberstadt, N.; Alberto Beswick, J. Caging and excited state emission of ICN trapped in cryogenic matrices: experiment and theory. *Phys. Chem. Chem. Phys.* **2000**, *2*, 4131–4138.
- (56) Goldfield, E. M.; Houston, P. L.; Ezra, G. S. Nonadiabatic interactions in the photodissociation of ICN. *J. Chem. Phys.* **1986**, *84*, 3120.
- (57) Benjamin, I.; Wilson, K. R. Proposed experimental probes of chemical reaction molecular dynamics in solution: ICN photodissociation. *J. Chem. Phys.* **1989**, *90*, 4176.
- (58) Micha, D. A. A self-consistent eikonal treatment of electronic transitions in molecular collisions. *J. Chem. Phys.* **1983**, *78*, 7138–7145.
- (59) Greengard, L.; Rokhlin, V. A Fast Algorithm for Particle Simulations. *J. Comput. Phys.* **1987**, *73*, 325.
- (60) Rector, K. D.; Fayer, M. D. Vibrational dephasing mechanisms in liquids and glasses: Vibrational echo experiments. *J. Chem. Phys.* **1998**, *108*, 1794–1803.
- (61) Stenger, J.; Madsen, D.; Hamm, P.; Nibbering, E. T. J.; Elsaesser, T. Ultrafast Vibrational Dephasing of Liquid Water. *Phys. Rev. Lett.* **2001**, *87*, 027401.
- (62) Kang, H.; Lee, K. T.; Jung, B.; Ko, Y. J.; Kim, S. K. Intrinsic Lifetimes of the Excited State of DNA and RNA Bases. *J. Am. Chem. Soc.* **2002**, *124*, 12958–12959.
- (63) Ullrich, S.; Schultz, T.; Zgierski, M. Z.; Stolow, A. Electronic relaxation dynamics in DNA and RNA bases studied by time-resolved photoelectron spectroscopy. *Phys. Chem. Chem. Phys.* **2004**, *6*, 2796–2801.
- (64) Canuel, C.; Mons, M.; Piuze, F.; Tardivel, B.; Dimicoli, I.; Elhanine, M. Excited states dynamics of DNA and RNA bases: Characterization of a stepwise deactivation pathway in the gas phase. *J. Chem. Phys.* **2005**, *122*, 074316.
- (65) Hare, P. M.; Crespo-Hernández, C. E.; Kohler, B. Solvent-Dependent Photophysics of 1-Cyclohexyluracil: Ultrafast Branching in the Initial Bright State Leads Nonradiatively to the Electronic Ground State and a Long-Lived ¹nπ* State. *J. Phys. Chem. B* **2006**, *110*, 18641–18650.
- (66) Gustavsson, T.; Sarkar, N.; Lazzarotto, E.; Markovitsi, D.; Improta, R. Singlet excited state dynamics of uracil and thymine derivatives: A femtosecond fluorescence upconversion study in acetonitrile. *Chem. Phys. Lett.* **2006**, *429*, 551–557.
- (67) Hua, X.; Hua, L.; Liu, X. The methyl- and aza-substituent effects on nonradiative decay mechanisms of uracil in water: a transient

absorption study in the UV region. *Phys. Chem. Chem. Phys.* **2016**, *18*, 13904–13911.

(68) Matsika, S. Radiationless Decay of Excited States of Uracil through Conical Intersections. *J. Phys. Chem. A* **2004**, *108*, 7584–7590.

(69) Richter, M.; Mai, S.; Marquetand, P.; Gonzalez, L. Ultrafast intersystem crossing dynamics in uracil unravelled by ab initio molecular dynamics. *Phys. Chem. Chem. Phys.* **2014**, *16*, 24423–24436.

(70) Cornell, W. D.; Cieplak, P.; Bayly, C. I.; Gould, I. R.; Merz, K. M.; Ferguson, D. M.; Spellmeyer, D. C.; Fox, T.; Caldwell, J. W.; Kollman, P. A. A Second Generation Force Field for the Simulation of Proteins, Nucleic Acids, and Organic Molecules. *J. Am. Chem. Soc.* **1995**, *117*, 5179–5197.

(71) Zgarbová, M.; Otyepka, M.; Šponer, J.; Mládek, A.; Banáš, P.; Cheatham, T. E.; Jurečka, P. Refinement of the Cornell et al. Nucleic Acids Force Field Based on Reference Quantum Chemical Calculations of Glycosidic Torsion Profiles. *J. Chem. Theory Comput.* **2011**, *7*, 2886–2902.

(72) Jorgensen, W. L.; Chandrasekhar, J.; Madura, J. D.; Impey, R. W.; Klein, M. L. Comparison of simple potential functions for simulating liquid water. *J. Chem. Phys.* **1983**, *79*, 926–935.

(73) Yoshikawa, A.; Matsika, S. Excited electronic states and photophysics of uracil?water complexes. *Chem. Phys.* **2008**, *347*, 393–404.

(74) Nieber, H.; Doltsinis, N. L. Elucidating ultrafast nonradiative decay of photoexcited uracil in aqueous solution by ab initio molecular dynamics. *Chem. Phys.* **2008**, *347*, 405–412.

1.2. Multi-Configurational Ehrenfest

The Ehrenfest approach, as presented in the previous section, performs well for very fast processes. However, it does not treat the correlation between the quantum and classical part of the system due to the simple structure of the product ansatz in eq. (1.4). When Ehrenfest is applied to the separation of electrons and nuclei, correct dynamics for more than a few fs are only obtained if the potential energy surfaces of the various electronic states that make up the system’s wavepacket are similar in topology and energy. When two states with different gradients are coupled, wavepacket splitting occurs, which is not captured by Ehrenfest dynamics.[29] For the system-environment dynamics presented here, an analogous problem exists. The environment experiences different forces due to different positions of the system wavepacket on the PES. As long as the wavepacket is localized, this does not lead to problems. However, the interaction with the environment and the anharmonic nature of the PES will cause the system’s wavepacket to spread. The environment will then experience an average force from the spread-out wavepacket. In reality, the wavefunction should split, with large amplitude motions in the system becoming correlated with specific environment trajectories and small amplitude motions in the system becoming correlated with different environment trajectories. After the initial Ehrenfest time, this manifest as incorrect vibrational energy redistribution. In the long time limit, Ehrenfest dynamics violates detailed balance, which means that a Boltzmann distribution will not be reached.[80–82] How fast this problem becomes relevant is dependent on the system under study. For weak coupling to the environment and a harmonic system, the Ehrenfest time will be very long. For a harmonic system with strong coupling or an anharmonic system with weak coupling, likely intermediate Ehrenfest times will be obtained, which should cover a few vibrational periods. The example of Uracil in water discussed in the previous section was such an example with a fairly anharmonic PES but weak coupling. In this section, we will treat the dissociation of I_2 in a solid krypton matrix, which features both a very anharmonic PES and strong coupling to the environment.

Thus, we hope to extend the time for which the simulation stays valid while still being able to treat many degrees of freedom in a somewhat classical environment. For this, we use a multiconfigurational approach, the MCE method.[24–28] For the quantum/quantum TDSCF method, a multiconfigurational approach lead to the development of multi-configuration time-dependent Hartree (MCTDH),[83–86] which very accurately describes the dynamics of systems with a few tens of degrees of freedom. However, it still scales exponentially with the number of degrees of freedom and requires a special form for the potential that is not easily compatible with classical force fields. In principle, both of these shortcomings can be overcome by MCE. The MCE method has so far only been used for the separation of the electronic and nuclear degrees of freedom in molecules. In this work, the first implementation that allows the separation between a system’s nuclear degrees of freedom (propagated as a wavepacket on a pre-calculated PES) and the nuclear degrees of freedom of an environment is presented.

In this approach, an ensemble of Ehrenfest trajectories is used as a basis in which to solve the TDSE. In the MCEv2-formulation introduced in [25], the total wavefunction is expressed as a linear combination of N Ehrenfest configurations, with each configuration consisting of a vibronic system wavepacket Ψ_k^S evolving according to eq. (1.7) and its associated classical trajectory evolving according to eq. (1.8). Accordingly, the full

wavefunction is

$$\Psi = \sum_k^N c_k \Psi_k^S \Psi_k^E \quad (1.9)$$

with Ψ_k^E obtained by broadening the classical trajectories $\{\mathbf{p}_k, \mathbf{q}_k\}$ with a multi-dimensional frozen Gaussian[87]

$$\Psi_k^E(\mathbf{x}) = \mathcal{N}_k \exp\left(-(\mathbf{x} - \mathbf{q}_k) \cdot \mathbf{a}(\mathbf{x} - \mathbf{q}_k) + \frac{i}{\hbar} \mathbf{p}_k \cdot (\mathbf{x} - \mathbf{q}_k) + \frac{i}{\hbar} \gamma_k(t)\right). \quad (1.10)$$

Here, \mathbf{a} is the width-matrix of the Gaussians. It is usually assumed to be diagonal and is taken to be time-independent in the frozen Gaussian ansatz. \mathcal{N}_k normalizes the Gaussians, and $\gamma_k(t)$ is an arbitrary time-dependent phase factor usually chosen as the semi-classical phase $\frac{\mathbf{p}_k \cdot \mathbf{q}_k}{2}$. These frozen Gaussians introduce some quantum features back into the environment. If the Gaussians cover the entire phase space of the environment once for each vibronic system state, the exact solution for the full wavefunction is recovered in principle. In practice, we hope that at the beginning of the simulation, with an appropriate set of initial conditions, the Gaussians will cover a large enough amount of environment phase space to recover some correlation and extend the applicability of Ehrenfest dynamics.

The multi-dimensional Gaussians can be expressed as a product of the one-dimensional Gaussians for each environment mode m

$$\Psi_k^E(\mathbf{x}) = \prod_{m=1} g_{m,k}(q_{m,k}, p_{m,k}). \quad (1.11)$$

The vector of coefficients $\mathbf{C} = \{c_k\}$ is determined variationally by solving

$$i\hbar \frac{\partial}{\partial t} \mathbf{C} = \mathbf{S}^{-1} (\mathbf{H} - i\hbar \mathbf{T}) \mathbf{C} \quad (1.12)$$

with the overlap matrix

$$S_{kl} = \langle \Psi_k^S | \Psi_l^S \rangle \langle \Psi_k^E | \Psi_l^E \rangle \quad (1.13)$$

the time-derivative overlap matrix

$$T_{kl} = \langle \Psi_k^S | \Psi_l^S \rangle \langle \Psi_k^E | \frac{\partial}{\partial t} \Psi_l^E \rangle + \langle \Psi_k^S | \frac{\partial}{\partial t} \Psi_l^S \rangle \langle \Psi_k^E | \Psi_l^E \rangle, \quad (1.14)$$

and the Hamiltonian matrix

$$H_{kl} = \langle \Psi_k^S | \hat{H}^S | \Psi_l^S \rangle \langle \Psi_k^E | \Psi_l^E \rangle + \langle \Psi_k^S | \Psi_l^S \rangle \langle \Psi_k^E | \hat{H}^E | \Psi_l^E \rangle + \langle \Psi_k^S \Psi_k^E | \hat{V}^{ES} | \Psi_l^S \Psi_l^E \rangle. \quad (1.15)$$

We represent the wavefunction of the system Ψ_S on a grid using the discrete variable representation (DVR).[64, 88] This means, all integrals containing only Ψ_S ($\langle \Psi_k^S | \Psi_l^S \rangle$ and $\langle \Psi_k^S | \hat{H}^S | \Psi_l^S \rangle$) can be evaluated by numerical integration. The overlap integral of two frozen Gaussians $\langle \Psi_k^E | \Psi_l^E \rangle$ as well as the time-derivative overlap $\langle \Psi_k^E | \frac{\partial}{\partial t} \Psi_l^E \rangle$ can be evaluated analytically. The integral $\langle \Psi_k^E | \hat{H}^E | \Psi_l^E \rangle$ can also be calculated analytically by approximating the potential in \hat{H}^E as a power series in the environment coordinates. The interaction term, $\langle \Psi_k^S \Psi_k^E | \hat{V}^{ES} | \Psi_l^S \Psi_l^E \rangle$ can be evaluated by combining numerical and analytical integration. To do this, the interaction potential \hat{V}^{ES} is expressed as a power series in the environment coordinates for each gridpoint on the grid of the system coordinates. Then, the integration over the environment coordinates is performed

analytically for each point of the DVR grid, followed by numerical integration over the DVR grid.

Expectation values $\langle \Psi | \hat{O}^{(m)} | \Psi \rangle$, that only depend on the coordinate of a single mode m can be calculated efficiently in the MCE approach as

$$\langle \hat{O}^{(m)} \rangle(q_m, t) = \sum_{k,l}^N \bar{S}_{kl}^{(m)} c_k^* c_l \langle \Psi_k^{(m)} | \hat{O}^{(m)} | \Psi_l^{(m)} \rangle. \quad (1.16)$$

Here, we assume a system with one mode $m = 1$ represented on a grid ($\Psi_k^{(1)} = \Psi_k^S$), and several environment modes $m > 1$ represented by Gaussians ($\Psi_k^{(m)} = g_{m,k}$). $\bar{S}_{kl}^{(m)}$ is a product of overlaps over all modes except the one that is investigated. It is given as

$$\bar{S}_{kl}^{(m)} = \prod_{n \neq m} \langle \Psi_k^{(n)} | \Psi_l^{(n)} \rangle. \quad (1.17)$$

To implement a coupled propagation of equations eq. (1.7), eq. (1.8), and eq. (1.12), attention must be paid to a few details. The Ehrenfest trajectories can be integrated independently of the coefficients \mathbf{C} . To do this, usually, a fixed time step is chosen. However, stable integration of \mathbf{C} requires adaptive integrators like Runge-Kutta Cash-Karp[89] or Runge-Kutta Dopri5[90] which do not have a fixed time-step length. Thus, careful interpolation of Ψ_k^S , $\frac{\partial}{\partial t} \Psi_k^S$, \mathbf{p}_k and \mathbf{q}_k is necessary. This is a challenging task, and inexact interpolation leads to severe problems in norm and energy conservation. Thus, in our implementation equations eq. (1.7), eq. (1.8) and eq. (1.12) are integrated in a fully coupled way, using the same adaptive integrator for all three equations. This is, however, more computationally demanding and prevents us from implementing eq. (1.12) as a simple post-processing step, which could be performed after running all Ehrenfest trajectories in parallel.

The implementation is tested on a 7-dimensional model of an iodine (I_2) molecule embedded in a Krypton cluster (I_2Kr_{18}). This model was created by David Picconi in the group of Irene Burghardt to study the dynamics and spectroscopy of dihalogens in noble gas matrices and is described in detail in [91, 92]. The I_2Kr_{18} fragment is embedded in a larger cluster, of which the atoms are kept fixed. The vibration of the I_2 molecule in its electronically excited B state is described with the quantum system coordinate q_1 . The environment is described by six vibrational modes of the Kr_{18} cage, ($q_4, q_{22}, q_{27}, q_{34}, q_{40}, q_{60}$). These modes were selected from all 60 modes of the cluster according to their activity in classical dynamics simulations and are visualized in fig. 3 of ref. [91]. As an initial wavefunction, a multi-dimensional Gaussian, corresponding to the lowest eigenstate of the electronic ground state, is used. Displacements in all modes are expressed in dimensionless normal coordinates

$$q_m = \sqrt{\frac{\omega_m}{\hbar}} \tilde{q}_m, \quad (1.18)$$

where ω_m is the ground state vibrational frequency in the mode m . Thus, the initial wavepacket has the same width in each mode. The wavepacket is then transferred to the excited B state to initialize the dynamics. To produce initial conditions for the Ehrenfest configurations in our approach, initial values $\mathbf{p}_k, \mathbf{q}_k$ for the bath modes are randomly sampled from a Wigner distribution. A special trajectory is added, with initial $\mathbf{p}_0, \mathbf{q}_0$ equal to zero in all bath coordinates. The initial c_k are set to zero for all Ehrenfest

configurations, except for c_0 , which was set to 1. This choice of coefficients makes the initial conditions equal to the initial conditions in ref. [91] for MCE simulations and approximately equal to the initial conditions in ref. [91] for ordinary Ehrenfest simulations.

To visualize the dynamics, fig. 1.1 shows the time-dependent reduced probability densities for the I_2 vibration, and fig. 1.2 shows the time-dependent reduced probability densities for the vibrations of the noble gas cage. The reduced probability densities are calculated by integrating the total probability density over all modes except the mode m that is investigated

$$\varrho^{(m)}(q_m, t) = \int_{-\infty}^{\infty} |\Psi(\mathbf{q})|^2 \prod_{n \neq m} dq_n. \quad (1.19)$$

This expression can be evaluated using eq. (1.16).

As seen from fig. 1.1 the I_2 vibration in the B state is highly anharmonic. After the initial excitation, rapid elongation of the I_2 bond is observed. At 200 fs, the molecule starts interacting with the krypton cage and is reflected. The Franck-Condon (FC) region is reached again between 400 fs and 500 fs, and the wavepacket is again reflected. At this point, visible nodes in the wavepacket show interference between the different parts of the reflected wavepacket. During the simulation, two more periods are observed, with smaller amplitudes due to the loss of energy in the initial collision and the changing shape of the interaction potential due to the movement of the krypton cage.

An essential aspect that has to be analyzed when running simulations in the MCEv2 approach is the convergence with the number of trajectories, i. e. how many independent Ehrenfest configurations are coupled together by the coefficients in eq. (1.12). The situations with 200 and 2000 configurations are compared in fig. 1.1 a) and b). Their general shape agrees well, suggesting that 200 configurations are sufficient to capture the important features of the system's dynamics. The most noticeable difference between these two simulations is a lower amount of interference at the inner and outer turning points when comparing fig. 1.1 b) to fig. 1.1 a). A greater amount of interference is retained at the inner turning point, while the interference patterns that are visible at the outer turning point during the second and third vibrational periods disappear almost completely.

The modes of the cage are nearly harmonic. As seen from fig. 1.2, after the initial collision, they start vibrating with periods of 700 to 1000 fs. There is not a large difference between the simulation with 200 and 2000 configurations, and they are in good agreement with the numerically exact MCTDH results presented in fig. 6 of ref. [91].

The differences in the interference patterns between fig. 1.1 a) and b) already hint at an improved description of decoherence when more Ehrenfest configurations are included. To further investigate this, the complete reduced density matrix for the system mode was evaluated. The reduced density matrix in the MCE approach is obtained as

$$\varrho^S(q_1, q'_1, t) = \sum_{k,l}^N c_k c_l^* \langle \Psi_l^E | \Psi_k^E \rangle | \Psi_k^S \rangle \langle \Psi_l^S | \quad (1.20)$$

with the previously discussed reduced probability density $\varrho^{(1)}(q_1, t)$ (eq. (1.19)) on its diagonal. The size of the off-diagonal elements of the density matrix is a measure of coherence. In the position representation, a large off-diagonal element implies a fixed phase relationship between parts of the wavepacket at different bond distances. In contrast, a small off-diagonal element implies that the interaction with the environment has

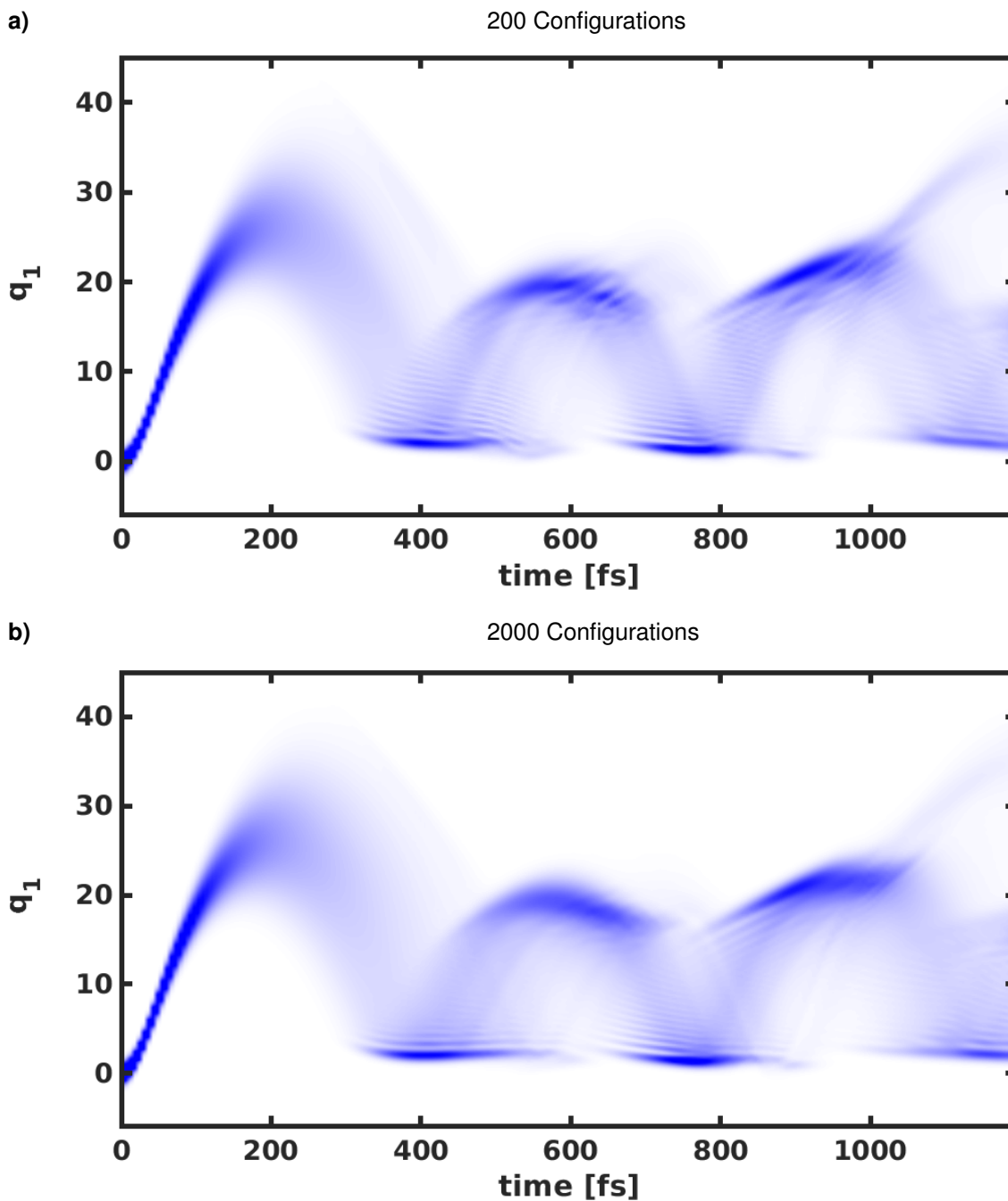


Figure 1.1.: One-dimensional reduced probability density $\varrho^{(1)}(q_1, t)$ of the I_2 stretching mode as a function of time, calculated using the MCE method with (a) 200 (b) 2000 Ehrenfest configurations.

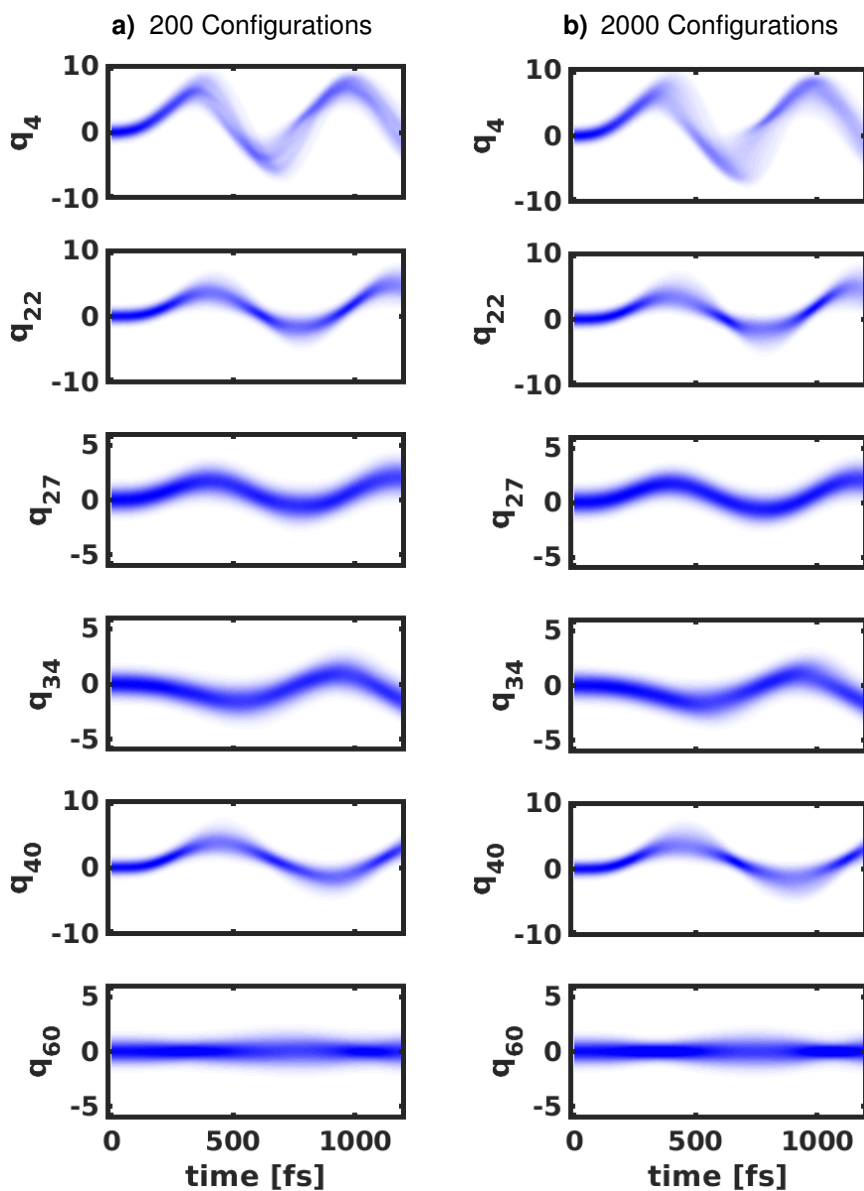


Figure 1.2.: One-dimensional reduced probability density $\varrho^{(m)}(q_m, t)$ of the vibrational modes of the Kr_{18} cage as a function of time, calculated using the MCE method with (a) 200 (b) 2000 Ehrenfest configurations.

destroyed this phase relationship. In the simulation with only 200 Ehrenfest configurations shown in fig. 1.3 a, the off-diagonal elements of the density matrix are slightly more prominent than in the simulation with 2000 Ehrenfest configurations shown in fig. 1.3 b. For example, at 720 fs, which corresponds to the inner turning point of the vibration, a faint blue square-like pattern is visible in the range $1 < q_1 < 22$ in fig. 1.3 a), which means that parts of the wavepacket are to some extent coherently connected over the whole range of bond-lengths. When compared to the numerically exact calculations in [92], this should not be the case. Instead, the coherence far from the diagonal, which appears noise-like in fig. 1.3 a) should be damped. MCE with 2000 Ehrenfest configurations (fig. 1.3 b) achieves this and yields density matrices that are visually indistinguishable from the numerically exact calculations until 1080 fs. There are no long-range coherences visible in fig. 1.3 b) that are not also present in numerically exact calculations. However, at long times (1440 fs and 1560 fs), this is not the case, and coherences spuriously reappear when compared to the numerically exact calculations.

The difference between 200 and 2000 Ehrenfest configurations is also visible in the energy representation of the density matrix (fig. 1.4). Qualitatively, both fig. 1.4 a) and fig. 1.4 b) show similar behavior. Before the collision of the wavepacket with the krypton cage, the wavepacket is fully coherent, as evident from the approximately Gaussian shape at 0 and 120 fs. This is followed by a remarkable decrease in coherence after 240 fs, with coherences only remaining between vibrational levels that are energetically close. This corresponds to the time after the initial collision when the wavepacket returns to the FC region. There, most of the energy of the wavepacket dissipates into the environment, and the atoms of the solvent cage start moving. Due to different couplings, the motion of the environment does not affect the energy and the time-dependent phase of each vibrational level in the same way. Similar perturbations for energetically similar states and very different perturbations for energetically different states lead to a scrambling of phase information that manifests as decoherence. With only 200 configurations, weak coherences between states of quite different energies are still visible in fig. 1.4 a), for example, as wing-like features at 360 fs and 1080 fs. These features are absent in fig. 1.4 b) as well as in the MCTDH reference calculations in [92]. At 1080 fs, a faint tail of density matrix elements along the diagonal between $3 \cdot 10^3 \text{ cm}^{-1}$ and $5 \cdot 10^3 \text{ cm}^{-1}$ emerges in both fig. 1.4 a) and b), that is absent from numerically exact calculations. This indicates that high-lying vibrational states become erroneously occupied at long times. However, for the first three vibrational periods (until 1080 fs), where most of the energy transfer between the system and the environment takes place, the exact MCTDH reference and MCE with 2000 configurations agree nearly quantitatively.

Next, we will inspect the total energy of the quantum system more closely. Figure 1.5 shows the expectation value $\langle \hat{T}^S + \hat{V}^S + \hat{V}^{ES} \rangle$ for the system mode. In the initial 240 fs, the energy rises slightly since the wavepacket approaches the cage and $\langle \hat{V}^{ES} \rangle$ increases, while the atoms of the cage have not started moving yet. Between 240 fs and 500 fs, a large drop in energy of ca. 17 kJ/mol occurs, and energy is transferred into potential and kinetic energy of the environment (see fig. 1.2). After this initial drop in energy, in the MCTDH reference calculation, energy moves back and forth between the system and the environment twice more within the 2500 fs of simulation time. Each time, an additional 1.5 kJ/mol is transferred into the environment. When comparing this behavior to Ehrenfest dynamics or TDH, one can clearly see that both methods capture the initial drop in energy but fail to reproduce the long-time relaxation behavior.

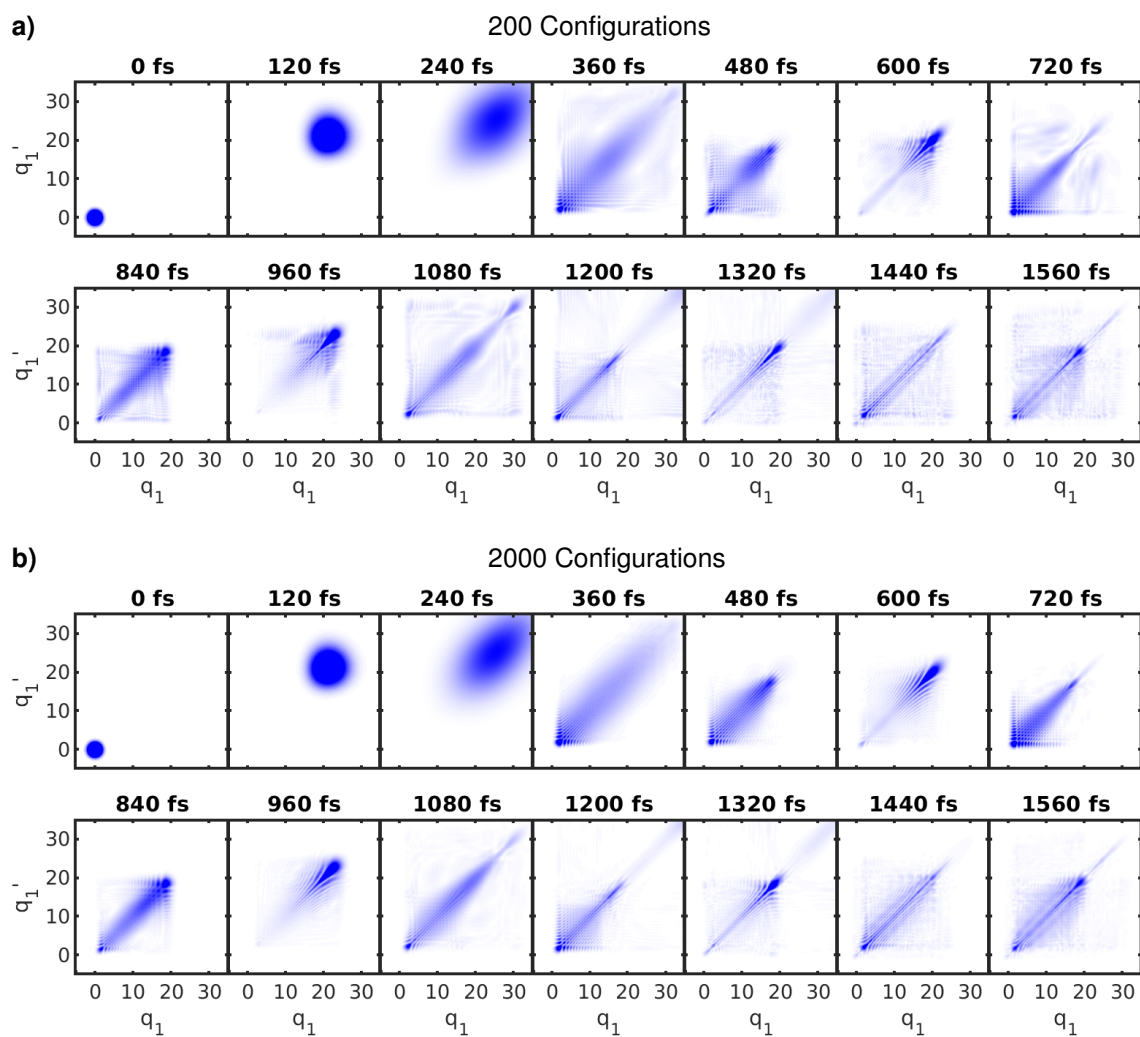


Figure 1.3.: Absolute value of the reduced density matrix $|\rho(q_1, q'_1, t)|$ of the I_2 stretching mode in the coordinate representation, calculated at different times using MCE with 200 trajectories (top) and 2000 trajectories (bottom).

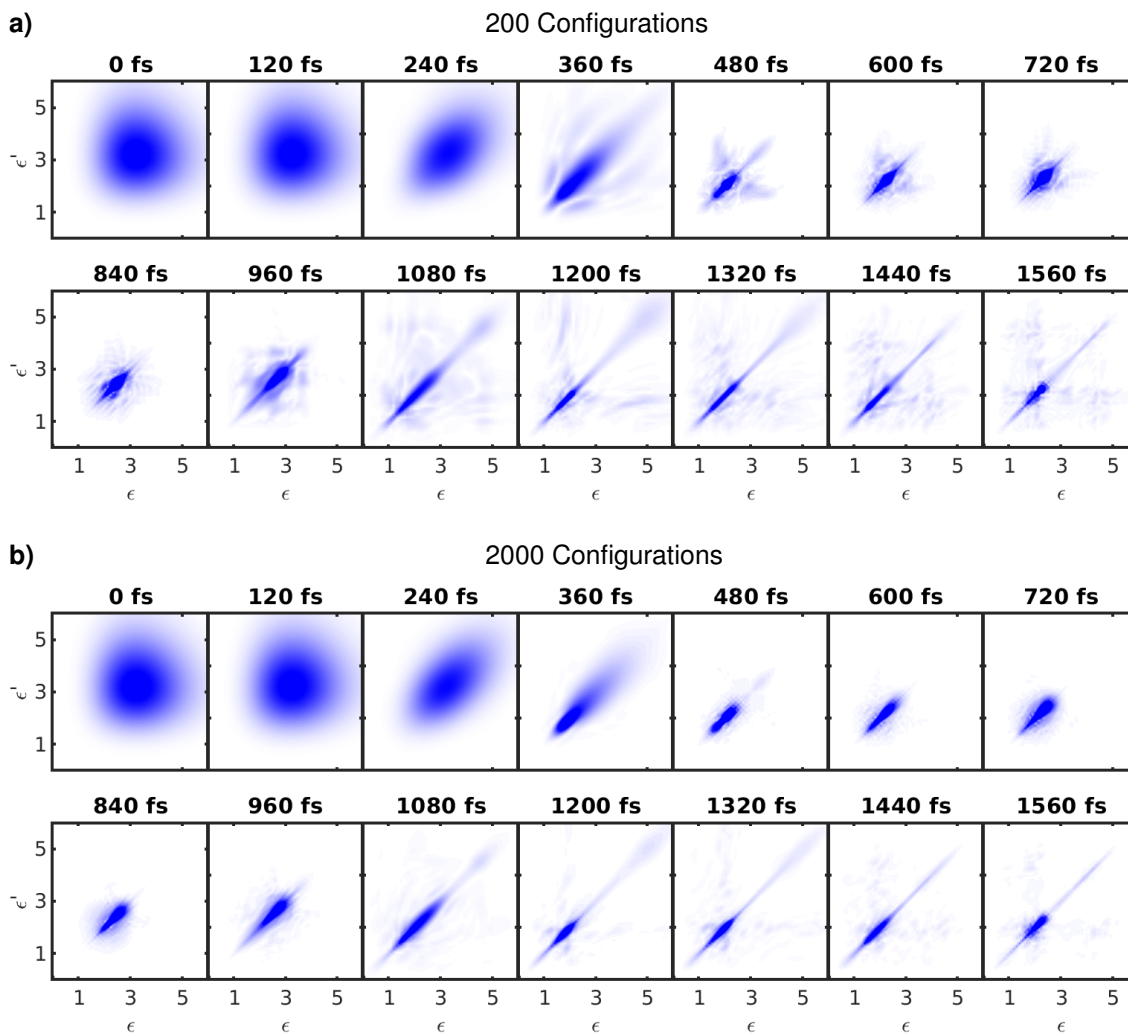


Figure 1.4.: Absolute value of the reduced density matrix $|\varrho(\epsilon_1, \epsilon'_1, t)|$ of the I_2 stretching mode in the representation of the eigenstates of the B state I_2 Hamiltonian, calculated at different times using MCE with 200 trajectories (top) and 2000 trajectories (bottom). Eigenenergies ϵ_1, ϵ'_1 are shifted by the ground state of \hat{H}^S and given in units of 10^3 cm^{-1} .

Instead, they approach a higher-lying artificial equilibrium state and fail to obey detailed balance.[80] The relaxation curve for MCE lies between the curves for Ehrenfest and MCTDH. It captures the initial drop very well and stays close to the MCTDH curve until ca. 1080 fs, when energy is transferred from the system to the environment for the second time. After this time, in the high dimensional space configuration space, the overlap between the frozen Gaussians describing the environment approaches zero. Thus, the expectation value for the energy, calculated using eq. (1.16), will approach a weighted sum of the expectation values for all the Ehrenfest configurations, as $\bar{S}_{kl}^{(m)}$ becomes diagonal. Since each Ehrenfest trajectory approaches the wrong limit, the same will happen for MCE. However, as long as there is sufficient overlap between the Gaussians describing the environment, the MCE wavefunction is able to describe the vibrational energy redistribution better than Ehrenfest dynamics. Interestingly, fully classical dynamics follows the exact quantum solution for the entire simulation time. This implies that even though interference effects can be observed in both the reduced probability fig. 1.1 and the density matrix fig. 1.3, the energy transfer itself is well described by a fully classical model.

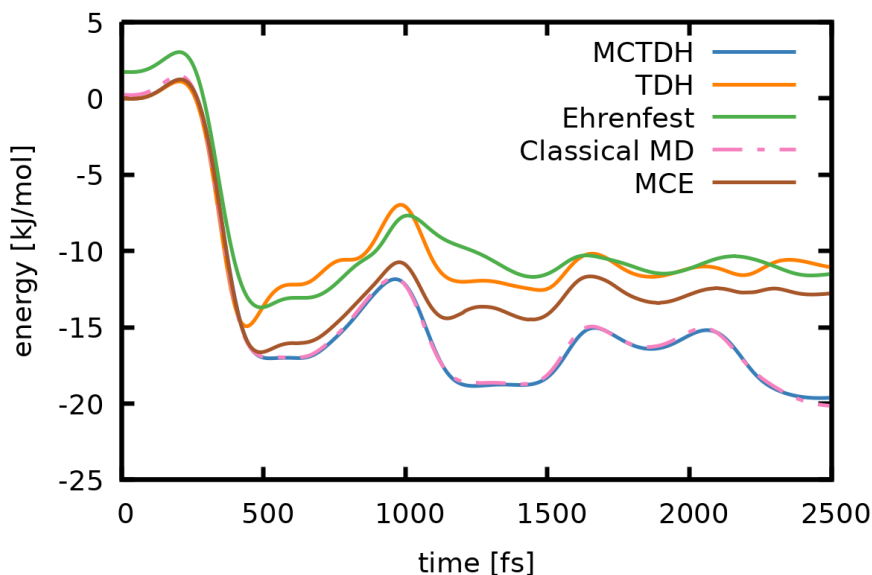


Figure 1.5.: Energy transfer between I_2 and krypton cage calculated using different dynamics methods. Ehrenfest, MCE, and classical MD use 2000 trajectories each.

In summary, a MCE approach adapted to the coupling between the vibrational modes of a quantum system and a classical environment was developed and implemented. The approach was tested on the dynamics of a 7-dimensional model of an I_2Kr_{18} cluster. The method reproduces the numerically exact MCTDH dynamics well and is able to correctly treat the decoherence induced in the system in the initial collision with the solvent cage. MCE can describe the energy transfer out of the quantum system and into the environment at intermediate times better than ordinary Ehrenfest dynamics or TDH. In detail, both MCE and Ehrenfest dynamics accurately describe the initial collision of the system's atoms with the environment, and MCE (with 2000 Ehrenfest configurations) extends the description to the first three vibrational periods of the molecule inside the cage. However, in the long time limit, MCE violates detailed balance like ordinary

Ehrenfest dynamics and approaches the same wrong equilibrium state. To significantly increase the time span for which MCE is able to describe the energy redistribution, a large number of coupled Ehrenfest trajectories are required. Running these Ehrenfest trajectories has a much higher computational cost than running a similar amount of classical trajectories. Solving the equation for the coefficients (eq. (1.12)) also causes high cost since multiple $N \times N$ matrices need to be constructed and multiplied multiple times per time-step. Thus, if a quantum description of the system is required for more than a few vibrational periods, these systems are treated more efficiently by G-MCTDH, which requires a much smaller number of Gaussian wavepackets to describe the dynamics of the environment.[91, 92] Classical dynamics performs very well in the description of vibrational energy redistribution in our test case, which involves fairly heavy atoms. Thus, in similar cases, if a quantum description is not required *a priori*, this should be the method of choice. One might add quantum effects into these classical simulations *a posteriori* with frozen Gaussians, for example, using the original approach by Heller,[87] the Herman-Kluk propagator[93–95] or a path integral based approach.[95, 96] However, one might also envision a strategy where an initial MCE wavepacket gradually transforms into swarms of classical trajectories as the overlap is lost between different configurations due to the motion of the environment. The MCE method, as it stands, can be used for short to intermediate times, where it can simulate vibrational dynamics very accurately.

1.3. Trajectory Surface Hopping

Coupling a classical environment to a quantum system is a challenging problem with no unique solution. The TSH approach is an alternative to the approaches based on Ehrenfest dynamics presented in the previous sections. As is the case for Ehrenfest dynamics, TSH is usually presented for the separation between electronic and nuclear degrees of freedom. We will do the same here but remain consistent with the notation from previous chapters. To compare the two perspectives, one should have in mind that $\hat{H}^S + \hat{V}^{ES} = \hat{H}_{el}$ with the electronic Hamiltonian \hat{H}_{el} , and $\hat{H}^E = \hat{T}_{nuc}$ with the kinetic operator of the nuclei \hat{T}_{nuc} . We define $\hat{H}_{el} = H_{mol} - \hat{T}_{nuc}$ and $\hat{T}_{nuc} = \sum_A -\hbar^2/(2M_A)\nabla_A^2$ with a sum over all nuclei. Accordingly, the wavefunction of the quantum system Ψ^S represents an electronic wavepacket, and the trajectories of classical environment $\{\mathbf{p}_k, \mathbf{q}_k\}$ are the trajectories of the nuclei of the molecule. It is pointed out that there are also examples of the successful application of TSH approaches to system-bath problems in model systems.[82, 97, 98]

The equation of motion for the quantum system in the TSH approach is identical to the one in the Ehrenfest approach (eq. (1.7)).[23] The electronic wavepacket Ψ^S is expanded in an orthonormal time-dependent basis

$$\Psi^S(t) = \sum_k c_k(t)\phi_k^S(t). \quad (1.21)$$

In most cases, the basis is formed by the adiabatic states of the electronic system, such that $(H^S + V^{ES}(t))\phi_k^S(t) = E_k^S(t)\phi_k^S(t)$. However, the general case will be discussed in the following.

Inserting the basis set expansion into the TDSE, one obtains

$$i\hbar \frac{\partial}{\partial t} \mathbf{C} = (\mathbf{H} - i\hbar \mathbf{T}) \mathbf{C}, \quad (1.22)$$

with the Hamiltonian matrix \mathbf{H} with matrix elements

$$H_{kl} = \langle \phi_k^S(t) | H^S + V^{ES} | \phi_l^S(t) \rangle \quad (1.23)$$

and the time-derivative coupling matrix \mathbf{T} with matrix elements

$$T_{kl} = \langle \phi_k^S | \frac{\partial}{\partial t} | \phi_l^S \rangle. \quad (1.24)$$

\mathbf{T} can be calculated as

$$T_{kl} = \langle \phi_k^S(t) | \nabla | \phi_l^S(t) \rangle \cdot \mathbf{v}. \quad (1.25)$$

In the adiabatic basis, $\langle \phi_k^S(t) | \nabla | \phi_l^S(t) \rangle$ is called the non-adiabatic coupling vector. \mathbf{v} is the velocity vector of the nuclei. The matrix elements $\langle \phi_k^S | \frac{\partial}{\partial t} | \phi_l^S \rangle$ can also be obtained via a finite differencing scheme directly from the overlaps between the time-dependent basis functions at different time-steps.[99] Alternatively, the overlaps can be used to perform a local diabatisation and avoid explicit construction of \mathbf{T} . [100, 101]

The crucial difference between the Ehrenfest and TSH methods lies in the description of the classical part. In TSH, the forces acting on the nuclei are not derived from the entire wavefunction of the quantum system Ψ^S as in the Ehrenfest method eq. (1.8), but from the so-called active state ϕ_λ , which is one of the basis functions in eq. (1.21). If the

adiabatic representation was chosen, ϕ_λ is an electronic eigenstate in the BO picture. This means that the nuclei are propagated on a single BO surface according to

$$m^E \frac{\partial^2 q^E}{\partial t^2} = -\nabla \left(V^E + \langle \phi_\lambda^S | V^{ES} | \phi_\lambda^S \rangle \right) \quad (1.26)$$

in contrast to eq. (1.7) for Ehrenfest dynamics. In an ensemble of many simulation runs, we assign an active state to each run in the beginning and then perform abrupt switches (hops) to different states during the simulation. The time of these hops is determined probabilistically by a hopping procedure. The expression ‘the trajectory in state λ ’ signifies which state ϕ_λ is currently assigned to the simulation run. Since a specific active state needs to be chosen, the results of a TSH simulation depend on the choice of basis states (adiabatic, diabatic, or otherwise). This is in contrast to the Ehrenfest method (and the exact solution of the TDSE for the full system), where the dynamics do not change when the basis, which is used to represent the electronic wavepacket, is changed, as long as the basis is complete. This inconsistency of TSH is known as representation dependence.[30] It is, in most cases, a smaller problem when compared to the inability of Ehrenfest dynamics to describe wavepacket splitting when two states with different gradients are simultaneously occupied. A correct description of wavepacket splitting is especially relevant at a conical intersection (CoIn), where the gradients of the two coupled states are, in general, very different. CoIns are encountered ubiquitously in electronic relaxation processes.

We now turn our attention to the hopping procedure that determines how the active state is chosen. The most well-known hopping procedure is the fewest switches algorithm developed by Tully.[29] The population ρ_{kk} of the basis state ϕ_k^S is given by $\rho_{kk} = c_k c_k^*$. Inserting into eq. (1.22) gives the following expression for the time-derivative of the population:

$$\frac{\partial \rho_{kk}}{\partial t} = \sum_{l \neq k} 2\hbar^{-1} \text{Im}(c_k^* c_l H_{kl}) - 2 \text{Re}(c_k^* c_l T_{kl}) = \sum_{l \neq k} b_{kl}. \quad (1.27)$$

The aim is to find a probability $P_{\lambda \rightarrow k}$ to switch the active state from λ to k while minimizing the number of switches. We assume that the states only interact in pairs, and we only care about probability transfer from the current active state λ to other states. Thus, for a state k , the only relevant term on the right-hand side of the equation above is $b_{k\lambda}$. In an ensemble of N simulation runs, the number of trajectories in λ at time t should approximately be given by

$$N_\lambda \approx N \rho_{\lambda\lambda}(t). \quad (1.28)$$

To minimize the number of switches, a small time-step Δt is considered. If $\frac{\partial \rho_{kk}}{\partial t}$ is negative, then the population in k is decreasing during Δt and no trajectories should switch from λ to k ($P_{\lambda \rightarrow k} = 0$). If $\frac{\partial \rho_{kk}}{\partial t}$ is positive, then the population in k is increasing during Δt and $N \frac{\partial \rho_{kk}}{\partial t} \Delta t = N b_{k\lambda} \Delta t$ trajectories should switch from λ to k . Since there are $N \rho_{\lambda\lambda}$ trajectories in λ , the probability for a single one to switch is

$$P_{\lambda \rightarrow k} = \frac{b_{k\lambda} \Delta t}{\rho_{\lambda\lambda}}. \quad (1.29)$$

A random number ξ in the interval $[0, 1]$ is drawn to determine whether a hop takes place. A hop to state κ is performed if

$$\sum_{k \neq \lambda}^{\kappa-1} P_{\lambda \rightarrow k} < \xi \leq \sum_{k \neq \lambda}^{\kappa} P_{\lambda \rightarrow k}. \quad (1.30)$$

After this general introduction to the TSH algorithm, a few more details that are necessary ingredients to a surface hopping simulation will be discussed. These are velocity rescaling, frustrated hops, decoherence correction, and the transformation into an approximate adiabatic basis.

When a hop is performed, energy is generally not conserved along a trajectory. Thus, to enforce energy conservation, the velocities of the nuclei are rescaled whenever a hop occurs. The rescaling can be performed parallel to the velocity vector or in the direction of the non-adiabatic coupling vector $\langle \phi_\lambda^S(t) | \nabla | \phi_k^S(t) \rangle$. The rescaling in the direction of the non-adiabatic coupling vector is more physically meaningful.[102] However, rescaling parallel to the velocity vector can still be performed in cases where non-adiabatic coupling vectors are expensive to compute with errors that are negligible in most cases.[103]

If the hop occurs from a state that is higher in energy to one that is lower in energy, velocity rescaling is always possible. However, when the hop occurs from a lower energy state to one that is higher in energy, the nuclei might not have enough kinetic energy. In this case, a hop is called frustrated and is not performed. It has been argued that the velocity component along the non-adiabatic coupling vector should be reversed after a frustrated hop.[104, 105] Frustrated hops are an essential part of the TSH method since they break the inherent symmetry between hops to higher states and hops to lower states. This enables surface hopping to approximately obey detailed balance even though it is based on an Ehrenfest-like equation of motion for the quantum system. When adiabatic states are used to represent the electronic wavepacket, the number of trajectories N_λ in each state generally approach a Boltzmann distribution quite well in the long-time limit.[80, 106] However, this comes with a drawback. The symmetry breaking between hops to higher states and hops to lower states happens only for the number of (classical) trajectories in λ and not for the (quantum) populations $\rho_{\lambda\lambda}$. Therefore, the approximate equality in eq. (1.28) is violated.

Due to the Ehrenfest-like equation of motion for the electronic system, TSH is overcoherent and needs to be corrected for decoherence effects.[30, 107–110] These decoherence corrections also re-align $\rho_{\lambda\lambda}$ with the number of trajectories in each state N_λ , if there is ever a mismatch (for example due to frustrated hops). The decoherence correction can be done either by using a stochastic algorithm to periodically collapse the quantum system wavefunction to the active state (as, for example, in the augmented fewest switches surface hopping algorithm by Jain and Subotnik[111]) or by modifying eq. (1.22) to reduce the amplitude of coefficients of inactive states over time (as, for example, in the energy-based decoherence correction by Granucci and Persico[112]).

It has been shown that surface hopping, when applied to the separation between electronic and nuclear degrees of freedom, is most accurate in the adiabatic basis. A reason for this is that couplings in the adiabatic representation are very localized, and thus an instantaneous transition from one state to another can be better justified.[113–116] In this basis, the surface hopping prescription can be rationalized by a derivation from the semi-classical Liouville equation[113, 117] and reproduces the classical dynamics on potential energy surfaces produced by the exact factorization approach.[118, 119] When surface hopping simulations are performed *ab initio* for a molecular system, the quantum chemistry package generally only diagonalizes the molecular Coulomb Hamiltonian (MCH). The MCH is equal to the electronic Hamiltonian \hat{H}_{el} if only Coulomb interactions are included in the potential part of the molecular Hamiltonian H_{mol} . Thus, there may be remaining off-diagonal couplings, such as those introduced by an external laser

field eq. (1.2) or by spin-orbit coupling (SOC). These residual coupling can be treated by the surface hopping with arbitrary couplings (SHARC) approach.[114–116] In this approach, the total Hamiltonian in the basis of the MCH states is diagonalized at each time-step by a unitary matrix \mathbf{U} :

$$\mathbf{H}^{diag} = \mathbf{U}^\dagger \mathbf{H}^{MCH} \mathbf{U}. \quad (1.31)$$

If eq. (1.22) is used to propagate the coefficients, \mathbf{T} needs to be transformed according to

$$\mathbf{T}^{diag} = \mathbf{U}^\dagger \mathbf{T}^{MCH} \mathbf{U} + \mathbf{U}^\dagger \frac{\partial}{\partial t} \mathbf{U}. \quad (1.32)$$

Evaluating the second term is numerically unstable.[116] Instead, one can propagate in the MCH representation and transform the coefficients at each step since the propagation of the coefficients is independent of the representation. This is equivalent to transforming the time-evolution operator $\mathcal{U}(t, t + \Delta t)$

$$\mathbf{C}^{diag}(t + \Delta t) = \mathcal{U}^{diag}(t, t + \Delta t) \mathbf{C}^{diag}(t) \quad (1.33)$$

$$= \mathbf{U}^\dagger \mathcal{U}^{MCH}(t, t + \Delta t) \mathbf{U} \mathbf{C}^{diag}(t), \quad (1.34)$$

where the superscript *MCH* or *diag* specifies the basis for the matrix representation of the operator. The hopping probabilities (eq. (1.29)) are also slightly altered to use a form that is still consistent with the fewest-switches criterion while avoiding the evaluation of $\mathbf{U}^\dagger \frac{\partial}{\partial t} \mathbf{U}$;[100, 116]

$$P_{\lambda \rightarrow k} = \left(1 - \frac{|c_\lambda(t + \Delta t)|^2}{|c_\lambda(t)|^2} \right) \frac{\text{Re} [c_\lambda(t + \Delta t) \mathcal{U}_{\lambda k}^*(t, t + \Delta t) c_k^*(t)]}{|c_\lambda(t)|^2 - \text{Re} [c_\lambda(t + \Delta t) \mathcal{U}_{\lambda \lambda}(t, t + \Delta t)^* c_\lambda^*(t)]}. \quad (1.35)$$

Here, all quantities are in the diagonal representation. Finally, the gradients also need to be transformed such that the classical system can be propagated:

$$\nabla \langle \phi_\lambda^{S,diag} | V^{ES} | \phi_\lambda^{S,diag} \rangle = \sum_{\mu\nu} U_{\mu\lambda}^* U_{\nu\lambda} \nabla \langle \phi_\mu^{S,MCH} | V^{ES} | \phi_\nu^{S,MCH} \rangle. \quad (1.36)$$

The diagonal elements $\mu = \nu$ of the right-hand side are just the gradients in the MCH representation (weighted by $|U_{\mu\lambda}|^2$) and the non-diagonal element are energy-difference weighted non-adiabatic coupling vectors in the MCH representation (weighted by $U_{\mu\lambda}^* U_{\nu\lambda}$). Those would require explicit evaluations of the non-adiabatic coupling vectors by the quantum chemistry package. Often, the cross terms containing the non-adiabatic coupling vectors are small and can be neglected.[116] In this way, the SHARC approach enables numerically stable TSH simulations in the adiabatic representation even if non-diagonal terms are initially present in the Hamiltonian.

In this work, several modifications to the existing TSH code SHARC2.1[120] were made, this includes an adaptive time-stepping algorithm,[121] an interface to the FermiONS++ program and an interface to perform surface hopping at the XMS-CASPT2[61, 62, 122] level of theory with analytical gradients computed by BAGEL[123] and spin-orbit couplings calculated by OpenMolcas.[124] The SHARC-OpenMolcas-BAGEL interface was used to study the excited state dynamics of cyclohex-2-enone and its Lewis acid-base complex with BF_3 , while the SHARC-FermiONS++ interface was used to study the behavior of this complex in solution. These studies are presented in chapter 4.

2. Energy Transfer in Linear Spectroscopy

The mechanism with which energy is transferred from the electric field to a molecular sample is of fundamental importance in spectroscopy. The theory of energy transfer is well known in most limits. The energy transfer from the point of view of the molecule can be well described by the Schrödinger equation (eq. (1.1)) and a field term in the dipole approximation (eq. (1.2)). The field itself can be described by the Maxwell equations with a susceptibility determined by the electronic properties of the molecule. For almost all spectroscopies, this is sufficient.[125] It fails when short wavelengths (smaller than a few times the size of a molecule), very strong fields, or effects due to the quantized nature of the field (optical cavities, spontaneous emission) must be considered.[126–128]

Novel techniques can also illuminate new details. Field-resolved spectroscopy is one of these recent developments that can be used to study the energy transfer between molecular vibrations with a laser field.[35, 129, 130] Using this experimental technique, the infrared field passing through a sample is recorded with sub-optical-cycle time resolution. Thus, vibrational spectra can be measured with high precision. Additionally, the time-resolved nature of the measurement can provide direct insight into the state of the molecular system not only before and after excitation but also during the interaction with the laser pulse. This way, direct observation of the energy transfer between the vibrating molecules and the electric field is possible. In this context, phenomena that have not yet been described in the context of vibrational spectroscopy are observed, such as periodic coherent transients in the interaction with a chirped laser pulse and step-wise energy uptake with each half-cycle of the electric field. An accurate description of the molecules themselves, their condensed phase environment, and their interaction with the laser field are required to understand and model the observed phenomena. An approach that achieves this goal will be presented in the following.

In principle, two sets of parameters govern the interaction of a molecular sample with an oscillating electric field. These are transition dipole moments μ_k and transition frequencies ω_k of the k relevant vibrational transitions. We will look at the example of a small molecule in a solvent environment in which a few modes are vibrationally excited. These modes are coupled to many lower frequency modes, mainly hindered rotations and translations (librations) of the molecule in its solvent cage and librations of the solvent molecules themselves. These motions are not resolved individually but influence the observed vibrational transitions' lineshape. It is neither necessary nor computationally feasible to determine μ_k and ω_k for the coupled system and thus include these low-frequency modes in the quantum description of the molecule. Instead, for Lorentzian lineshapes, a single parameter for each vibrational mode is sufficient. These dephasing rates Γ_k form a third set of parameters describing the molecule-field interaction. For a dilute solution of mass concentration β , containing dissolved molecules of mass m , the

linear susceptibility can then be directly obtained as

$$\chi^{(1)}(\omega) = \sum_k \frac{2\beta\mu_k^2\omega_k}{3m\hbar\epsilon_0(\omega_k^2 - (\omega - i\Gamma_k)^2)}. \quad (2.1)$$

It is directly related to the absorbance of the medium (see appendix B.1).

In principle, all the parameters mentioned in the previous paragraph can be obtained from the dipole autocorrelation function of the molecular system and its environment, which would also include non-linear effects. However, quantum dynamical simulations of the dipole autocorrelation, which include a sufficient number of solute and solvent modes, are not feasible. However, a classical simulation of the dipole autocorrelation function is possible and, as shown in section 1.2, fig. 1.5, classical dynamics can provide a surprisingly accurate description of vibrational energy redistribution.

A convenient way to simulate the classical dipole autocorrelation function was presented by Thomas *et al.*, who computed the dipole autocorrelation function from a Voronoi decomposition of the electronic density of an *ab initio* MD simulation.[56, 57] This approach is implemented in the TRAVIS program package.[131] Computing the autocorrelation function requires MD runs of the solute molecule and its environment (10-100 molecules) of around 30-50 ps, which can be done at reasonable computational cost using pure density functionals with the CP2K code.[132] In our simulations we use the BLYP-D3 functional for this task.[133–135] While the general dynamics of the molecule and its interaction with the environment are well described at this level of theory, the frequencies and transition dipole moments are often not accurate enough. They can, however, be improved by using a density functional from a higher rung of Perdew’s Jacobs ladder,[136] such as M06-2X, which is highly accurate for vibrational transitions.[137] Thus, it is advantageous to combine the dephasing rates from the molecular dynamics simulations with more accurate frequencies and transition dipole moments. The effects of solvation at the higher level can be described using either only a polarizable continuum model[138] or using explicit solvation by taking clusters sampled from MD simulations and embedding them in a polarizable continuum model.[139] For the most interesting normal modes, a potential energy surface can be built on a grid.[140] For these modes, transition frequencies and transition dipole moments can be evaluated numerically by diagonalizing the resulting vibrational Hamiltonian. This numerical diagonalization is especially necessary for modes where anharmonic effects or a non-linear dependence of the dipole moment on displacement are expected. For the remaining modes, an ordinary harmonic frequency analysis is sufficient.

Suppose the vibrational transition is homogeneously broadened (approximately Lorentzian lineshape). In that case, the static distribution of transition frequencies obtained from the simulation of solute-solvent clusters can not be used to model the broadening due to motional narrowing, which is an explicitly dynamic effect.[141] Thus, the final results are averaged over all MD snapshots and broadening must be extracted from the *ab initio* MD at the lower level (BLYP). The most basic way to do this is to fit Lorentzian lineshapes to the Fourier-transformed classical dipole autocorrelation function to obtain approximate dephasing rates.

A convenient model system for investigations using field-resolved spectroscopy is DMSO₂ in an aqueous solution. In this system, well-separated asymmetric and symmetric stretching vibrations of the SO₂ moiety can be observed at 1135 and 1280 cm⁻¹. The responses of these modes to an impulsive excitation and a chirped excitation in the

infrared region are studied using field-resolved spectroscopy and are modeled using the methods outlined above.

The article “Sub-optical-cycle light-matter energy transfer in molecular vibrational spectroscopy” was published in *Nature Communications*. The key findings presented in the article are:

- During the vibrational excitation of DMSO₂ by a few-fs pulse, alternating absorption and stimulated emission can be observed with each half-cycle of the electric field (sub-cycle dynamics). This is caused by terms in the expression for the coherence that oscillate with the sum of the vibrational and field frequencies and are usually neglected in the rotating wave approximation (RWA).
- On a femtosecond to picosecond timescale, another series of absorption and emission events can be observed when a chirped laser field is used. These coherent transients are known from the optical spectroscopy of atoms in the gas phase but are first observed here in the context of vibrational spectroscopy in the condensed phase. They are caused by the fact that the phase relationship between the excitation field and the molecular vibration changes over time due to the chirp. Dephasing of the molecular vibrations has to be included in the theory to describe the dampening of these transients, even though only the coherent part of the molecular response is observed by field-resolved spectroscopy.
- Sub-cycle dynamics and coherent transients are both directly connected to the time evolution of the vibrational coherence in the complex plane. The coherent transients observed in the interaction with a chirped pulse are connected to a spiral pattern formed by vibrational coherence. The observed sub-cycle dynamics are connected to a cycloid pattern. A more detailed view of the equations describing the dynamics of the vibrational coherence in the complex plane can be found in appendix B.2.
- The model describing the observed energy transfer can be parametrized using *ab initio* calculations, more specifically (time-averaged) vibrational transition dipole moments and frequencies obtained from static density functional theory (DFT) calculations and dephasing rates obtained from *ab initio* MD simulations. This leads to good agreement between the observed and calculated spectral shapes. The curves for the coherent energy transfer ($CET(t)$) are also reproduced well by the *ab initio* parametrization. The influences of the solvation environment on the vibrational transition dipole moments and frequencies are well described by either a polarizable continuum model or by explicit solvation.
- In the impulsive excitation regime, energy transfer ratios characterizing the efficiency of the spectroscopic method can be defined. The fraction of the maximally absorbed energy to the excitation energy scales linear with concentration, while the fraction of the emitted energy to the excitation energy scales quadratic with concentration.

Hereafter, the article “Sub-optical-cycle light-matter energy transfer in molecular vibrational spectroscopy” published in *Nature Communications* is reproduced. Supplementary information is available online. Additional Information can also be found in appendix B.2.



Sub-optical-cycle light-matter energy transfer in molecular vibrational spectroscopy

Received: 2 June 2022

Accepted: 19 September 2022

Published online: 06 October 2022

Check for updates

Martin T. Peschel^{1,5}, Maximilian Högner^{2,3,5}, Theresa Buberl^{2,3,5}, Daniel Keefer^{1,4}, Regina de Vivie-Riedle¹ ✉ & Ioachim Pupeza^{2,3} ✉

The evolution of ultrafast-laser technology has steadily advanced the level of detail in studies of light-matter interactions. Here, we employ electric-field-resolved spectroscopy and quantum-chemical modelling to precisely measure and describe the complete coherent energy transfer between octave-spanning mid-infrared waveforms and vibrating molecules in aqueous solution. The sub-optical-cycle temporal resolution of our technique reveals alternating absorption and (stimulated) emission on a few-femtosecond time scale. This behaviour can only be captured when effects beyond the rotating wave approximation are considered. At a femtosecond-to-picosecond timescale, optical-phase-dependent coherent transients and the dephasing of the vibrations of resonantly excited methylsulfonylmethane (DMSO₂) are observed. Ab initio modelling using density functional theory traces these dynamics back to molecular-scale sample properties, in particular vibrational frequencies and transition dipoles, as well as their fluctuation due to the motion of DMSO₂ through varying solvent environments. Future extension of our study to nonlinear interrogation of higher-order susceptibilities is fathomable with state-of-the-art lasers.

Static or vibrationally-induced asymmetric charges in molecules cause electric dipole moments, responsible for efficient coupling to infrared (IR) radiation¹. Optical energy transferred from an excitation IR field to vibrating molecules can either dissipate incoherently in the form of heat, or can be re-emitted with a fixed phase relation to the excitation field, i.e., coherently. Traditional frequency-domain vibrational spectroscopy methods such as direct-absorption spectroscopy or Fourier-transform spectroscopy provide wavelength-resolved absorbance (and phase) information, obtained via temporal integration over the duration of the interaction^{2–4}. Figure 1a illustrates the result of such a measurement for a Lorentzian-shaped absorption line which is typical for linearly-interrogated, homogeneously-broadened resonances of molecules embedded in a solvent⁵.

IR molecular absorption spectra contain rich information about molecular composition, abundance and conformation, making

vibrational spectroscopy a widely-applied tool in fields including fundamental science^{1,6}, analytical chemistry⁷, and the life sciences^{2,8}. However, in traditional frequency-domain spectroscopy, temporal integration hides the transient energy transfer between the light field and the material sample, obscuring deeper insight into the underlying dynamic light-matter interaction.

This work presents a quantitative study of the complete dynamics of the coherent energy transfer between broadband mid-IR optical waveforms and vibrating molecules in aqueous solution, with sub-optical-cycle temporal resolution. Field-resolved IR spectroscopy⁹ permits the differentiation between the qualitatively different transient energy transfer for few-cycle excitation (FCE) and chirped-pulse excitation (CPE). In both cases, sub-cycle resolution allows us to observe ultrafast dynamics caused by effects beyond the rotating wave approximation (RWA). Furthermore, FCE allows for temporal

¹Ludwig-Maximilians-Universität München, Butenandtstraße 5-13, 81377 Munich, Germany. ²Max-Planck-Institut für Quantenoptik, Hans-Kopfermann-Straße 1, 85748 Garching, Germany. ³Ludwig-Maximilians-Universität München, Am Coulombwall 1, 85748 Garching, Germany. ⁴Department of Chemistry, University of California, Irvine, CA 92697, USA. ⁵These authors contributed equally: Martin T. Peschel, Maximilian Högner, Theresa Buberl.

✉ e-mail: regina.de_vivie@cup.uni-muenchen.de; ioachim.pupeza@mpq.mpg.de

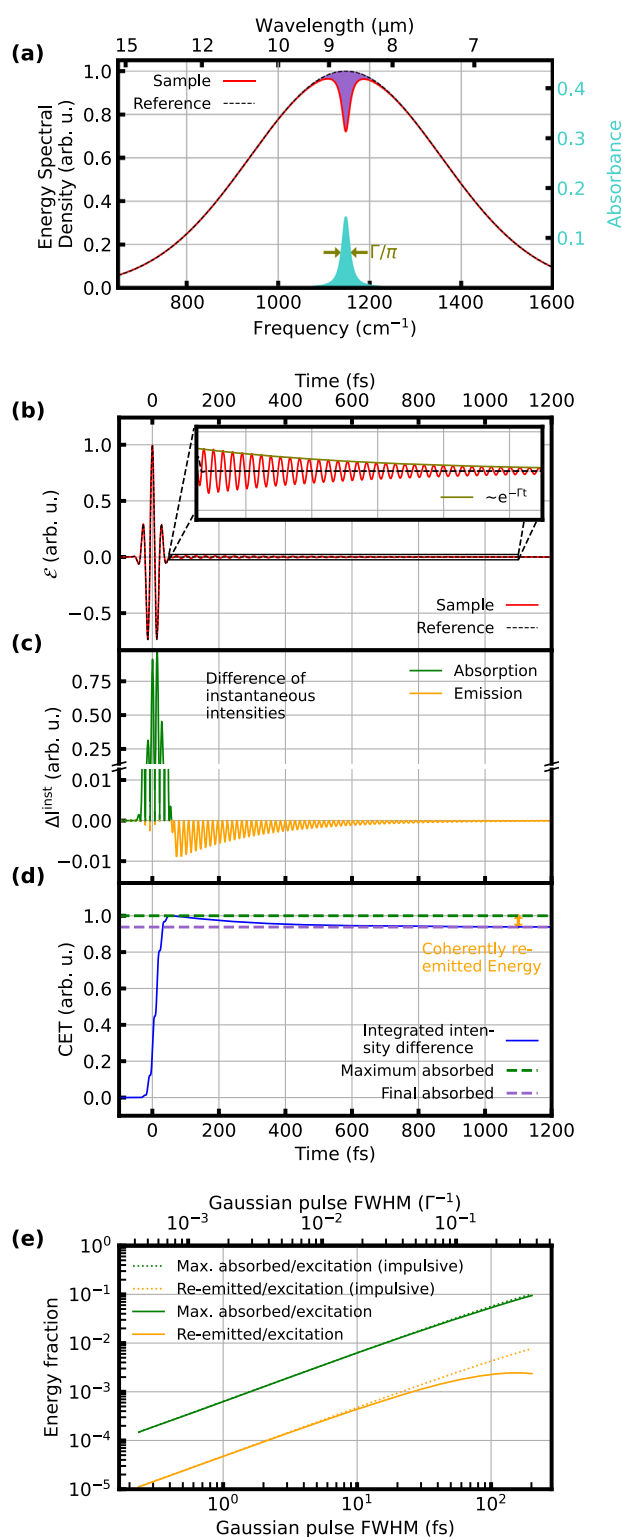


Fig. 1 | Time-integrated and time-resolved broadband vibrational spectroscopy. **a** Model spectrum before (black, dashed) and after (red) transmission through a Lorentzian absorber centered at 1148 cm^{-1} with a full-width-at-half-maximum (FWHM, Γ/π) of 19.4 cm^{-1} , shown for conventional (time-integrating) absorption spectroscopy. Purple shaded area: difference between the two spectra, amounting to the energy incoherently dissipated in the molecular sample. Turquoise shaded area: normalized absorbance, defined as the difference between the logarithms of the two spectra $\log_{10}(|\text{Reference}|) - \log_{10}(|\text{Sample}|)$. **b** Electric field $\varepsilon(t)$ of the 30-fs-full-width-half-maximum Gaussian excitation pulse (black, dashed) with the spectrum shown in black in **a**. Red: coherent response of the Lorentzian absorber shown in **a** to this few-cycle excitation (FCE). Olive: decay of the molecular response due to dephasing proportional to $e^{-\Gamma t}$. **c** Time-resolved difference $\Delta I^{\text{inst}}(t)$ of the instantaneous intensities of the electric fields in **b**. The positive values (green) correspond to absorption, the negative values (yellow) to coherent emission. For FCE, the coherent emission event has no contribution from the excitation. **d** Integration of $\Delta I^{\text{inst}}(t)$ shown in **c** yields the coherent energy transfer CET(t). Green dashed line: maximum of CET(t), i.e., the maximum transiently absorbed energy. Purple dashed line: end value of CET(t), equal to the purple shaded area in **a**. Orange double arrow: difference between maximum and end value, corresponding to the energy which is coherently re-emitted by the Lorentzian absorber. **e** Ratio of the maximum transiently absorbed energy (green) and the coherently-re-emitted energy (yellow) to the excitation pulse energy, as a function of the FCE-pulse duration. These ratios deviate by less than 30% from the values for the impulsive excitation regime (dotted lines, see also Supplementary Information) for pulse durations below one-tenth of the typical Lorentzian decay time Γ^{-1} (here, 548 fs).

sample susceptibility, which is determined by the microscopic vibrational transition dipole moments, eigenfrequencies, and dephasing times of the vibrational modes^{13–16}.

Results and discussion

Energy balance in the impulsive regime

We define absorption and coherent emission as events of energy transfer from the impinging coherent light beam to the molecules and vice versa. For a FCE (Fig. 1b), the events of absorption and coherent emission (in analogy to the nuclear magnetic resonance phenomenon of free induction decay¹⁰) are separated in time to a large extent (Fig. 1c, d). While the absorption event is governed by an interference between the excitation waveform and the molecular response, the coherent emission consists only of the latter (after the decay of the excitation). The brevity of the absorption event implies little spectral specificity. In fact, for an impulsive excitation, the absorption information reduces to a frequency-independent scalar equal to the total oscillator strength of the sample in the spectral region covered by the excitation. In contrast, the emitted field after the FCE contains the frequency-dependent sample-specific spectroscopic information. The ratio of its integrated energy to the excitation energy (Fig. 1e, yellow) is indicative of the efficiency with which spectroscopic information can be extracted from the sample. It depends on the environment-dependent transition dipole moments and dephasing times of the molecular sample. The ratios of the maximum absorbed as well as coherently re-emitted energy to the excitation energy are plotted in Fig. 1e as functions of the duration of a Gaussian FCE, showing that FCEs can be regarded as impulsive for pulse durations below one-tenth of the typical Lorentzian decay time (in our experiment, hundreds of femtoseconds).

Few cycle excitation (FCE)

In our experiment, the 1- μm pulses of an Yb:YAG thin-disk oscillator were compressed to 15 fs, subsequently driving intrapulse difference-frequency generation in a nonlinear crystal. This resulted in waveform-stable IR pulses covering the 850-to-1670- cm^{-1} spectral range, which were transmitted through a 30- μm liquid cuvette containing either pure water (reference measurement) or a 10-mg/ml solution of methylsulfonylmethane (DMSO_2) in water (sample measurement).

After transmission through the liquid cuvette, the waveforms were recorded via electro-optic sampling⁹ (see also Supplementary

separation between absorption and emission, two processes that are qualitatively different in that only coherent re-emission is affected by solvation dynamics. For CPE, additional coherent transients emerge^{10–12}. These are caused by the interference between the resonant system response and the non-resonant part of the chirped light wave, which causes additional series of absorption and emission. The discussed effects are quantitatively described by the macroscopic

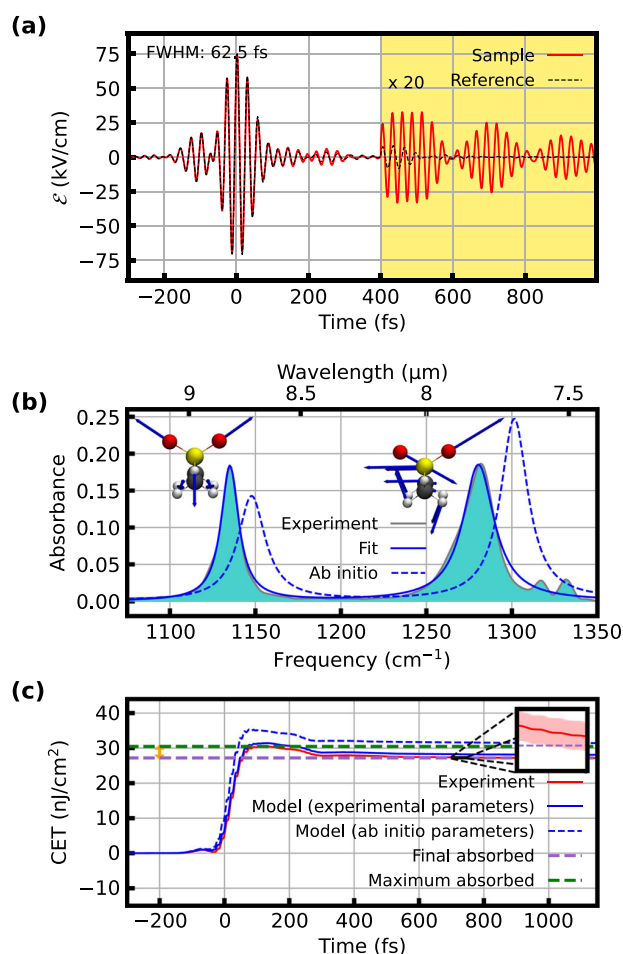


Fig. 2 | Few-cycle excitation (FCE). **a** Electric field of the compressed excitation pulse after transmission through a 30- μm thick layer of water (black, dashed) and a solution of 10 mg/ml DMSO₂ in water (red). **b** Absorbance derived from the measurements in **a**. The molecular structures illustrate the corresponding displacement vectors (blue arrows) of the vibrational modes responsible for the two main absorption bands, the symmetric (left) and asymmetric (right) SO₂ stretching vibrations. Solid blue: Lorentzian fits, dashed blue: ab initio calculations (see text). **c** Coherent energy transfer CET(t) between the excitation field and the DMSO₂ sample, extracted from the experimental data (solid red line: mean value of three consecutive measurements, each comprising 20 scans, shaded red area: error corridor determined with Gaussian error propagation, see Methods), from modeling with the fitted Lorentzian parameters (solid blue line), and with Lorentzian parameters obtained ab initio (dashed blue line). The dashed green and purple lines show the maximum and end level of the CET, respectively. Their difference is the coherently emitted energy, which is 11% of the maximum absorbed energy (orange double arrow).

Information). In the first experiment, the reference waveform was compressed to a duration of 62.5 fs (Fig. 2a). Figure 2b shows the corresponding sample absorbance, dominated by the resonances of the asymmetric and symmetric stretching vibrations of the SO₂ group.

Temporal integration of the instantaneous intensity difference between reference and sample signals from a time instant t_0 well before the pulse until the (variable) instant t yields the coherent energy transfer between sample and light field, CET(t) (Fig. 2c):

$$\text{CET}(t) = \int_{t_0}^t (I_{\text{ref}}^{\text{inst}}(t') - I_{\text{sam}}^{\text{inst}}(t')) dt', \quad (1)$$

where $I_{\text{ref,sam}}^{\text{inst}}(t) = c\epsilon_0 |\mathcal{E}_{\text{ref,sam}}(t)|^2$ is the instantaneous intensity, defined as the magnitude of the Poynting vector, with the real electric field $\mathcal{E}_{\text{ref,sam}}(t)$. This macroscopic quantity is identical to the microscopic coherent energy transfer between the light field and individual molecules, if the reference measurement is taken as the excitation waveform instead of the actual, propagation-dependent electric field (see Supplementary Information). The level asymptotically approached by CET(t) for $t \rightarrow \infty$ corresponds to the integrated difference of the energy spectral density (ESD) measured in frequency-domain spectroscopy (cf. purple shaded area in Fig. 2b). In our measurement, around 11% of the absorbed energy (0.4% of the impinging energy) is coherently re-emitted (Fig. 2c). For a laser pulse described by a Dirac delta function, we obtained a value of 10% using the ab initio numerical model (see Supplementary Information), confirming that our experimental conditions are close to the impulsive excitation regime.

Chirped pulse excitation (CPE)

In a second experiment, we used a 5-mm-thick CaF₂ substrate in the IR beam path to chirp the excitation pulse (Fig. 3a). This leads to a longer pulse duration, such that in contrast to the FCE, a significant portion of the coherent emission now overlaps temporally with the excitation pulse. While the time-integrated ESD (Fig. 3b) yields absorbance information equivalent to that obtained in the FCE case, evaluating the coherent energy transfer with Eq. 1 reveals oscillations in CET(t) which are not observed in the case of the FCE (Fig. 3c). The maxima of these oscillations, visible in the ab initio model calculations around 420 fs and 720 fs, can be attributed to the symmetric stretching vibration and the one around -180 fs to the asymmetric stretching vibration. They occur in the experiment around 80 fs later since the ab initio calculations are blue-shifted with respect to the experiment. Our model (see below) allows us to only include certain vibrational modes in the simulation, thus enabling us to clearly identify certain features with corresponding vibrational modes. The first oscillation maxima are clearly visible, the later maxima of the asymmetric stretch overlap with the signal due to the symmetric stretch. The oscillations are damped by dephasing and by the pulse intensity decreasing over time.

The emerging alternating sequence of absorption and coherent emission, also known as coherent transients¹⁷, was previously observed for atomic transitions in the visible spectral range^{11,12,18,19}. It is caused by the fact that after the resonant transition, the phase of the chirped pulse shifts with respect to the phase of the oscillating system. Whether emission or absorption occurs, depends on the current phase relationship. In addition, there is a second effect that is revealed by a more detailed look at CET(t) (Fig. 3d). Underlying sub-optical-cycle dynamics can be observed: Energy is absorbed or emitted in a stepwise fashion with each half-cycle of the electric field.

Theoretical model

To quantitatively explain the energy transfer dynamics observed in the experiment, we built a model based on time-dependent first-order perturbation theory. Under the assumption of a linear sample response with respect to the impinging power (which is experimentally confirmed within the precision of our measurement²⁰), according to the optical Bloch equations the susceptibility $\chi^{(1)}(\omega)$ of a molecular solution of concentration β of a molecule of mass m is given by^{6,21}:

$$\chi^{(1)}(\omega) = \sum_k \frac{2}{3} \frac{\beta}{m\hbar\epsilon_0} \frac{\mu_{0k}^2 \omega_k}{\omega_k^2 - (\omega - i\Gamma_k)^2}. \quad (2)$$

Thus, in the spectral range covered by our laser field $\mathcal{E}(t)$, each vibrational mode k forms a Lorentz oscillator, parametrized by three parameters: the central frequency ω_k , the transition dipole moment μ_{0k} and the homogeneous dephasing rate Γ_k . We consider all 27 vibrational modes of DMSO₂. The parameters ω_k , μ_{0k} and Γ_k can either

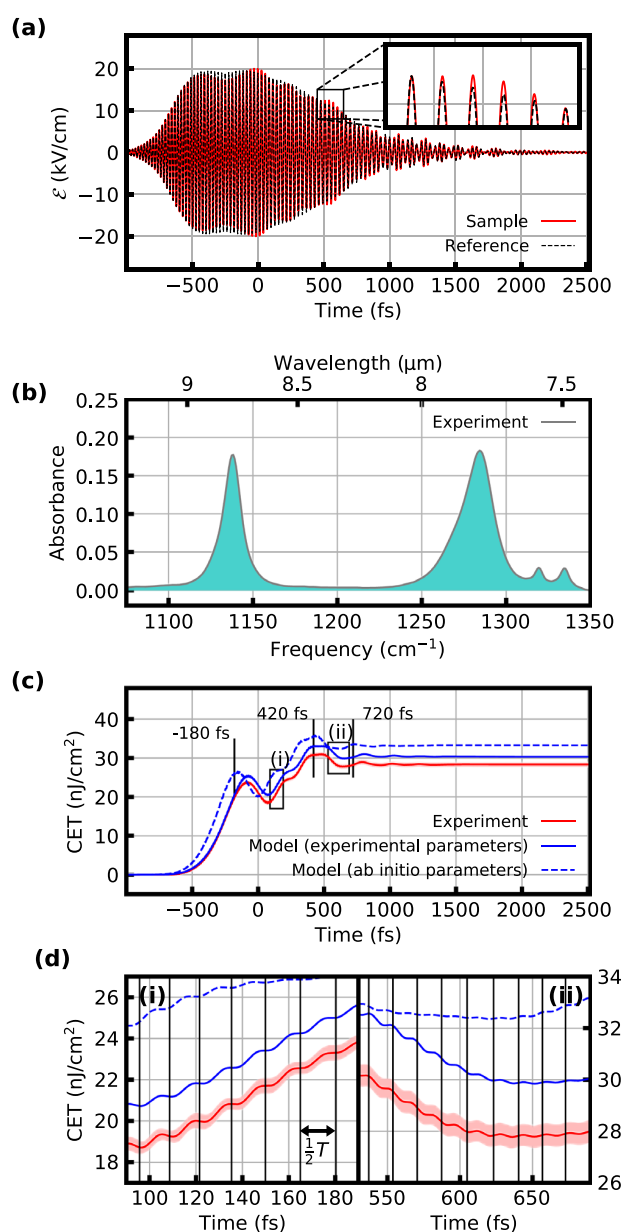


Fig. 3 | Chirped-pulse excitation (CPE). **a** Electric field of the chirped excitation pulse after transmission through a 30- μm thick layer of water (black, dashed) and 10-mg/ml solution of DMSO₂ in water (red). **b** Absorbance, calculated from the measurements in **a**. **c** Coherent energy transfer CET(t) between the excitation field and the DMSO₂ solution, extracted from the experimental data (solid red line: mean value of three consecutive measurements, each comprising 20 traces, shaded red area: error corridor determined with Gaussian error propagation, see Methods), from modeling with the fitted Lorentzian parameters (solid blue line, see Fig. 2), and with Lorentzian parameters obtained ab initio (dashed blue line). The maxima of CET(t) around -180 fs, 420 fs, and 720 fs are marked by vertical black lines (see also the discussion in the main text and Fig. 4d). **d** Magnified displays of the sections enclosed by the dashed black rectangles (i) and (ii) in **c**, revealing the sub-optical-cycle structure of absorption and stimulated emission. The zeros of the electric field are marked by vertical black lines, showing that each absorption or emission step corresponds to one half-cycle ($\frac{1}{2}T$) of the electric field.

be fitted to the experimental data, or they can be determined by ab initio quantum-chemical calculations. The simulation curves shown in Fig. 2b, c and Fig. 3c, d were obtained from the total susceptibility as described in the Supplementary Information.

In a time-domain description, the interaction of the laser field $\mathcal{E}(t)$ with each vibrational mode leads to a coherence⁶

$$\rho_{0k}^{(1)}(t) = \frac{i}{\hbar} \mu_{0k} \int_0^\infty \mathcal{E}(t-t_1) e^{i\omega_k t_1} e^{-\Gamma_k t_1} dt_1, \quad (3)$$

which causes a polarization

$$P_k^{(1)}(t) = F^{-1} \{ \epsilon_0 \cdot \chi_k^{(1)}(\omega) \cdot \mathcal{E}(\omega) \}(t) = \frac{2\beta N_A}{3M} \mu_{0k} \text{Re}(\rho_{0k}^{(1)}). \quad (4)$$

The fields thus created from each infinitesimal sample volume (DMSO₂ molecules and their immediate solvent environment) interfere with each other and with the incident field to create the observed response in the transverse mode of the laser.

Sub-optical-cycle dynamics

The curves in Fig. 4a–c show the evolution of the coherence of one exemplary vibrational mode, the symmetric stretching vibration, in the complex plane, calculated using Eq. 3. One may invoke the RWA²², which neglects terms oscillating with the sum of the vibrational and field frequencies to obtain the curves in Fig. 4a, c. However, field-resolved spectroscopy resolves sub-optical-cycle dynamics, directly revealing the influence of these terms. It is evident comparing Fig. 4a–d that the sub-cycle dynamics vanish under the RWA. The term neglected in the RWA imprints a cycloid structure onto the polarization, which corresponds to the step-like patterns and sub-cycle oscillations in Fig. 3d.

Coherent transients

The coherent transients observed with CPE are illustrated by the spiral shapes in Fig. 4c, d, when considering that CET(t) in Fig. 3c is proportional to the squared absolute value of the coherence (see Supplementary Information). The system starts at $t=t_0$ in equilibrium at the origin. Then, the chirped pulse interacts with the system. At first, this interaction is off-resonant, which leads to a spiraling around the origin with increasing amplitude and decreasing frequency, as resonance is approached. This spiral corresponds to a slow increase of CET(t) in Fig. 3c at early times. At resonance, a large increase in the magnitude of the coherence is observed. Finally, the off-resonant interaction once more leads to a spiral pattern, which manifests as the damped oscillation in Fig. 3c at later times, as the magnitude of the polarization increases and decreases with each loop. Thus, the contributions of the non-resonant excitation to the complex amplitude cause the sequence of absorption and stimulated emission. Figure 4d also illustrates that the maxima in Fig. 3c around 420 fs and 720 fs are caused by the symmetric stretching vibration. The marked time points correspond to maxima in the squared absolute value of the coherence.

Ab initio quantum chemical calculations

The ab initio model permits an in-depth study of the influence of the surrounding solvent on the vibrating molecules. The transition frequency distribution of the DMSO₂-water clusters demonstrates that the observed dephasing is mainly due to the dynamics of the molecule in the solvent (homogeneous broadening) and not due to their static structure (inhomogeneous broadening). This agrees with the experimentally observed Lorentzian line shapes, which can also be observed in ab initio molecular dynamics simulations (see Methods section and Supplementary Figs. 3 and 4).

The calculated frequencies and transition dipole moments for the different models are presented in Table 1. Due to solvation, absorption maxima are red-shifted, and transition dipole moments increase significantly. As a result of the latter, the absorbed and coherently re-emitted fractions of the impinging energy are larger in the polarizable continuum model (PCM, see Fig. 4e). It must be

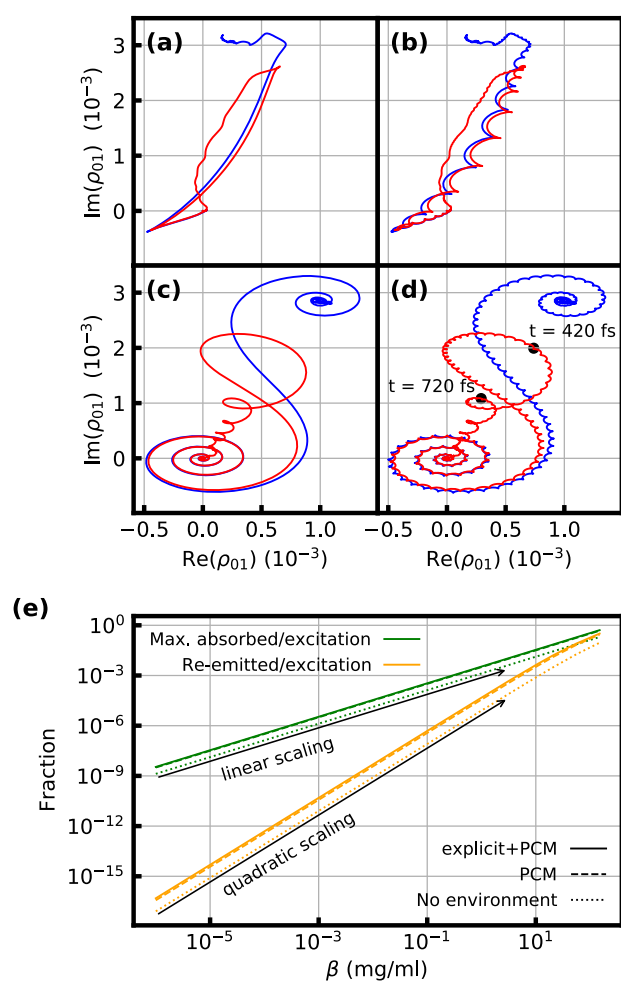


Fig. 4 | Calculated coherence and energy transfer ratios. Calculated vibrational molecular coherence in the symmetric stretching vibrational mode of the DMSO₂ molecule in solution displayed in a frame rotating with the vibrational eigenfrequency. The calculations are done with **a** the compressed pulse using the RWA, **b** the compressed pulse without the RWA, **c** the chirped pulse using the RWA, and **d** the chirped pulse without the RWA. The red curves include relaxation; the blue curves do not include relaxation. Each bump of the cycloid in **b** corresponds to one half-cycle of the electric field, showing that energy transfer from the excitation field to the molecular system is completed after 3 to 4 field cycles (Fig. 2b) in the case of the FCE. In **d**, the time points that are maxima of CET(t) caused by the symmetric stretching vibration are marked with black dots. **e** Re-emitted (orange) and maximum absorbed (green) fraction of the impinging pulse energy versus concentration. The results were obtained from the impulsive-regime model (see Supplementary Information) with the FCE and ab initio Lorentz parameters. The solid lines include direct interactions with the surrounding water and the screening effect of the polarizable continuum, the dashed lines only the latter, and the dotted lines neither. For small concentrations, the maximum absorbed energy scales linearly with concentration. In contrast, the coherent re-emission, containing the spectroscopic information, scales quadratically with concentration.

noted that these fractions also depend on the concentration of the sample molecules. For small concentrations, the maximum absorbed energy scales linearly with the concentration. The coherent re-emission, containing the spectroscopic information, scales quadratically with the concentration due to the absence of homodyning with the excitation field (see Supplementary Information). This scaling behavior is in line with the Beer–Lambert law and derives from the linear relationship between the concentration and the amplitude difference caused by the sample.

Table 1 | Parameters characterizing the resonances of DMSO₂

| | $\tilde{\nu}_{01}$ (cm ⁻¹) | | μ_{01} (D) | |
|----------------------------------|--|------------|----------------|------------|
| | Symmetric | Asymmetric | Symmetric | Asymmetric |
| Calculation (no environment) | 1192 | 1311 | 0.24 | 0.26 |
| Calculation (explicit solvation) | 1148 | 1301 | 0.33 | 0.41 |
| Calculation (PCM) | 1142 | 1288 | 0.32 | 0.37 |
| Experiment | 1135 | 1280 | 0.30 | 0.38 |

Calculated and experimental absorption wavenumbers $\tilde{\nu}_{01}$ and transition dipole moments μ_{01} for the symmetric and asymmetric stretching vibration of DMSO₂, which are the main modes contributing to the observed spectral range (Fig. 2b). The calculations used the M06-2X density functional¹⁹ and were performed on a single molecule without an environment, a single molecule embedded in a PCM or using explicit solvation. In the latter case, different DMSO₂-water clusters were embedded in a PCM. The experimental values were obtained by fitting Lorentzians to the data presented in Fig. 2b.

To explain the increase of the transition dipole moments due to the PCM, we examined partial charges of the oxygen atoms in the density-functional theory simulations. This shows that the environment reduces the electrostatic interaction between different parts of the molecule, leading to a more asymmetric charge distribution. This causes higher dipole moments and less rigid bonds. The static polarizability of the solvent environment thus enhances the molecule-field interaction. This effect is equally well described by both the explicit solvent model and the PCM. However, with the explicit solvent model the molecular dynamics of the entire system can be simulated, which provides qualitative estimates of the dephasing rate Γ (see Eq. 2 and Supplementary Fig. 4).

In conclusion, sub-optical-cycle-temporal-resolution field-resolved spectroscopy together with ab initio modeling provides quantitative, molecular-scale insight into the complete dynamics of the coherent energy transfer between broadband infrared light and vibrating molecules in solution. For an ultra-brief, broadband excitation, time-domain detection allows for the distinction between two qualitatively different light-matter energy transfer regimes: Absorption is governed by the strengths of the transition dipole moments for each individual molecule, independently. The generation of vibrational coherence with each half-cycle of the electric field is resolved. Emission yields a coherent sample-specific spectroscopic fingerprint carrying dephasing information due to molecular motion in varying environments. For spectroscopic techniques that allow for the separation of these two regimes in time^{9,23,24} or in space^{25,26}, the ratio of the coherently transferred optical energy to the excitation energy (Fig. 4e) provides an indicator for the required spectroscopic detection sensitivity. For example, for our test molecule DMSO₂ at physiologically relevant²⁷ sub-ng/ml concentrations in water, the energy coherently re-emitted as a spectroscopic fingerprint amounts to $<10^{-16}$ of the excitation energy (and to $<10^{-8}$ of the absorbed energy), providing quantitative guidelines for the design of corresponding spectroscopic experiments. Our experimentally-validated ab initio model directly connects these energy transfer ratios to vibrational transition frequencies and dipole moments of the DMSO₂ molecules that are modulated by static and dynamic solvent interactions. We resolve sub-cycle effects beyond the RWA in the vibrational molecular coherence, and observe coherent transients in the context of field-resolved infrared spectroscopy.

The peak field strengths of less than 75 kV/cm in our experiment populate the first excited state only on the order of 10^{-3} , rendering nonlinearities in the sample response negligible. With the availability of high-intensity, broadband, waveform-stable mid-IR sources^{28–31} the extension of our study to field-resolved nonlinear (multidimensional) coherent spectroscopies^{6,32–34} in the molecular fingerprint region becomes promising in the near future. This would enable studies of the coupling between vibrational modes and of the correlation functions

describing the fluctuating environments using phase-sensitive direct observation of the electrical field with unprecedented time resolution.

Methods

Field-resolved spectroscopy

The setup used for field-resolved spectroscopy (see also Supplementary Fig. 1) is similar to the one previously reported⁹. In short, all-solid-state spectral broadening via self-phase modulation in a two-stage multi-pass cell and subsequent compression driven by an Yb:YAG thin-disk oscillator operating at a repetition rate of 28 MHz serves as a high peak and average power source for the experiments. The resulting 15-fs output pulses centered at a wavelength of 1030 nm, and with an average power of 66 W generated, by frequency-down-converting, phase-stable mid-infrared (MIR) waveforms via intrapulse difference frequency mixing in a 1-mm thick LiGaS₂ crystal. After transmission of the super-octave MIR waveforms, covering the 850-to-1670-cm⁻¹ spectral range with an average power of 52 mW, through a 30- μ m thick liquid cuvette (focus size 300 μ m), a set of six customized dispersive mirrors is utilized to temporally compress their duration. The liquid cuvette is connected to a robotic liquid-handling system to automatically exchange the purified-water reference and the 10-mg/ml DMSO₂ solution.

The electric field of the MIR waveform emerging after the liquid cuvette is detected via electro-optic sampling (EOS) using a variably-delayed copy of the 15-fs, near-infrared driving pulse with an average power of 350 mW for gating. An 85- μ m thick GaSe crystal under an angle of incidence of $\theta = 43^\circ$ was used for EOS⁹. A mechanical chopper placed before the cuvette enables lock-in detection at a frequency of 7.5 kHz. The mutual delay between the MIR wave and sampling pulse was measured with interferometric delay tracking³⁵. To avoid molecular background signal due to water vapor the system was operated at a pressure of 10⁻³ mbar from the MIR generation downstream. For the data shown in Figs. 2 and 3, the stage was scanned by 1.07 mm alternately in forward and backward direction, and 20 traces with a measurement time of 4.3 s each were averaged. This procedure was repeated three times to allow for quantification of the measurement error. The error bars for the normalized reference traces and their norm itself was estimated by the standard deviation of the three measurements. Each sample measurement was normalized to the average reference measurement, within the same spectral interval, to compensate for fluctuations in the MIR power. Normalization was done on the energy contained in the spectral interval 984–1051 cm⁻¹, where no significant molecular resonances are expected. Gaussian error propagation was used to compute the error of the CET.

Quantum chemical calculations

The ground state geometry of DMSO₂ was obtained by geometry optimization with the M06-2X functional¹³ and the 6-31+g** basis set in the program package Gaussian16 (see Supplementary Table 1)³⁶. Default convergence parameters were used. Subsequent harmonic frequency analysis showed no imaginary vibrational modes, thus confirming that the minimum energy structure had been found. Modes 14 and 15 were identified as the symmetric and asymmetric O-S-O stretching vibrations observed in the experiment (see Supplementary Tables 2 and 3).

To include anharmonicities in the description, an approach that explicitly calculates the potential energy surface for the vibrational modes 14 and 15 was chosen. Thus, single-point calculations were performed on DMSO₂ geometries that were displaced in steps along the two most relevant normal modes (see Supplementary Table 2, stepsizes: 0.2 Bohr for Mode 14, 0.1 Bohr for Mode 15) using M06-2X/6-31g*, with and without a PCM as implemented in the program package Gaussian16. The vibrational eigenfrequencies ω_{0k} and vibrational eigenstates ψ_k were determined numerically using the Fourier-grid Hamiltonian method³⁷. This also yielded transition dipole moments by

numerically evaluating the integral $\langle \psi_0 | \mu | \psi_k \rangle$. The grids on which dipole moment and energies were evaluated were built from the single-point values by interpolation using cubic splines. The results of this procedure are shown in Supplementary Fig. 2. For the other normal modes, the values the harmonic vibrational frequencies and IR intensities (Supplementary Table 3) were scaled such that the mean frequencies/IR intensities for modes 14 and 15 match the mean frequencies/IR intensities calculated by the procedure described above and reported in Table 1 (gas phase, PCM).

The transition frequencies and transition dipole moments in solution were also obtained by studying static snapshots of DMSO₂ in water obtained via classical molecular dynamics simulations. The GROMACS package³⁸ was used with the OPLSAA forcefield³⁹ for DMSO₂ and TP3P⁴⁰ for water. The optimized geometry of DMSO₂ (see Supplementary Table 1) was placed at the center of a 30-Å box with 879 molecules of water and was equilibrated at a temperature of 298.15 K. During all MD runs, the coordinates of the central solute were kept frozen. From NVT trajectories with a total duration of 30 ns, snapshots of the solvent shell were extracted at a random time point every second 5 ps interval. All solvent molecules not within 7.5 Å of the solute molecule were removed. Into these solvent shells, DMSO₂ geometries were inserted in place of the central DMSO₂ molecule, where the atoms were displaced along the two relevant normal modes (see Supplementary Table 2). Vibrational frequencies and vibrational transition dipole moments were then evaluated as described in the previous paragraph and atoms in the solvent shell were explicitly included in the DFT calculation. The obtained frequency distributions for modes 14 and 15 are shown in Supplementary Fig. 3. The ensemble average over these distributions then yielded the central frequencies and transition dipole moments in Table 1 (explicit solvation).

To estimate the dephasing rate Γ_k we conducted on-the-fly semi-classical dynamics simulations of DMSO₂ in water. A box was prepared containing one DMSO₂ molecule and 46 water molecules and was pre-equilibrated using classical molecular dynamics as described previously. The chosen force field was OPLSAA for DMSO₂ and TIP4P2005f⁴¹ for water. The NPT pre-equilibration to 300 K, 1 bar yielded a box size of 11.7302 Å side length, corresponding to a density of 0.95 g/cm³. Then, on-the-fly semi-classical dynamics simulations using the BLYP-D3 functional and GTH pseudopotentials as implemented in the program package cp2k (version 6.1) were performed^{42,43}. All calculations used four multigrids, a CUTOFF of 350 Ry and a REL_CUTOFF of 40 Ry. After NVT equilibration at 300 K for 11 ps, a 30 ps NVE trajectory was run with a time-step of 0.5 fs. The obtained geometries and electron densities were used to calculate the classical dipole autocorrelation function using the tessellation method by refs. 15, 16 as implemented in TRAVIS⁴⁴. An estimate of Γ_k was then obtained by fitting Lorentz functions to the Fourier transformed dipole autocorrelation function (Supplementary Fig. 4).

In summary, the ab initio model as presented in Figs. 2b, c and 3c uses the parameters displayed in Table 1 under explicit solvation for the transition frequencies and dipole moments, as well as the averaged estimate for the dephasing rate presented in Supplementary Fig. 4.

Data availability

Source data for the figures in the main text are provided by the Source Data file. Additional information regarding the transient absorption setup, the quantum chemical calculations, and the theoretical model are provided by the Supplementary Information. Other data are available from the authors upon reasonable request.

References

- Demtröder, W. *Molecular Physics*. (Wiley-VCH Verlag GmbH, 2005).
- Griffiths, P. R. & De Haseth, J. A. *Fourier Transform Infrared Spectrometry*. (Wiley-Interscience, 2007).

3. Hayden, J., Hugger, S., Fuchs, F. & Lendl, B. A quantum cascade laser-based Mach–Zehnder interferometer for chemical sensing employing molecular absorption and dispersion. *Appl. Phys. B* **124**, 29 (2018).
4. Picqué, N. & Hänsch, T. W. Frequency comb spectroscopy. *Nat. Photon* **13**, 146–157 (2019).
5. Laubereau, A. & Kaiser, W. Vibrational dynamics of liquids and solids investigated by picosecond light pulses. *Rev. Mod. Phys.* **50**, 607–665 (1978).
6. Mukamel, S. *Principles of Nonlinear Optical Spectroscopy*. (Oxford University Press, Inc., 1995).
7. Haas, J. & Mizaikoff, B. Advances in mid-infrared spectroscopy for chemical analysis. *Annu. Rev. Anal. Chem.* **9**, 45–68 (2016).
8. Baker, M. J. et al. Using Fourier transform IR spectroscopy to analyze biological materials. *Nat. Protoc.* **9**, 1771–1791 (2014).
9. Pupeza, I. et al. Field-resolved infrared spectroscopy of biological systems. *Nature* **577**, 52–59 (2020).
10. Jacobsohn, B. A. & Wangsness, R. K. Shapes of nuclear induction signals. *Phys. Rev.* **73**, 942–946 (1948).
11. Rothenberg, J. E. & Grischkowsky, D. Measurement of the phase of a frequency-swept ultrashort optical pulse. *J. Optical Soc. Am. B* **2**, 626 (1985).
12. Zamith, S. et al. Observation of coherent transients in ultrashort chirped excitation of an undamped two-level system. *Phys. Rev. Lett.* **87**, 033001 (2001).
13. Zhao, Y. & Truhlar, D. G. The M06 suite of density functionals for main group thermochemistry, thermochemical kinetics, noncovalent interactions, excited states, and transition elements: two new functionals and systematic testing of four M06-class functionals and 12 other functionals. *Theor. Chem. Acc.* **120**, 215–241 (2008).
14. Li, S., Schmidt, J. R., Corcelli, S. A., Lawrence, C. P. & Skinner, J. L. Approaches for the calculation of vibrational frequencies in liquids: comparison to benchmarks for azide/water clusters. *J. Chem. Phys.* **124**, 204110 (2006).
15. Thomas, M., Brehm, M., Fligg, R., Vöhringer, P. & Kirchner, B. Computing vibrational spectra from ab initio molecular dynamics. *Phys. Chem. Chem. Phys.* **15**, 6608 (2013).
16. Thomas, M., Brehm, M. & Kirchner, B. Voronoi dipole moments for the simulation of bulk phase vibrational spectra. *Phys. Chem. Chem. Phys.* **17**, 3207–3213 (2015).
17. del Campo, A., García-Calderón, G. & Muga, J. G. Quantum transients. *Phys. Rep.* **476**, 1–50 (2009).
18. Rothenberg, J. E. & Grischkowsky, D. Subpicosecond transient excitation of atomic vapor and the measurement of optical phase. *J. Optical Soc. Am. B* **3**, 1235 (1986).
19. Monmayrant, A., Chatel, B. & Girard, B. Quantum state measurement using coherent transients. *Phys. Rev. Lett.* **96**, 2–5 (2006).
20. Huber, M. et al. Optimum sample thickness for trace analyte detection with field-resolved infrared spectroscopy. *Anal. Chem.* **92**, 7508–7514 (2020).
21. Andreev, S. N., Mikhailov, A. V., Ochkin, V. N., Pestovskiy, N. V. & Savinov, S. Y. Self-radiation of an absorbing medium induced by a fast frequency-tuning laser. *Laser Phys.* **25**, 025701 (2015).
22. Agarwal, G. S. Rotating-wave approximation and spontaneous emission. *Phys. Rev. A* **4**, 1778–1781 (1971).
23. Kowlig, A. S. et al. Infrared electric field sampled frequency comb spectroscopy. *Sci. Adv.* **5**, eaaw8794 (2019).
24. Lanin, A. A., Voronin, A. A., Fedotov, A. B. & Zheltikov, A. M. Time-domain spectroscopy in the mid-infrared. *Sci. Rep.* **4**, 6670 (2015).
25. Buberl, T., Sulzer, P., Leitenstorfer, A., Krausz, F. & Pupeza, I. Broadband interferometric subtraction of optical fields. *Opt. Express* **27**, 2432 (2019).
26. Tomberg, T., Muraviev, A., Ru, Q. & Vodopyanov, K. L. Background-free broadband absorption spectroscopy based on interferometric suppression with a sign-inverted waveform. *Optica* **6**, 147 (2019).
27. Geyer, P. E., Holdt, L. M., Teupser, D. & Mann, M. Revisiting biomarker discovery by plasma proteomics. *Mol. Syst. Biol.* **13**, 1–15 (2017).
28. Junginger, F. et al. Single-cycle multiterahertz transients with peak fields above 10 MV/cm. *Opt. Lett.* **35**, 2645 (2010).
29. Schubert, O. et al. Sub-cycle control of terahertz high-harmonic generation by dynamical Bloch oscillations. *Nat. Photonics* **8**, 119–123 (2014).
30. Gaida, C. et al. Watt-scale super-octave mid-infrared intrapulse difference frequency generation. *Light. Sci. Appl.* **7**, 94 (2018).
31. Elu, U. et al. Seven-octave high-brightness and carrier-envelope-phase-stable light source. *Nat. Photonics* **15**, 277–280 (2021).
32. Hamm, P. & Zanni, M. *Concepts and Methods of 2D Infrared Spectroscopy*. (Cambridge University Press, 2011). <https://doi.org/10.1017/CBO9780511675935>.
33. Hamm, P. & Shalit, A. Perspective: echoes in 2D-Raman-THz spectroscopy. *J. Chem. Phys.* **146**, 130901 (2017).
34. Baiz, C. R. et al. Vibrational spectroscopic map, vibrational spectroscopy, and intermolecular interaction. *Chem. Rev.* **120**, 7152–7218 (2020).
35. Schweinberger, W., Vamos, L., Xu, J., Baune, C. & Rode, S. Interferometric delay tracking for low-noise Mach-Zehnder-type scanning measurements. *Opt. Express* **27**, 4789–4798 (2019).
36. Frisch, M. J. et al. Gaussian 16 Revision C.01. (2016).
37. Marston, C. C. & Balint-Kurti, G. G. The Fourier grid Hamiltonian method for bound state eigenvalues and eigenfunctions. *J. Chem. Phys.* **91**, 3571–3576 (1989).
38. Abraham, M. J. et al. GROMACS: high-performance molecular simulations through multi-level parallelism from laptops to supercomputers. *SoftwareX* **1–2**, 19–25 (2015).
39. Jorgensen, W. L., Chandrasekhar, J., Madura, J. D., Impey, R. W. & Klein, M. L. Comparison of simple potential functions for simulating liquid water. *J. Chem. Phys.* **79**, 926–935 (1983).
40. Jorgensen, W. L. Quantum and statistical mechanical studies of liquids. 10. Transferable intermolecular potential functions for water, alcohols, and ethers. Application to liquid water. *J. Am. Chem. Soc.* **103**, 335–340 (1981).
41. González, M. A. & Abascal, J. L. F. A flexible model for water based on TIP4P/2005. *J. Chem. Phys.* **135**, 224516 (2011).
42. Goedecker, S., Teter, M. & Hutter, J. Separable dual-space Gaussian pseudopotentials. *Phys. Rev. B* **54**, 1703–1710 (1996).
43. Hutter, J., Iannuzzi, M., Schiffmann, F. & VandeVondele, J. cp2k: atomistic simulations of condensed matter systems: cp2k simulation software. *WIREs Comput. Mol. Sci.* **4**, 15–25 (2014).
44. Brehm, M. & Kirchner, B. TRAVIS - a free analyzer and visualizer for Monte Carlo and molecular dynamics trajectories. *J. Chem. Inform. Model.* **51**, 2007–2023 (2011).

Acknowledgements

We thank Ferenc Krausz and Marinus Huber for useful discussions. This research was undertaken thanks, in part, to funding from the Technology Transfer Program of the Max Planck Society, and the Max Planck-UBC-UTokyo Center for Quantum Materials. R.d.V.-R. acknowledges funding by the German Research Foundation (DFG) under Germany's excellence strategy EXC 2089/1-39077620.

Author contributions

M.T.P., M.H., T.B., R.d.V.-R., and I.P. designed the experiments and the theoretical framework. T.B. performed the experiments. T.B. and M.H. analyzed the experimental data. M.T.P. and D.K. performed the density functional theory simulations. M.H. and M.T.P. developed the model and analyzed the simulation data. M.T.P., M.H., and I.P. wrote the manuscript with input from all other authors. I.P. and R.d.V.-R. supervised the project.

Article<https://doi.org/10.1038/s41467-022-33477-5>**Funding**

Open Access funding enabled and organized by Projekt DEAL.

Competing interests

The authors declare no competing interests.

Additional information

Supplementary information The online version contains supplementary material available at <https://doi.org/10.1038/s41467-022-33477-5>.

Correspondence and requests for materials should be addressed to Regina de Vivie-Riedle or Ioachim Pupeza.

Peer review information *Nature Communications* thanks the anonymous reviewer(s) for their contribution to the peer review of this work. Peer reviewer reports are available.

Reprints and permission information is available at <http://www.nature.com/reprints>

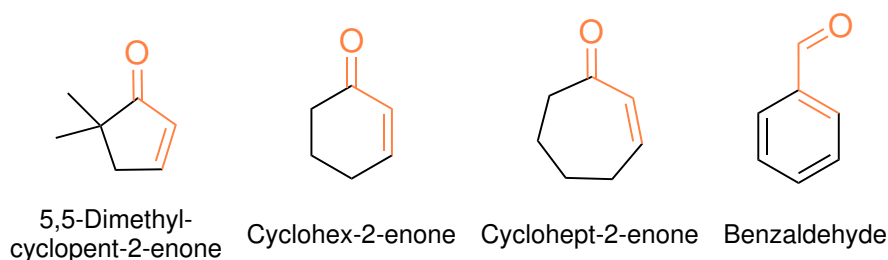
Publisher's note Springer Nature remains neutral with regard to jurisdictional claims in published maps and institutional affiliations.

Open Access This article is licensed under a Creative Commons Attribution 4.0 International License, which permits use, sharing, adaptation, distribution and reproduction in any medium or format, as long as you give appropriate credit to the original author(s) and the source, provide a link to the Creative Commons license, and indicate if changes were made. The images or other third party material in this article are included in the article's Creative Commons license, unless indicated otherwise in a credit line to the material. If material is not included in the article's Creative Commons license and your intended use is not permitted by statutory regulation or exceeds the permitted use, you will need to obtain permission directly from the copyright holder. To view a copy of this license, visit <http://creativecommons.org/licenses/by/4.0/>.

© The Author(s) 2022

3. Excited State Properties and Reactivities of Cyclic 2-Enones

Organic compounds containing both a C=C double bond and a conjugated C=O double bond, 2-enones, are versatile tools in organic synthesis.[142, 143] Some of the oldest known photoreactions are documented for this class of compounds.[40, 144] These photoreactions are particularly important since they give rise to unique structural motifs highly prevalent in natural and pharmaceutically relevant compounds. It is worthwhile to explore the excited state reactivity of 2-enones to discover new reactions or to achieve an increase in the selectivity of known reactions. In this work, high-level XMS-CASPT2 calculations are used to explore the excited state landscape of 2-enones, from which their relaxation behavior and their reactivity is inferred.



Scheme 1: 5,5-Dimethylcyclopent-2-enone, cyclohex-2-enone, cyclohept-2-enone and benzaldehyde; four 2-enones with different photoreactivity. The conjugated bonds of the 2-enone functionality are marked in orange.

We will only discuss conjugated enones and focus mainly on cyclic enones with small ring sizes (see scheme 1). The excited state reactivity of enones after excitation in the ultraviolet (UV) is governed by the tight interplay between their lowest five excited states.[45, 145, 146] One of these is a nearly dark $^1n\pi^*$ state caused by the transition of an electron from the oxygen lone pair into the antibonding orbital of the conjugated system. Another is a generally bright $^1\pi\pi^*$ - state caused by a transition inside the conjugated system. The other two states are the corresponding dark triplets $^3n\pi^*$ and $^3\pi\pi^*$. [46] Upon slightly elongating the α -C-C bond, $n\sigma^*$ states become relevant.[45, 147] In fig. 3.1, the orbitals characterizing these states are shown for the example cyclohex-2-enone.

Concerning the energetic order of these states, the triplet states are generally lower than the corresponding singlet states, and the $n\pi^*$ states are generally lower than the $\pi\pi^*$ states. However, the latter is only valid in the FC region, where the $n\pi^*$ states are close to their minimum. Upon a twist of the R-C=C-R dihedral, the $\pi\pi^*$ states are stabilized and cross the $n\pi^*$ states at a CoIn. Since intersystem crossing (ISC) is also possible along this path due to relatively high SOC, interconversion between all states can occur

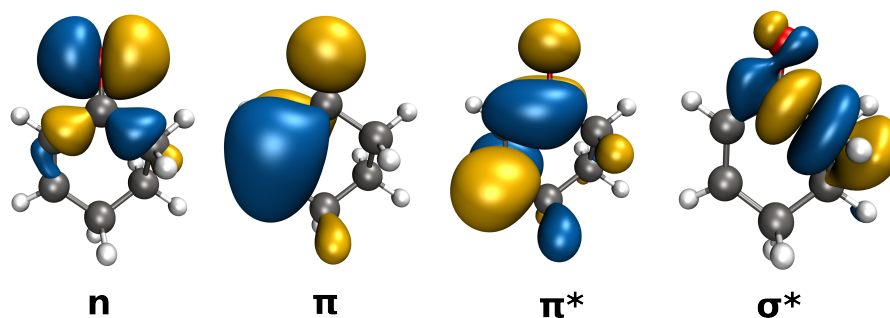


Figure 3.1.: Orbitals to describe the low-lying states of cyclohex-2-enone (isovalue: 0.02). These orbitals are most important to describe the photoreactivity of 2-enones after excitation in the UV.

rapidly.[2, 147, 148] The excitation wavelength in synthetic experiments is usually tuned to the red edge of the absorption in a way that only the lowest singlet state is excited, which is of $n\pi^*$ character in most cases. The ensuing photoreactivity then arises from the lowest excited state minimum, whose character depends on the structure of the enone. The absorption properties and the character of the lowest excited state minimum can also be influenced by the addition of photo-catalysts (for example, Lewis-Acids) which can lead to altered reactivity patterns (see chapter 4 and references therein). A sketch of an excited state energy landscape that illustrates reactive and non-reactive relaxation pathways is shown in fig. 3.2. The PES in fig. 3.2 is hypothetical, and cyclohex-2-enone is only shown exemplarily to illustrate the geometric changes. Likely, no single 2-enone system features all these pathways simultaneously. In general, starting from $^1n\pi^*$, cyclic 2-enones can either relax back to the ground state or rearrange to different products via different triplet states. From the triplet minima, bimolecular reactions like [2+2] cycloadditions can also take place.

Reactions occur mainly from the $^3\pi\pi^*$ states or the $^3n\pi^*$ states. Comparing these two channels, we will discuss the reactivity of four exemplary molecules, 1) cyclohept-2-enone, 2) 5,5-dimethylcyclopent-2-enone, 3) cyclohex-2-enone, and 4) benzaldehyde (see scheme 1). Upon UV excitation, they preferentially react in 4 different ways: 1) Z/E isomerization[43, 44], 2) cleavage of the α -C-C bond (Norrish-type-I reaction[37, 150–152]), 3) [2+2]-cycloaddition at the C=C double bond [40, 41], and 4) [2+2]-cycloaddition at the C=O double bond (Paternò-Büchi reaction[144, 153–156]).

The reactions of cyclohept-2-enone and 5,5-dimethylcyclopent-2-enone (examples 1 and 2) are discussed in detail in their respective sections, section 3.1 and section 3.2. In cyclohept-2-enone, Z/E isomerization is the dominant relaxation pathway and occurs via the $\pi\pi^*$ states.[43, 44] In comparison, the cleavage of the C1-C5 bond in 5,5-dimethylcyclopent-2-enone occurs via the $n\pi^*$ states and leads to the formation of a ketene.[37, 152] This can be understood in the context of fig. 3.2. In cyclopentenone, due to the small ring size, torsion of the H-C=C-H dihedral is disfavored due to the small ring size and the $^3\pi\pi^*$ and $^3n\pi^*$ minima are similar in energy. An additional 5,5-dimethyl substitution stabilizes the $^3n\sigma^*$ state, such that IC from $^3n\pi^*$ and subsequent ring opening becomes the dominant pathway. The large ring size in cycloheptenone leads to less strain upon torsion of the H-C=C-H dihedral. This motion strongly stabilizes the $\pi\pi^*$ minima. In addition, the doubly excited $^1(\pi^*)^2$ state is stabilized sufficiently,

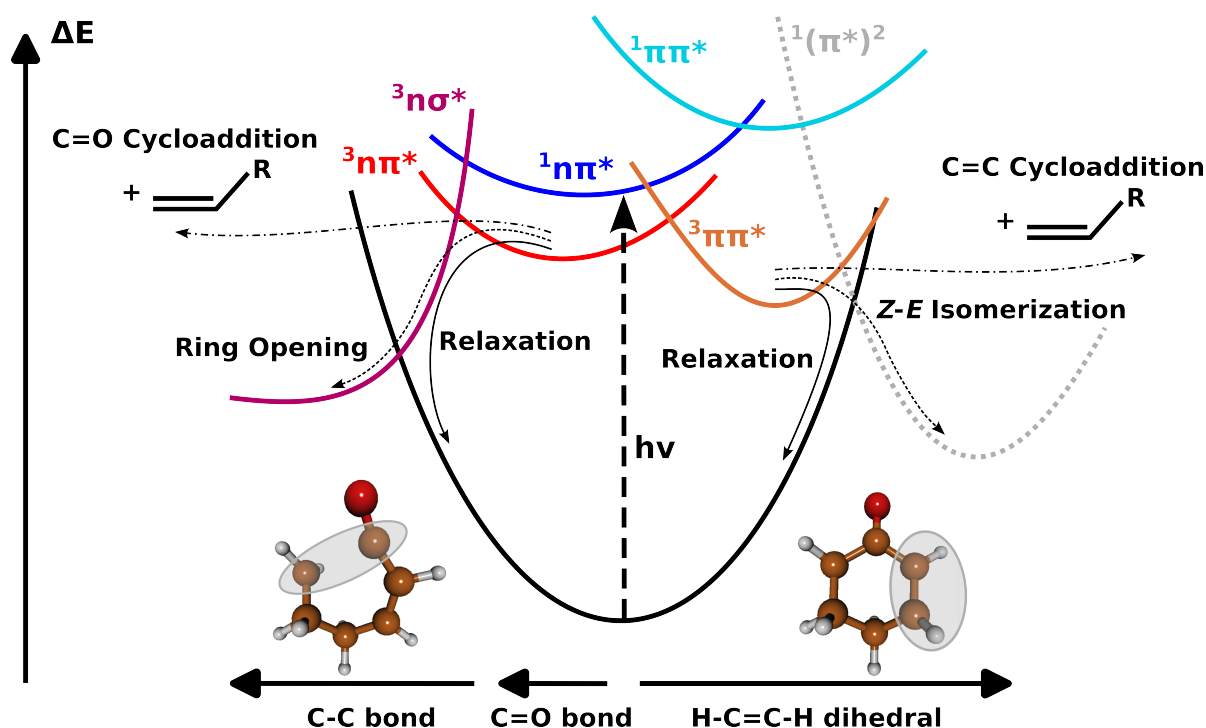
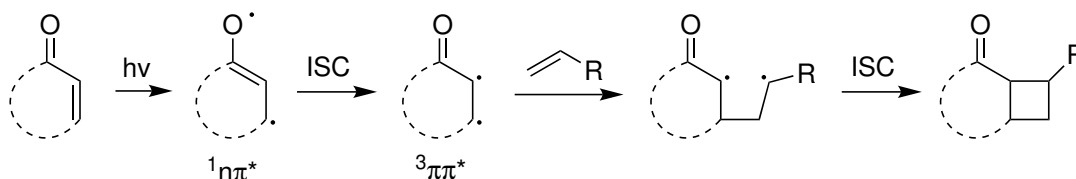


Figure 3.2.: Excited states and possible reaction and relaxation pathways in the triplet states. The states as shown are given for a hypothetical 2-enone where all pathways are possible. Cyclohex-2-enone is used as an example to illustrate geometric changes. Excitation in the UV populates the $1n\pi^*$ state. From here, the triplets $3n\pi^*$ and $3\pi\pi^*$ are populated via ISC from $1n\pi^*$ to $3\pi\pi^*$ (El-Sayed rule[149]) and IC between the triplets. The most prominent relaxation pathways are characterized by an elongation of the α -C-C bond (ring-opening) for $3n\pi^*$ or by a twist around the H-C=C-H dihedral for $\pi\pi^*$. The ring opening pathway can lead to cleavage in a Norrish-Type-I Reaction, while the twist leads to Z/E isomerization if the ring is sufficiently large. Cycloadditions can occur directly from the triplet minima. These are [2+2]-cycloadditions at the C=O bond (Paternò-Büchi reaction) for the $3n\pi^*$ or [2+2]-cycloadditions at the C=C bond for $3\pi\pi^*$.

such that a stable *E* isomer exists in the ground state. Thus, ISC from $^3\pi\pi^*$ to the ground state leads to *Z/E* isomerization as the main relaxation pathway. In summary, these two molecules demonstrate how the influence of $^3\pi\pi^*$ leads to a different reactivity $^3n\pi^*$ state in a monomolecular context.

Since these two molecules have efficient relaxation pathways, their triplet states are short-lived.[46, 157–159] A long-lived triplet often leads to bimolecular reactions in the excited state. We will discuss two molecules (examples 3 and 4), cyclohex-2-enone, and benzaldehyde, with long-lived triplet states.[158–161] The [2+2]-cycloaddition at the C=C double bond is one of the most well-known and synthetically useful reactions of cyclic enones.[41, 154] Without a reaction partner, it leads to photodimerization, but it can be performed in a crossed fashion as well, yielding various cyclobutanes. It can be a dominant reaction pathway whenever the lowest excited state minimum is of $\pi\pi^*$ character since the highest π orbital and lowest π^* orbital are both localized mainly at the C=C bond (see fig. 3.1). In cyclohexenone, this state is the long-lived triplet $^3\pi\pi^*$. Consequently, the [2+2]-cycloaddition does not happen in a concerted fashion but via a (triplet) biradical, and the Woodward-Hoffmann rules[162] do not apply. The reaction proceeds as follows: 1) Excitation to $^1n\pi^*$, 2) ISC to $^3\pi\pi^*$, 3) diabatic relaxation to the $^3\pi\pi^*$ minimum with an H–C=C–H dihedral approaching 90° , 4) reaction with the unsaturated partner, forming an open triplet biradical, and 5) a second ISC event back to the singlet manifold that leads to the closure cyclobutane ring. These steps are shown in scheme 2.

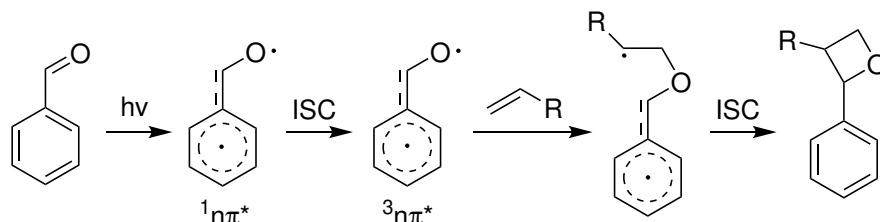


Scheme 2: Mechanism of the [2+2]-photocycloaddition of an olefin to a cyclic 2-enone via the excited triplet state $^3\pi\pi^*$ (adapted from [41]).

The [2+2] cycloaddition can be steered through the complexation of the enone by a Lewis acid. Enantioselective [2+2] photocycloaddition is possible with the help of photocatalytic chiral Lewis acids.[42, 53, 54, 163] Since the relaxation to the $^3\pi\pi^*$ plays a crucial role in the [2+2] cycloaddition, it is exciting to investigate how this relaxation takes place in the presence of a Lewis acid. This is done in section 4.1, where we show that the $^3\pi\pi^*$ minimum can be directly observed in Lewis-acid-enone complexes with ultrafast TA spectroscopy.

As a final molecule, we will discuss benzaldehyde, where the C=C double bond of the enone is embedded in an aromatic π -system. The aromatic character leads to unique features in the excited state reactivity of benzaldehyde. Firstly, even though the $^1\pi\pi^*$ state is redshifted by ca. 0.8 eV compared to simple 2-enones due to the larger conjugated system, the $^1n\pi^*$ state is still the lowest excited singlet state in benzaldehyde. Furthermore, the aromaticity hinders H–C=C–H torsion; thus, the $\pi\pi^*$ minimum is above the $n\pi^*$ minimum. Moreover, bond cleavage is also prevented since the σ^* of the C–H bond in benzaldehyde is much higher in energy than the σ^* of the C–C bond in cyclic enones.[164–167] Accordingly, benzaldehyde deactivates by phosphorescence from

its ${}^3n\pi^*$ state at low temperatures in aprotic solvents and by intermolecular hydrogen transfer at high temperatures and in protic solvents.[160, 161, 168] If a suitable reaction partner is present, the dominant reaction pathway will be the [2+2]-cycloaddition at the C=O bond, which is the well-known Paternò-Büchi reaction. The mechanism of which is shown in scheme 3.



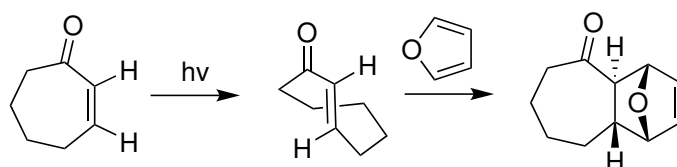
Scheme 3: Mechanism of the Paternò-Büchi of benzaldehyde and an olefin via the excited triplet state ${}^3n\pi^*$.

The reaction proceeds similarly to the [2+2] cycloaddition at the C=C double bond that was discussed in the previous paragraph: 1) Excitation to ${}^1n\pi^*$, 2) ISC to ${}^3\pi\pi^*$ 3) IC to ${}^3n\pi^*$ [167], followed by 4) reaction with the unsaturated partner, forming an open triplet biradical, and 5) ISC to the ground state which closes the oxetane ring.

As will be discussed in section 4.3, Lewis acids completely change the excited state landscape of benzaldehyde. The dative bond with the Lewis acid makes the $n\pi^*$ states inaccessible. Thus, $\pi\pi^*$ reactivity is expected.[169] It turns out that, in the special case of boron trichloride, the Lewis acid is not an innocent ligand. After photoexcitation, unexpected redox activity leading to the formation of chlorine radicals is observed.[5]

3.1. *Z/E* Isomerization and Diels-Alder Reaction of Cyclohept-2-enones

After excitation in the UV, cyclohept-2-enones can undergo *Z/E* isomerization.[43, 44] The resulting highly strained *E* isomers are potent dienophiles in Diels-Alder reactions. Thus, by irradiating mixtures of dienes and cycloheptenone derivatives, photo-induced Diels-Alder reactions can be performed (see scheme 4).



Scheme 4: Photochemical *Z/E* isomerization of cycloheptenone and Diels-Alder reaction with Furan.

In contrast to thermal Diels-Alder reactions of cyclic dienophiles, the resulting two rings in the products are *trans*-fused.[170, 171] Such *trans*-bicyclo[5.4.0]undecane skeletons feature prominently in many terpenes, a class of compounds known for their high pharmacological relevance. Consequently, the total synthesis of natural compounds has been the central application area for this reaction.[172–174] The computational investigation presented in this work focuses on two aspects of this reaction; 1) the mechanism of the photochemical isomerization and 2) the barrier heights of the subsequent thermal Diels-Alder reaction, which govern the observed stereoselectivity.

Mechanistically, the first step of the reaction is very similar to the photoisomerization of other unsaturated compounds. Here, a few points will be discussed that set the double-bond isomerization in cycloheptenone apart. In contrast to most other unsaturated compounds, the $\pi\pi^*$ state is not the lowest excited state in 2-enones. With the excitation energies chosen in the experiment, excitation occurs to $S_1(n\pi^*)$. Due to the state character, the double bond is not immediately broken ($\pi\pi^*$, formal C–C bond order one), but a partial double bond remains ($n\pi^*$, formal bond order 1.5). Accordingly, the S_1 state shows a shallow minimum in the FC region, and a small barrier has to be overcome to change the character of the S_1 state and achieve bond rotation in the singlet states. XMS-CASPT2 calculations show that, in cycloheptenone, this barrier lies below the FC point and can be overcome using the excitation energy, which enables *Z/E* isomerization via the singlet states. This is backed up by experiments that show that the isomerization takes place even in the presence of triplet quenchers.

Z/E isomerization (180° H–C=C–H dihedral angle) is not possible in rings of size smaller than six due to steric constraints[46] and cycloheptenone is the smallest enone that possesses an *E* configured minimum in the ground state. The smaller enones still relax by a rotation around the double bond but do not continue the isomerization beyond a twist angle of approximately 90° . This 90° twist is achieved in the $^3\pi\pi^*$ state. In the $^1n\pi^*$ minimum, the triplet states $^3\pi\pi^*$ and $^3n\pi^*$ are both close in energy to the $^1n\pi^*$ and SOC is between 30 and 40 cm^{-1} . Thus, triplet states play a higher role in the isomerization of enones than in the isomerizations of other unsaturated compounds. This triplet mechanism is likely also active in cycloheptenone simultaneously with the

singlet pathway discussed in the previous paragraph. After ISC from $^1n\pi^*$ to $^3\pi\pi^*$, per El Sayed's rule,[149] the $^3\pi\pi^*$ minimum is reached at a 90° dihedral angle, geometrically close to the thermal transition state in the ground state. In cycloheptenone, ISC near this geometry can lead to the *E* and *Z* isomers, while the *Z* isomer is the only stable isomer in smaller enones.

The second step of the reaction is a well-known thermal Diels-Alder addition, and the reader may be referred to the literature for a mechanistic overview (see [175] for a review, [176] for a historical perspective). Here, just a few points comparing the Diels-Alder reactions of (*E*)-cycloheptenone to the Diels-Alder reactions of (*Z*)-cycloheptenone shall be mentioned. In contrast to the reaction of (*Z*)-cycloheptenone, activation barriers for (*E*)-cycloheptenone are much lower (around 85 kJ/mol, compared to around 110-150 kJ/mol for comparable transition states in (*Z*)-cycloenones[177, 178]). Thus, the reaction can be performed without needing a catalyst or elevated temperatures (for reaction conditions of the Diels-Alder reaction of (*Z*)-cycloheptenone, see [179]). Calculations at the transition state show much lower strain energy according to the distortion/interaction-activation strain model[180] for (*E*)-cycloheptenone.[178] This means that (*E*)-cycloheptenone has to be distorted less to reach the transition state and is easier to distort. Interestingly, the same holds for the diene reaction partner in our example furan. Furan is less strained at the transition state when reacting with (*E*)-cycloheptenone compared to (*Z*)-cycloheptenone. Since the reaction is exergonic, the transition state is more educt-like in accordance with the Hammond-Leffler postulate.[181, 182] This might also explain the lower regioselectivity in reactions with asymmetric dienes since the electronic and steric influence of the diene on the structure of the transition state is smaller since the reactants are further apart.

The article "Diels-Alder Reaction of Photochemically Generated (*E*)-Cyclohept-2-enones: Diene Scope, Reaction Pathway, and Synthetic Application" was published in *Journal of Organic Chemistry*. The following points briefly summarize the article, focusing on the theoretical results.

- XMS-CASPT2 calculations reproduced the absorption spectra and could be used to study the isomerization process computationally. Based on the optimization of critical points in the lowest excited singlet and triplet states, a mechanism for *Z/E* isomerization was derived, featuring two parallel pathways, one via singlet states and one via triplet states.
- The pathway via the triplets proceeds as follows: ISC from $S_1(n\pi^*)$ to $T_2(\pi\pi^*)$ close to the Franck-Condon region and the $S_1(n\pi^*)$ minimum. Then, diabatic relaxation in the triplet $\pi\pi^*$ state towards the $T_1(\pi\pi^*)$ minimum with a geometry featuring torsion of the H-C=C-H dihedral. These first steps are analogously observed in other enones.[46] However, in contrast to smaller cyclic enones, where *Z/E* isomerization is not possible, the torsion angle in $T_1(\pi\pi^*)$ is nearly 90° and at a slightly larger torsion angle, a transition state in the electronic ground state exists, that is of comparable height to $T_1(\pi\pi^*)$. A minimum energy crossing point was optimized 27.7 kJ/mol above the $T_1(\pi\pi^*)$ minimum enabling efficient ISC into the ground state, where the bond twist either continues towards the *E* isomer or enter a loss channel back to the *Z* isomer is entered.
- A pathway via singlets is also possible: After relaxation in the $S_1(n\pi^*)$, a small barrier can be overcome to reach a three-state crossing between S_1 , T_1 and S_0 ,

which is stabilized by a transannular interaction of a hydrogen atom across the ring system. This crossing is located at a geometry with a bond twist close to 90° . Thus, a transition into the ground state at this point can lead to double-bond isomerization. This path explains how the bond isomerization proceeds even though the dienes added in excess for the Diels-Alder reaction are efficient triplet quenchers. However, it could not be ruled out that isomerization in the triplets is also fast enough to compete with quenching.

- When Dienes were added during the irradiation, a Diels-Alder reaction was observed without needing a catalyst. The scope of the reaction was explored for various dienes and substituted cycloheptenones. Yields ranged from 64 to 98%. However, regioselectivity was limited for asymmetric dienes.
- The Diels-Alder reaction of the strained *E* isomer with cyclic dienes leads to two different diastereomers (*endo*, *exo*). The diastereomeric ratio could be predicted from the relative barrier heights calculated at the DLPNO-CCSD(T)/CBS(3/4, cc) level of theory. The *endo* transition state is higher in energy; thus, the *exo* product is preferentially formed. The identity of the different diastereomers was determined using X-ray crystallography. In the case of cyclopentadiene, where no crystals were available, the assignment could be performed comparing 1H chemical shifts between experiment and simulation.
- The developed experimental methodology was employed in a concise total synthesis of *trans*- α -himalachene (4 steps, 14% overall yield).

Hereafter, The article “Diels-Alder Reaction of Photochemically Generated (*E*)-Cyclohept-2-enones: Diene Scope, Reaction Pathway, and Synthetic Application” published in *Journal of Organic Chemistry* is reproduced. Copyright 2022 American Chemical Society. The supporting information is available online.

Diels–Alder Reaction of Photochemically Generated (*E*)-Cyclohept-2-enones: Diene Scope, Reaction Pathway, and Synthetic Application

Daniel P. Schwinger, Martin T. Peschel, Constantin Jaschke, Christian Jandl, Regina de Vivie-Riedle, and Thorsten Bach*



Cite This: *J. Org. Chem.* 2022, 87, 4838–4851



Read Online

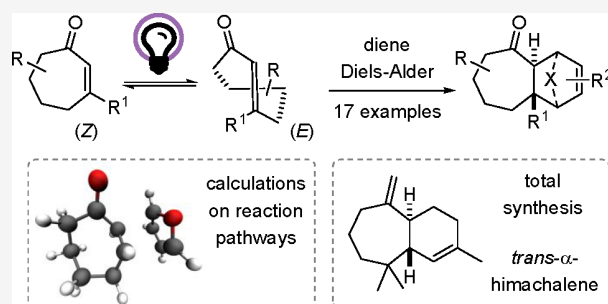
ACCESS |

Metrics & More

Article Recommendations

Supporting Information

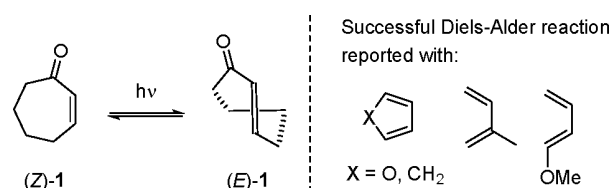
ABSTRACT: Upon irradiation at $\lambda = 350$ nm, cyclohept-2-enone undergoes an isomerization to the strained (*E*)-isomer. The process was studied by XMS-CASPT2 calculations and found to proceed by two competitive reaction channels on either the singlet or the triplet hypersurface. (*E*)-Cyclohept-2-enone is a reactive dienophile in thermal [4 + 2] cycloaddition reactions with various dienes. Ten different dienes were probed, most of which—except for 1,3-cyclohexadiene—underwent a clean Diels–Alder reaction and gave the respective *trans*-fused six-membered rings in good yields (68–98%). The reactions with furan were studied in detail, both experimentally and by DLPNO–CCSD(T) calculations. Two diastereoisomers were formed in a ratio of 63/35 with the *exo*-product prevailing, and the configuration of both diastereoisomers was corroborated by single crystal X-ray crystallography. The outcome of the photoinduced Diels–Alder reaction matched both qualitatively and quantitatively the calculated reaction pathway. Apart from cyclohept-2-enone, five additional cyclic hept-2-enones and cyclooct-2-enone were employed in their (*E*)-form as dienophiles in the Diels–Alder reaction with 1,3-cyclopentadiene (80–98% yield). The method was eventually applied to a concise total synthesis of racemic *trans*- α -himachalene (four steps, 14% overall yield).



INTRODUCTION

Photochemical reactions are particularly useful if they provide access to intermediates that cannot be generated by conventional (thermal) transformations. They open unprecedented reaction channels, which in turn can lead to novel, structurally unique products.¹ Along these lines, the *Z/E* isomerization of cyclic alkenes has received intensive attention,² and outstanding contributions were made by the group of Y. Inoue,³ who focused on the preparation of chiral (*E*)-cycloalkenes in enantiomerically enriched form.⁴ In recent years, the ring strain of cyclic (*E*)-alkenes has been favorably used to facilitate biochemical ligation reactions.⁵ From a synthetic perspective, the high ring strain in (*E*)-cycloalkenes and specifically (*E*)-cycloalk-2-enones allows for consecutive reactions that are not feasible thermally or require activation by a catalyst. In back-to-back publications, the groups of Corey⁶ and Eaton⁷ reported in 1965 on the photochemical formation of (*E*)-cyclohept-2-enone⁸ and its consecutive reaction with either 1,3-cyclopentadiene or furan as diene components in a Diels–Alder reaction (Scheme 1).⁹ Despite the fact that the Diels–Alder adducts, which are—unlike thermal products¹⁰—intrinsically *trans*-fused,¹¹ hold promise for the total synthesis of naturally occurring cycloheptanes, the number of subsequent publications on the topic has remained limited. Hiraku et al. studied

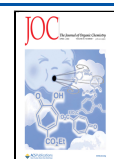
Scheme 1. Photochemical Isomerization of (*Z*)-Cyclohept-2-enone [(*Z*)-1] to Its (*E*)-Isomer [(*E*)-1] and Structures of Dienes Known to Undergo a Diels–Alder Reaction with (*E*)-1



the photochemical reaction of cyclohept-2-enone with cyclopentadiene and isoprene claiming the formation of structurally defined products as single isomers.¹² Dorr and Rawal recognized that the regioselectivity of the reaction can be

Received: January 26, 2022

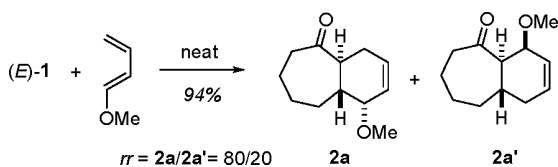
Published: March 22, 2022



favorably controlled in an intramolecular reaction and reported on the formation of polycyclic cyclohept-2-enone adducts by a cascade of photochemical *Z/E* isomerization and intramolecular Diels–Alder reaction.¹³

The hitherto most comprehensive study on the photochemical reaction of cyclohept-2-enones with dienes was performed by Autschbach, Davies, and co-workers.¹⁴ In the context of a projected total synthesis of vibsananin E, they studied the reaction of various cyclohept-2-enones with isoprene, 2,4-hexadiene, and 1-methoxy-1,3-butadiene. For the parent compound cyclohept-2-enone (**1**), they observed upon reaction with neat 1-methoxy-1,3-butadiene two major products in a ratio of 4/1 to which they assigned the structures **2a** and **2a'** (Scheme 2). On the basis of DFT calculations on

Scheme 2. Previous Study¹⁴ on the Diels–Alder Reaction of 1-Methoxy-1,3-butadiene with (*E*)-Cyclohept-2-enone [(*E*)-1**] to Regioisomeric Bicyclic Products **2a** and **2a'****



the B3LYP/6-31G(d) level of theory, they could rationalize the outcome of the reactions by analyzing the transition state energies for the approach of the diene to substrate (*E*)-**1**.

Ghosh, Datta, and co-workers studied the photochemical reaction of chiral cyclohept-2-enones with various dienes focusing on its use for diterpene total synthesis. For furan as diene, they found a single addition product, the selective formation of which was explained by the fact that its formation was most exothermic according to DFT calculations.¹⁵ With nonsymmetric dienes, the formation of regioisomeric products was observed. In a recent study, Wang et al. employed the photoinduced Diels–Alder reaction for the construction of a

spirooliganin library.¹⁶ They also analyzed structures and relative energies of Diels–Alder products and transition states for the reaction of isoprene and 4,4-dimethylcyclohept-2-enone by DFT calculations at the ω B97X-D/def2-QZVPP// ω B97X-D/def2-TZVP level of theory.

Our interest in the photochemistry of cyclohept-2-enone and its derivatives was kindled by the intrinsic chirality of (*E*)-cyclohept-2-enones (vide supra), which could potentially be exploited for enantioselective transformations.¹⁷ Since a procedure to access racemic compounds was needed and since it seemed desirable to establish the constitution and relative configuration of the Diels–Alder products, we studied the photoinduced reaction of various cyclohept-2-enones with dienes in detail. We herein describe the results of our experiments, which were combined with computational studies and which led to the application of the photoinduced Diels–Alder reaction to the synthesis of the natural product *trans*- α -himachalene.

RESULTS AND DISCUSSION

Cyclohept-2-enone displays two notable absorption bands in the UV–vis spectrum. At $\lambda = 226$ nm, a strong absorption ($\epsilon = 10\,475$ L mol⁻¹ cm⁻¹) is recorded in dichloromethane solution, while the long-wavelength absorption at $\lambda = 325$ nm is weak ($\epsilon = 64.4$ L mol⁻¹ cm⁻¹). The spectrum calculated at XMS-CASPT2(6,5)/cc-pvtz level of theory matched the experimental data well and allowed us to assign the blue-shifted absorption ($\lambda_{\text{calc}} = 220$ nm) to a bright $\pi\pi^*$ transition and the red-shifted absorption ($\lambda_{\text{calc}} = 336$ nm) to an almost dark, forbidden $n\pi^*$ transition (see the SI for further details). The XMS-CASPT2 optimizations of critical points in the excited states of cyclohept-2-enone indicated two ultrafast relaxation pathways that allow for the observed *Z/E* isomerization, a triplet pathway via intersystem crossing (ISC) as well as a singlet pathway via internal conversion (Figure 1). After photoexcitation to the $S_1(n\pi^*)$ state, the (*Z*)-isomer of cyclohept-2-enone, (*Z*)-**1**, starts to relax. Already close to the

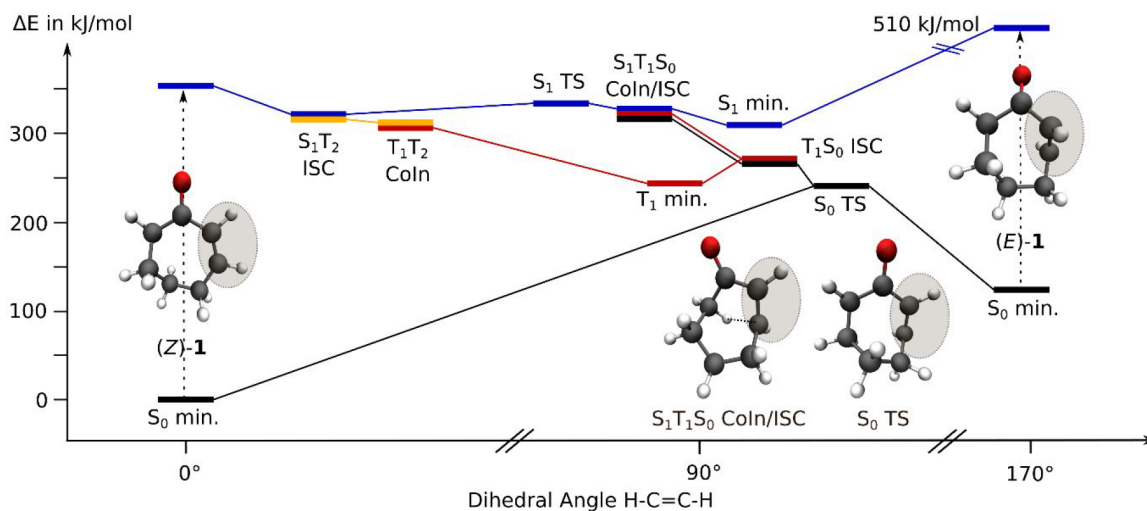


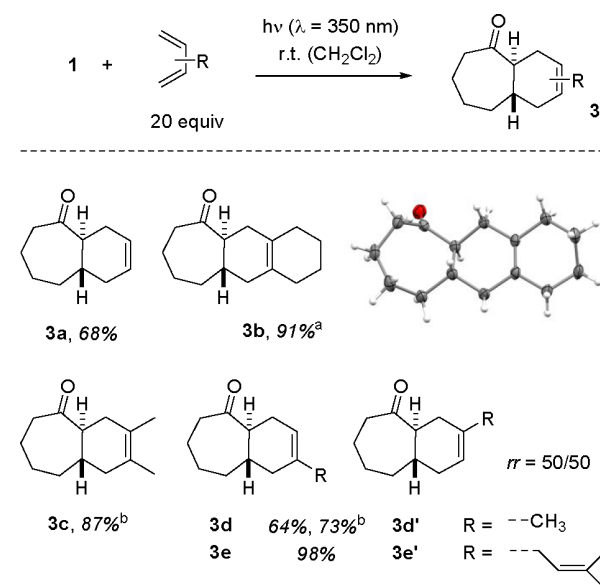
Figure 1. Critical points in the S_0 (black), S_1 (blue), T_1 (red), and T_2 (yellow) states along the *Z/E* photoisomerization pathways of cyclohept-2-enone optimized using XMS-CAPT2(6,5)/cc-pvtz.²¹ The three most critical points on the left lie close to the Franck–Condon region with H—C=C—H torsion angles (indicated by gray ellipses) close to 0°, the six critical points in the middle have torsion angles close to 90° and the lowest lying (*E*)-conformer has a torsion angle of 170°. As examples, we explicitly show the molecular structures of the lowest lying (*Z*)- and (*E*)-isomer, the transition state (TS) connecting them, as well as the structure of the $S_1T_1S_0$ CoIn/ISC, where a transannular interaction between C-3 and the hydrogen atom at C-7 is indicated.

Franck–Condon region, intersystem crossing between S_1 and T_2 can occur as both states become degenerate (S_1T_2 ISC). From there, following the T_2 , the system arrives at a conical intersection between T_1 and T_2 (T_1T_2 CoIn), allowing a transition to T_1 . Relaxation in the T_1 leads to a torsion of the double bond by 90° and a T_1 minimum of $\pi\pi^*$ character is reached. A barrier of 27.7 kJ mol^{-1} has to be overcome to reach the crossing region with the S_0 state (T_1S_0 ISC). This region is geometrically close to the thermal *Z/E* transition state in the S_0 (S_0 TS). Two pathways are now possible, either back to (*Z*)-1 or continuing the rotation toward the (*E*)-isomer, (*E*)-1. The final geometry of (*E*)-1 is characterized by a double bond torsion of 170° , which deviates from the classical value of 180° due to ring strain. For smaller enones¹⁸ this ring strain is even stronger and prevents full isomerization. Only the larger and more flexible cyclohept-2-enone can undergo complete isomerization in the triplet states as has already been shown by García-Expósito et al. at the CASSCF level.¹⁹ At the XMS-CASPT2 level, we identified another possible isomerization pathway exclusively via singlet states. Only a small barrier in the S_1 state (S_1 TS), lying 20.5 kJ mol^{-1} below the Franck–Condon point, has to be overcome to reach a three state crossing between S_1 , T_1 , and S_0 . Here the double bond torsion is also close to 90° . Furthermore, the structure is stabilized by a transannular interaction of C-3 and the hydrogen at C-7. As internal conversion is typically faster than intersystem crossing, we expect preferential population of the S_0 state and the possibility of *Z/E* isomerization by relaxation in the S_0 toward (*E*)-1. In case of the studied Diels–Alder reactions, dienes are used in excess, which can act as efficient triplet quenchers.²⁰ This would lead to an additional loss channel when following the triplet pathway. However, the excited molecules might have sufficient energy and momentum to overcome the barrier associated with the T_1S_0 ISC before quenching can occur. Thus, the possibility of isomerization along the triplet path should still be considered.

A first set of preparative experiments were performed with cyclohept-2-enone (**1**) and some substituted 1,3-butadienes (Scheme 3). It was found that the reactions worked best in dichloromethane solution at an irradiation wavelength of $\lambda = 350 \text{ nm}$ (emission maximum of the fluorescent lamps). The diene component was used in excess to secure an efficient trapping of the strained (*E*)-intermediate. With 1,3-butadiene itself (product **3a**) and symmetrical 2,3-disubstituted dienes (products **3b**, **3c**), only a single product was obtained for each reaction. [2 + 2] Photocycloaddition reactions between the enone and 1,3-dienes were not observed.²²

The *trans*-fusion of the newly formed cyclohexene ring was corroborated by a single crystal X-ray analysis of product **3b** derived from 1,2-bis(methylene)cyclohexane. The reaction with 2-substituted 1,3-butadienes led to a mixture of regioisomers, and no preference was observed (*rr* = regioisomeric ratio). The minor differences in the spectroscopic properties of the isoprene adducts **3d** and **3d'** may have been difficult to detect by the techniques available in the 1970s, which in turn accounts for a previous report on regioselective formation of **3d**.¹² A similar observation as with isoprene was also made with myrcene which gave the *trans*-fused products **3e** and **3e'** as a mixture of inseparable regioisomers. The reaction scale was irrelevant for the yields, which were consistently good to excellent. The limited regiocontrol exerted by the alkyl substituent in 2-position appeared to be due to its low electron-donating properties, and

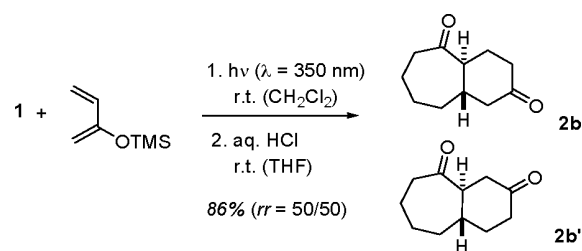
Scheme 3. Photoinduced Diels–Alder Reaction of Cyclohept-2-enone (**1**) with 1,3-Butadiene and Related Alkyl-substituted 1,3-Dienes^c



^a0.1 mmol scale. ^b1.0 mmol scale. ^c0.2 mmol scale. Molecular structure of **3b** in the solid state with ellipsoids at the 50% probability level.

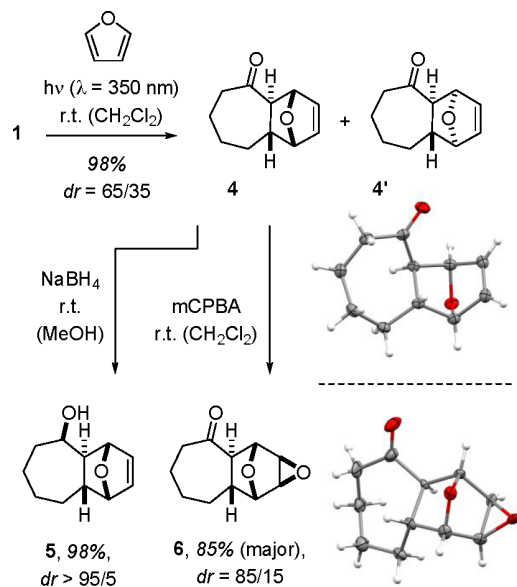
a better regiocontrol was expected for more electron-donating substituents.²³ However, the lack of regioselectivity persisted for stronger electron donors. 2-Trimethylsiloxy-1,3-butadiene, for example, is known to react with (*Z*)-enones under thermal conditions with high regioselectivity, even in the absence of a Lewis acid.²⁴ In contrast, no selectivity was observed in the reaction with photochemically generated (*E*)-enone (*E*)-1. Ketones **2b** and **2b'** were obtained after hydrolysis of the silyl enol ether in an equimolar ratio (Scheme 4).

Scheme 4. Photoinduced Diels–Alder Reaction of Cyclohept-2-enone (**1**) with 2-Trimethylsiloxy-1,3-butadiene Delivering *trans*-Fused Products **2b** and **2b'**



It seems reasonable to assume that stereoelectronic parameters play a smaller role in the reaction of the twisted (*E*)-enone as compared to reactions of cyclic (*Z*)-enone. We thus anticipated that the *endo/exo*-selectivity might also be less pronounced. The reaction with furan had been previously studied by Eaton and Lin who reported the formation of two diastereomeric products when irradiating cyclohept-2-enone in furan as the solvent.⁷ Under our conditions, the high yield of the reaction was confirmed (Scheme 5) and the products were further analyzed (*dr* = diastereomeric ratio). The minor diastereoisomer **4'** gave crystals that were suitable for X-ray

Scheme 5. Photoinduced Diels–Alder Reaction of Cyclohept-2-enone (1) with Furan: Structure Proof and Subsequent Diastereoselective Reactions to Alcohol 5 and Epoxide 6^a



^aMolecular structures of 4' and 6 in the solid state with ellipsoids at the 50% probability level.

crystallographic analysis. In this tricyclic product, the former α -hydrogen atom of the α,β -unsaturated enone is positioned *exo* to the double bond, the former β -hydrogen atom *endo*. The keto group is also positioned *endo* to the double bond, which is why we refer to 4' and related products as *endo*-products. The *exo*-product 4 was the major diastereoisomer the relative configuration of which was established by X-ray crystallographic analysis of its epoxidation product 6. Unlike the reduction of the ketone to alcohol 5, which proceeded with perfect diastereoselectivity, the epoxidation led to two diastereoisomers in a ratio of 85/15.

Since the photoinduced Diels–Alder reaction is irreversible, product formation occurs under kinetic control. For the furan cycloaddition, we probed the predictive character of DLPNO–CCSD(T) calculations by comparing their results with the experimental data. The calculations (Figure 2) confirmed that the (*E*)-isomer of cyclohept-2-enone, (*E*)-1, can undergo an uncatalyzed Diels–Alder reaction with furan. The activation barrier was calculated to be between 80 and 90 kJ mol^{-1} . Similar barrier heights were obtained in previous work for the reaction of isoprene with (*E*)-4,4-dimethylcyclohept-2-enone.¹⁶

The respective lowest transition states for an *exo*- vs an *endo*-approach of furan to (*E*)-1 are depicted in Figure 2. They are energetically close to each other and lead to products 4 and 4'. The reaction is found to be exergonic with a Gibbs free reaction energy $\Delta_r G^\circ$ of -105.1 and -102.7 kJ mol^{-1} , respectively. The *endo*-transition state is higher in energy and the expected dr can be calculated from the relative barrier heights $\Delta^\ddagger G^\circ$. The calculated value ($dr = 76/24$) is in remarkably good agreement with the experiment. The optimized molecular structure of 4' matches closely the experimental structure of the compound in its crystal.

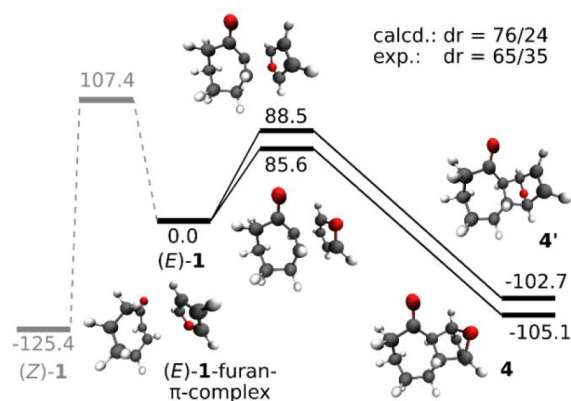
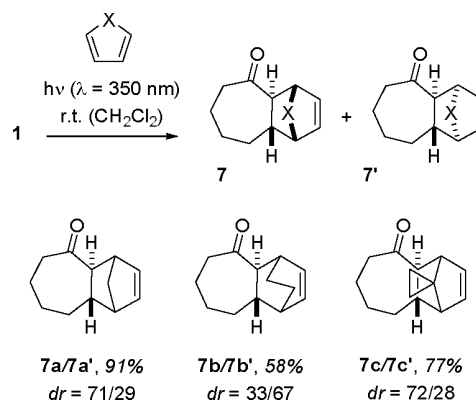


Figure 2. Transition states for the Diels–Alder reaction of (*E*)-1 with furan to form products 4 and 4' (black) and for the thermal isomerization back to (*Z*)-1 (gray). Gibbs free activation energies $\Delta^\ddagger G^\circ$ for the Diels–Alder reactions and Gibbs free reaction energies $\Delta_r G^\circ$ for all reactions were calculated using DLPNO–CCSD(T)/CBS(3/4, cc)²⁵// ω B97xD/aug-cc-pvtz.²⁶ Gibbs free activation energies $\Delta^\ddagger G^\circ$ for the *Z/E* Isomerization were calculated using XMS-CASPT2(6,5)/cc-pVTZ// ω B97xD/aug-cc-pvtz. All values are given in kJ mol^{-1} . The calculated diastereomeric ratio dr and the experimental dr are shown, as well as the structure of a π -complex of (*E*)-1 and furan.

Scheme 6. Photoinduced Diels–Alder Reaction of Cyclohept-2-enone (1) with Various Bridged Dienes Delivering *trans*-Fused Products 7 and 7'



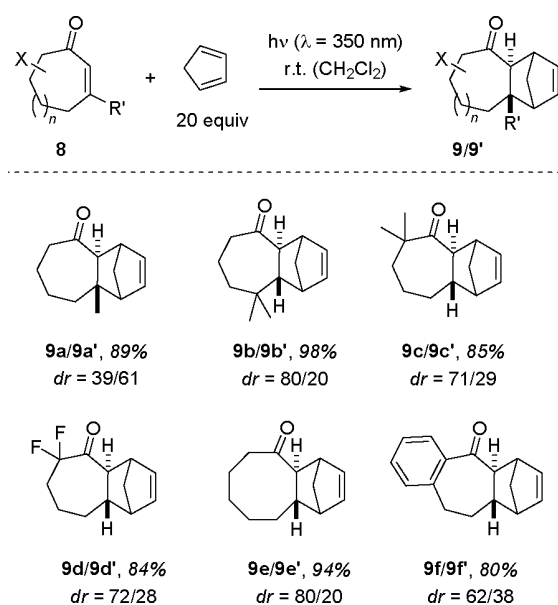
Expectedly, 1,3-cyclopentadienes reacted well in the Diels–Alder reaction with (*E*)-cyclohept-2-enone (Scheme 6, products 7a/7a' and 7c/7c'). The configuration assignment was based on analogy to the furan products, which means that the major product was *exo*-configured. This assignment is in line with previous work⁶ in which the *exo*-isomer was described. We could further corroborate the analogous assignment by comparison of the experimental with calculated ¹H NMR data for both 4/4' and 7a/7a'; in both cases the olefinic signals of the *exo*-isomer are well separated while those of the *endo*-isomer overlap and lie in-between the signals of the *exo*-isomer (see SI for more details). However, we could not confirm that the product with cyclopentadiene was a single diastereoisomer,⁶ even if the reaction was performed at low temperature ($dr = 75/25$ at -70 °C). This is again in agreement with the DLPNO–CCSDT calculations, which predict a barrier height of 77.7 kJ mol^{-1} for the *exo* approach leading to 7a and a barrier height of 81.7 kJ mol^{-1} for the *endo*

approach leading to **7a'**, corresponding to a predicted diastereomeric ratio of $dr = 83/17$.

The reaction with 1,3-cyclohexadiene was sluggish, as expected from the poor reactivity of this diene²⁷ in thermal Diels–Alder reactions. On the basis of the ¹H NMR data we assign the *endo*-isomer **7b'** to be the major diastereoisomer. In general, if trapping with a diene was not successful (e.g., with thiophene), a series of polar spots were detected on TLC, stemming from $[\pi 2_s + \pi 2_a]$ dimerization products⁸ of cyclohept-2-enone. When a solution of cyclohept-2-enone was irradiated without diene, the substrate was consumed within the same time period typically required for completion of a photoinduced Diels–Alder reaction (2–4 h; see SI for more information on corresponding studies). This dimerization—in addition to thermal reversion to the (*Z*)-isomer—precludes an isolation of (*E*)-**1** at noncryogenic temperatures.

The scope section of this study was completed by submitting other readily available, seven-membered cyclic enones to the conditions of the photoinduced Diels–Alder reaction. 1,3-Cyclopentadiene was employed as the diene component (Scheme 7). In all cases, a mixture of *exo*- (**9**) and *endo*-

Scheme 7. Photoinduced Diels–Alder Reaction of Various Cycloalk-2-enones **8** with Cyclopentadiene to *trans*-Products **9** and **9'**

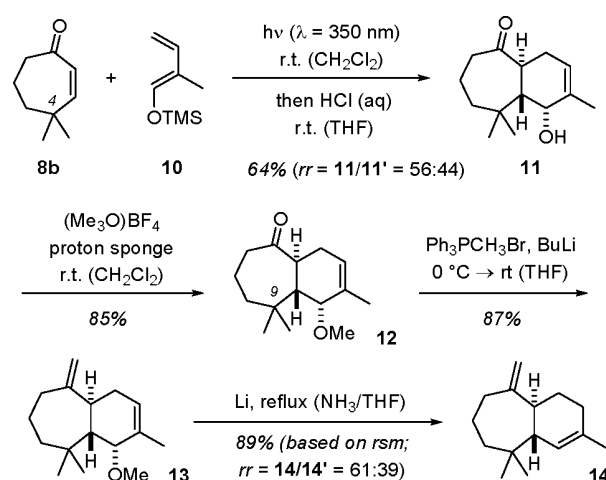


products (**9'**) was obtained. The reaction proved remarkably robust toward a potential steric hindrance by methyl substituents. Yields remained high irrespective whether a methyl or dimethyl substitution was introduced in the 3-, 4-, or 7-position of the cyclohept-2-enone (products **9a/9a'**, **9b/9b'**, and **9c/9c'**). A difluorosubstitution was also well tolerated and gave the respective tricyclic products **9d/9d'** in high yield. The result is relevant for possible applications since it enables the introduction of fluorine atoms into a strained scaffold by a photochemical method. The reaction of cyclooct-2-enone with 1,3-cyclopentadiene was previously reported to yield a single product.¹² Under our conditions, we did not observe a single product but a mixture of two diastereoisomers (**9e/9e'**) in a ratio that was similar to the dr of the cyclohept-2-enone

addition (Scheme 6, **7a/7a'**). Eventually, the Diels–Alder reaction was performed with 8,9-dihydrobenzocyclohepten-5-one which also reacted cleanly to products **9f/9f'** upon irradiation. In all cases but **9a/9a'**, the *exo*-product was again the major diastereoisomer.

As mentioned in the introduction, applications of the photoinduced Diels–Alder reaction in total synthesis are infrequent despite the fact that several natural products display *trans*-annulated bicyclo[5.4.0]undecane skeletons. As a potential target, the sesquiterpene *trans*- α -himachalene (**14**) was selected, which was isolated as (+)-**14** by Bartelt and co-workers²⁸ in 2001 from the male flea beetle *Phyllotreta cruciferae* and which had been previously synthesized from (*R*)-carvone by Srikrishna and Kumar.²⁹ The literature-known¹⁶ starting material **8b** was shown to be a competent substrate for the reaction (cf. Scheme 7) despite its geminal dimethylsubstitution at C-4. Reaction with silylenolether **10**³⁰ was initiated by irradiation at $\lambda = 350$ nm and resulted in a mixture of regioisomeric cycloaddition products **11** and **11'** ($rr = 56/44$). Remarkably, the major regioisomer of the reaction, which was isolated in a yield of 36% after hydrolysis, was found to be diastereomerically pure (Scheme 8).

Scheme 8. Concise Total Synthesis of *trans*- α -Himachalene (**14**) by a Photoinduced Diels–Alder Reaction as Key Step



The relative configuration could be assigned after methylation of the free hydroxy group with a strong methylating agent (Meerwein salt) in the presence of 1,8-bis(dimethylamino)naphthalene (proton sponge) as Brønsted base. NOE contacts were observed between one C-9 methyl group and the bridgehead hydrogen atom in α -position to the carbonyl group as well as between the other C-9 methyl group and the hydrogen atom geminal to the methoxy group. Consequently, these hydrogen atoms need to be on opposite sides of the ring system confirming the depicted relative configuration of product **11**. In turn, this means that the attack of the diene had occurred with *exo*-selectivity on the intermediate (*E*)-enone. The result is in good agreement with the outcome of the above-mentioned reaction of 1-methoxycyclobutadiene (product **2a**, Scheme 2).¹⁴ Methylenation of the carbonyl group of ketone **12** was performed by a Wittig olefination, which produced diene **13** in 87% yield. The final step of the synthesis followed a literature-known²⁹ elimination under strongly reducing conditions. After release of the methoxide,

the allylic anion is not protonated with perfect selectivity, which required separation of the natural product **14** from its regioisomer by column chromatography using AgNO₃-impregnated silica. The brevity of the synthesis is mainly due to the fact that the *trans*-junction of the annulated ring does not require a sequential introduction of the two stereogenic centers but was established in the [4 + 2] cycloaddition step.

CONCLUSION

In summary, we have shown that the sequence of *Z/E* isomerization/Diels–Alder reaction is a versatile tool to obtain *trans*-fused bicyclic ring systems from cyclohept-2-enones. Formation of the (*E*)-isomer can occur on the triplet or on the singlet hypersurface. The high ring strain of (*E*)-cyclohept-2-enones is responsible for their high reactivity toward dienes and the Diels–Alder reaction occurs in the absence of any catalyst. If cyclic dienes were employed, a notable *exo/endo* selectivity was recorded, mostly in favor of the *exo*-isomer. With substituted acyclic 1,3-dienes the regioselectivity was not very pronounced. Still, the method invites applications in total synthesis due to the unique bond formation it entails.

EXPERIMENTAL SECTION

General Methods. All air or moisture sensitive reactions were carried out in heat gun-dried glassware under an argon atmosphere using standard Schlenk techniques. Photochemical experiments were carried out in heat gun-dried Duran tubes in a positive geometry setup (cylindrical array of 16 fluorescent light tubes, see SI for datasheet) with the sample placed in the center of the illumination chamber. As cooling baths, ice/water (0 °C) and dry ice/isopropanol (−78 °C) mixtures were used. Commercially available chemicals were used without further purification unless otherwise noted. The following compounds were synthesized according to literature procedures: 1,2-dimethylenecyclohexane,³¹ trimethyl((2-methylbuta-1,3-dien-1-yl)-oxy)silane.³² For moisture sensitive reactions, tetrahydrofuran (THF), diethyl ether (Et₂O), and dichloromethane (CH₂Cl₂) were dried by a MBSPS 800 MBraun solvent purification system. All other dry solvents were purchased from Acros Organics (extra dry, over molecular sieves) and used without further purification. For photochemical reactions, dry dichloromethane was degassed by three freeze–pump–thaw cycles and stored over 3 Å molecular sieves (10% w/v), and all dienes were degassed by three freeze–pump–thaw cycles. For extractions or column chromatography, technical solvents were distilled prior to use. Flash column chromatography was performed on silica 60 (Merck, 230–400 mesh) with the indicated eluent mixtures. Thin layer chromatography (TLC) was performed on silica-coated glass plates (Merck, silica 60 F₂₅₄) with detection by UV-light (λ = 254 nm) [UV] and/or by staining with a potassium permanganate solution (3.00 g KMnO₄, 20.0 g K₂CO₃ and 5.00 mL of 5% aq. NaOH solution in 300 mL H₂O) [KMnO₄] followed by heat treatment. Melting points were determined using a Büchi M-565 melting point apparatus. Nuclear magnetic resonance spectra were recorded at room temperature on a Bruker AVHD-400, AVHD-500, or AV-III-500 (equipped with a CryoProbe). ¹H NMR spectra were referenced to the residual proton signal of the deuterated solvent [δ(CHCl₃) = 7.26 ppm, δ(CHDCl₂) = 5.32 ppm, δ(C₆HD₅) = 7.16 ppm, δ(CHD₂CN) = 1.94 ppm]. ¹³C NMR spectra were referenced to the carbon signal of the deuterated solvent [δ(CDCl₃) = 77.16 ppm, δ(CD₂Cl₂) = 53.84 ppm, δ(C₆D₆) = 128.06 ppm, δ(CD₃CN) = 118.26 ppm]. ¹⁹F NMR spectra were not referenced. Apparent multiplets that occur as a result of coupling constant equality between magnetically nonequivalent protons are marked as virtual (*virt.*). The following abbreviations for single multiplicities were used: br (broad), s (singlet), d (doublet), t (triplet), q (quartet), m (multiplet). Composition of isomeric mixtures was determined by ¹H NMR analysis of the crude product. Infrared spectra (IR) were recorded on a PerkinElmer Frontier IR-

FTR spectrometer by ATR technique. The signal intensity is assigned using the following abbreviations: br (broad), vs (very strong), s (strong), m (medium), w (weak). UV–vis spectra were recorded on a PerkinElmer Lambda 35 UV–vis spectrometer, using a Hellma precision cell made of quartz SUPRASIL with a pathway of 1.0 mm. Mass spectrometry (MS) and high resolution mass spectrometry (HRMS) was performed on a Thermo Scientific DFS-HRMS spectrometer (EI).

Synthetic Procedures and Analytical Data. *3-Methylcyclohept-2-en-1-one (8a)*. Based on a literature procedure.³³ 3.75 mL of a solution of MeLi (1.6 M, 6.00 mmol, 1.2 equiv) was added dropwise to a solution of 551 mg cyclohept-2-en-1-one (5.00 mmol, 1.0 equiv) in dry Et₂O (10 mL) at −78 °C. After stirring for 4 h, H₂O (5.0 mL) was added and the mixture allowed to warm to rt. The layers were separated and the aqueous layer was extracted with Et₂O (3 × 10 mL). The combined organic layers were washed with brine (10 mL), dried over Na₂SO₄, filtered, and concentrated in vacuo. The crude tertiary allylic alcohol was dissolved in dry CH₂Cl₂ (15 mL) and 2.07 g pyridinium dichromate (5.50 mmol, 1.1 equiv) were added. The mixture was vigorously stirred for 18 h. Et₂O (10 mL) was added and the mixture filtered through a pad of silica gel with Et₂O as eluent. After removing the solvent in vacuo and subsequent purification by column chromatography (2.5 cm × 20 cm, P/Et₂O = 4/1 → 2/1), 321 mg enone **8a** (2.59 mmol, 52%) were obtained as a colorless oil. TLC R_f = 0.50 (Hex/EtOAc = 3/1) [UV, KMnO₄]. ¹H NMR (500 MHz, CDCl₃, 300 K) δ [ppm] = 5.93 (q, J = 1.3 Hz, 1H), 2.58 (dd, J = 7.2, 5.2 Hz, 2H), 2.41 (dd, J = 6.9, 4.6 Hz, 2H), 1.96 (d, J = 1.3 Hz, 3H), 1.86–1.73 (m, 4H). ¹³C NMR{¹H} (126 MHz, CDCl₃, 300 K) δ [ppm] = 204.0, 158.7, 130.0, 42.7, 34.7, 27.8, 25.3, 21.6. UV–vis (CH₂Cl₂) λ_{max} (ε) = 235 (11576), 322 nm (72.3 M^{−1} cm^{−1}). The data obtained matched those reported in the literature.³⁴

2,2-Dimethyl-6-oxoheptanoic acid. Based on a literature procedure.³⁵ 6.10 mL β-Ionone (5.77 g, 30.0 mmol, 1.0 equiv) were dissolved in acetone (150 mL) and cooled at 0 °C. 47.4 g KMnO₄ (300 mmol, 10 equiv) were added in small portions so that the temperature of the solution stayed below 10 °C. The mixture was stirred for 2 h at rt. After removing the solvent carefully in vacuo, the residue was suspended in water and cooled at 0 °C. Then, 15 g Na₂SO₃ and 150 mL of a diluted aqueous H₂SO₄ solution (conc. H₂SO₄/H₂O = 1/2) were added in portions. While more diluted aqueous H₂SO₄ solution was added until the solution became clear, portions of Na₂SO₃ were added to keep the pH-value between 2 and 7. Once gas evolution stopped and the solution was clear, the pH-value was adjusted to pH = 2 with conc. H₂SO₄. The solution was extracted with CH₂Cl₂ (6 × 100 mL) and the combined organic layers were dried over MgSO₄, filtered, and concentrated in vacuo. After purification by Kugelrohr distillation (0.1 mbar, 150 °C), 1.06 g 2,2-dimethyl-6-oxoheptanoic acid (6.17 mmol, 21%) were obtained as a yellowish oil. ¹H NMR (500 MHz, CDCl₃, 300 K) δ [ppm] = 2.45 (t, J = 6.9 Hz, 2H), 2.16 (s, 3H), 1.66–1.52 (m, 5H), 1.24 (s, 6H). ¹³C NMR{¹H} (126 MHz, CDCl₃, 300 K) δ [ppm] = 209.0, 183.9, 43.9, 42.1, 39.6, 30.0, 24.9, 19.2. The data obtained matched those reported in the literature.³⁵

2,2-Dimethyl-6-oxoheptanal. Based on literature procedures.³⁶ To a stirred suspension of 661 mg LiAlH₄ (17.4 mmol, 3.0 equiv) in dry THF (60 mL) at 0 °C was added a solution of 1.00 g 2,2-dimethyl-6-oxoheptanoic acid (5.81 mmol, 1.0 equiv) in dry THF (10 mL). After stirring for 30 min at rt, the mixture was heated at 80 °C for 2.5 h. The mixture was allowed to cool to rt and was diluted with wet Et₂O (60 mL). 6.6 g Celite were added and the mixture vigorously stirred. H₂O was added until gas evolution ceased. The mixture was filtered and concentrated in vacuo. The crude diol was dissolved in wet CH₂Cl₂ (450 mL) and cooled at 0 °C. A mixture of 16.0 g Dess–Martin periodinane (37.7 mmol, 6.5 equiv) and 6.34 g NaHCO₃ (75.5 mmol, 13 equiv) was added in portions. After the resulting suspension was stirred for 2 h at 0 °C and for 2 h at rt, 450 mL of a sat. aq. NaHCO₃/Na₂S₂O₃ solution (1:1) were added and the solution stirred for 15 min. The aqueous layer was extracted with Et₂O (3 × 200 mL). The combined organic layers were washed with brine (200 mL), dried over Na₂SO₄, filtered, and concentrated in

vacuo. After purification by column chromatography (4.0 cm × 20 cm, P/Et₂O = 4/1), 823 mg 2,2-dimethyl-6-oxoheptanal (5.27 mmol, 91%) were obtained as a yellowish oil. TLC *R_f* = 0.21 (P/Et₂O = 4/1) [KMnO₄]. ¹H NMR (500 MHz, CDCl₃, 300 K) δ [ppm] = 9.45 (s, 1H), 2.43 (t, *J* = 6.9 Hz, 3H), 2.13 (d, *J* = 1.2 Hz, 4H), 1.54–1.38 (m, 6H), 1.06 (s, 6H). ¹³C NMR{¹H} (126 MHz, CDCl₃, 300 K) δ [ppm] = 208.5, 206.2, 45.8, 43.8, 36.4, 30.0, 21.3, 18.5.

3-Hydroxy-4,4-dimethylcycloheptan-1-one. Based on a literature procedure.³⁷ 50.0 mg 2,2-dimethyl-6-oxoheptanal (320 μmol, 1.0 equiv) and 314 mg NPh₃ (1.28 mmol, 4.0 equiv) were dissolved in dry PhMe (40 mL) and cooled at –78 °C. 960 μL of a 1.0 M LiHMDS in PhMe solution (960 μmol, 3.0 equiv) were added dropwise and the solution was stirred for 2 h. After allowing the solution to warm to rt, sat. aq. NH₄Cl (10 mL) was added, the layers separated and the aqueous one extracted with EtOAc (3 × 20 mL). The combined organic layers were washed with brine (20 mL), dried over Na₂SO₄, filtered, and concentrated in vacuo. After purification by column chromatography (1.5 cm × 20 cm, P/Et₂O = 1/1), 33.1 mg 3-hydroxy-4,4-dimethylcycloheptan-1-one (212 μmol, 66%) were obtained as a yellow oil. TLC *R_f* = 0.16 (P/Et₂O = 1/1) [KMnO₄]. ¹H NMR (500 MHz, CDCl₃, 300 K) δ [ppm] = 3.62 (dd, *J* = 8.0, 1.9 Hz, 1H), 2.85 (dd, *J* = 15.3, 1.9 Hz, 1H), 2.69 (dd, *J* = 15.3, 8.0 Hz, 1H), 2.55–2.39 (m, 2H), 1.79–1.61 (m, 4H), 1.04 (s, 3H), 1.01 (s, 3H). ¹³C NMR{¹H} (126 MHz, CDCl₃, 300 K) δ [ppm] = 212.9, 75.0, 47.2, 44.2, 38.2, 38.0, 26.6, 25.8, 19.2. IR (ATR) $\tilde{\nu}$ [cm⁻¹] = 3438 (br m), 2952 (s), 2932 (s), 2871 (m), 1691 (vs), 1627 (w). MS (EI, 70 eV) *m/z* (%) = 95 (100), 109 (38), 123 (50), 139 (71), 156 (4) [M]⁺. HRMS (EI, 70 eV) calcd for C₉H₁₆O₂ [M]⁺: 156.1145, found 156.1136.

4,4-Dimethylcyclohept-2-en-1-one (8b). 50.0 mg 3-hydroxy-4,4-dimethylcycloheptan-1-one (320 μmol, 1.0 equiv) were dissolved in dry PhMe (25 mL) and 6.09 mg *p*-toluenesulfonic acid monohydrate (32.0 μmol, 10 mol %) were added. A Dean–Stark trap filled with dry PhMe was attached and the mixture heated at 150 °C for 1 h. After allowing the solution to cool to rt, sat. aq. NaHCO₃ (5.0 mL) was added. The aqueous layer was extracted with EtOAc (3 × 10 mL). The combined organic layers were washed with brine (10 mL), dried over Na₂SO₄, filtered, and concentrated in vacuo. After purification by column chromatography (2.0 cm × 20 cm, P/Et₂O = 4/1), 36.7 mg ketone **8b** (266 μmol, 83%) were obtained as a yellowish oil. TLC *R_f* = 0.51 (H/EtOAc = 3/1) [UV, KMnO₄]. ¹H NMR (500 MHz, CDCl₃, 300 K) δ [ppm] = 6.04 (d, *J* = 12.9 Hz, 1H), 5.76 (d, *J* = 12.9 Hz, 1H), 2.64–2.57 (m, 2H), 1.85–1.77 (m, 2H), 1.76–1.70 (m, 2H), 1.12 (s, 6H). ¹³C NMR{¹H} (126 MHz, CDCl₃, 300 K) δ [ppm] = 204.9, 153.9, 127.6, 45.2, 40.7, 39.7, 29.9, 18.8. UV–vis (CH₂Cl₂) λ_{max} (ε) = 226 (11311), 292 nm (89.7 M⁻¹ cm⁻¹). The data obtained matched those reported in the literature.¹⁶

General Procedure for α -Derivatization of Enones. Based on a literature procedure.³⁸ A solution of 165 mg cyclohept-2-en-1-one (1.50 mmol, 1.0 equiv) in dry THF (7.5 mL) was cooled at –78 °C and 2.0 mL of a 1.0 M LiHMDS solution in THF (1.95 mmol, 1.3 equiv) were added dropwise. After stirring for 30 min, the electrophile (2.25 mmol, 1.5 equiv) was added as a 500 mM solution in dry THF. The solution was allowed to warm to rt and stirred for 1 h. Then, sat. aq. NH₄Cl (10 mL) was added, the layers were separated and the aqueous one extracted with Et₂O (3 × 10 mL). The combined organic layers were washed with brine (10 mL), dried over Na₂SO₄, filtered, and concentrated in vacuo. The crude product was purified by column chromatography.

7,7-Dimethylcyclohept-2-en-1-one (8c). Following the general procedure, 165 mg cyclohept-2-en-1-one (1.50 mmol, 1.0 equiv) were converted with two times 0.14 mL MeI (319 mg, 2.25 mmol, 1.5 equiv). After purification by column chromatography (2.0 cm × 20 cm, P/Et₂O = 95/5), 85.9 mg ketone **8c** (622 μmol, 41%) were obtained as a yellowish liquid. TLC *R_f* = 0.57 (Hex/EtOAc = 3/1)

[UV, KMnO₄]. ¹H NMR (500 MHz, CD₂Cl₂, 300 K) δ [ppm] = 6.28 (dt, *J* = 12.6, 4.3 Hz, 1H), 5.88 (dt, *J* = 12.6, 2.0 Hz, 1H), 2.37 (tdd, *J* = 6.2, 4.3, 2.0 Hz, 2H), 1.80–1.66 (m, 4H), 1.56 (s, 2H), 1.12 (s, 6H). ¹³C NMR{¹H} (126 MHz, CD₂Cl₂, 300 K) δ [ppm] = 209.9, 142.4, 130.2, 49.0, 38.2, 33.4, 27.1, 22.8. UV–vis (CH₂Cl₂) λ_{max} (ε) = 225 (9034), 321 nm (112 M⁻¹ cm⁻¹). The data obtained matched those reported in the literature.³⁹

7,7-Difluorocyclohept-2-en-1-one (8d). Following the general procedure, 165 mg cyclohept-2-en-1-one (1.50 mmol, 1.0 equiv) were converted with two times 710 mg *N*-fluorobenzenesulfonimide (2.25 mmol, 1.5 equiv). After purification by column chromatography (2.0 cm × 20 cm, P/Et₂O = 7/1), 51.8 mg ketone **8d** (355 μmol, 24%) were obtained as a yellowish liquid. TLC *R_f* = 0.33 (Hex/EtOAc = 3/1) [UV, KMnO₄]. ¹H NMR (500 MHz, CD₂Cl₂, 300 K) δ [ppm] = 6.84–6.76 (m, 1H), 6.10–6.03 (m, 1H), 2.54–2.46 (m, 2H), 2.34–2.22 (m, 2H), 1.93–1.84 (m, 2H). ¹³C NMR{¹H} (126 MHz, CD₂Cl₂, 300 K) δ [ppm] = 190.6 (t, *J* = 28.3 Hz), 150.2, 127.1, 118.2 (t, *J* = 247.7 Hz), 33.5 (t, *J* = 23.9 Hz), 30.6, 20.8 (t, *J* = 6.0 Hz). ¹⁹F NMR (376 MHz, CD₂Cl₂, 300 K) δ [ppm] = –98.3 (t, *J* = 16.6 Hz). IR (ATR) $\tilde{\nu}$ [cm⁻¹] = 2941 (w), 1670 (vs), 1686 (vs), 1627 (w). UV–vis (CH₂Cl₂) λ_{max} (ε) = 235 (8351), 305 nm (167 M⁻¹ cm⁻¹). MS (EI, 70 eV) *m/z* (%) = 109 (100), 115 (18), 125 (14), 146 (4) [M]⁺. HRMS (EI, 70 eV) calcd for C₇H₈OF₂ [M]⁺: 146.0538, found 146.0536.

General Procedure for the α -Bromination of Ketones. Based on a literature procedure.⁴⁰ A solution of a cycloalkanone (1.0 equiv) in dry Et₂O (1.0 M) was placed in a water bath. *N*-Bromosuccinimide (1.05 equiv; recrystallized from 10 mL water per g NBS; dissolved at approximately 90 °C, cooled in ice bath for 3 h, colorless crystals filtered and washed with water, dried in vacuo overnight, stored dark under inert gas in fridge) and subsequently NH₄OAc (10 mol %) were added to the solution. The mixture was stirred at rt until full conversion was reached as determined by TLC. After filtration (Et₂O as eluent), the filtrate was washed with water and brine, dried over Na₂SO₄, filtered, and concentrated in vacuo. The crude product was purified by column chromatography.

General Procedure for the Elimination of α -Bromoketones to Enones. Based on literature procedures.⁴¹ LiBr (2.5 equiv) and Li₂CO₃ (2.5 equiv) were added to a solution of a 2-bromocycloalkanone (1.0 equiv) in dry DMF (500 mM). The mixture was stirred at 130 °C until full conversion was reached as determined by TLC. After cooling to rt, the mixture was diluted to double its volume with EtOAc and filtered over a pad of Celite (EtOAc as eluent). The filtrate was washed with water (3×) and brine (2×), dried over Na₂SO₄, filtered, and concentrated in vacuo. The crude product was purified by column chromatography.

2-Bromocyclooctan-1-one. Following the general procedure, 2.52 g cyclooctanone (20.0 mmol, 1.0 equiv) were converted with 154.0 mg NH₄OAc (2.00 mmol, 10 mol %) and 3.74 g NBS (21.0 mmol, 1.05 equiv) within 4 h. After purification by column chromatography (5.0 cm × 20 cm, P/Et₂O = 95/5), 3.29 g ketone 2-bromocyclooctan-1-one (16.0 mmol, 80%) were obtained as a yellowish oil. TLC *R_f* = 0.67 (Hex/EtOAc = 2/1) [KMnO₄]. ¹H NMR (500 MHz, CDCl₃, 300 K) δ [ppm] = 4.27 (dd, *J* = 11.3, 4.0 Hz, 1H), 2.87 (virt. td, *J* = 12.1, 3.7 Hz, 1H), 2.44–2.26 (m, 3H), 1.98–1.87 (m, 1H), 1.83–1.63 (m, 3H), 1.63–1.50 (m, 2H), 1.46–1.35 (m, 1H), 1.24–1.12 (m, 1H). ¹³C NMR{¹H} (126 MHz, CDCl₃, 300 K) δ [ppm] = 208.9, 54.5, 36.3, 32.8, 28.9, 26.7, 25.5, 24.1. The data obtained matched those reported in the literature.⁴²

(*Z*)-Cyclooct-2-en-1-one (8e). Following the general procedure, 3.08 g ketone **S3** (15.0 mmol, 1.0 equiv) were converted with 3.26 g LiBr (37.5 mmol, 2.5 equiv) and 2.77 g Li₂CO₃ (37.5 mmol, 2.5 equiv) within 5 h. After purification by column chromatography (4.5 cm × 20 cm, P/Et₂O = 5/1), 513 mg enone **8e** (4.13 mmol, 28%) were obtained as a yellowish oil. TLC *R_f* = 0.58 (Hex/EtOAc = 2/1) [UV, KMnO₄]. ¹H NMR (300 MHz, CDCl₃, 300 K) δ [ppm] = 6.35 (dt, *J* = 12.4, 7.0 Hz, 1H), 6.06–5.95 (m, 1H), 2.65 (t, *J* = 6.8 Hz, 2H), 2.58–2.45 (m, 2H), 1.90–1.75 (m, 2H), 1.71–1.51 (m, 4H). ¹³C NMR{¹H} (126 MHz, CDCl₃, 300 K) δ [ppm] = 214.1, 131.5, 124.2, 44.3, 42.2, 27.1, 25.7, 24.7. UV–vis (CH₂Cl₂) λ_{max} (ε) = 227

(8222), 315 nm ($77.3 \text{ M}^{-1} \text{ cm}^{-1}$). The data obtained matched those reported in the literature.⁴³

6-Bromo-6,7,8,9-tetrahydro-5H-benzo[7]annulen-5-one. Following the general procedure, 1.60 g 1-benzosuberone (10.0 mmol, 1.0 equiv) were converted with 77.0 mg NH_4OAc (1.00 mmol, 10 mol %) and 1.87 g NBS (10.5 mmol, 1.05 equiv) within 5 h. After purification by column chromatography (4.0 cm \times 20 cm, P/Et₂O = 95/5), 1.23 g ketone 6-bromo-6,7,8,9-tetrahydro-5H-benzo[7]annulen-5-one (5.14 mmol, 51%) were obtained as a yellow oil. TLC R_f = 0.40 (Hex/EtOAc = 9/1) [KMnO_4]. ¹H NMR (500 MHz, CDCl_3 , 300 K) δ [ppm] = 7.60 (dd, J = 7.7, 1.5 Hz, 1H), 7.42 (virt. td, J = 7.5, 1.5 Hz, 1H), 7.30 (virt. td, J = 7.6 Hz, 1.2, 1H), 7.23–7.16 (m, 1H), 4.86 (dd, J = 7.8, 4.1 Hz, 1H), 3.10–2.84 (m, 2H), 2.52–2.19 (m, 2H), 2.09–1.95 (m, 2H). ¹³C NMR{¹H} (126 MHz, CDCl_3 , 300 K) δ [ppm] = 200.2, 139.7, 137.8, 132.3, 129.8, 129.7, 126.9, 126.9, 54.5, 33.9, 33.4, 24.1.

8,9-Dihydro-5H-benzo[7]annulen-5-one (8f). Following the general procedure, 1.08 g ketone **54** (4.50 mmol, 1.0 equiv) were converted with 977 mg LiBr (11.3 mmol, 2.5 equiv) and 831 mg Li_2CO_3 (11.3 mmol, 2.5 equiv) within 3 h. After purification by column chromatography (2.5 cm \times 20 cm, P/Et₂O = 9/1), 265 mg enone **8f** (1.67 mmol, 37%) were obtained as a yellow oil. TLC R_f = 0.30 (Hex/EtOAc = 9/1) [UV, KMnO_4]. ¹H NMR (500 MHz, CDCl_3 , 300 K) δ [ppm] = 7.68 (dd, J = 7.8, 1.5 Hz, 1H), 7.44–7.32 (m, 1H), 7.28–7.19 (m, 1H), 7.13 (d, J = 7.3 Hz, 1H), 6.69 (dt, J = 12.0, 4.7 Hz, 1H), 6.21 (dt, J = 12.0, 1.9 Hz, 1H), 3.03–2.97 (m, 2H), 2.57–2.50 (m, 2H). ¹³C NMR{¹H} (126 MHz, CDCl_3 , 300 K) δ [ppm] = 195.2, 147.2, 140.1, 139.9, 132.6, 132.3, 129.8, 129.0, 126.9, 34.6, 29.9. UV-vis (CH_2Cl_2) λ_{max} (ϵ) = 232 (8287), 351 nm ($178 \text{ M}^{-1} \text{ cm}^{-1}$). The data obtained matched those reported in the literature.⁴⁴

General Procedure for the Photoinduced Diels–Alder Reaction. The dienophile (1.0 equiv) was transferred as a solution in dry CH_2Cl_2 (1.5 mL) to a Duran phototube. Then, the diene (20 equiv) was added and the solution diluted with dry CH_2Cl_2 to reach a total volume of 10 mL. The mixture was irradiated with fluorescent light tubes (λ_{max} = 350 nm) until full conversion of dienophile was reached as determined by TLC (2–4 h), concentrated in vacuo, and purified by column chromatography.

(4aS*,9aS*)-1,4,4a,6,7,8,9,9a-Octahydro-5H-benzo[7]annulen-5-one (3a). Following the general procedure, 22.0 mg cyclohept-2-en-1-one (200 μmol , 1.0 equiv) were converted with 2.35 mL butadiene in hexanes (15% w/w, 4.00 mmol, 20 equiv). After purification by column chromatography (1.5 cm \times 20 cm, P/Et₂O = 9/1), 22.2 mg ketone **3a** (135.1 μmol , 68%) were obtained as a colorless oil. TLC R_f = 0.58 (Hex/EtOAc = 3/1) [KMnO_4]. ¹H NMR (500 MHz, CDCl_3 , 300 K) δ [ppm] = 5.69–5.65 (m, 2H), 2.66 (virt. td, J = 11.3, 3.2 Hz, 1H), 2.44–2.34 (m, 1H), 2.30 (virt. td, J = 10.8, 6.3 Hz, 1H), 2.19–2.04 (m, 3H), 1.99–1.87 (m, 2H), 1.87–1.78 (m, 1H), 1.76–1.65 (m, 2H), 1.53–1.45 (m, 2H), 1.30–1.17 (m, 1H). ¹³C NMR{¹H} (126 MHz, CDCl_3 , 300 K) δ [ppm] = 216.9, 127.2, 125.6, 55.1, 41.2, 36.8, 35.6, 33.8, 29.6, 29.2, 26.5. The data obtained matched those reported in the literature.¹⁰

(5aS*,10aS*)-1,2,3,4,5,5a,7,8,9,10,10a,11-Dodecahydro-6H-cyclohepta[b]naphthalen-6-one (3b). Following the general procedure, 11.0 mg cyclohept-2-en-1-one (100 μmol , 1.0 equiv) were converted with 216 mg 1,2-dimethylenecyclohexane (2.00 mmol, 20 equiv). After purification by column chromatography (1.5 cm \times 15 cm, P/Et₂O = 9/1), 19.8 mg ketone **3b** (90.5 μmol , 91%) were obtained as a colorless oil. TLC R_f = 0.65 (Hex/EtOAc = 3/1) [KMnO_4]. mp 74.9 °C. ¹H NMR (500 MHz, CDCl_3 , 300 K) δ [ppm] = 2.67 (virt. td, J = 11.4, 3.2 Hz, 1H), 2.40–2.32 (m, 1H), 2.27 (ddd, J = 11.7, 10.5, 5.3 Hz, 1H), 2.08–1.80 (m, 9H), 1.80–1.63 (m, 5H), 1.52–1.43 (m, 4H), 1.28–1.17 (m, 1H). ¹³C NMR{¹H} (126 MHz, CDCl_3 , 300 K) δ [ppm] = 217.2, 128.2, 126.7, 55.8, 41.3, 39.1, 37.3, 35.5, 34.6, 30.0, 29.8, 29.3, 26.5, 23.2, 23.1. IR (ATR) $\tilde{\nu}$ [cm^{-1}] = 2919 (s), 2857 (s), 2824 (m), 1694 (vs). MS (EI, 70 eV) m/z (%) = 91 (96), 131 (40), 145 (38), 161 (29), 189 (23), 218 (100) [M]⁺. HRMS (EI, 70 eV) calcd for $\text{C}_{15}\text{H}_{22}\text{O}$ [M]⁺: 218.1665, found 218.1669. Crystals for X-ray analysis were obtained through preparing a concentrated solution of **3b** in CH_2Cl_2 and allowing the solvent to

slowly evaporate at room temperature (see SI for information on crystal measurement).

(4aS*,9aS*)-2,3-Dimethyl-1,4,4a,6,7,8,9,9a-octahydro-5H-benzo[7]annulen-5-one (3c). Following the general procedure, 110 mg cyclohept-2-en-1-one (1.00 mmol, 1.0 equiv) were converted with 2.26 mL 2,3-dimethylbuta-1,3-diene (20.0 mmol, 20 equiv). After purification by column chromatography (2.0 cm \times 20 cm, P/Et₂O = 9/1), 168 mg ketone **3c** (874 μmol , 87%) were obtained as a colorless oil. TLC R_f = 0.71 (Hex/EtOAc = 3/1) [KMnO_4]. ¹H NMR (500 MHz, CDCl_3 , 300 K) δ [ppm] = 2.66 (virt. td, J = 11.4, 3.2 Hz, 1H), 2.39–2.32 (m, 1H), 2.24 (virt. td, J = 11.4, 5.3 Hz, 1H), 2.16–2.03 (m, 1H), 2.02–1.76 (m, 5H), 1.77–1.62 (m, 2H), 1.60 (s, 6H), 1.51–1.42 (m, 2H), 1.28–1.15 (m, 1H). ¹³C NMR{¹H} (126 MHz, CDCl_3 , 300 K) δ [ppm] = 217.1, 125.9, 124.3, 55.8, 41.3, 40.4, 37.4, 35.8, 35.4, 29.3, 26.4, 18.9, 18.6. IR (ATR) $\tilde{\nu}$ [cm^{-1}] = 2911 (s), 2858 (m), 2826 (w), 1699 (vs). MS (EI, 70 eV) m/z (%) = 91 (37), 107 (53), 119 (36), 135 (23), 159 (39), 177 (28), 192 (100) [M]⁺. HRMS (EI, 70 eV) calcd for $\text{C}_{13}\text{H}_{20}\text{O}$ [M]⁺: 192.1509, found 192.1510; calcd for $\text{C}_{12}\text{H}_{18}\text{O}$ [M]⁺: 193.1542, found 193.1541.

(4aS*,9aS*)-2-/-3-Methyl-1,4,4a,6,7,8,9,9a-octahydro-5H-benzo[7]annulen-5-one (3d/3d'). Following the general procedure, 110 mg cyclohept-2-en-1-one (1.00 mmol, 1.0 equiv) were converted with 2.00 mL isoprene (20.0 mmol, 20 equiv). After purification by column chromatography (2.0 cm \times 15 cm, P/Et₂O = 9/1), 129.7 mg ketones **3d/3d'** (728 μmol , 73%, rr = 50:50) were obtained as a colorless oil. Mixture of **3d/3d'** (assignments to a specific isomer not possible): TLC R_f = 0.66 (Hex/EtOAc = 3/1) [KMnO_4]. ¹H NMR (500 MHz, CDCl_3 , 300 K) δ [ppm] = 5.40–5.33 (m, 2H), 2.71–2.59 (m, 2H), 2.40–2.15 (m, 4H), 2.15–1.58 (m, 22H), 1.54–1.41 (m, 4H), 1.31–1.17 (m, 2H). ¹³C NMR{¹H} (126 MHz, CDCl_3 , 300 K) δ [ppm] = 217.2, 216.9, 134.4, 132.8, 121.2, 119.5, 55.5, 55.1, 41.3, 41.2, 38.8, 37.1, 36.8, 35.5, 35.4, 34.2, 34.1, 29.8, 29.3, 29.2, 26.5, 26.4, 23.4, 23.2. IR (ATR) $\tilde{\nu}$ [cm^{-1}] = 2913 (s), 2858 (m), 2830 (w), 1700 (vs). MS (EI, 70 eV) m/z (%) = 93 (56), 105 (42), 145 (38), 163 (26) [$\text{C}_{11}\text{H}_{15}\text{O}$]⁺, 178 (100) [M]⁺. HRMS (EI, 70 eV) calcd for $\text{C}_{12}\text{H}_{18}\text{O}$ [M]⁺: 178.1352, found 178.1354; calcd for $\text{C}_{11}\text{H}_{18}\text{O}$ [M]⁺: 179.1386, found 179.1392.

(4aS*,9aS*)-2-/-3-(3'-Methylbut-2'-en-1'-yl)-1,4,4a,6,7,8,9,9a-octahydro-5H-benzo[7]annulen-5-one (3e/3e'). Following the general procedure, 22.0 mg cyclohept-2-en-1-one (200 μmol , 1.0 equiv) were converted with 616 μL myrcene (4.00 mmol, 20 equiv). After purification by column chromatography (1.5 cm \times 15 cm, P/Et₂O = 9/1), 45.5 mg ketone **3e/3e'** (196 μmol , 98%, rr = 50:50) were obtained as a colorless oil. Mixture of **3e/3e'** (assignments to a specific isomer not possible): TLC R_f = 0.69 (Hex/EtOAc = 3/1) [KMnO_4]. ¹H NMR (500 MHz, CDCl_3 , 300 K) δ [ppm] = 5.41–5.35 (m, 2H), 5.13–5.04 (m, 2H), 2.66 (virt. tdd, J = 11.3, 5.0, 3.2 Hz, 2H), 2.41–2.32 (m, 2H), 2.28 (virt. td, J = 11.2, 5.5 Hz, 1H), 2.21 (virt. td, J = 11.2, 5.4 Hz, 1H), 2.16–1.44 (m, 35H), 1.30–1.17 (m, 3H). ¹³C NMR{¹H} (126 MHz, CDCl_3 , 300 K) δ [ppm] = 217.2, 217.1, 138.1, 136.5, 131.8, 124.2, 120.8, 119.1, 55.5, 55.3, 41.3, 41.2, 37.5, 37.4, 37.2, 37.1, 36.9, 35.6, 35.4, 34.0, 32.7, 29.8, 29.3, 29.2, 26.5, 26.4, 25.9, 17.9 (due to overlapping signals, the number of reported signals is smaller than the number of magnetically inequivalent carbon atoms). IR (ATR) $\tilde{\nu}$ [cm^{-1}] = 2918 (s), 2857 (m), 1702 (vs). MS (EI, 70 eV) m/z (%) = 91 (99), 105 (100), 159 (73), 177 (27), 203 (78), 232 (4) [M]⁺. HRMS (EI, 70 eV) calcd for $\text{C}_{16}\text{H}_{24}\text{O}$ [M]⁺: 232.1822, found 232.1818.

(4aS*,9aS*)-Octahydro-1H-benzo[7]annulene-2,5-dione/-2,9-dione (2b/2b'). Following the general procedure, 22.0 mg cyclohept-2-en-1-one (200 μmol , 1.0 equiv) were converted with 702 μL (buta-1,3-dien-2-yloxy)trimethylsilane (4.00 mmol, 20 equiv). The reaction mixture was concentrated in vacuo and filtered through a SiO_2 plug (100 mL of P/Et₂O = 4/1 as eluent). After concentrating in vacuo, the crude product (rr = 50:50) was dissolved in THF (10 mL) and conc. HCl (aq.) (100 μL) was added. The solution was stirred for 15 min, after which H_2O (5.0 mL) and sat. aq. NaHCO_3 (2.0 mL) were added. The layers were separated and the aqueous one extracted with EtOAc (3 \times 10 mL). The combined organic layers were washed with brine (10 mL), dried over Na_2SO_4 , filtered, and concentrated in

vacuo. After purification by column chromatography (1.5 cm × 20 cm, P/Et₂O = 1/1), 15.4 mg ketone **2b** (84.4 μmol, 43%) and 15.6 mg ketone **2b'** (86.6 μmol, 43%) were obtained as colorless oils. *Head-to-tail isomer (2b)*: TLC *R_f* = 0.31 (Hex/EtOAc = 1/1) [KMnO₄]. ¹H NMR (500 MHz, CD₂Cl₂, 300 K) δ [ppm] = 2.75 (ddd, *J* = 12.5, 10.7, 4.4 Hz, 1H), 2.63 (ddd, *J* = 14.8, 12.5, 1.0 Hz, 1H), 2.58–2.49 (m, 2H), 2.42–2.33 (m, 1H), 2.29 (dddd, *J* = 14.8, 4.8, 3.1, 2.2 Hz, 1H), 2.18 (ddd, *J* = 14.8, 4.4, 2.1 Hz, 1H), 2.04 (*virt. ddt*, *J* = 13.1, 6.0, 3.4 Hz, 1H), 1.98–1.86 (m, 3H), 1.75–1.49 (m, 3H), 1.39–1.30 (m, 2H). ¹³C NMR{¹H} (126 MHz, CD₂Cl₂, 300 K) δ [ppm] = 212.3, 210.8, 54.9, 43.1, 42.0, 40.8, 39.6, 37.2, 34.5, 27.5, 24.0. IR (ATR) $\tilde{\nu}$ [cm⁻¹] = 2923 (m), 2856 (w), 1704 (vs). MS (EI, 70 eV) *m/z* (%) = 109 (63), 135 (43), 151 (100), 180 (91) [M]⁺. HRMS (EI, 70 eV) calcd for C₁₁H₁₆O₂ [M]⁺: 180.1145, found 180.1151. *Head-to-head isomer (2b')*: TLC *R_f* = 0.25 (Hex/EtOAc = 1/1) [KMnO₄]. ¹H NMR (500 MHz, CD₂Cl₂, 300 K) δ [ppm] = 2.58–2.50 (m, 2H), 2.50–2.43 (m, 1H), 2.41–2.27 (m, 3H), 2.17 (dd, *J* = 14.6, 12.8 Hz, 1H), 2.07–1.71 (m, 6H), 1.62–1.51 (m, 1H), 1.47–1.31 (m, 2H). ¹³C NMR{¹H} (126 MHz, CD₂Cl₂, 300 K) δ [ppm] = 214.6, 210.0, 55.1, 48.6, 42.8, 40.7, 40.1, 37.7, 28.5, 28.4, 25.1. IR (ATR) $\tilde{\nu}$ [cm⁻¹] = 2925 (m), 2859 (w), 1702 (vs). MS (EI, 70 eV) *m/z* (%) = 110 (43), 125 (40), 152 (11), 180 (100) [M]⁺. HRMS (EI, 70 eV) calcd for C₁₁H₁₆O₂ [M]⁺: 180.1145, found 180.1153.

(1*R**,4*S**,4*aR**,9*aR**)-(1*S**,4*R**,4*aR**,9*aR**)-1,4,4*a*,6,7,8,9,9*a*-Octahydro-5*H*-1,4-epoxybenzo[7]annulen-5-one (**4/4'**). Following the general procedure, 110.0 mg cyclohept-2-en-1-one (1.00 mmol, 1.0 equiv) were converted with 1.45 mL furan (4.00 mmol, 20 equiv). After purification of the crude product (*dr* = 65:35) by column chromatography (2.5 cm × 20 cm, P/Et₂O = 1/1), 115 mg ketone **4** (645 μmol, 64%) and 61.2 mg ketone **4'** (343 μmol, 34%) were obtained as colorless solids. *Major isomer (4)*: TLC *R_f* = 0.32 (P/Et₂O = 1/1) [KMnO₄]. mp 69.8 °C. ¹H NMR (500 MHz, C₆D₆, 300 K) δ [ppm] = 6.02 (dd, *J* = 5.8, 1.7 Hz, 1H), 5.78 (dd, *J* = 5.8, 1.7 Hz, 1H), 5.24 (s, 1H), 4.47–4.42 (m, 1H), 2.23 (ddd, *J* = 18.7, 6.2, 2.3 Hz, 1H), 2.06 (ddd, *J* = 18.7, 12.2, 2.6 Hz, 1H), 1.66 (d, *J* = 7.2 Hz, 1H), 1.58–1.47 (m, 2H), 1.38 (*virt. ddt*, *J* = 12.7, 5.1, 2.6 Hz, 1H), 1.33–1.23 (m, 1H), 1.06 (*virt. ddt*, *J* = 14.5, 12.2, 2.0 Hz, 1H), 1.00–0.83 (m, 1H), 0.46–0.34 (m, 1H). ¹³C NMR{¹H} (126 MHz, C₆D₆, 300 K) δ [ppm] = 208.8, 138.4, 131.2, 81.1, 77.0, 57.6, 43.8, 42.8, 31.0, 30.2, 23.8. IR (ATR) $\tilde{\nu}$ [cm⁻¹] = 2925 (s), 2856 (m), 1709 (vs). MS (EI, 70 eV) *m/z* (%) = 68 (100) [C₄H₄O]⁺, 81 (47), 178 (7) [M]⁺. HRMS (EI, 70 eV) calcd for C₁₁H₁₄O₂ [M]⁺: 178.0988, found 178.0989; calcd for C₁₀¹³CH₁₄O₂ [M]⁺: 179.1022, found 179.1023. *Minor isomer (4')*: TLC *R_f* = 0.39 (P/Et₂O = 1/1) [KMnO₄]. mp 88.1 °C. ¹H NMR (500 MHz, C₆D₆, 300 K) δ [ppm] = 6.48 (dd, *J* = 5.8, 1.6 Hz, 1H), 6.05 (dd, *J* = 5.8, 1.7 Hz, 1H), 4.94–4.89 (m, 1H), 4.21–4.17 (m, 1H), 2.59 (dd, *J* = 6.9, 3.6 Hz, 1H), 2.15–2.06 (m, 1H), 1.86–1.75 (m, 1H), 1.68–1.50 (m, 2H), 1.31 (*virt. qd*, *J* = 12.3, 4.2 Hz, 1H), 1.26–1.13 (m, 2H), 1.06–0.94 (m, 1H), 0.94–0.85 (m, 1H). ¹³C NMR{¹H} (126 MHz, C₆D₆, 300 K) δ [ppm] = 210.0, 137.6, 133.2, 82.5, 79.3, 58.8, 45.7, 43.1, 33.6, 30.4, 24.0. IR (ATR) $\tilde{\nu}$ [cm⁻¹] = 2924 (s), 2854 (m), 1707 (vs). MS (EI, 70 eV) *m/z* (%) = 81 (100), 178 (6) [M]⁺. HRMS (EI, 70 eV) calcd for C₁₁H₁₄O₂ [M]⁺: 178.0988, found 178.0988; calcd for C₁₀¹³CH₁₄O₂ [M]⁺: 179.1022, found 179.1025. Crystals for X-ray analysis were obtained through preparing a concentrated solution of **4'** in CH₂Cl₂ and allowing the solvent to slowly evaporate at room temperature (see SI for information on crystal measurement).

(1*R**,4*S**,4*aS**,5*R**,9*aR**)-4,4*a*,5,6,7,8,9,9*a*-Octahydro-1*H*-1,4-epoxybenzo[7]annulen-5-ol (**5**). To a solution of 35.7 mg **4** (200 μmol, 1.0 equiv) in dry MeOH (2.0 mL) was added 15.1 mg NaBH₄ (400 μmol, 2.0 equiv) and the solution stirred at rt for 2 h. A small amount of SiO₂ was added and the volatiles removed in vacuo. After purification by column chromatography (dry load, 1.5 cm × 15 cm, Hex/EtOAc = 1/4), 35.5 mg alcohol **5** (197 μmol, 98%) were obtained as a colorless oil. TLC *R_f* = 0.38 (Hex/EtOAc = 1/4) [KMnO₄]. ¹H NMR (500 MHz, C₆D₆, 300 K) δ [ppm] = 6.00 (dd, *J* = 5.9, 1.8 Hz, 1H), 5.83 (dd, *J* = 5.9, 1.6 Hz, 1H), 4.42 (d, *J* = 4.8 Hz, 1H), 4.39 (s, 1H), 4.08–4.02 (m, 1H), 2.19 (*virt. ddt*, *J* = 12.8, 5.9,

4.0 Hz, 1H), 2.06 (br s, 1H), 1.74 (ddd, *J* = 12.8, 8.1, 4.8 Hz, 1H), 1.66–1.09 (m, 7H), 0.90 (dd, *J* = 5.9, 2.6 Hz, 1H). ¹³C NMR{¹H} (126 MHz, C₆D₆, 300 K) δ [ppm] = 137.4, 131.8, 81.6, 81.1, 69.8, 48.3, 38.4, 36.2, 29.2, 27.8, 22.0. IR (ATR) $\tilde{\nu}$ [cm⁻¹] = 3430 (br m), 2988 (w), 2921 (s), 2855 (m). MS (EI, 70 eV) *m/z* (%) = 97 (100), 111 (72), 125 (42), 180 (5) [M]⁺. HRMS (EI, 70 eV) calcd for C₁₁H₁₆O₂ [M]⁺: 180.1145, found 180.1144.

(1*aR**,2*R**,2*aR**,7*aR**,8*S**,8*aS**)-Decahydro-3*H*-2,8-epoxycyclohepta[4,5]benzo[1,2-*b*]oxiren-3-one (**6**). A solution of 35.7 mg **4** (200 μmol, 1.0 equiv) in dry CH₂Cl₂ (2.0 mL) was cooled at 0 °C and 89.6 mg *meta*-chloroperoxybenzoic acid (77% w/w, 400 μmol, 2.0 equiv) were added. After stirring the mixture at rt for 24 h, CH₂Cl₂ (5.0 mL) was added, the solution washed with sat. aq. Na₂S₂O₃ (50 mL) and the aqueous layer extracted with CH₂Cl₂ (50 mL). The combined organic layers were washed with sat. aq. NaHCO₃ (50 mL), brine (20 mL), dried over MgSO₄, filtered, and concentrated in vacuo. After purification by column chromatography (1.5 cm × 15 cm, EtOAc), 33.1 mg epoxide **6** (170 μmol, 85%) were obtained as colorless crystals. TLC *R_f* = 0.47 (EtOAc) [KMnO₄]. mp 125.8 °C. ¹H NMR (500 MHz, CD₃CN, 300 K) δ [ppm] = 4.62 (s, 1H), 4.23 (d, *J* = 4.3 Hz, 1H), 3.42 (d, *J* = 3.4 Hz, 1H), 3.33 (d, *J* = 3.4 Hz, 1H), 2.65 (d, *J* = 8.1 Hz, 1H), 2.41 (ddd, *J* = 19.3, 6.1, 3.0 Hz, 1H), 2.33 (ddd, *J* = 19.3, 11.5, 3.0 Hz, 1H), 2.11–2.04 (m, 1H), 2.03–1.96 (m, 2H), 1.88–1.68 (m, 2H), 1.56–1.37 (m, 2H). ¹³C NMR{¹H} (126 MHz, CD₃CN, 300 K) δ [ppm] = 210.2, 77.4, 73.3, 58.6, 50.7, 50.0, 48.5, 42.7, 30.7, 28.8, 24.2. IR (ATR) $\tilde{\nu}$ [cm⁻¹] = 2981 (w), 2927 (m), 2861 (w), 1707 (vs). MS (EI, 70 eV) *m/z* (%) = 97 (100), 135 (61), 165 (44), 194 (6) [M]⁺. HRMS (EI, 70 eV) calcd for C₁₁H₁₄O₃ [M]⁺: 194.0937, found 194.0941. Crystals for X-ray analysis were obtained through preparing a concentrated solution of **6** in CH₂Cl₂ and allowing the solvent to slowly evaporate at room temperature (see SI for information on crystal measurement).

(1*R**,4*S**,4*aS**,9*aS**)-(1*S**,4*R**,4*aS**,9*aS**)-1,4,4*a*,6,7,8,9,9*a*-Octahydro-5*H*-1,4-methanobenzo[7]annulen-5-one (**7a/7a'**). Following the general procedure, 22.0 mg cyclohept-2-en-1-one (200 μmol, 1.0 equiv) were converted with 336 μL cyclopentadiene (4.00 mmol, 20 equiv). After purification by column chromatography (1.5 cm × 15 cm, P/Et₂O = 9/1) 32.1 mg ketones **7a/7a'** (182 μmol, 91%, *dr* = 71:29) were obtained as a colorless oil. TLC *R_f* = 0.67 (Hex/EtOAc = 3/1) [KMnO₄]. *Major isomer (7a)*: ¹H NMR (500 MHz, CDCl₃, 300 K) δ [ppm] = 6.26 (dd, *J* = 5.7, 3.1 Hz, 1H), 6.03 (dd, *J* = 5.7, 2.9 Hz, 1H), 2.96 (s, 1H), 2.78 (s, 1H), 2.50 (ddd, *J* = 19.0, 5.7, 3.0 Hz, 1H), 2.40 (dd, *J* = 11.8, 3.0 Hz, 1H), 2.15 (dd, *J* = 7.6, 1.8 Hz, 1H), 2.06–1.98 (m, 1H), 1.91 (*virt. ddt*, *J* = 13.0, 4.8, 2.7 Hz, 1H), 1.87–1.76 (m, 2H), 1.71 (*virt. ddt*, *J* = 14.5, 12.2, 2.3 Hz, 1H), 1.54–1.43 (m, 2H), 1.37–1.32 (m, 1H), 1.04 (*virt. qd*, *J* = 12.2, 4.4 Hz, 1H). ¹³C NMR{¹H} (126 MHz, CDCl₃, 300 K) δ [ppm] = 215.0, 138.4, 133.1, 58.2, 48.5, 47.8, 45.7, 43.2, 41.6, 33.6, 30.3, 24.1. *Minor isomer (7a')*: ¹H NMR (500 MHz, CDCl₃, 300 K) δ [ppm] = 6.19–6.11 (m, 2H), 3.01–2.97 (m, 1H), 2.86 (dd, *J* = 7.2, 2.7 Hz, 1H), 2.45–2.41 (m, 3H), 2.35 (dd, *J* = 11.8, 3.0 Hz, 1H), 2.29–2.18 (m, 1H), 2.15–2.06 (m, 1H), 2.05–2.00 (m, 1H), 1.88–1.80 (m, 2H), 1.58–1.39 (m, 2H), 1.35–1.29 (m, 1H). ¹³C NMR{¹H} (126 MHz, CDCl₃, 300 K) δ [ppm] = 214.0, 138.1, 134.2, 59.8, 47.0, 46.4, 46.2, 43.4, 43.3, 35.7, 30.9, 24.5. The data obtained matched those reported in the literature.⁶

(1*R**,4*S**,4*aS**,9*aS**)-(1*S**,4*R**,4*aS**,9*aS**)-1,4,4*a*,6,7,8,9,9*a*-Octahydro-5*H*-1,4-ethanobenzo[7]annulen-5-one (**7b/7b'**). Following the general procedure, 22.0 mg cyclohept-2-en-1-one (200 μmol, 1.0 equiv) were converted with 381 μL cyclohexa-1,3-diene (4.00 mmol, 20 equiv). After purification of the crude product (*dr* = 33:67) by column chromatography (1.5 cm × 15 cm, P/Et₂O = 9/1), 9.7 mg ketone **7b** (50.7 μmol, 25%) and 12.5 mg ketone **7b'** (65.4 μmol, 33%) were obtained as colorless oils. *Minor isomer (7b)*: TLC *R_f* = 0.59 (P/Et₂O = 9/1) [KMnO₄]. ¹H NMR (500 MHz, CDCl₃, 300 K) δ [ppm] = 6.32 (ddd, *J* = 8.0, 6.6, 1.3 Hz, 1H), 6.18 (ddd, *J* = 8.0, 6.3, 1.2 Hz, 1H), 2.79–2.70 (m, 1H), 2.55–2.46 (m, 1H), 2.45–2.30 (m, 2H), 2.19–2.10 (m, 1H), 2.06–1.95 (m, 1H), 1.90–1.74 (m, 3H), 1.72–1.58 (m, 1H), 1.57–1.38 (m, 2H), 1.35–1.05 (m, 4H). ¹³C NMR{¹H} (126 MHz, CDCl₃, 300 K) δ [ppm] = 214.8, 135.0, 132.5,

57.6, 43.9, 41.8, 38.6, 38.0, 30.5, 30.0, 27.9, 24.2, 18.6. IR (ATR) $\tilde{\nu}$ [cm⁻¹] = 3046 (w), 2923 (s), 2866 (m), 1702 (vs). MS (EI, 70 eV) m/z (%) = 85 (71), 97 (51), 111 (34), 141 (26), 149 (100), 167 (23), 190 (3) [M]⁺. HRMS (EI, 70 eV) calcd for C₁₃H₁₈O [M]⁺: 190.1352, found 190.1345. Major isomer (7b⁺): TLC R_f = 0.47 (P/Et₂O = 9/1) [KMnO₄]. ¹H NMR (500 MHz, CDCl₃, 300 K) δ [ppm] = 6.35–6.15 (m, 2H), 2.78–2.74 (m, 1H), 2.52–2.23 (m, 4H), 2.19–2.05 (m, 1H), 1.87–1.61 (m, 4H), 1.55–1.37 (m, 2H), 1.33–1.10 (m, 4H). ¹³C NMR{¹H} (126 MHz, CDCl₃, 300 K) δ [ppm] = 213.8, 135.2, 133.1, 57.1, 44.1, 42.4, 36.5, 35.8, 30.6, 29.9, 26.9, 24.2, 18.3. IR (ATR) $\tilde{\nu}$ [cm⁻¹] = 3042 (w), 2923 (s), 2863 (m), 1701 (vs). MS (EI, 70 eV) m/z (%) = 91 (52), 161 (7), 111 (100), 190 (11) [M]⁺. HRMS (EI, 70 eV) calcd for C₁₃H₁₈O [M]⁺: 190.1352, found 190.1348; calcd for C₁₂¹³CH₁₈O: 191.1386, found 191.1387.

(1⁺R*,4⁺S*,4a⁺R*,9a⁺S*)-/-(1⁺S*,4⁺R*,4a⁺R*,9a⁺S*)-1⁺,4⁺,4a⁺,6⁺,7⁺,8⁺,9⁺,9a⁺-Octahydro-5⁺H-spiro[cyclopropane-1,10⁺-[1,4]methanobenzo[7]annulen]-5⁺-one (7c/7c⁺). Following the general procedure, 22.0 mg cyclohept-2-en-1-one (200 μ mol, 1.0 equiv) were converted with 401 μ L spiro[2.4]hepta-4,6-diene (4.00 mmol, 20 equiv). After purification of the crude product (*dr* = 72:28) by column chromatography (1.5 cm \times 20 cm, P/Et₂O = 9/1), 31.3 mg ketones 7c/7c⁺ (155 μ mol, 77%) were obtained as colorless oil. TLC R_f = 0.30 (P/Et₂O = 9/1) [KMnO₄]. Major isomer (7c): ¹H NMR (500 MHz, CDCl₃, 300 K) δ [ppm] = 6.35 (dd, *J* = 5.8, 3.1 Hz, 1H), 6.12 (dd, *J* = 5.8, 2.1 Hz, 1H), 2.54–2.38 (m, 3H), 2.27–2.22 (m, 1H), 2.15–2.00 (m, 3H), 1.96–1.80 (m, 2H), 1.76–1.62 (m, 1H), 1.55–1.44 (m, 1H), 1.21–1.08 (m, 1H), 0.68–0.60 (m, 1H), 0.48–0.39 (m, 2H), 0.33–0.25 (m, 1H). ¹³C NMR{¹H} (126 MHz, CDCl₃, 300 K) δ [ppm] = 213.9, 138.0, 133.0, 60.0, 53.1, 46.5, 45.9, 44.9, 43.4, 33.6, 30.6, 24.3, 8.8, 5.4. Minor isomer (7c⁺): ¹H NMR (500 MHz, CDCl₃, 300 K) δ [ppm] = 6.34 (dd, *J* = 5.8, 3.1 Hz, 1H), 6.11 (dd, *J* = 5.8, 2.7 Hz, 1H), 2.59–2.37 (m, 3H), 2.28–2.21 (m, 1H), 2.16–1.99 (m, 2H), 1.95–1.79 (m, 2H), 1.77–1.63 (m, 1H), 1.55–1.41 (m, 1H), 1.25 (s, 1H), 1.22–1.07 (m, 1H), 0.68–0.59 (m, 1H), 0.48–0.39 (m, 2H), 0.33–0.24 (m, 1H). ¹³C NMR{¹H} (126 MHz, CDCl₃, 300 K) δ [ppm] = 214.1, 137.8, 134.4, 60.3, 52.5, 48.9, 48.2, 43.4, 43.1, 34.7, 31.2, 24.5, 8.5, 4.0. Mixture of 7c/7c⁺: IR (ATR) $\tilde{\nu}$ [cm⁻¹] = 3060 (w), 2924 (s), 2855 (m), 1705 (vs). MS (EI, 70 eV) m/z (%) = 91 (51), 92 (100), 105 (21), 117 (12), 130 (6), 202 (5) [M]⁺. HRMS (EI, 70 eV) calcd for C₁₄H₁₈O [M]⁺: 202.1352, found 202.1353; calcd for C₁₃¹³CH₁₈O: 203.1386, found 203.1392.

(1⁺R*,4⁺S*,4a⁺S*,9a⁺S*)-/-(1⁺S*,4⁺R*,4a⁺S*,9a⁺S*)-9a-Methyl-1,4,4a,6,7,8,9,9a-octahydro-5H-1,4-methanobenzo[7]annulen-5-one (9a/9a⁺). Following the general procedure, 24.8 mg enone 8a (200 μ mol, 1.0 equiv) were converted with 336 μ L cyclopentadiene (4.00 mmol, 20 equiv). After purification by column chromatography (1.5 cm \times 15 cm, P/Et₂O = 9/1), 33.9 mg ketones 9a/9a⁺ (178 μ mol, 89%, *dr* = 61:39) were obtained as a colorless oil. TLC R_f = 0.63 (Hex/EtOAc = 3/1) [KMnO₄]. Minor isomer (9a): ¹H NMR (500 MHz, CDCl₃, 300 K) δ [ppm] = 6.33 (dd, *J* = 5.8, 3.1 Hz, 1H), 6.10 (dd, *J* = 5.8, 3.0 Hz, 1H), 2.85 (s, 1H), 2.51 (s, 1H), 2.45 (s, 1H), 2.29–2.16 (m, 1H), 1.95–1.69 (m, 6H), 1.65–1.60 (m, 1H), 1.43–1.38 (m, 1H), 1.30–1.21 (m, 1H), 1.05 (s, 3H). ¹³C NMR{¹H} (126 MHz, CDCl₃, 300 K) δ [ppm] = 215.1, 140.2, 134.3, 60.9, 55.7, 45.2, 43.3, 42.6, 41.5, 39.5, 25.8, 24.6, 22.8. Major isomer (9a⁺): ¹H NMR (500 MHz, CDCl₃, 300 K) δ [ppm] = 6.27 (dd, *J* = 5.8, 3.0 Hz, 1H), 6.15 (dd, *J* = 5.8, 3.1 Hz, 1H), 3.31 (d, *J* = 2.3 Hz, 1H), 2.89 (s, 1H), 2.44–2.36 (m, 2H), 2.29–2.17 (m, 1H), 2.04–1.69 (m, 6H), 1.67 (d, *J* = 8.5 Hz, 1H), 1.48 (d, *J* = 8.5 Hz, 1H), 0.80 (s, 3H). ¹³C NMR{¹H} (126 MHz, CDCl₃, 300 K) δ [ppm] = 213.9, 138.2, 133.9, 62.2, 53.2, 48.4, 46.6, 45.0, 42.7, 41.1, 26.2, 25.1, 20.2. Mixture of 9a/9a⁺: IR (ATR) $\tilde{\nu}$ [cm⁻¹] = 3060 (w), 2930 (s), 2864 (m), 1704 (vs). MS (EI, 70 eV) m/z (%) = 91 (44), 105 (41), 125 (100), 171 (16), 190 (16) [M]⁺. HRMS (EI, 70 eV) calcd for C₁₃H₁₈O [M]⁺: 190.1352, found 190.1369.

(1⁺R*,4⁺S*,4a⁺S*,9a⁺S*)-/-(1⁺S*,4⁺R*,4a⁺S*,9a⁺S*)-9,9-Dimethyl-1,4,4a,6,7,8,9,9a-octahydro-5H-1,4-methanobenzo[7]annulen-5-one (9b/9b⁺). Following the general procedure, 13.8 mg enone 8b (100 μ mol, 1.0 equiv) were converted with 168 μ L cyclopentadiene

(2.00 mmol, 20 equiv). After purification by column chromatography (1.5 cm \times 15 cm, P/Et₂O = 9/1), 20.0 mg ketone 9b/9b⁺ (97.9 μ mol, 98%, *dr* = 80:20) were obtained as a colorless oil. TLC R_f = 0.60 (Hex/EtOAc = 3/1) [KMnO₄]. Major isomer (9b): ¹H NMR (500 MHz, CDCl₃, 300 K) δ [ppm] = 6.13 (dd, *J* = 5.7, 3.2 Hz, 1H), 6.03 (dd, *J* = 5.7, 2.9 Hz, 1H), 3.03–2.97 (m, 1H), 2.93–2.88 (m, 1H), 2.51–2.42 (m, 1H), 2.42–2.32 (m, 2H), 1.85–1.72 (m, 2H), 1.71–1.51 (m, 2H), 1.49–1.39 (m, 1H), 1.37–1.21 (m, 2H), 1.02 (s, 3H), 0.74 (s, 3H). ¹³C NMR{¹H} (126 MHz, CDCl₃, 300 K) δ [ppm] = 215.2, 135.9, 135.0, 53.8, 52.1, 49.7, 46.6, 45.6, 43.7, 42.0, 34.9, 31.2, 22.2, 19.8. Minor isomer (9b⁺): ¹H NMR (500 MHz, CDCl₃, 300 K) δ [ppm] = 6.21 (dd, *J* = 5.6, 2.7 Hz, 1H), 6.17 (dd, *J* = 5.6, 3.2 Hz, 1H), 3.01–2.96 (m, 2H), 2.64–2.59 (m, 1H), 2.46–2.43 (m, 1H), 2.40–2.31 (m, 1H), 2.28–2.19 (m, 1H), 1.71–1.51 (m, 1H), 1.49–1.39 (m, 1H), 1.37–1.22 (m, 4H), 1.04 (s, 3H), 0.99 (s, 3H). ¹³C NMR{¹H} (126 MHz, CDCl₃, 300 K) δ [ppm] = 214.0, 138.4, 135.4, 53.2, 52.7, 46.5, 45.9, 44.0, 42.8, 42.8, 34.5, 31.0, 29.8, 22.3. Mixture of 9b/9b⁺: IR (ATR) $\tilde{\nu}$ [cm⁻¹] = 2955 (s), 2928 (s), 2870 (m), 1702 (vs). MS (EI, 70 eV) m/z (%) = 111 (100), 139 (61), 189 (22) [M-CH₃]⁺, 204 (15) [M]⁺. HRMS (EI, 70 eV) calcd for C₁₄H₂₀O [M]⁺: 204.1509, found 204.1512.

(1⁺R*,4⁺S*,4a⁺S*,9a⁺S*)-/-(1⁺S*,4⁺R*,4a⁺S*,9a⁺S*)-6,6-Dimethyl-1,4,4a,6,7,8,9,9a-octahydro-5H-1,4-methanobenzo[7]annulen-5-one (9c/9c⁺). Following the general procedure, 13.8 mg enone 8c (100 μ mol, 1.0 equiv) were converted with 168 μ L cyclopentadiene (2.00 mmol, 20 equiv). After purification by column chromatography (1.5 cm \times 15 cm, P/Et₂O = 95/5), 17.4 mg ketone 9c/9c⁺ (85.0 μ mol, 85%, *dr* = 71:29) were obtained as a colorless oil. TLC R_f = 0.63 (Hex/EtOAc = 3/1) [KMnO₄]. Major isomer (9c): ¹H NMR (500 MHz, CDCl₃, 300 K) δ [ppm] = 6.27 (*virt. dt*, *J* = 5.3, 2.3 Hz, 1H), 6.01 (*virt. dt*, *J* = 5.3, 2.3 Hz, 1H), 2.86 (s, 1H), 2.77 (s, 1H), 2.18 (d, *J* = 7.6 Hz, 1H), 1.92–1.71 (m, 3H), 1.71–1.51 (m, 3H), 1.50–1.38 (m, 2H), 1.17 (s, 3H), 1.04 (s, 3H), 1.00–0.87 (m, 1H). ¹³C NMR{¹H} (126 MHz, CDCl₃, 300 K) δ [ppm] = 218.9, 138.8, 133.0, 55.8, 48.3, 47.7, 46.7, 45.7, 42.4, 39.2, 33.3, 29.9, 24.9, 24.9. Minor isomer (9c⁺): ¹H NMR (500 MHz, CDCl₃, 300 K) δ [ppm] = 6.22–6.18 (m, 1H), 6.17–6.12 (m, 1H), 2.99–2.90 (m, 2H), 2.43 (s, 1H), 2.00–1.79 (m, 3H), 1.64–1.51 (m, 1H), 1.50–1.38 (m, 3H), 1.28–1.17 (m, 2H), 1.07 (s, 3H), 1.04 (s, 3H). ¹³C NMR{¹H} (126 MHz, CDCl₃, 300 K) δ [ppm] = 217.9, 137.3, 134.5, 57.6, 46.9, 46.5, 46.4, 46.2, 44.3, 39.4, 34.9, 30.0, 24.8 [*n.b.*: due to overlapping signals, number of reported signals is smaller than number of carbon atoms]. Mixture of 9c/9c⁺: IR (ATR) $\tilde{\nu}$ [cm⁻¹] = 2963 (m), 2925 (s), 2859 (m), 1701 (vs). MS (EI, 70 eV) m/z (%) = 111 (98), 126 (100), 139 (61), 189 (7) [M-CH₃]⁺, 204 (66) [M]⁺. HRMS (EI, 70 eV) calcd for C₁₄H₂₀O [M]⁺: 204.1509, found 204.1508; calcd for C₁₃¹³CH₂₀O [M]⁺: 205.1542, found 205.1540.

(1⁺R*,4⁺S*,4a⁺S*,9a⁺S*)-/-(1⁺S*,4⁺R*,4a⁺S*,9a⁺S*)-6,6-Difluoro-1,4,4a,6,7,8,9,9a-octahydro-5H-1,4-methanobenzo[7]annulen-5-one (9d/9d⁺). Following the general procedure, 14.6 mg 8d (100 μ mol, 1.0 equiv) were converted with 168 μ L cyclopentadiene (2.00 mmol, 20 equiv). After purification by column chromatography (1.5 cm \times 15 cm, P/Et₂O = 95/5), 17.8 mg ketone 9d/9d⁺ (83.7 μ mol, 84%, *dr* = 72:28) were obtained as a colorless oil. TLC R_f = 0.59 (Hex/EtOAc = 3/1) [KMnO₄]. Major isomer (9d): ¹H NMR (500 MHz, CDCl₃, 300 K) δ [ppm] = 6.32 (dd, *J* = 5.8, 3.1 Hz, 1H), 6.08 (dd, *J* = 5.8, 2.9 Hz, 1H), 3.08 (s, 1H), 2.90–2.86 (m, 1H), 2.28–1.77 (m, 7H), 1.60–1.39 (m, 2H), 1.12–0.99 (m, 1H). ¹³C NMR{¹H} (126 MHz, CDCl₃, 300 K) δ [ppm] = 200.2 (dd, *J* = 27.1, 23.9 Hz), 138.5, 133.6, 116.2 (dd, *J* = 255.1, 249.4 Hz), 54.9, 48.4, 47.6, 45.4, 41.5, 33.3 (*virt. t*, *J* = 23.6 Hz), 30.8, 22.1 (dd, *J* = 7.8, 4.1 Hz). ¹⁹F NMR{¹H} (376 MHz, CDCl₃, 300 K) δ [ppm] = -97.7 (d, *J* = 286.0 Hz), -105.2 (d, *J* = 286.0 Hz). Minor isomer (9d⁺): ¹H NMR (500 MHz, CDCl₃, 300 K) δ [ppm] = 6.24–6.18 (m, 2H), 3.12–3.09 (m, 1H), 2.83 (*virt. dt*, *J* = 6.9, 2.2 Hz, 1H), 2.55–2.51 (m, 1H), 2.27–1.76 (m, 5H), 1.62–1.41 (m, 4H). ¹³C NMR{¹H} (126 MHz, CDCl₃, 300 K) δ [ppm] = 198.4 (*virt. t*, *J* = 25.4 Hz), 138.2, 133.9, 56.3, 46.6, 46.5, 45.3, 43.2, 33.5 (*virt. t*, *J* = 23.7 Hz), 32.6, 22.3 (dd, *J* = 7.7, 3.7 Hz) [*n.b.*: due to low intensity, signal of CF₂ could not be detected]. ¹⁹F NMR{¹H} (376 MHz, CDCl₃, 300 K) δ [ppm]

= -97.5 (d, $J = 287.6$ Hz), -104.4 (d, $J = 287.6$ Hz). Mixture of **9d**/**9d'**: IR (ATR) $\tilde{\nu}$ [cm^{-1}] = 2943 (m), 2871 (w), 1742 (vs). MS (EI, 70 eV) m/z (%) = 81 (100), 91 (63), 105 (26), 134 (34), 147 (18), 212 (14) [M^+]. HRMS (EI, 70 eV) calcd for $\text{C}_{12}\text{H}_{14}\text{OF}_2$ [M^+]: 212.1007, found 212.0993; calcd for $\text{C}_{11}^{13}\text{CH}_{14}\text{OF}_2$ [M^+]: 213.1041, found 213.1036.

(1*R**, 4*S**, 4*aS**, 10*aS**)-(1*S**, 4*R**, 4*aS**, 10*aS**)-4,4*a*,6,7,8,9,10,10*a*-Octahydro-1,4-methanobenzo[8]annulene-5(1*H*)-one (**9e**/**9e'**). Following the general procedure, 24.8 mg enone **8e** (200 μmol , 1.0 equiv) were converted with 336 μL cyclopentadiene (4.00 mmol, 20 equiv). After purification by column chromatography (1.5 cm \times 15 cm, P/Et₂O = 9/1), 35.8 mg ketone **9e**/**9e'** (188 μmol , 94%, $dr = 80:20$) were obtained as a colorless oil. TLC $R_f = 0.74$ (Hex/EtOAc = 3/1) [KMnO_4]. Major isomer (**9e**): ¹H NMR (500 MHz, CDCl₃, 300 K) δ [ppm] = 6.22 (dd, $J = 5.7, 3.1$ Hz, 1H), 6.07 (dd, $J = 5.7, 2.9$ Hz, 1H), 3.00 (s, 1H), 2.74 (s, 1H), 2.63–2.44 (m, 2H), 2.14–2.06 (m, 2H), 1.96–1.34 (m, 9H), 1.07–0.96 (m, 1H). ¹³C NMR{¹H} (126 MHz, CDCl₃, 300 K) δ [ppm] = 216.7, 137.8, 135.1, 55.9, 48.4, 48.2, 46.0, 45.3, 44.6, 34.9, 28.1, 27.0, 25.8. Minor isomer (**9e'**): ¹H NMR (500 MHz, CDCl₃, 300 K) δ [ppm] = 6.16–6.10 (m, 2H), 3.14 (s, 1H), 2.65 (dd, $J = 5.6, 3.2$ Hz, 1H), 2.62–2.44 (m, 3H), 2.33 (ddd, $J = 13.9, 6.6, 2.6$ Hz, 1H), 1.97–1.33 (m, 10H). ¹³C NMR{¹H} (126 MHz, CDCl₃, 300 K) δ [ppm] = 215.1, 137.0, 135.5, 57.2, 48.7, 45.9, 44.9, 43.9, 43.1, 35.9, 27.1, 26.8, 25.4. The data obtained matched those reported in the literature.¹²

(1*R**, 4*S**, 4*aS**, 11*aS**)-(1*S**, 4*R**, 4*aS**, 11*aS**)-1,4,4*a*,10,11,11*a*-Hexahydro-5*H*-1,4-methanodibenzo[*a,d*]7annulene-5-one (**9f**/**9f'**). Following the general procedure, 31.6 mg enone **8f** (200 μmol , 1.0 equiv) were converted with 336 μL cyclopentadiene (4.00 mmol, 20 equiv). After purification of the crude product ($dr = 62:38$) by column chromatography (1.5 cm \times 20 cm, P/Et₂O = 95/5), 20.8 mg ketone **9f** (92.7 μmol , 46%) and 15.3 mg ketone **9f'** (68.0 μmol , 34%) were obtained as viscous yellowish oils. Major isomer (**9f**): TLC $R_f = 0.43$ (P/Et₂O = 95/5) [UV, KMnO_4]. ¹H NMR (400 MHz, CDCl₃, 300 K) δ [ppm] = 8.13 (dd, $J = 7.8, 1.6$ Hz, 1H), 7.45 (*virt. td*, $J = 7.4, 1.6$ Hz, 1H), 7.35 (*virt. td*, $J = 7.6, 1.3$ Hz, 1H), 7.24 (dd, $J = 7.5, 1.3$ Hz, 1H), 6.40 (dd, $J = 5.7, 3.1$ Hz, 1H), 6.14 (dd, $J = 5.7, 2.9$ Hz, 1H), 3.40 (d, $J = 2.9$ Hz, 1H), 3.05–2.91 (m, 2H), 2.80 (d, $J = 3.1$ Hz, 1H), 2.19 (dd, $J = 8.2, 1.7$ Hz, 1H), 2.04–1.89 (m, 2H), 1.62–1.56 (m, 1H), 1.38–1.24 (m, 2H). ¹³C NMR{¹H} (101 MHz, CDCl₃, 300 K) δ [ppm] = 203.1, 141.6, 139.0, 136.9, 133.6, 133.0, 132.0, 129.2, 127.0, 56.4, 49.9, 45.5, 42.5, 42.0, 35.7, 27.5. Minor isomer (**9f'**): TLC $R_f = 0.32$ (P/Et₂O = 95/5) [UV, KMnO_4]. ¹H NMR (500 MHz, CDCl₃, 300 K) δ [ppm] = 7.99 (dd, $J = 7.8, 1.6$ Hz, 1H), 7.42 (*virt. td*, $J = 7.4, 1.6$ Hz, 1H), 7.31 (*virt. td*, $J = 7.2, 1.2$ Hz, 1H), 7.25–7.20 (m, 1H), 6.19–6.12 (m, 2H), 3.35 (s, 1H), 3.22 (ddd, $J = 14.5, 11.6, 8.3$ Hz, 1H), 3.04–2.91 (m, 2H), 2.53 (dd, $J = 2.8, 1.5$ Hz, 1H), 2.07 (*virt. tt*, $J = 12.4, 6.6$ Hz, 1H), 1.70–1.57 (m, 3H), 1.42–1.32 (m, 1H). ¹³C NMR{¹H} (126 MHz, CDCl₃, 300 K) δ [ppm] = 207.4, 141.2, 138.9, 137.1, 134.2, 132.9, 131.8, 129.0, 127.0, 57.1, 47.1, 44.5, 42.9, 42.7, 34.8, 28.3. The data obtained matched those reported in the literature.^{41c}

(1*R**, 4*aS**, 9*aS**)-1-Hydroxy-2,9,9-trimethyl-1,4,4*a*,6,7,8,9,9*a*-octahydro-5*H*-benzo[7]annulene-5-one (**11**). Following the general procedure, 69.1 mg enone **8b** (500 μmol , 1.0 equiv) and 3.91 g (25.0 mmol, 50 equiv) trimethyl((2-methylbuta-1,3-dien-1-yl)oxy)silane (**10**) were irradiated for 3 h. Then, the mixture was concentrated in vacuo and filtered through a SiO₂ plug (100 mL of P/Et₂O = 4/1 as eluent). After concentrating in vacuo, the crude product ($rr = 56:44$) was dissolved in THF (50 mL) and conc. HCl(aq.) (500 μL) was added. The solution was stirred for 15 min, after which H₂O (25 mL) and sat. aq. NaHCO₃ (10 mL) were added. The layers were separated and the aqueous one extracted with EtOAc (3 \times 50 mL). The combined organic layers were washed with brine (50 mL), dried over Na₂SO₄, filtered, and concentrated in vacuo. After purification by column chromatography (2.5 cm \times 20 cm, P/Et₂O = 2/1), 39.9 mg ketone **11** (179 μmol , 36%) and 31.4 mg ketone **11'** (141 μmol , 28%) were obtained as colorless oils. Major isomer (**11**): TLC $R_f = 0.38$ (P/Et₂O = 1/1) [KMnO_4]. ¹H NMR (500 MHz, CDCl₃, 300 K) δ [ppm] = 5.53–5.47 (m, 1H), 4.12 (d, $J =$

3.1 Hz, 1H), 2.67 (ddd, $J = 13.5, 10.5, 2.9$ Hz, 1H), 2.59 (*virt. td*, $J = 12.0, 5.2$ Hz, 1H), 2.34–2.26 (m, 1H), 2.20–2.10 (m, 1H), 2.10–1.91 (m, 1H), 1.85–1.75 (m, 4H), 1.68–1.41 (m, 4H), 1.17 (s, 3H), 0.96 (s, 3H). ¹³C NMR{¹H} (126 MHz, CDCl₃, 300 K) δ [ppm] = 216.5, 136.5, 122.6, 70.1, 48.1, 47.5, 47.2, 40.5, 36.5, 31.0, 30.5, 22.8, 21.6, 21.2. IR (ATR) $\tilde{\nu}$ [cm^{-1}] = 3442 (*br m*), 2933 (s), 2871 (m), 1695 (vs). MS (EI, 70 eV) m/z (%) = 134 (100), 147 (79), 161 (53), 189 (24), 204 (31), 207 (9) [$\text{M}-\text{CH}_3$]⁺, 222 (8) [M^+]. HRMS (EI, 70 eV) calcd for $\text{C}_{14}\text{H}_{22}\text{O}_2$ [M^+]: 222.1614, found 222.1595. Minor isomer (**11'**) epimerized upon acid treatment.

(1*R**, 4*aS**, 9*aS**)-1-Methoxy-2,9,9-trimethyl-1,4,4*a*,6,7,8,9,9*a*-octahydro-5*H*-benzo[7]annulene-5-one (**12**). Based on a literature procedure.⁴⁵ A mixture of 133 mg trimethylxonium tetrafluoroborate (900 μmol , 6.0 equiv) and 289 mg 1,8-bis(dimethylamino)naphthalene (1.35 mmol, 9.0 equiv) was suspended in dry CH₂Cl₂ (9.0 mL). A solution of 33.4 mg ketone **11** (150 μmol , 1.00 equiv) in dry CH₂Cl₂ (1.0 mL) was added and the mixture stirred at rt for 16 h. Then, sat. aq. NaHCO₃ (5.0 mL) and CH₂Cl₂ (10 mL) were added. The layers were separated, and the organic layer was washed with 1.0 M aq. KHSO₄ (3 \times 6.0 mL) and brine (6.0 mL), dried over MgSO₄, filtered, and concentrated in vacuo. After purification by column chromatography (1.5 cm \times 15 cm, P/Et₂O = 4/1), 28.3 mg ketone **12** (127 μmol , 85%) were obtained as a pale yellow oil. TLC $R_f = 0.26$ (P/Et₂O = 4/1) [KMnO_4]. ¹H NMR (500 MHz, CDCl₃, 300 K) δ [ppm] = 5.57–5.51 (m, 1H), 3.74 (d, $J = 2.8$ Hz, 1H), 3.45 (s, 3H), 2.84 (*virt. td*, $J = 11.8, 5.8$ Hz, 1H), 2.63 (ddd, $J = 13.4, 10.7, 3.0$ Hz, 1H), 2.29–2.16 (m, 2H), 2.00–1.88 (m, 1H), 1.86 (d, $J = 1.7$ Hz, 3H), 1.83–1.72 (m, 1H), 1.65–1.52 (m, 3H), 1.50–1.39 (m, 1H), 1.08 (s, 3H), 0.92 (s, 3H). ¹³C NMR{¹H} (126 MHz, CDCl₃, 300 K) δ [ppm] = 216.7, 135.2, 123.8, 78.9, 58.1, 48.6, 47.4, 47.1, 40.3, 36.6, 30.9, 30.8, 24.0, 22.7, 21.3. IR (ATR) $\tilde{\nu}$ [cm^{-1}] = 2926 (s), 2827 (w), 1698 (vs). MS (EI, 70 eV) m/z (%) = 98 (99), 111 (85), 119 (80), 134 (98), 147 (100), 161 (87), 189 (44), 204 (77), 221 (9) [$\text{M}-\text{CH}_3$]⁺, 236 (10) [M^+]. HRMS (EI, 70 eV) calcd for $\text{C}_{15}\text{H}_{24}\text{O}_2$ [M^+]: 236.1771, found 236.1765.

(1*R**, 4*aS**, 9*aS**)-1-Methoxy-2,9,9-trimethyl-5-methylene-1,4,4*a*,6,7,8,9,9*a*-octahydro-1*H*-benzo[7]annulene-5-one (**13**). Based on a literature procedure.¹⁶ To a solution of 70.1 mg Ph₃PCH₃Br (196 μmol , 2.0 equiv) in THF (2.5 mL) at 0 °C was added 79 μL of a 2.5 M *n*-BuLi solution in hexanes (196 μmol , 2.0 equiv). After stirring for 30 min, a solution of 23.2 mg **12** (98.2 μmol , 1.0 equiv) in THF (1.0 mL) was added and the mixture stirred at rt for 18 h. Then, H₂O (2.5 mL) was added dropwise. The layers were separated and the aqueous one extracted with EtOAc (3 \times 5.0 mL). The combined organic layers were washed with brine (5.0 mL), dried over Na₂SO₄, filtered, and concentrated in vacuo. After purification by column chromatography (1.5 cm \times 15 cm, P/Et₂O = 95/5), 19.9 mg ether **13** (84.9 μmol , 87%) were obtained as a pale yellow liquid. TLC $R_f = 0.78$ (P/Et₂O = 9/1) [KMnO_4]. ¹H NMR (500 MHz, CDCl₃, 300 K) δ [ppm] = 5.52 (d, $J = 2.2$ Hz, 1H), 4.73 (d, $J = 2.4$ Hz, 1H), 4.70 (d, $J = 2.4$ Hz, 1H), 3.70 (d, $J = 2.8$ Hz, 1H), 3.53 (s, 3H), 2.74 (*virt. td*, $J = 11.4, 5.6$ Hz, 1H), 2.25–2.16 (m, 1H), 2.05–1.95 (m, 1H), 1.95–1.88 (m, 1H), 1.85 (*virt. q*, $J = 1.8$ Hz, 3H), 1.80–1.72 (m, 1H), 1.51–1.40 (m, 2H), 1.35 (dd, $J = 11.8, 2.8$ Hz, 1H), 1.31–1.23 (m, 2H), 1.04 (s, 3H), 1.03 (s, 3H). ¹³C NMR{¹H} (126 MHz, CDCl₃, 300 K) δ [ppm] = 156.9, 134.9, 126.0, 110.6, 81.3, 58.8, 50.8, 48.5, 40.1, 37.2, 36.9, 33.2, 31.6, 28.6, 23.8, 21.6. IR (ATR) $\tilde{\nu}$ [cm^{-1}] = 2921 (vs), 2858 (m), 2823 (w), 1638 (w). MS (EI, 70 eV) m/z (%) = 83 (97), 97 (100), 111 (59), 125 (33), 234 (25) [M^+]. HRMS (EI, 70 eV) calcd for $\text{C}_{16}\text{H}_{26}\text{O}$ [M^+]: 234.1978, found 234.1978.

(4*aS**, 9*aS**)-3,5,5-Trimethyl-9-methylene-2,4*a*,5,6,7,8,9,9*a*-octahydro-1*H*-benzo[7]annulene (*trans*- α -Himachalene, **14**). Based on a literature procedure.²⁹ To liquid NH₃ (25 mL) at -78 °C were added 3.5 mg Li (500 μmol , 10 equiv), turning the solution dark blue. Then a solution of 11.7 mg **13** (50 μmol , 1.0 equiv) in dry THF (2.5 mL) was added dropwise. The cooling bath was removed and the mixture was stirred at reflux for 30 min, using a dry ice reflux condenser. Afterward, 267 mg NH₄Cl (5.00 mmol, 100 equiv) were added in small portions. NH₃ was slowly evaporated and bubbled through conc. HCl(aq.). H₂O (5.0 mL) was added to the residue and

the mixture was extracted with CH_2Cl_2 (3×5.0 mL). The combined organic layers were washed with brine (5.0 mL), dried over Na_2SO_4 , filtered, and concentrated in vacuo. After purification of the crude product ($rr = 61:39$) by column chromatography (AgNO_3 -impregnated SiO_2 , 10% w/w; 1.5 cm \times 20 cm, P/Et₂O = 199/1), 4.6 mg **14** (22.5 μmol , 54% based on 17% recovered starting material) were obtained as a pale yellow oil. TLC $R_f = 0.80$ (P) [KMnO_4]. ¹H NMR (500 MHz, CDCl_3 , 300 K) δ [ppm] = 5.31 (dd, $J = 2.3, 1.2$ Hz, 1H), 4.79 (virt. dt, $J = 2.1, 0.9$ Hz, 1H), 4.72 (virt. dt, $J = 2.1, 1.2$ Hz, 1H), 2.34–2.18 (m, 2H), 2.07–1.95 (m, 2H), 1.92–1.81 (m, 2H), 1.74–1.56 (m, 6H), 1.50–1.40 (m, 1H), 1.33–1.20 (m, 2H), 0.96 (s, 3H), 0.71 (s, 3H). ¹³C NMR{¹H} (126 MHz, CDCl_3 , 300 K) δ [ppm] = 156.3, 134.2, 123.6, 109.3, 50.5, 40.6, 40.5, 36.3, 34.7, 31.8, 30.8, 29.6, 24.0, 22.9, 20.2. The data obtained matched those reported in the literature.²⁹ *Minor regioisomer*: ¹H NMR (500 MHz, CDCl_3 , 300 K) δ [ppm] = 5.40–5.30 (m, 1H), 4.71–4.67 (m, 1H), 4.67–4.64 (m, 1H), 2.25–2.15 (m, 2H), 2.07–1.74 (m, 6H), 1.68–1.63 (m, 3H), 1.54–1.27 (m, 4H), 0.88 (s, 3H), 0.84 (s, 3H). ¹³C NMR{¹H} (126 MHz, CDCl_3 , 300 K) δ [ppm] = 157.6, 134.6, 120.9, 110.2, 46.8, 46.5, 45.3, 37.4, 36.4, 34.1, 33.1, 31.4, 28.2, 23.7, 19.6. HRMS (EI, 70 eV) calcd for $\text{C}_{15}\text{H}_{24}$ [M]⁺: 204.1873, found 204.1854.

■ ASSOCIATED CONTENT

Supporting Information

The Supporting Information is available free of charge at <https://pubs.acs.org/doi/10.1021/acs.joc.2c00186>.

Data sheets of light sources; ¹H and ¹³C{¹H} NMR spectra for all new compounds; spectroscopic and computational studies; X-ray crystallographic details (compounds **3b**, **4'**, **6**) (PDF)

FAIR data, including the primary NMR FID files, for compounds **2b**, **2b'**, **3b**, **3c**, **3d/3d'**, **3e/3e'**, **5**, **6**, **7b**, **7b'**, **7c/7c'**, **8d**, **9a/9a'**, **9b/9b'**, **9c/9c'**, **9d/9d'**, **11**, **12**, **13**, 3-hydroxy-4,4-dimethylcycloheptan-1-one (ZIP)

Cartesian coordinates of computationally optimized molecular structures (all calculated structures as part of the manuscript and the supporting information, e.g. minima in the ground and excited states but also transition states, 48 in total) (XYZ)

Accession Codes

CCDC 2130527–2130529 contain the supplementary crystallographic data for this paper. These data can be obtained free of charge via www.ccdc.cam.ac.uk/data_request/cif, or by emailing data_request@ccdc.cam.ac.uk, or by contacting The Cambridge Crystallographic Data Centre, 12 Union Road, Cambridge CB2 1EZ, UK; fax: +44 1223 336033.

■ AUTHOR INFORMATION

Corresponding Author

Thorsten Bach – School of Natural Sciences, Department of Chemistry and Catalysis Research Center (CRC), Technical University of Munich, 85747 Garching, Germany;

✉ orcid.org/0000-0002-1342-0202;

Email: thorsten.bach@ch.tum.de

Authors

Daniel P. Schwinger – School of Natural Sciences, Department of Chemistry and Catalysis Research Center (CRC), Technical University of Munich, 85747 Garching, Germany; ✉ orcid.org/0000-0002-3144-462X

Martin T. Peschel – Department Chemie, Ludwig-Maximilians-Universität München, 81377 München, Germany

Constantin Jaschke – Department Chemie, Ludwig-Maximilians-Universität München, 81377 München, Germany

Christian Jandl – School of Natural Sciences, Department of Chemistry and Catalysis Research Center (CRC), Technical University of Munich, 85747 Garching, Germany

Regina de Vivie-Riedle – Department Chemie, Ludwig-Maximilians-Universität München, 81377 München, Germany; ✉ orcid.org/0000-0002-7877-5979

Complete contact information is available at:

<https://pubs.acs.org/10.1021/acs.joc.2c00186>

Notes

The authors declare no competing financial interest.

■ ACKNOWLEDGMENTS

Financial support by the Deutsche Forschungsgemeinschaft (DFG, German Research Foundation)—TRR 325 (B1, C5)—444632635 is gratefully acknowledged. D.P.S. thanks the Studienstiftung des deutschen Volkes for a Ph.D. fellowship.

■ REFERENCES

- Reviews: (a) Kärkäs, M. D.; Porco, J. A.; Stephenson, C. R. J. Photochemical Approaches to Complex Chemotypes: Applications in Natural Product Synthesis. *Chem. Rev.* **2016**, *116*, 9683–9747. (b) Bach, T.; Hehn, J. P. Photochemical Reactions as Key Steps in Natural Product Synthesis. *Angew. Chem., Int. Ed.* **2011**, *50*, 1000–1045. (c) Hoffmann, N. Photochemical Reactions as Key Steps in Organic Synthesis. *Chem. Rev.* **2008**, *108*, 1052–1103.
- Reviews: (a) Nevesely, T.; Wienhold, M.; Molloy, J. J.; Gilmour, R. Advances in the *E* → *Z* Isomerization of Alkenes Using Small Molecule Photocatalysts. *Chem. Rev.* **2022**, *122*, 2650–2694. (b) Turque, O.; Greer, A.; Wauchope, O. R. Synthetic feasibility of oxygen-driven photoisomerizations of alkenes and polyenes. *Org. Biomol. Chem.* **2020**, *18*, 9181–9190. (c) Cameron, D.; Eisler, S. Photoswitchable double bonds: Synthetic strategies for tunability and versatility. *J. Phys. Org. Chem.* **2018**, *31*, No. e3858. (d) Arai, T.; Tokumaru, K. Photochemical one-way adiabatic isomerization of aromatic olefins. *Chem. Rev.* **1993**, *93*, 23–39.
- (a) Inoue, Y.; Yokoyama, T.; Yamasaki, N.; Tai, A. An optical yield that increases with temperature in a photochemically induced enantiomeric isomerization. *Nature* **1989**, *341*, 225–226. (b) Hoffmann, R.; Inoue, Y. Trapped Optically Active (*E*)-Cycloheptene Generated by Enantiodifferentiating *Z*–*E* Photoisomerization of Cycloheptene Sensitized by Chiral Aromatic Esters. *J. Am. Chem. Soc.* **1999**, *121*, 10702–10710. (c) Maeda, R.; Wada, T.; Mori, T.; Kono, S.; Kanomata, N.; Inoue, Y. Planar-to-Planar Chirality Transfer in the Excited State. Enantiodifferentiating Photoisomerization of Cyclooctenes Sensitized by Planar-Chiral Paracyclophane. *J. Am. Chem. Soc.* **2011**, *133*, 10379–10381.
- For related recent work and additional references on the synthesis of (*E*)-cycloalkenes, see: Singh, K.; Trinh, W.; Weaver, J. D. An elusive thermal [2 + 2] cycloaddition driven by visible light photocatalysis: tapping into strain to access C2-symmetric tricyclic rings. *Org. Biomol. Chem.* **2019**, *17*, 1854–1861.
- Recent examples: (a) Ruivo, E.; Elvas, F.; Adhikari, K.; Vangestel, C.; Van Haesendonck, G.; Lemièrre, F.; Staelens, S.; Stroobants, S.; Van der Veken, P.; Wyffels, L.; Augustyns, K. Preclinical Evaluation of a Novel ¹⁸F-Labeled dTCO-Amide Derivative for Bioorthogonal Pretargeted Positron Emission Tomography Imaging. *ACS Omega* **2020**, *5*, 4449–4456. (b) Ferreira, V. F. C.; Oliveira, B. L.; D'Onofrio, A.; Farinha, C. M.; Gano, L.; Paulo, A.; Bernardes, G. J. L.; Mendes, F. In Vivo Pretargeting Based on Cysteine-Selective Antibody Modification with IEDDA Bioorthogonal Handles for Click Chemistry. *Bioconjugate Chem.* **2021**, *32*, 121–132. (c) Liu, X.; Xiang, M.-H.; Zhou, W.-J.; Wang, F.; Chu, X.; Jiang, J.-H.

- Clicking of organelle-enriched probes for fluorogenic imaging of autophagic and endocytic fluxes. *Chem. Sci.* **2021**, *12*, 5834–5842.
- (d) Fairhall, J. M.; Camilli, J. C.; Gibson, B. H.; Hook, S.; Gamble, A. B. EGFR-targeted prodrug activation using bioorthogonal alkene-azide click-and-release chemistry. *Bioorg. Med. Chem.* **2021**, *46*, 116361.
- (6) Corey, E. J.; Tada, M.; LaMahieu, R.; Libit, L. *trans*-2-Cycloheptenone. *J. Am. Chem. Soc.* **1965**, *87*, 2051–2052.
- (7) Eaton, P. E.; Lin, K. *trans*-2-Cycloheptenone. *J. Am. Chem. Soc.* **1965**, *87*, 2052–2054.
- (8) For further references on the dimerization of (*E*)-cycloalkenones, see: (a) Vallée, M. R. J.; Inhülsen, I.; Margaretha, P. Photoannulation Reactions of 3-(Alk-1-ynyl)cyclohept-2-en-1-ones. *Helv. Chim. Acta* **2010**, *93*, 17–24. (b) Schmidt, K.; Margaretha, P. Photocyclodimers of ‘Made-to-Measure’ Seven- and Six-Membered Cyclic Enones. *Helv. Chim. Acta* **2012**, *95*, 423–427.
- (9) For an additional early contribution to the photochemical isomerization of cycloalk-2-enones, see: Lange, G. L.; Neidert, E. Photochemistry of 2,4-Cyclooctadienone I. In *Benzene and Toluene*. *Can. J. Chem.* **1973**, *51*, 2207–2214.
- (10) For a recent example, see: Kumar, S. N.; Yu, I. F.; Chein, R.-J. Oxathiaborolium: A Type of Chiral Lewis Acid Catalyst and Its Application in Catalytic and Highly Enantioselective Diels–Alder Reactions. *Org. Lett.* **2017**, *19*, 22–25.
- (11) For thermal formation of *trans*-fused Diels–Alder reaction by base-induced isomerization, see: Fringuelli, F.; Pizzo, F.; Taticchi, A.; Halls, T. D. J.; Wenkert, E. Diels–Alder Reactions of Cycloalkenones. 1. Preparation and Structure of the Adducts. *J. Org. Chem.* **1982**, *47*, 5056–5065.
- (12) Shiozaki, H.; Arai, S.; Tada, M. The Photoinduced Diels–Alder Reaction of 2-Cycloocten-1-one and 2-Cyclohepten-1-one. *Bull. Chem. Soc. Jpn.* **1976**, *49*, 821–822.
- (13) Dorr, H.; Rawal, V. H. The Intramolecular Diels–Alder Reactions of Photochemically Generated *trans*-Cycloalkenones. *J. Am. Chem. Soc.* **1999**, *121*, 10229–10230.
- (14) Nikolai, J.; Loe, Ø.; Dominiak, P. M.; Gerlitz, O. O.; Autschbach, J.; Davies, H. M. L. Mechanistic Studies of UV Assisted [4 + 2] Cycloadditions in Synthetic Efforts toward Vibsanin E. *J. Am. Chem. Soc.* **2007**, *129*, 10763–10772.
- (15) Ghosh, S.; Bose, S.; Jana, A.; Nijamudheen, A.; Datta, A. Influence of ring fusion stereochemistry on the stereochemical outcome in photo-induced Diels–Alder reaction of fused bicycloheptenone derivatives. *Tetrahedron* **2014**, *70*, 9783–9790.
- (16) Wang, R.-B.; Ma, S.-G.; Jamieson, C. S.; Gao, R.-M.; Liu, Y.-B.; Li, Y.; Wang, X.-J.; Li, Y.-H.; Houk, K. N.; Qu, J.; Yu, S.-S. Library construction of stereochemically diverse isomers of spirooliganin: their total synthesis and antiviral activity. *Chem. Sci.* **2021**, *12*, 7003–7011.
- (17) For accounts on contributions from our group to the field, see: (a) Schwinger, D. P.; Bach, T. Chiral 1,3,2-Oxazaborolidine Catalysts for Enantioselective Photochemical Reactions. *Acc. Chem. Res.* **2020**, *53*, 1933–1943. (b) Burg, F.; Bach, T. Lactam Hydrogen Bonds as Control Elements in Enantioselective Transition-Metal-Catalyzed and Photochemical Reactions. *J. Org. Chem.* **2019**, *84*, 8815–8836.
- (18) Peschel, M. T.; Kabaciński, P.; Schwinger, D. P.; Thyraug, E.; Cerullo, G.; Bach, T.; Hauer, J.; de Vivie-Riedle, R. Activation of 2-Cyclohexenone by BF₃ Coordination: Mechanistic Insights from Theory and Experiment. *Angew. Chem., Int. Ed.* **2021**, *60*, 10155–10163.
- (19) García-Expósito, E.; Bearpark, M. J.; Ortuño, R. M.; Branchadell, V.; Robb, M. A.; Wilsey, S. The T₁³(π - π^*)/S₀ Intersections and Triplet Lifetimes of Cyclic α,β -Enones. *J. Org. Chem.* **2001**, *66*, 8811–8814.
- (20) (a) Stephenson, L. M.; Hammond, G. S. Fate of the excitation energy in the quenching of fluorescence by conjugated dienes. *Pure Appl. Chem.* **1968**, *16*, 125–136. (b) Schuster, D. I.; Fabian, A. C.; Kong, N. P.; Barringer, W. C.; Curran, W. V.; Sussman, D. H. Photochemistry of unsaturated ketones in solution. XVIII. Efficiencies of quenching of short-lived excited triplet states of ketones with dienes. *J. Am. Chem. Soc.* **1968**, *90*, 5027–5028. (c) Schuster, D. I.; Dunn, D. A.; Heibel, G. E.; Brown, P. B.; Rao, J. M.; Woning, J.; Bonneau, R. Enone Photochemistry. Dynamic Properties of Triplet Excited States of Cyclic Conjugated Enones as Revealed by Transient Absorption Spectroscopy. *J. Am. Chem. Soc.* **1991**, *113*, 6245–6255.
- (21) (a) Shiozaki, T.; Györfy, W.; Celani, P.; Werner, H.-J. Communication: Extended multi-state complete active space second-order perturbation theory: Energy and nuclear gradients. *J. Chem. Phys.* **2011**, *135*, 081106. As implemented in BAGEL, see: (b) Shiozaki, T. BAGEL: Brilliantly Advanced General Electronic-structure Library. *WIRE’s Comput. Mol. Sci.* **2018**, *8*, No. e1331.
- (22) Review: Margaretha, P. Retrospective View on Recent Developments in Cyclobutane Synthesis via [2 + 2] Photocycloaddition of Unsaturated Ketones to Acyclic Dienes. *Helv. Chim. Acta* **2014**, *97*, 1027–1035.
- (23) (a) Inukai, T.; Kojima, T. Aluminum Chloride Catalyzed Diene Condensation. VI. Partial Rate Factors of 2-Phenyl-, 2-Chloro-, 2-Trifluoromethyl-, and 2-Cyanobutadienes in Reactions with Methyl Acrylate. Differential Hammett Correlation. *J. Org. Chem.* **1971**, *36*, 924–928. (b) Alston, P. V.; Ottenbrite, R. M.; Shillady, D. D. Secondary Orbital Interactions Determining Regioselectivity in the Diels–Alder Reaction. *J. Org. Chem.* **1973**, *38*, 4075–4077.
- (24) Laugraud, S.; Guingant, A.; d’Angelo, J. Synthesis of (\pm) 11-Deoxydaunomycinone and 4-Demethoxy Analogue by Sequential Diels–Alder Cycloadditions. *Tetrahedron Lett.* **1989**, *30*, 83–86.
- (25) (a) Guo, Y.; Riplinger, C.; Becker, U.; Liakos, D. G.; Minenkov, Y.; Cavallo, L.; Neese, F. Communication: An improved linear scaling perturbative triples correction for the domain based local pair-natural orbital based singles and doubles coupled cluster method [DLPNO-CCSD(T)]. *J. Chem. Phys.* **2018**, *148*, 011101. As implemented in ORCA, see: (b) Neese, F.; Wennmohs, F.; Becker, U.; Riplinger, C. The ORCA quantum chemistry program package. *J. Chem. Phys.* **2020**, *152*, 224108.
- (26) (a) Chai, J.-D.; Head-Gordon, M. Long-range corrected hybrid density functionals with damped atom-atom dispersion corrections. *Phys. Chem. Chem. Phys.* **2008**, *10*, 6615–6620. As implemented in GAUSSIAN: (b) Frisch, M. J.; Trucks, G. W.; Schlegel, H. B.; Scuseria, G. E.; Robb, M. A.; Cheeseman, J. R.; Scalmani, G.; Barone, V.; Petersson, G. A.; Nakatsuji, H.; Li, X.; Caricato, M.; Marenich, A. V.; Bloino, J.; Janesko, B. G.; Gomperts, R.; Mennucci, B.; Hratchian, H. P.; Ortiz, J. V.; Izmaylov, A. F.; Sonnenberg, J. L.; Williams-Young, D.; Ding, F.; Lipparini, F.; Ergidi, F.; Goings, J.; Peng, B.; Ehara, M.; Toyota, K.; Fukuda, R.; Hasegawa, J.; Ishida, M.; Nakajima, T.; Honda, Y.; Kitao, O.; Nakai, H.; Vreven, T.; Throssell, K.; Montgomery, J. A.; Peralta, J. E.; Ogliaro, F.; Baerpark, M. J.; Heyd, J. J.; Brothers, E. N.; Kudin, K. N.; Staroverov, V. N.; Keith, T. A.; Kobayashi, R.; Normand, J.; Raghavari, K.; Rendell, A. P.; Burant, J. C.; Iyengar, S. S.; Tomasi, J.; Cossi, M.; Milliam, J. M.; Klene, M.; Adamo, C.; Cammi, R.; Ochterski, J. W.; Martin, R. L.; Morokuma, K.; Farkas, O.; Foresman, J. B.; Fox, D. J. *Gaussian 16*, Revision A.03; Gaussian, Inc.: Wallingford, CT, 2016.
- (27) Levandowski, B. J.; Houk, K. N. Theoretical Analysis of Reactivity Patterns in Diels–Alder Reactions of Cyclopentadiene, Cyclohexadiene, and Cycloheptadiene with Symmetrical and Unsymmetrical Dienophiles. *J. Org. Chem.* **2015**, *80*, 3530–3537.
- (28) Bartelt, R. J.; Cossé, A. A.; Zilkowski, B. W.; Weisleder, D.; Momany, F. A. Male-Specific Sesquiterpenes from *Phyllotreta* and *Aphthona* Flea Beetles. *J. Chem. Ecol.* **2001**, *27*, 2397–2423.
- (29) (a) Srikrishna, A.; Kumar, R. Enantiospecific synthesis of (+)-*trans*- α -himachalene via an intramolecular type II carbonyl ene reaction. *Tetrahedron Lett.* **2004**, *45*, 6867–6870. (b) Srikrishna, A.; Kumar, P. R. Enantiospecific synthesis of (+)-*trans*- α -himachalene via an intramolecular type II carbonyl ene reaction. *Indian J. Chem.* **2008**, *47B*, 1414–1422.
- (30) Balcells, S.; Haughey, M. B.; Walker, J. C. L.; Josa-Culleré, L.; Towers, C.; Donohoe, T. J. Asymmetric Total Synthesis of (–)-(3*R*)-Inthomycin C. *Org. Lett.* **2018**, *20*, 3583–3586.
- (31) (a) Groesbeck, M.; van Galen, A. J. J.; Ippel, J. H.; Berden, J. A.; Lugtenburg, J. Three Bacteriorhodopsins with Ring-Didemethylated

6-s-Locked Chromophores and Their Properties. *Recl. Trav. Chim. Pays-Bas* **1993**, *112*, 237–246. (b) Brinker, U. H.; Lin, G.; Xu, L.; Smith, W. B.; Miesusset, J.-L. Dihalocarbene Insertion Reactions into C–H Bonds of Compounds Containing Small Rings: Mechanisms and Regio- and Stereoselectivities. *J. Org. Chem.* **2007**, *72*, 8434–8451.

(32) Balcells, S.; Haughey, M. B.; Walker, J. C. L.; Josa-Culleré, L.; Towers, C.; Donohoe, T. J. Asymmetric Total Synthesis of (–)-(3R)-Inthomycin C. *Org. Lett.* **2018**, *20*, 3583–3586.

(33) Leverenz, M.; Merten, C.; Dreuw, A.; Bach, T. Lewis Acid Catalyzed Enantioselective Photochemical Rearrangements on the Singlet Potential Energy Surface. *J. Am. Chem. Soc.* **2019**, *141*, 20053–20057.

(34) Müller, D.; Tissot, M.; Alexakis, A. New Experimental Conditions for Tandem hydroalumination/Cu-Catalyzed Asymmetric Conjugate Additions to β -Substituted Cyclic Enones. *Org. Lett.* **2011**, *13*, 3040–3043.

(35) Burton, G. W.; Daroszewski, J.; Nickerson, J. G.; Johnston, J. B.; Mogg, T. J.; Nikiforov, G. B. β -Carotene autoxidation: oxygen copolymerization, non-vitamin A products, and immunological activity. *Can. J. Chem.* **2014**, *92*, 305–316.

(36) (a) For the LiAlH_4 reduction, see ref 26b. (b) For the DMP oxidation, see: Wienhold, S.; Fritz, L.; Judt, T.; Hackl, S.; Neubauer, T.; Sauerer, B.; Bach, T. Studies towards the Synthesis of (–)-Pulvomycin: Construction of the C12–C40 Segment by a Stereoselective Aldol Reaction. *Synthesis* **2021**, *53*, 4246–4262.

(37) O'Brien, E. M.; Li, J.; Carroll, P. J.; Kozlowski, M. C. Synthesis of the Cores of Hypocrellin and Shiraichrome: Diastereoselective 1,8-Diketone Aldol Cyclization. *J. Org. Chem.* **2010**, *75*, 69–73.

(38) Economou, C.; Tomanik, M.; Herzon, S. B. Synthesis of Myrocin G, the Putative Active Form of the Myrocin Antitumor Antibiotics. *J. Am. Chem. Soc.* **2018**, *140*, 16058–16061.

(39) Bartelt, R. J.; Weisleder, D.; Momany, F. A. Total Synthesis of Himachalene Sesquiterpenes of *Aphthona* and *Phyllotreta* Flea Beetles. *Synthesis* **2003**, 117–123.

(40) Tanemura, K.; Suzuki, T.; Nishida, Y.; Satsumabayashi, K.; Horaguchi, T. A mild and efficient procedure for α -bromination of ketones using *N*-bromosuccinimide catalysed by ammonium acetate. *Chem. Commun.* **2004**, 470–471.

(41) (a) Roosen, P. C.; Vanderwal, C. D. Investigations into an Anionic Oxy-Cope/Transannular Conjugate Addition Approach to 7,20-Diisocyanoadociane. *Org. Lett.* **2014**, *16*, 4368–4371. (b) Paquette, L. A.; Stepanian, M.; Mallavadhani, U. V.; Cutarelli, T. D.; Lowinger, T. B.; Klemeyer, H. J. Definition of Several Control Elements Relevant to the Stereodefined Serial Elaboration of Belted Poly(spirotetrahydrofurans) Fitted with a Cyclohexane Core. *J. Org. Chem.* **1996**, *61*, 7492–7507. (c) Ghosh, S.; Saha Roy, S.; Saha, G. An expeditious route to trans fused 5–7–6 and 6–7–6 carbocycles through photoisomerisation-cycloaddition of benzocycloheptenone. *Tetrahedron* **1988**, *44*, 6235–6240.

(42) Moriyama, K.; Hamada, T.; Nakamura, Y.; Togo, H. Catalytic dehydrogenative dual functionalization of ethers: dealkylation–oxidation–bromination accompanied by C–O bond cleavage via aerobic oxidation of bromide. *Chem. Commun.* **2017**, *53*, 6565–6568.

(43) Kuga, T.; Sasano, Y.; Iwabuchi, Y. IBX as a catalyst for dehydration of hydroperoxides: green entry to α,β -unsaturated ketones via oxygenative allylic transposition. *Chem. Commun.* **2018**, *54*, 798–801.

(44) Beltran, F.; Bergamaschi, E.; Funes-Ardoiz, I.; Teskey, C. J. Photocontrolled Cobalt Catalysis for Selective Hydroboration of α,β -Unsaturated Ketones. *Angew. Chem., Int. Ed.* **2020**, *132*, 21362–21368.

(45) Poock, C.; Kalesse, M. Total Synthesis of Nannocystin Ax. *Org. Lett.* **2017**, *19*, 4536–4539.

Recommended by ACS

Expanding the Chiral Monoterpene Pool: Enantioselective Diels–Alder Reactions of α -Acylxy Enones

Skyler D. Mendoza, Sarah E. Reisman, *et al.*

MAY 20, 2022
ORGANIC LETTERS

READ 

A New Organocatalytic Desymmetrization Reaction Enables the Enantioselective Total Synthesis of Madangamine E

Shinya Shiomi, Darren J. Dixon, *et al.*

JANUARY 17, 2022
JOURNAL OF THE AMERICAN CHEMICAL SOCIETY

READ 

Quaternary Ammonium Ion-Tethered (Ambient-Temperature) HDDA Reactions

Chenlong Zhu and Thomas R. Hoye

APRIL 20, 2022
JOURNAL OF THE AMERICAN CHEMICAL SOCIETY

READ 

Photochemical Dearomative Cycloadditions of Quinolines and Alkenes: Scope and Mechanism Studies

Renyu Guo, M. Kevin Brown, *et al.*

SEPTEMBER 15, 2022
JOURNAL OF THE AMERICAN CHEMICAL SOCIETY

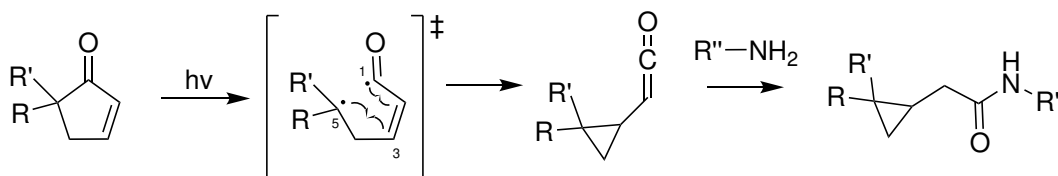
READ 

Get More Suggestions >

3.2. α -Cleavage and Ring Contraction of 5,5-Dialkylcyclopent-2-enones

The Z/E isomerization described in section 3.1 can not occur in cyclopentenones due to the restrictions imposed by the 5-membered ring. Due to these steric constraints, which counteract a torsion of the H-C=C-H dihedral, the $^3\pi\pi^*$ minimum that plays a crucial role in the Z/E isomerization (and the [2+2] cycloaddition) is much higher in energy. Consequently, it is closer in energy to the minima of the other states, $^1n\pi^*$ and $^3n\pi^*$. Thus, after the excitation of cyclopentenones to $^1n\pi^*$, processes originating from all of these states can be observed depending on the substitution pattern and the reaction conditions.

As a part of this thesis, the cleavage of the α -C-C-bond (1,5-C-C bond), a process that proceeds via the $n\pi^*$ states, was investigated. This process requires the $n\sigma^*$ states to cross the $n\pi^*$ states (in the singlets or the triplets). For these crossings to happen at low energies, the biradicaloid structure associated with these crossings must be stabilized. In practice, this can be achieved by a 5,5-dialkyl substitution, which stabilizes the radical in position 5 via hyperconjugation. This biradical can close the ring with position 3, forming a 2,2-dialkylcyclopropyl ketene (see scheme 5). If the initial α -cleavage occurs in the triplet state, ring closure can also occur directly in the triplet, leading to an excited ketene. In this case, ISC returns the ketene to the ground state at a crossing point close to its triplet minimum.[183] The ketene derivatives that result from the rearrangement can not be purified under ambient conditions; thus, a nucleophile is added in excess to trap the ketene *in situ*. Primary amines are suitable for this role (see scheme 5).



Scheme 5: Mechanism of α -cleavage and ring contraction in 5,5-dialkylcyclopent-2-enones. The ketene is subsequently captured by addition to a primary amine.

We used XMS-CASPT2(8,7)/cc-pvtz calculations at critical points along the reaction path to follow this photochemical rearrangement and explain experimental observations related to adding triplet sensitizers and triplet quenchers.

The article “Photochemical Ring Contraction of 5,5-Dialkylcyclopent-2-enones and *in situ* Trapping by Primary Amines” was published in *Journal of Organic Chemistry*. The following points briefly summarize the article.

- 5,5-Dialkylcyclopent-2-enones undergo a photochemical rearrangement to ketenes. [37, 152] These ketenes can be trapped by primary amines, yielding 2,2-disubstituted cyclopropaneacetic amides.
- The reaction proceeded optimally by irradiation at 300 nm with an excess of trapping agent. The scope of the reaction was explored. 24 Examples are reported with yields ranging from 49 to 91%.

- The reaction slowed down upon adding a triplet quencher but could not be completely suppressed even when a large excess was added. The reaction could be performed by irradiating at 366 nm and adding benzophenone as a triplet sensitizer. This suggests that the rearrangement might be possible on either the singlet or the triplet hypersurface.
- XMS-CASPT2 calculations showed that the crossing points of the states of $n\pi^*$ character with the S_0 that are associated with α -cleavage are sufficiently low lying in both the singlets and the triplets. The barrier is slightly lower in the triplets.
- In cyclopent-2-enones, the ${}^3n\pi^*$ and ${}^3\pi\pi^*$ were found to be similar in energy. Thus, in the triplet states, α -cleavage in ${}^3n\pi^*$ likely competes with relaxation via the $T_1(\pi\pi^*)S_0$ minimum energy crossing point (H–C=C–H torsion pathway).
- Comparison to unsubstituted cyclopent-2-enone illustrates the importance of the 5,5-dialkyl substitution. The ring-opened structures were calculated to be stabilized by approximately 25 kJ/mol through 5,5-dialkyl substitution. By lowering this barrier, α -cleavage in the $n\pi^*$ states can compete with relaxation via the ${}^3\pi\pi^*$ state. A larger SOC was found at the crossing points of the ring opening pathway compared to the H–C=C–H torsion pathway.
- In conclusion, without additives, ring opening proceeds via the singlets and the triplets. When a triplet quencher is added, the faster path via the triplets is suppressed, reducing the reaction rate. When a triplet sensitizer is added, population is directly transferred into the triplet states. Likely, the reaction then proceeds via the triplets only.

Hereafter, The article “Photochemical Ring Contraction of 5,5-Dialkylcyclopent-2-enones and *in situ* Trapping by Primary Amines” published in *Journal of Organic Chemistry* is reproduced. Copyright 2022 American Chemical Society. The supporting information is available online.

Photochemical Ring Contraction of 5,5-Dialkylcyclopent-2-enones and *in situ* Trapping by Primary Amines

Noah Jeremias, Martin T. Peschel, Constantin Jaschke, Regina de Vivie-Riedle, and Thorsten Bach*

Cite This: <https://doi.org/10.1021/acs.joc.2c01156>

Read Online

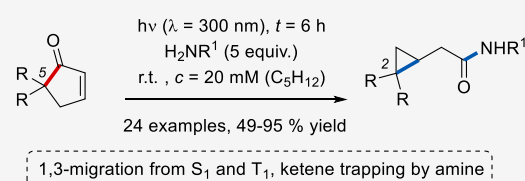
ACCESS |

Metrics & More

Article Recommendations

Supporting Information

ABSTRACT: If substituted in the 5,5-position, cyclopent-2-enones undergo a smooth photochemical rearrangement to ketenes. A concomitant cyclopropane formation occurs due to a 1,3-shift of the C5 carbon atom from the carbonyl carbon atom (C1) to carbon atom C3. In this study, the cyclopropyl-substituted ketene intermediates were trapped *in situ* by primary amines providing an efficient entry into 2,2-disubstituted cyclopropaneacetic amides (24 examples, 49–95% yield). A remarkable feature of the reaction is the fact that the photochemical rearrangement can occur from either the first excited singlet (S_1) or the respective triplet state (T_1). In line with experimental results (triplet quenching, sensitization), XMS-CASPT2 calculations support the existence of efficient reaction pathways to the intermediate ketene both on the singlet and on the triplet hypersurface.

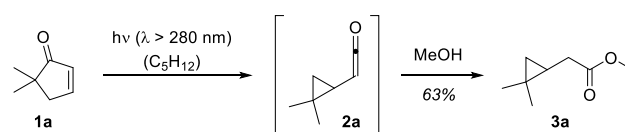


INTRODUCTION

The photochemistry of cyclic enones has been associated for decades mainly with their use in [2 + 2] photocycloaddition reactions.¹ In particular, cyclopent-2-enones and cyclohex-2-enones represent ideal substrates for this transformation.² They can be directly excited at relatively long wavelengths ($\lambda = 300\text{--}350\text{ nm}$), and their reactive triplet states are populated rapidly by an efficient intersystem crossing (ISC).^{3,4} For most enones, conformational relaxation leads to the lowest lying triplet state T_1 that is located at the double bond and is $\pi\pi^*$ in character.⁵ The conformational restriction of the carbocyclic skeleton prohibits *Z/E* isomerization^{6,7} and the long-lived triplet state is efficiently trapped by olefins in an inter- or intramolecular addition reaction. An initial C–C bond formation is followed by ISC and subsequent cyclobutane formation.^{1,8} There are literally thousands of [2 + 2] photocycloaddition reactions known today, and the number of their applications in total synthesis⁹ continues to grow. Against this background, other reaction pathways which are accessible to photochemically excited enones have received less attention, despite the fact that they lead to unique product skeletons. In the context of our work on enantioselective photochemical reactions,¹⁰ more specifically on the activation of chromophores by chiral Lewis acids,¹¹ we have studied cyclic enones in greater detail. In this context, we have developed enantioselective [2 + 2] photocycloaddition reaction of enones¹² and we have also revisited some of the less frequently studied reaction classes, such as the *E/Z*-isomerization, the [6 π] photocyclization, and the oxadi- π -methane rearrangement.^{7,13} In particular, the latter reaction demonstrated that minor changes in the structure of a given enone can lead to different reaction pathways involving C–C bond fission. Along these lines, another remarkable reaction was first described in 1969 by Agosta, Kende, and co-

workers.¹⁴ They found that 5,5-dialkylsubstituted cyclopent-2-enones,¹⁵ such as 5,5-dimethylcyclopent-2-enone (**1a**), underwent a rapid rearrangement upon irradiation with a mercury lamp through a pyrex filter ($\lambda > 280\text{ nm}$). 1,3-Migration leads to a ketene **2a** as intermediate which could be characterized by IR spectroscopy and which was trapped by methanol as methyl ester **3a** (Scheme 1).

Scheme 1. Previous Report¹⁴ on the Photochemical Ring Contraction of 5,5-Dimethylcyclopent-2-enone (**1a**) and Trapping of Ketene Intermediate **2a** by Methanol



The volatility of methyl ester **3a** rendered its isolation difficult, and the yield of 63% was determined by calibrated vapor phase chromatography (vpc). To the best of our knowledge,¹⁶ the reaction has not been further studied thereafter¹⁶ and, apart from methyl ester **3a**, consecutive products of the rearrangement have not been reported. We now revisited the reaction and attempted to trap the photochemically generated ketene intermediates with primary amines. The reaction enables a straightforward synthesis of 2,2-

Special Issue: Progress in Photocatalysis for Organic Chemistry

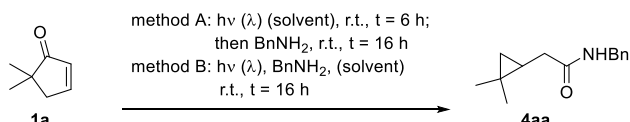
Received: May 18, 2022

disubstituted cyclopropaneacetic amides. In addition, mechanistic observations were made which triggered calculations at the XMS-CASPT2(8,7)/cc-pvtz level of theory. The results of our combined synthetic and theoretic study are summarized in this report.

RESULTS AND DISCUSSION

Preliminary experiments were performed with enone **1a** and *N*-benzylamine as the trapping reagent. After 6 h of irradiation, the amine was added and the mixture was stirred for 16 h (Table 1, method A). At an irradiation wavelength of $\lambda = 300$

Table 1. Optimization of Reaction Conditions for the Cascade Reaction of Photochemical Ring Contraction and *N*-Benzylamine Addition Leading to Amide **4aa**



| entry | method ^a | λ (nm) ^b | solvent | yield ^c (%) |
|-----------------|---------------------|-----------------------------|---------------------------------|------------------------|
| 1 | A | 254 | C ₅ H ₁₂ | — ^d |
| 2 | A | 300 | C ₅ H ₁₂ | 58 |
| 3 | A | 366 | C ₅ H ₁₂ | — ^d |
| 4 | A | 300 | CH ₂ Cl ₂ | — ^d |
| 5 | A | 300 | C ₆ H ₁₄ | 51 |
| 6 | A | 300 | PhH | 41 |
| 7 | A | 300 | PhCH ₃ | 34 |
| 8 | A | 300 | PhCF ₃ | 35 |
| 9 ^e | A | 300 | C ₅ H ₁₂ | 49 |
| 10 ^f | A | 300 | C ₅ H ₁₂ | 55 |
| 11 ^g | A | 300 | C ₅ H ₁₂ | 38 |
| 12 ^h | A | 300 | C ₅ H ₁₂ | 22 |
| 13 | B | 300 | C ₅ H ₁₂ | 68 |
| 14 ^e | B | 300 | C ₅ H ₁₂ | 91 |

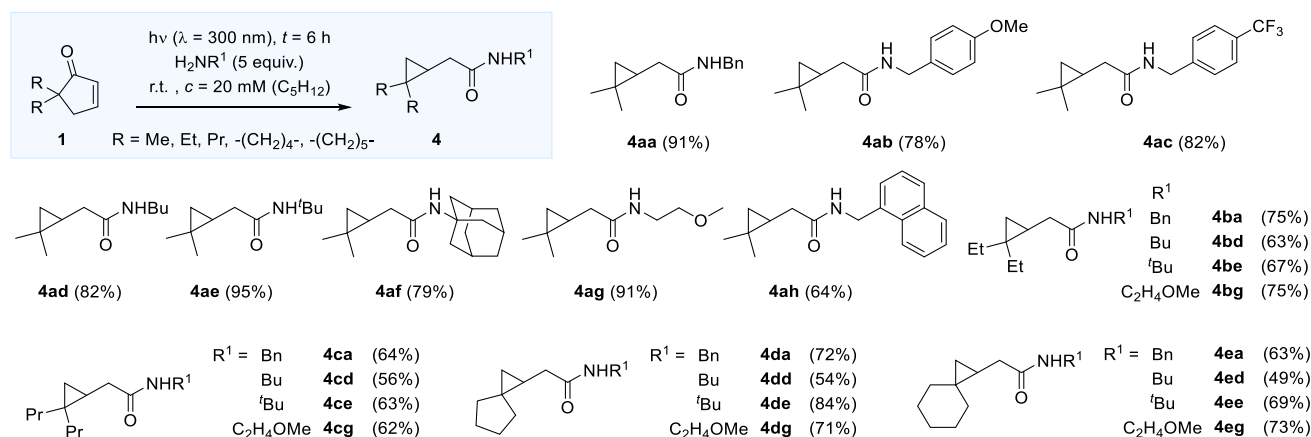
^aUnless otherwise noted, 23 equiv of the amine were added. Reactions were performed under argon at a concentration of $c = 20$ mM. ^bThe emission maximum of the respective light source is provided (for details see the Supporting Information). Irradiation experiments at $\lambda = 254$ nm and $\lambda = 300$ nm were performed in quartz equipment. ^cYield of isolated product. ^dNo conversion of the starting material was observed. ^eFive equivalents of BnNH₂ were used. ^f25 Equivalents of BnNH₂ were added in THF solution. ^gThe reaction was performed at 0 °C. ^hThe reaction was performed at -20 °C.

nm, product formation was indicated in pentane as the solvent while the use of shorter ($\lambda = 254$ nm) and longer wavelength ($\lambda = 366$ nm) did not lead to any conversion (entries 1–3). At $\lambda = 300$ nm, product **4aa** was isolated in 58% yield (entry 2). Other solvents like dichloromethane, hexane, benzene, toluene, or trifluorotoluene showed inferior results (entries 4–8). The amount of excess amine and its solvent had little influence on the efficiency of the reaction (entries 9–10), and a decrease in the reaction temperature led to a decrease in yield (entries 11–12). The key discovery that eventually paved the way to a high yielding, reproducible procedure was the unexpected finding that the amine and the enone do not interfere with the irradiation conditions. Typically, amines get oxidized by photoexcited carbonyl compounds¹⁷ but this side reaction was not observed with enone **1a** and *N*-benzylamine (entry 13). Instead, the desired transformation proceeded smoothly upon irradiation of a mixture of the enone and the amine in pentane for 16 h ($\lambda = 300$ nm). The best yield (91%, entry 14) was obtained when five equivalents of amine were used as the trapping reagent.

Under optimized conditions, five different cycloprop-2-enones and various primary amines were studied in the photocatalytic ketene formation (Scheme 2). All reactions were performed on a scale of 0.2 mmol, but it was shown for product **4aa** that the reactions can be easily performed also on larger scale (1.0 mmol, 86% yield). Apart from benzylamine (product **4aa**), substituted benzylamines (products **4ab**, **4ac**) and alkylamines (products **4ad**, **4ae**, **4af**) reacted smoothly with enone **1a**. Steric bulk within the alkyl group was found to be not prohibitive for the reaction. Alkoxyethylamine (product **4ag**) and a naphthyl-substituted amine (product **4ah**) reacted equally well. In general, any primary amine is expected to react provided its solubility allows for a conversion in pentane as the solvent.

Additional 5,5-dialkylsubstituted cycloprop-2-enones **1b–1e** were obtained from 2,2-dialkylacetic acids by allylation followed by a SnCl₄-catalyzed cyclization.¹⁸ Substrates **1d** and **1e** are literature-known compounds.¹⁹ Their reactivity was similar to the 5,5-dimethylsubstituted enone **1a**, but it should be noted that both the 5,5-diethyl- and the 5,5-dipropyl-derivative display hydrogen atoms which are susceptible to intramolecular hydrogen abstraction. Remarkably, the rearrangement remained the preferred reaction pathway and yields for products **4ba**, **4bd**, **4be**, and **4bg** and **4ca**, **4cd**, **4ce**, and

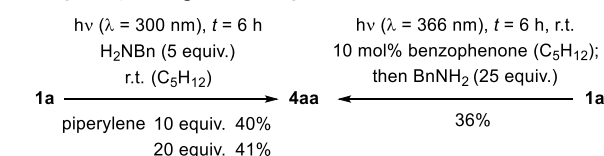
Scheme 2. Scope for the Formation of Amides **4** from Various Enones **1** and Primary Amines



4cg were uniformly well above 50%. Similarly, the spirocyclic enones **1d** and **1e** reacted cleanly and delivered the respective amides **4da**, **4dd**, **4de**, **4dg** and **4ea**, **4ed**, **4ee**, and **4eg** in yields of 49–84%. Secondary amines are not competent to add cleanly to the intermediary ketenes and no cyclopropane products could be isolated following either method A or B (cf. Table 1). In detail, dimethylamine, *N*-benzylmethylamine, *N*-benzylhydroxylamine, and *N,O*-dimethylhydroxylamine were employed as potential nucleophiles. With the three latter amines, there was conversion but the product mixture was complex and there was no indication for the formation of the desired amide.

Mechanistically, previous observations on the reaction course were corroborated.¹⁴ The reaction slowed down when the triplet quencher piperylene was added (Scheme 3).

Scheme 3. Mechanistic Experiments Addressing the Multiplicity (Singlet or Triplet) of the Excited State



However, a residual reactivity remained and even a large excess of piperylene (20 equiv) did not lead to a further decrease of the reaction rate. At an irradiation wavelength of $\lambda = 366$ nm, which had turned out to be unsuitable for a reaction according to method A (Table 1, entry 3), benzophenone addition led to ketene formation as evidenced by the isolation of amide **4aa**. Since benzophenone is a well-established triplet sensitizer,²⁰ the latter result suggests the intermediacy of a triplet enone.

To explain the dichotomy of the mechanistic results depicted in Scheme 3, we started by reviewing recent calculations by Cao and Xie²¹ on the internal conversion and ISC in α,β -unsaturated enones, most notably in cyclopent-2-enone, which is related to enone **1a**. Excitation at $\lambda = 300$ nm leads to population of the S_1 state which is of $n\pi^*$ character. The authors then noted that there was a trajectory for ketene formation on the singlet hypersurface via a thermally accessible transition state in the S_1 . They also found crossing points for the S_1 , T_1 , and T_2 states prior to the transition state for the rearrangement. Although most of the cyclopent-2-enone molecules relax to T_1 , it is reasonable to assume that 5,5-dimethylsubstitution favors the former reaction pathway and facilitates a rearrangement in the S_1 . Our own calculations on the topic considered both 5,5-dimethylcyclopent-2-enone (**1a**) and the unsubstituted cyclopent-2-enone for comparison. They were performed at the XMS-CASPT2(8,7)/cc-pvtz level of theory,²² including all π and π^* orbitals, the oxygen n orbital, and the σ and σ^* orbitals of the C1–C5 bond in the active space. Optimized critical points in the excited states of 5,5-dimethylcyclopent-2-enone (**1a**) and along the rearrangement pathway leading to ketene **2a** are shown in Figure 1.

Plausible reaction pathways of both singlet and triplet multiplicity were discovered. In the singlet manifold, after excitation to the $S_1(n\pi^*)$ state, the molecule relaxes toward S_1 min (Figure 1, central panel), which is associated with a slight increase in the C1–O bond length. From S_1 min, a S_1S_0 conical intersection associated with α -cleavage of the C1–C5 bond can be reached (Figure 1, left panel). After α -cleavage, some small conformational changes and closure of the C1–C3 bond lead to ketene **2a**. Figure 2 compares unsubstituted cyclopent-2-enone and enone **1a**. In contrast to cyclopent-2-enone,²¹ the cleavage pathway is strongly favored for **1a** due to a stabilization of the α -cleavage S_1S_0 CoIn, which is mainly

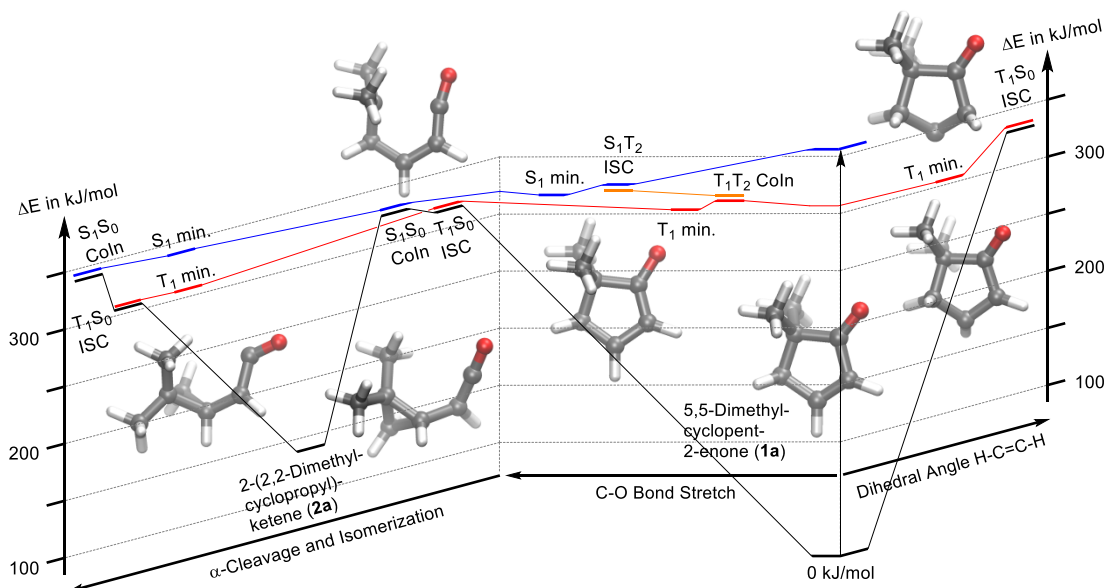


Figure 1. Critical points in the S_0 (black), S_1 (blue), T_1 (red), and T_2 (orange) states along the photoisomerization pathways of 5,5-dimethylcyclopent-2-enone (**1a**) optimized using XMS-CAPT2(8,7)/cc-pvtz. The figure depicts the three most relevant reaction coordinates for the photorelaxation processes. Starting from a vertical excitation at the ground state minimum of enone **1a**, the relaxation path into the $n\pi^*$ minima of S_1 and T_1 is shown along the C–O bond stretching (central panel). On the right panel, the path to the T_1 $\pi\pi^*$ minimum and the S_0T_1 ISC is shown along the torsional motion of the H–C=C–H dihedral. Finally, the coordinate on the left depicts the isomerization to ketene **2a**. This coordinate combines the α -cleavage of the C1–C5 bond, pyramidalization at the C3 position, ring closure, and bending of the C2=C1=O angle.

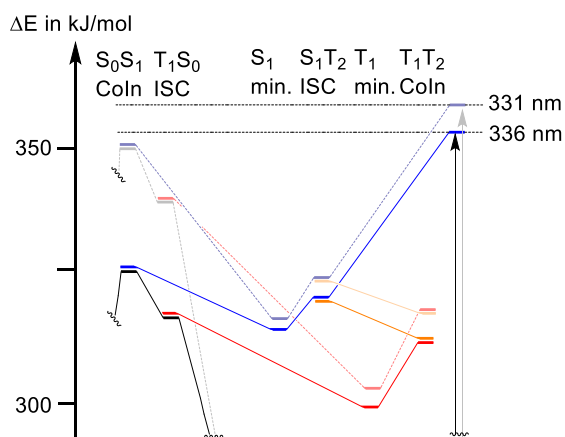


Figure 2. Comparison of critical points in the S_0 (black), S_1 (blue), T_1 (red), and T_2 (orange) states between 5,5-dimethylcyclopent-2-enone (**1a**) (saturated colors) and cyclopent-2-enone without the 5,5-dimethyl substitution (desaturated colors). All points in the Franck–Condon region (S_1 min, S_1T_2 ISC, T_1 min, and T_1T_2 CoIn) are stabilized by roughly the same amount due to the 5,5-dimethyl substitution. The points associated with the α -cleavage (S_0S_1 CoIn, T_1S_0 ISC) are stabilized significantly more in the 5,5-dimethyl derivative, which in turn makes this pathway more easily accessible for **1a**.

caused by hyperconjugation of the 1,5 singlet biradical and the methyl groups.

The same stabilization applies to an analogous 1,5 triplet biradical. Thus, an additional pathway on the triplet hypersurface can be invoked and was identified. Starting in the Franck–Condon region of the $S_1(n\pi^*)$ state, a slight elongation of the C1–O bond leads to an intersection with the $T_2(\pi\pi^*)$ (S_1T_2 ISC, Figure 1, central panel). Here, efficient ISC can take place, as has been observed in nonadiabatic molecular dynamics simulations on cyclopent-2-enone²¹ and cyclohex-2-enone.⁵ From T_2 , the T_1T_2 CoIn can be reached leading to an increase in the H–C=C–H dihedral and to a $T_1(\pi\pi^*)$ minimum from where the T_1S_0 ISC is accessible (Figure 1, right panel). This CoIn is the main relaxation pathway of unsubstituted cyclopent-2-enone⁴ and does not lead to ketene formation. In enone **1a**, however, another pathway is favored. From the T_1T_2 CoIn, a minimum of $n\pi^*$ character can be reached (Figure 1, central panel), whose energy is similar to the $T_1(\pi\pi^*)$ minimum. From there, a T_1S_0 crossing facilitates α -cleavage (Figure 1, left panel), which lies 13.1 kJ/mol lower in energy than the H–C=C–H torsion T_1S_0 ISC. After α -cleavage, closure of the C1–C3 bond leads to the formation of ketene **2a**. It is also possible to perform the isomerization to the ketene entirely in the T_1 and cross back into S_0 at a T_1S_0 ISC with a bent C=C=O angle, which is well-known from calculations of unsubstituted ketene.²³ An additional factor in the preference for the α -cleavage toward **2a** over the unproductive H–C=C–H torsion pathway can also be found in the spin–orbit couplings between T_1 and S_0 at the respective ISCs. While the coupling at the H–C=C–H torsion T_1S_0 ISC is calculated to be small (2.7 cm^{-1}), the coupling at the α -cleavage T_1S_0 ISC is much larger (20.3 cm^{-1}). Thus, we propose the following mechanism that explains the experimental observations summarized in Scheme 3: (1) Without triplet quencher or triplet sensitizer, both the singlet and the triplet pathway are active. When the triplet quencher is added, energy transfer from **1a** in state T_1 to the

quencher opens up an additional unproductive relaxation channel and thus decreases the yield. The pathway via the singlets stays unaffected. (2) When a triplet sensitizer is added, it becomes possible to perform the reaction at a lower excitation energy ($\lambda = 366 \text{ nm}$). The triplet state energy of benzophenone has been reported as $E_T = 287 \text{ kJ mol}^{-1}$ (77 K, isopentane/methylcyclohexane = 1/5).²⁴ As can be seen from Figure 2, a (slightly endergonic) triplet energy transfer to **1a** is feasible. Thus, after the T_1 is populated by energy transfer from benzophenone, the isomerization still occurs, most likely only via the triplets.

Two additional experimental observations deserve to be mentioned. Although Lewis acids, such as BF_3 , led to a bathochromic absorption shift of the bright $\pi\pi^*$ transition, there was no indication for a successful catalysis with various Lewis acids under a diverse set of conditions (see the Supporting Information for details). Employing method A, the reaction **1a** \rightarrow **4aa** was either not observed or only decomposition products were detected. The second observation relates to a potential interaction of the primary amine with the enone. Although the UV/vis spectrum of compound **1a** remained virtually unchanged in the long wavelength regime ($\lambda > 280 \text{ nm}$) upon successive addition of *N*-butylamine, irradiation at $\lambda = 366 \text{ nm}$ led under the conditions of method B to a rapid reaction. Product **4ad** was isolated in 77% yield. As already mentioned (Table 1, entry 3), the substrate itself is not reactive at this wavelength. There is precedence for amines enabling reactions at longer wavelength despite no clearly detectable absorption change.²⁵ Possible implications for the current reaction warrant further studies.

CONCLUSION

In summary, a synthetic route to 2,2-disubstituted cyclopropaneacetic amides has been developed starting from 5,5-disubstituted cyclopent-2-enone and primary amines. The reaction is favorably performed at $\lambda = 300 \text{ nm}$ under direct irradiation conditions, but a sensitization with benzophenone at $\lambda = 366 \text{ nm}$ is possible. The reaction includes a photochemical rearrangement to a ketene intermediate which is trapped by addition of the amine. On the basis of XMS-CASPT2 calculations, the yet unresolved photochemistry of 5,5-disubstituted cyclopent-2-enones can be understood. Reaction pathways leading from both S_1 and T_1 to the ketene intermediate were identified, and the reaction is feasible on both the singlet and the triplet hypersurface.

EXPERIMENTAL SECTION

General Methods. All air- or moisture-sensitive reactions were carried out in heat gun-dried glassware under an argon atmosphere using standard Schlenk techniques. Photochemical experiments were carried out in heat gun-dried Duran (366 nm) or quartz tubes (254 and 300 nm) in a positive geometry setup (cylindrical array of 16 fluorescent light tubes, see the Supporting Information for datasheets) with the sample placed in the center of the illumination chamber.¹² Photochemical experiments with an LED as the light source were carried out in a Schlenk tube (diameter = 1 cm) with a polished quartz rod as an optical fiber, which was roughened by sandblasting at one end.²⁶ The roughed end has to be completely submerged in the solvent during the reaction, in order to guarantee optimal and reproducible irradiation conditions. Ice/water (0 °C) and dry ice/isopropanol (−78 °C) mixtures were used as cooling baths. Reactions at elevated temperatures were performed in silicone oil baths, and the temperature was regulated by a contact thermometer. Commercially available chemicals were used without further purification unless

otherwise noted. For moisture-sensitive reactions, tetrahydrofuran (THF), diethyl ether (Et₂O), and dichloromethane (CH₂Cl₂) were dried by a MBSPS 800 MBraun solvent purification system. All other dry solvents were purchased from Acros Organics (extra dry, over molecular sieves) and used without further purification. When alkanes (pentane, hexane) were used as solvents for photochemical reactions, they were used after simple distillation. Analytical thin layer chromatography (TLC) was performed on silica gel 60 (F₂₅₄) glass plates. The TLC plates were visualized by treatment with potassium permanganate (KMnO₄) stain (3.00 g KMnO₄, 20.0 g K₂CO₃, and 5.00 mL of 5% aq NaOH solution in 300 mL H₂O) followed by gentle heating. Purification of products was accomplished by flash chromatography on silica gel 60 (230–400 mesh). All solvents for chromatography, e.g., ethyl acetate (EtOAc), were distilled prior to use. Melting points were determined using a Büchi M-565 melting point apparatus. Nuclear magnetic resonance spectra were recorded at room temperature on a Bruker AVHD-400, AVHD-500, or AV-III-500. ¹H NMR spectra were referenced to the residual proton signal of the deuterated solvent [δ (CHCl₃) = 7.26 ppm]. ¹³C NMR spectra were referenced to the carbon signal of the deuterated solvent [δ (CDCl₃) = 77.16 ppm]. ¹⁹F NMR spectra were not referenced. Apparent multiplets that occur as a result of coupling constant equality between magnetically nonequivalent protons are marked as virtual (virt). The following abbreviations for single multiplicities were used: br (broad), s (singlet), d (doublet), t (triplet), q (quartet), quint (quintet), m (multiplet). Infrared spectra (IR) were recorded on a PerkinElmer Frontier IR-FTR spectrometer by ATR technique. The signal intensity is assigned using the following abbreviations: s (strong), m (medium), and w (weak). UV/vis spectra were recorded on a PerkinElmer Lambda 35 UV/vis spectrometer, using a Hellma precision cell made of quartz SUPRASIL with a pathway of 1.0 mm. High-resolution mass spectrometry (HRMS) was performed on a LTQ FT Ultra (Thermo), a linear ion trap with a Fourier transform ion cyclotron resonance detector (ESI).

5,5-Dimethylcyclopent-2-en-1-one (1a). On the basis of literature procedures:¹⁸ To a solution of 2,2-dimethylcyclopentanone (5.00 g, 44.6 mmol, 1.00 equiv) in Et₂O (50 mL) cooled by a water bath were added *N*-bromosuccinimide (8.33 g, 46.8 mmol, 1.05 equiv) and NH₄OAc (344 mg, 4.46 mmol, 10 mol %). The mixture was stirred for 6 h and then filtrated over Celite. The filtrate was washed with H₂O (2 × 50 mL), Na₂S₂O₃ solution (50 mL), and brine (50 mL), dried over Na₂SO₄, filtrated, and concentrated under reduced pressure.

The crude product was directly submitted to the next step and was dissolved in DMF (50 mL). Li₂CO₃ (9.88 g, 134 mmol, 3.00 equiv) and LiBr (11.6 g, 134 mmol, 3.00 equiv) were added to the solution and the mixture heated to 130 °C for 3 h. The reaction was then stopped by the addition of H₂O (100 mL), and the mixture was extracted with Et₂O (3 × 100 mL). The combined organic layers were washed with H₂O (5 × 100 mL) and brine (100 mL), dried over Na₂SO₄, filtrated and concentrated under reduced pressure. The crude product was purified by flash chromatography over silica (3 × 20 cm, pentane/Et₂O = 10/1) and successive distillation under reduced pressure. Enone **1a** (1.84 g, 16.7 mmol, 37%) was obtained as a colorless liquid. TLC: *R*_f = 0.14 (pentane/Et₂O = 10/1) [KMnO₄]. ¹H NMR (CDCl₃, 300 K, 500 MHz): δ (ppm) = 7.61 (dt, ³J = 5.6 Hz, ³J = 2.7 Hz, 1 H), 6.13 (dt, ³J = 5.9 Hz, ⁴J = 2.2 Hz, 1 H), 2.55 (virt t, ³J ≈ ⁴J = 2.4 Hz, 2 H), 1.11 (s, 6 H). ¹³C NMR{¹H} (CDCl₃, 300 K, 101 MHz): δ (ppm) = 215.0, 161.9, 132.0, 45.7, 42.8, 25.0. The data obtained matched those reported in the literature.^{14b}

General Procedure for the Synthesis of Cyclopentenones 1b–1e. On the basis of a literature procedure:¹⁴ To a solution of diisopropylamine (2.70 equiv) in THF (1 mM) was added *n*-butyllithium (2.5 M in hexanes, 2.50 equiv) at 0 °C. After 5 min, a solution of the carboxylic acid (1.00 equiv) in THF (2 mM) was added dropwise. The mixture was stirred at room temperature for 30 min and at 60 °C for 1 h before it was cooled down to 0 °C. At this temperature, allyl bromide (2.50 equiv) was added dropwise and the mixture stirred at room temperature for another 2 h. The reaction was quenched with water, the aqueous layer washed with Et₂O (3×),

acidified to pH = 2 with 2 M HCl, and extracted with Et₂O (3×). The combined organic layers were dried over Na₂SO₄, filtrated, and concentrated under reduced pressure. Residual starting material was removed by a short flash chromatography over silica (hexane/EtOAc), and the allylated acid was obtained in sufficient purity for the following step.

The allylated acid (1.00 equiv) was dissolved in CH₂Cl₂ (1 mM), and oxalyl chloride (3.00 equiv) was added dropwise at 0 °C. The mixture was stirred at this temperature for 3 h, and all volatiles were removed under reduced pressure. CH₂Cl₂ (1 mM) was added to the crude acid chloride and SnCl₄ (2.20 equiv) was added dropwise at 0 °C. The mixture was stirred for 1 h at room temperature and then poured into ice water. The aqueous layer was extracted with CH₂Cl₂ (3×), and the combined organic layers were washed with 1 M HCl and NaHCO₃ solution, dried over Na₂SO₄, filtrated, and concentrated under reduced pressure. The crude product was purified by flash chromatography over silica (pentane/Et₂O) and successive distillation under reduced pressure.

5,5-Diethylcyclopent-2-en-1-one (1b). In accordance with the general procedure, 2-ethylbutanoic acid (2.00 g, 17.2 mmol) was converted to enone **1b** (790 mg, 5.71 mmol, 33%) which was obtained as a colorless liquid. TLC: *R*_f = 0.23 (pentane/Et₂O = 10/1) [KMnO₄]. ¹H NMR (CDCl₃, 300 K, 500 MHz): δ (ppm) = 7.68 (dt, ³J = 5.6 Hz, ³J = 2.7 Hz, 1 H), 6.17–6.12 (m, 1 H), 2.52–2.49 (m, 2 H), 1.60–1.44 (m, 4 H), 0.75 (t, ³J = 7.4 Hz, 3 H), 0.74 (t, ³J = 7.4 Hz, 3 H). ¹³C NMR{¹H} (CDCl₃, 300 K, 126 MHz): δ (ppm) = 215.3, 163.6, 134.6, 50.9, 39.4, 29.7, 8.6. IR (ATR): $\tilde{\nu}$ [cm⁻¹] = 2964 (m), 2879 (w), 2856 (w), 1701 (s), 1590 (w), 1461 (m), 1199 (m), 1085 (w), 938 (m), 815 (m), 743 (w), 681 (m). HRMS (ESI): *m/z*: calcd for C₉H₁₄O [M + H]⁺: 139.1118; found: 139.1117.

5,5-Dipropylcyclopent-2-en-1-one (1c). In accordance with the general procedure, 2-propylpentanoic acid (2.00 g, 13.9 mmol) was converted to enone **1c** (712 mg, 4.28 mmol, 31%) which was obtained as a colorless liquid. TLC: *R*_f = 0.20 (pentane/Et₂O = 10/1) [KMnO₄]. ¹H NMR (CDCl₃, 300 K, 500 MHz): δ (ppm) = 7.65 (dt, ³J = 5.6 Hz, ³J = 2.7 Hz, 1 H), 6.13 (dt, ³J = 5.6 Hz, ⁴J = 2.2 Hz, 1 H), 2.53 (virt t, ³J ≈ ⁴J = 2.5 Hz, 2 H), 1.51–1.37 (m, 4 H), 1.25–1.13 (m, 2 H), 1.13–1.02 (m, 2 H), 0.85 (t, ³J = 7.3 Hz, 6 H). ¹³C NMR{¹H} (CDCl₃, 300 K, 126 MHz): δ (ppm) = 215.2, 163.3, 134.3, 50.4, 40.5, 39.7, 17.5, 14.8. IR (ATR): $\tilde{\nu}$ [cm⁻¹] = 2958 (m), 2932 (m), 2873 (w), 1702 (s), 1591 (w), 1465 (w), 1344 (m), 1190 (m), 1128 (w), 810 (m), 730 (w), 686 (w). HRMS (ESI): *m/z*: calcd for C₁₁H₁₈O [M + H]⁺: 167.1431; found: 167.1429.

Spiro[4.4]non-2-en-1-one (1d). In accordance with the general procedure, cyclopentanecarboxylic acid (2.00 g, 17.5 mmol) was converted to enone **1d** (465 mg, 3.42 mmol, 20%) which was obtained as a colorless liquid. TLC: *R*_f = 0.30 (pentane/Et₂O = 4/1) [KMnO₄]. ¹H NMR (CDCl₃, 300 K, 500 MHz): δ (ppm) = 7.64 (dt, ³J = 5.6 Hz, ³J = 2.7 Hz, 1 H), 6.19 (dt, ³J = 5.8 Hz, ⁴J = 2.2 Hz, 1 H), 2.59 (virt t, ³J ≈ ⁴J = 2.4 Hz, 2 H), 1.92–1.82 (m, 4 H), 1.76–1.65 (m, 2 H), 1.53–1.45 (m, 2 H). ¹³C NMR{¹H} (CDCl₃, 300 K, 126 MHz): δ (ppm) = 214.8, 162.4, 133.4, 54.4, 46.3, 38.2, 25.7. The data obtained matched those reported in the literature.^{19a}

Spiro[4.5]dec-2-en-1-one (1e). In accordance with the general procedure, cyclohexanecarboxylic acid (2.00 g, 15.6 mmol) was converted to enone **1e** (934 mg, 6.22 mmol, 40%) which was obtained as a colorless liquid. TLC: *R*_f = 0.23 (pentane/Et₂O = 4/1) [KMnO₄]. ¹H NMR (CDCl₃, 300 K, 500 MHz): δ (ppm) = 7.63 (dt, ³J = 5.7 Hz, ³J = 2.7 Hz, 1 H), 6.13 (dt, ³J = 5.7 Hz, ⁴J = 2.1 Hz, 1 H), 2.55 (virt t, ³J ≈ ⁴J = 2.4 Hz, 2 H), 1.79–1.65 (m, 3 H), 1.57 (td, ³J = 12.6 Hz, ³J = 3.7 Hz, 2 H), 1.39–1.24 (m, 5 H). ¹³C NMR{¹H} (CDCl₃, 300 K, 126 MHz): δ (ppm) = 215.1, 162.7, 132.5, 48.1, 42.1, 33.3, 25.4, 23.2. The data obtained matched those reported in the literature.^{19b}

General Procedure for the Synthesis of Amides 4. Cyclopentenones **1** (0.20 mmol, 1.0 equiv) were dissolved in pentane (10 mL), and the respective amine (1.00 mmol, 5.0 equiv) was added. The reaction mixtures were then irradiated at λ = 300 nm for 16 h.

The crude products were dry-loaded onto Celite and purified by flash chromatography over silica (hexane/EtOAc).

N-Benzyl-2-(2,2-dimethylcyclopropyl)acetamide (4aa). 0.20 mmol Scale. In accordance with the general procedure, enone **1a** (22.0 mg) and benzylamine (0.11 mL, 107 mg) were converted to amide **4aa**. Flash chromatography (2 × 20 cm, hexane/EtOAc = 2/1) led to 39.7 mg (0.18 mmol, 91%) of **4aa** which was isolated as a pale yellow solid.

1.0 mmol Scale. Cyclopentenone **1a** (1.00 mmol, 110 mg, 1.0 equiv) was dissolved in pentane (25 mL), and benzylamine (0.55 mL, 5.00 mmol, 5.0 equiv) was added. The reaction mixture was irradiated at $\lambda = 300$ nm for 16 h. The crude product was dry-loaded onto Celite and purified by flash chromatography over silica (3 × 20 cm, hexane/EtOAc = 2/1). 187 mg (0.17 mmol, 86%) of amide **4aa** were isolated as a pale yellow solid. TLC: $R_f = 0.30$ (hexane/EtOAc = 1/1) [KMnO₄]. Mp = 46–49 °C. ¹H NMR (CDCl₃, 300 K, 500 MHz): δ (ppm) = 7.37–7.32 (m, 2 H), 7.31–7.26 (m, 3 H), 6.06 (br s, 1 H), 4.51 (dd, ²J = 14.8 Hz, ³J = 5.7 Hz, 1 H), 4.46 (dd, ²J = 14.8 Hz, ³J = 5.5 Hz, 1 H), 2.36 (dd, ²J = 16.6 Hz, ³J = 7.2 Hz, 1 H), 2.26 (dd, ²J = 16.6 Hz, ³J = 7.9 Hz, 1 H), 1.06 (s, 3 H), 1.05 (s, 3 H), 0.78 (virt tdd, ³J ≈ ³J ≈ 8.2 Hz, ³J = 7.2 Hz, ³J = 5.3 Hz, 1 H), 0.56 (dd, ³J = 8.4 Hz, ²J = 4.4 Hz, 1 H), 0.07 (virt t, ²J ≈ ³J ≈ 4.9 Hz, 1 H). ¹³C NMR{¹H} (CDCl₃, 300 K, 126 MHz): δ (ppm) = 172.9, 138.5, 128.9, 127.8, 127.6, 43.7, 37.1, 27.2, 20.3, 20.1, 19.8, 15.8. IR (ATR): $\tilde{\nu}$ [cm⁻¹] = 3252 (m), 3066 (w), 2936 (m), 1641 (s), 1561 (s), 1452 (m), 1344 (m), 1287 (m), 1028 (m), 738 (m), 709 (s), 677 (m). HRMS (ESI): m/z : calcd for C₁₄H₁₉NO [M + Na]⁺: 240.1359; found: 240.1349.

2-(2,2-Dimethylcyclopropyl)-N-(4-methoxybenzyl)acetamide (4ab). In accordance with the general procedure, enone **1a** (22.0 mg) and 4-methoxybenzylamine (0.13 mL, 137 mg) were converted to amide **4ab**. Flash chromatography (2 × 20 cm, hexane/EtOAc = 4/1 → 1/1) led to 38.8 mg (0.16 mmol, 78%) of **4ab** which was isolated as a colorless solid. TLC: $R_f = 0.26$ (hexane/EtOAc = 1/1) [KMnO₄]. Mp = 41–43 °C. ¹H NMR (CDCl₃, 300 K, 500 MHz): δ (ppm) = 7.23–7.19 (m, 2 H), 6.89–6.85 (m, 2 H), 6.01 (br s, 1 H), 4.43 (dd, ²J = 14.5 Hz, ³J = 5.5 Hz, 1 H), 4.38 (dd, ²J = 14.5 Hz, ³J = 5.3 Hz, 1 H), 3.80 (s, 3 H), 2.35 (dd, ²J = 16.6 Hz, ³J = 7.2 Hz, 1 H), 2.25 (dd, ²J = 16.6 Hz, ³J = 8.0 Hz, 1 H), 1.05 (s, 3 H), 1.04 (s, 3 H), 0.80–0.72 (m, 1 H), 0.55 (dd, ³J = 8.4 Hz, ²J = 4.4 Hz, 1 H), 0.06 (virt t, ²J ≈ ³J ≈ 4.9 Hz, 1 H). ¹³C NMR{¹H} (CDCl₃, 300 K, 126 MHz): δ (ppm) = 172.8, 159.0, 130.4, 129.1, 114.1, 55.3, 43.1, 36.9, 27.1, 20.2, 20.0, 19.7, 15.7. IR (ATR): $\tilde{\nu}$ [cm⁻¹] = 3291 (m), 2942 (w), 2868 (w), 1639 (s), 1549 (s), 1512 (s), 1436 (m), 1251 (s), 1173 (m), 1031 (s), 814 (m), 739 (m), 675 (m). HRMS (ESI): m/z : calcd for C₁₅H₂₁NO₂ [M + Na]⁺: 270.1464; found: 270.1457.

2-(2,2-Dimethylcyclopropyl)-N-(4-(trifluoromethyl)benzyl)acetamide (4ac). In accordance with the general procedure, enone **1a** (22.0 mg) and 4-trifluoromethylbenzylamine (0.14 mL, 175 mg) were converted to amide **4ac**. Flash chromatography (2 × 20 cm, hexane/EtOAc = 4/1 → 1/1) led to 46.7 mg (0.16 mmol, 82%) of **4ac** which was isolated as a colorless solid. TLC: $R_f = 0.33$ (hexane/EtOAc = 1/1) [KMnO₄]. Mp = 51–54 °C. ¹H NMR (CDCl₃, 300 K, 500 MHz): δ (ppm) = 7.62–7.57 (m, 2 H), 7.42–7.38 (m, 2 H), 6.18 (br s), 4.56 (dd, ²J = 15.3 Hz, ³J = 5.8 Hz, 1 H), 4.51 (dd, ²J = 15.3 Hz, ³J = 6.2 Hz, 1 H), 2.40 (dd, ²J = 16.6 Hz, ³J = 7.0 Hz, 1 H), 2.26 (dd, ²J = 16.6 Hz, ³J = 8.0 Hz, 1 H), 1.07 (s, 3 H), 1.06 (s, 3 H), 0.79 (virt tdd, ³J ≈ ³J ≈ 8.2 Hz, ³J = 7.0 Hz, ³J = 5.3 Hz, 1 H), 0.58 (dd, ³J = 8.4 Hz, ²J = 4.4 Hz, 1 H), 0.08 (virt t, ²J ≈ ³J ≈ 4.8 Hz, 1 H). ¹³C NMR{¹H} (CDCl₃, 300 K, 126 MHz): δ (ppm) = 173.1, 142.7, 129.8, 127.9, 125.8, 124.2, 43.1, 37.0, 27.2, 20.3, 20.2, 19.8, 15.9. ¹⁹F NMR (CDCl₃, 300 K, 376 MHz): δ (ppm) = -62.5 (s). IR (ATR): $\tilde{\nu}$ [cm⁻¹] = 3246 (w), 3063 (w), 2928 (w), 1637 (m), 1565 (w), 1418 (w), 1317 (s), 1159 (s), 1118 (s), 1108 (s), 1019 (m), 848 (m), 757 (m), 677 (w). HRMS (ESI): m/z : calcd for C₁₅H₁₈F₃NO [M + H]⁺: 286.1413; found: 286.1403.

N-Butyl-2-(2,2-dimethylcyclopropyl)acetamide (4ad). In accordance with the general procedure, enone **1a** (22.0 mg) and *n*-butylamine (0.10 mL, 73.1 mg) were converted to amide **4ad**. Flash chromatography (2 × 20 cm, hexane/EtOAc = 4/1 → 1/1) led to 29.9 mg (0.16 mmol, 82%) of **4ad** which was isolated as a pale yellow

oil. TLC: $R_f = 0.40$ (hexane/EtOAc = 1/1) [KMnO₄]. ¹H NMR (CDCl₃, 300 K, 500 MHz): δ (ppm) = 5.92 (br s, 1 H), 3.36–3.20 (m, 2 H), 2.35–2.27 (m, 1 H), 2.27–2.18 (m, 1 H), 1.54–1.46 (m, 2 H), 1.41–1.31 (m, 2 H), 1.09 (s, 3 H), 1.06 (s, 3 H), 0.93 (t, ³J = 7.4 Hz, 3 H), 0.79–0.71 (m, 1 H), 0.56 (dd, ³J = 8.5 Hz, ²J = 4.3 Hz, 1 H), 0.07 (virt t, ²J ≈ ³J ≈ 4.9 Hz, 1 H). ¹³C NMR{¹H} (CDCl₃, 300 K, 126 MHz): δ (ppm) = 173.1, 39.4, 37.0, 31.8, 27.2, 20.3, 20.2, 20.1, 19.8, 15.8, 13.9. IR (ATR): $\tilde{\nu}$ [cm⁻¹] = 3291 (w), 2957 (m), 2928 (m), 2871 (w), 1642 (s), 1551 (s), 1457 (m), 1377 (w), 1199 (w), 736 (w), 675 (w). HRMS (ESI): m/z : calcd for C₁₁H₂₁NO [M + Na]⁺: 206.1515; found: 206.1510.

N-(tert-Butyl)-2-(2,2-dimethylcyclopropyl)acetamide (4ae). In accordance with the general procedure, enone **1a** (22.0 mg) and *tert*-butylamine (0.10 mL, 73.1 mg) were converted to amide **4ae**. Flash chromatography (2 × 20 cm, hexane/EtOAc = 4/1) led to 34.8 mg (0.19 mmol, 95%) of **4ae** which was isolated as a yellow solid. TLC: $R_f = 0.53$ (hexane/EtOAc = 1/1) [KMnO₄]. Mp = 101–103 °C. ¹H NMR (CDCl₃, 300 K, 500 MHz): δ (ppm) = 5.76 (br s, 1 H), 2.24 (virt ddt, ²J = 16.7 Hz, ³J = 7.4 Hz, ³J ≈ ³J ≈ 1.3 Hz, 1 H), 2.17 (virt ddt, ²J = 16.7 Hz, ³J = 7.6 Hz, ³J ≈ ³J ≈ 1.2 Hz, 1 H), 1.36 (s, 9 H), 1.09 (s, 3 H), 1.05 (s, 3 H), 0.75–0.68 (m, 1 H), 0.56 (dd, ³J = 8.5 Hz, ²J = 4.4 Hz, 1 H), 0.06 (virt t, ²J ≈ ³J ≈ 4.8 Hz, 1 H). ¹³C NMR{¹H} (CDCl₃, 300 K, 126 MHz): δ (ppm) = 172.5, 51.1, 38.1, 28.9, 27.3, 20.6, 20.1, 19.7, 15.7. IR (ATR): $\tilde{\nu}$ [cm⁻¹] = 3278 (m), 2964 (m), 2944 (w), 2927 (w), 1642 (s), 1552 (s), 1451 (m), 1360 (m), 1227 (m), 1120 (w), 863 (w), 698 (w), 675 (w). HRMS (ESI): m/z : calcd for C₁₁H₂₁NO [M + Na]⁺: 206.1515; found: 206.1515.

N-(Adamantan-1-yl)-2-(2,2-dimethylcyclopropyl)acetamide (4af). In accordance with the general procedure, enone **1a** (22.0 mg) and 1-adamantylamine (151 mg) were converted to amide **4af**. Flash chromatography (2 × 20 cm, hexane/EtOAc = 4/1) led to 41.5 mg (0.16 mmol, 79%) of **4af** which was isolated as a colorless solid. TLC: $R_f = 0.44$ (hexane/EtOAc = 2/1) [KMnO₄]. Mp = 150–154 °C. ¹H NMR (CDCl₃, 300 K, 400 MHz): δ (ppm) = 5.54 (br s, 1 H), 2.24 (dd, ²J = 16.8 Hz, ³J = 7.2 Hz, 1 H), 2.13 (dd, ²J = 16.8 Hz, ³J = 7.9 Hz, 1 H), 2.10–2.05 (m, 3 H), 2.03–1.98 (m, 6 H), 1.73–1.64 (m, 6 H), 1.09 (s, 3 H), 1.06 (s, 3 H), 0.76–0.66 (m, 1 H), 0.55 (dd, ³J = 8.5 Hz, ²J = 4.4 Hz, 1 H), 0.05 (virt t, ²J ≈ ³J ≈ 4.8 Hz, 1 H). ¹³C NMR{¹H} (CDCl₃, 300 K, 101 MHz): δ (ppm) = 172.3, 51.8, 41.9, 38.2, 36.5, 29.6, 27.3, 20.7, 20.2, 19.8, 15.7. IR (ATR): $\tilde{\nu}$ [cm⁻¹] = 3289 (m), 2907 (s), 2853 (m), 1631 (s), 1550 (s), 1456 (m), 1359 (m), 1199 (m), 935 (m), 870 (m), 698 (w), 678 (m). HRMS (ESI): m/z : calcd for C₁₇H₂₇NO [M + Na]⁺: 284.1985; found: 284.1960.

2-(2,2-Dimethylcyclopropyl)-N-(2-methoxyethyl)acetamide (4ag). In accordance with the general procedure, enone **1a** (22.0 mg) and 2-methoxyethylamine (0.09 mL, 75.1 mg) were converted to amide **4ag**. Flash chromatography (2 × 15 cm, hexane/EtOAc = 1/2 → EtOAc) led to 33.6 mg (0.18 mmol, 91%) of **4ag** which was isolated as a pale yellow oil. TLC: $R_f = 0.13$ (hexane/EtOAc = 1/2) [KMnO₄]. ¹H NMR (CDCl₃, 300 K, 500 MHz): δ (ppm) = 6.25 (br s, 1 H), 3.55–3.40 (m, 4 H), 3.37 (s, 3 H), 2.34–2.22 (m, 2 H), 1.10 (s, 3 H), 1.06 (s, 3 H), 0.80–0.71 (m, 1 H), 0.57 (dd, ³J = 8.5 Hz, ²J = 4.4 Hz, 1 H), 0.07 (virt t, ²J ≈ ³J ≈ 4.9 Hz, 1 H). ¹³C NMR{¹H} (CDCl₃, 300 K, 126 MHz): δ (ppm) = 173.1, 71.4, 58.9, 39.2, 37.1, 27.1, 20.2, 20.0, 19.8, 15.8. IR (ATR): $\tilde{\nu}$ [cm⁻¹] = 3300 (w), 2926 (m), 2871 (w), 1728 (w), 1646 (s), 1545 (m), 1377 (w), 1197 (m), 1122 (s), 1098 (m), 1024 (m), 701 (w), 674 (w). HRMS (ESI): m/z : calcd for C₁₀H₁₉NO₂ [M + Na]⁺: 208.1308; found: 208.1309.

2-(2,2-Dimethylcyclopropyl)-N-(naphthalen-1-ylmethyl)acetamide (4ah). In accordance with the general procedure, enone **1a** (22.0 mg) and naphthalen-1-ylmethanamine (0.10 mL, 113 mg) were converted to amide **4ah**. Flash chromatography (2 × 20 cm, hexane/EtOAc = 2/1) led to 34.0 mg (0.13 mmol, 64%) of **4ah** which was isolated as a colorless solid. TLC: $R_f = 0.42$ (hexane/EtOAc = 1/1) [KMnO₄]. Mp = 105–108 °C. ¹H NMR (CDCl₃, 300 K, 500 MHz): δ (ppm) = 8.05–8.00 (m, 1 H), 7.89 (dd, ³J = 7.8 Hz, ⁴J = 1.7 Hz, 1 H), 7.83 (dd, ³J = 7.4 Hz, ⁴J = 2.1 Hz, 1 H), 7.57–7.50 (m, 2 H), 7.47–7.42 (m, 2 H), 6.01 (br s, 1 H), 4.95 (dd, ²J = 14.5 Hz, ³J = 5.4 Hz, 1 H), 4.90 (dd, ²J = 14.5 Hz, ³J = 5.2 Hz, 1 H), 2.34 (dd, ²J = 16.6 Hz, ³J = 7.2 Hz, 1 H), 2.26 (dd, ²J = 16.6 Hz, ³J = 7.7 Hz, 1 H),

0.97 (s, 3 H), 0.96 (s, 3 H), 0.74 (virt qd, $^3J \approx ^3J \approx ^3J = 7.7$ Hz, $^3J = 5.3$ Hz, 1 H), 0.49 (dd, $^3J = 8.5$ Hz, $^2J = 4.5$ Hz, 1 H), 0.01 (virt t, $^2J \approx ^3J \approx 4.9$ Hz, 1 H). ^{13}C NMR{ ^1H } (CDCl₃, 300 K, 126 MHz): δ (ppm) = 172.7, 134.0, 133.8, 131.5, 128.9, 128.8, 126.8, 126.8, 126.2, 125.5, 123.7, 41.9, 37.1, 27.1, 20.3, 20.1, 19.7, 15.7. IR (ATR): $\tilde{\nu}$ [cm⁻¹] = 3247 (m), 3064 (w), 2927 (w), 1627 (s), 1555 (m), 1509 (m), 1435 (m), 1349 (w), 1197 (m), 1083 (w), 802 (m), 777 (s), 735 (m), 679 (m). HRMS (ESI): m/z : calcd for C₁₈H₂₁NO [M + Na]⁺: 290.1515; found: 290.1510.

N-Benzyl-2-(2,2-diethylcyclopropyl)acetamide (4ba). In accordance with the general procedure, enone **1b** (27.6 mg) and benzylamine (0.11 mL, 107 mg) were converted to amide **4ba**. Flash chromatography (2 \times 20 cm, hexane/EtOAc = 2/1) led to 37.4 mg (0.15 mmol, 75%) of **4ba** which was isolated as a yellow solid. TLC: R_f = 0.47 (hexane/EtOAc = 1/1) [KMnO₄]. Mp = 40–43 °C. ^1H NMR (CDCl₃, 300 K, 500 MHz): δ (ppm) = 7.34–7.28 (m, 2 H), 7.27–7.21 (m, 3 H), 6.10 (br s, 1 H), 4.48–4.40 (m, 2 H), 2.44 (dd, $^2J = 16.5$ Hz, $^3J = 6.4$ Hz, 1 H), 2.19 (dd, $^2J = 16.5$ Hz, $^3J = 8.6$ Hz, 1 H), 1.35–1.19 (m, 3 H), 1.13 (dq, $^2J = 14.5$ Hz, $^3J = 7.4$ Hz, 1 H), 0.87 (t, $^3J = 7.4$ Hz, 3 H), 0.81–0.74 (m, 1 H), 0.80 (t, $^3J = 7.5$ Hz, 3 H), 0.49 (dd, $^3J = 8.4$ Hz, $^2J = 4.4$ Hz, 1 H), 0.00 (virt t, $^2J \approx ^3J \approx 4.9$ Hz, 1 H). ^{13}C NMR{ ^1H } (CDCl₃, 300 K, 126 MHz): δ (ppm) = 173.0, 138.4, 128.9, 127.9, 127.7, 43.7, 36.6, 29.4, 25.9, 23.1, 20.1, 18.3, 11.0, 10.5. IR (ATR): $\tilde{\nu}$ [cm⁻¹] = 3274 (m), 2961 (m), 2913 (w), 2871 (w), 1636 (s), 1556 (m), 1454 (m), 1371 (w), 1224 (w), 1019 (m), 738 (s), 695 (s). HRMS (ESI): m/z : calcd for C₁₆H₂₃NO [M + Na]⁺: 268.1672; found: 268.1667.

N-Butyl-2-(2,2-diethylcyclopropyl)acetamide (4bd). In accordance with the general procedure, enone **1b** (27.6 mg) and *n*-butylamine (0.10 mL, 73.1 mg) were converted to amide **4bd**. Flash chromatography (2 \times 20 cm, hexane/EtOAc = 2/1) led to 26.8 mg (0.13 mmol, 63%) of **4bd** which was isolated as a yellow oil. TLC: R_f = 0.45 (hexane/EtOAc = 1/1) [KMnO₄]. ^1H NMR (CDCl₃, 300 K, 500 MHz): δ (ppm) = 5.82 (br s, 1 H), 3.28 (m, 2 H), 2.39 (dd, $^2J = 16.5$ Hz, $^3J = 6.5$ Hz, 1 H), 2.17 (dd, $^2J = 16.5$ Hz, $^3J = 8.4$ Hz, 1 H), 1.53–1.46 (m, 2 H), 1.41–1.32 (m, 4 H), 1.32–1.24 (m, 1 H), 1.24–1.15 (m, 1 H), 0.95–0.87 (m, 9 H), 0.78 (virt tdd, $^3J \approx ^3J \approx 8.3$ Hz, $^3J = 6.5$ Hz, $^3J = 5.4$ Hz, 1 H), 0.54 (dd, $^3J = 8.4$ Hz, $^2J = 4.4$ Hz, 1 H), 0.03 (virt t, $^2J \approx ^3J \approx 4.9$ Hz, 1 H). ^{13}C NMR{ ^1H } (CDCl₃, 300 K, 126 MHz): δ (ppm) = 173.0, 39.3, 36.7, 31.9, 29.5, 25.8, 23.1, 20.3, 20.1, 18.2, 13.9, 11.0, 10.6. IR (ATR): $\tilde{\nu}$ [cm⁻¹] = 3290 (m), 2961 (m), 2933 (m), 2874 (w), 1642 (s), 1552 (m), 1460 (m), 1376 (w), 1228 (w), 1152 (w), 737 (w), 666 (w). HRMS (ESI): m/z : calcd for C₁₃H₂₅NO [M + Na]⁺: 234.1828; found: 234.1826.

N-(tert-Butyl)-2-(2,2-diethylcyclopropyl)acetamide (4be). In accordance with the general procedure, enone **1b** (27.6 mg) and *tert*-butylamine (0.10 mL, 73.1 mg) were converted to amide **4be**. Flash chromatography (2 \times 20 cm, hexane/EtOAc = 4/1) led to 28.2 mg (0.13 mmol, 67%) of **4be** which was isolated as a colorless solid. TLC: R_f = 0.54 (hexane/EtOAc = 2/1) [KMnO₄]. Mp = 66–69 °C. ^1H NMR (CDCl₃, 300 K, 500 MHz): δ (ppm) = 5.62 (br s, 1 H), 2.25 (dd, $^2J = 16.3$ Hz, $^3J = 7.1$ Hz, 1 H), 2.15 (dd, $^2J = 16.5$ Hz, $^3J = 7.9$ Hz, 1 H), 1.42–1.33 (m, 11 H), 1.25 (dq, $^2J = 14.7$ Hz, $^3J = 7.4$ Hz, 1 H), 1.16 (dq, $^2J = 14.5$ Hz, $^3J = 7.6$ Hz, 1 H), 0.92 (t, $^3J = 7.4$ Hz, 3 H), 0.89 (t, $^3J = 7.4$ Hz, 3 H), 0.76 (virt tdd, $^3J \approx ^3J \approx 8.1$ Hz, $^3J = 7.0$ Hz, $^3J = 5.3$ Hz, 1 H), 0.52 (dd, $^3J = 8.5$ Hz, $^2J = 4.3$ Hz, 1 H), 0.01 (virt t, $^2J \approx ^3J \approx 4.9$ Hz, 1 H). ^{13}C NMR{ ^1H } (CDCl₃, 300 K, 126 MHz): δ (ppm) = 172.4, 51.1, 37.8, 29.5, 29.0, 25.8, 23.0, 20.4, 18.2, 11.0, 10.7. IR (ATR): $\tilde{\nu}$ [cm⁻¹] = 3276 (w), 2964 (s), 2929 (w), 2875 (w), 1640 (s), 1561 (s), 1452 (m), 1360 (m), 1226 (m), 1048 (w), 900 (w), 706 (w), 666 (w). HRMS (ESI): m/z : calcd for C₁₃H₂₅NO [M + H]⁺: 212.2009; found: 212.2006.

2-(2,2-Diethylcyclopropyl)-N-(2-methoxyethyl)acetamide (4bg). In accordance with the general procedure, enone **1b** (27.6 mg) and 2-methoxyethylamine (0.09 mL, 75.1 mg) were converted to amide **4bg**. Flash chromatography (2 \times 15 cm, EtOAc) led to 32.2 mg (0.15 mmol, 75%) of **4bg** which was isolated as a pale yellow oil. TLC: R_f = 0.34 (EtOAc) [KMnO₄]. ^1H NMR (CDCl₃, 300 K, 500 MHz): δ (ppm) = 6.19 (br s, 1 H), 3.50–3.43 (m, 4 H), 3.36 (s, 3 H), 2.37 (dd, $^2J = 16.4$ Hz, $^3J = 6.8$ Hz, 1 H), 2.20 (dd, $^2J = 16.4$ Hz,

$^3J = 8.2$ Hz, 1 H), 1.36 (dq, $^2J = 14.5$ Hz, $^3J = 7.2$ Hz, 2 H), 1.27 (dt, $^2J = 14.4$ Hz, $^3J = 7.4$ Hz, 1 H), 1.23–1.15 (m, 1 H), 0.92 (t, $^3J = 7.6$ Hz, 3 H), 0.89 (t, $^3J = 7.5$ Hz, 3 H), 0.80 (virt tdd, $^3J \approx ^3J \approx 8.3$ Hz, $^3J = 6.8$ Hz, $^3J = 5.3$ Hz, 1 H), 0.53 (dd, $^3J = 8.4$ Hz, $^2J = 4.4$ Hz, 1 H), 0.02 (virt t, $^2J \approx ^3J \approx 4.9$ Hz, 1 H). ^{13}C NMR{ ^1H } (CDCl₃, 300 K, 126 MHz): δ (ppm) = 173.1, 71.4, 58.9, 39.2, 36.7, 29.4, 25.8, 23.0, 20.0, 18.2, 11.0, 10.5. IR (ATR): $\tilde{\nu}$ [cm⁻¹] = 3294 (w), 2962 (m), 2932 (w), 2875 (w), 1644 (s), 1546 (m), 1460 (m), 1197 (m), 1124 (s), 1025 (m), 704 (w), 665 (w). HRMS (ESI): m/z : calcd for C₁₂H₂₃NO₂ [M + H]⁺: 214.1802; found: 214.1797.

N-Benzyl-2-(2,2-dipropylcyclopropyl)acetamide (4ca). In accordance with the general procedure, enone **1c** (33.3 mg) and benzylamine (0.11 mL, 107 mg) were converted to amide **4ca**. Flash chromatography (2 \times 20 cm, hexane/EtOAc = 2/1) led to 35.0 mg (0.13 mmol, 64%) of **4ca** which was isolated as a pale yellow oil. TLC: R_f = 0.39 (hexane/EtOAc = 1/1) [KMnO₄]. ^1H NMR (CDCl₃, 300 K, 500 MHz): δ (ppm) = 7.34–7.28 (m, 2 H), 7.27–7.22 (m, 3 H), 6.06 (br s, 1 H), 4.48–4.39 (m, 2 H), 2.42 (dd, $^2J = 16.5$ Hz, $^3J = 6.3$ Hz, 1 H), 2.16 (dd, $^2J = 16.5$ Hz, $^3J = 8.6$ Hz, 1 H), 1.40–1.16 (m, 6 H), 1.13–1.05 (m, 1 H), 0.98 (ddd, $^3J = 12.7$ Hz, $^3J = 10.4$ Hz, $^3J = 4.8$ Hz, 1 H), 0.85 (t, $^3J = 7.1$ Hz, 3 H), 0.80 (t, $^3J = 7.1$ Hz, 3 H), 0.74 (virt tt, $^3J \approx ^3J \approx 8.5$ Hz, $^3J \approx ^3J \approx 5.9$ Hz, 1 H), 0.50 (dd, $^3J = 8.4$ Hz, $^2J = 4.4$ Hz, 1 H), 0.02 (virt t, $^2J \approx ^3J \approx 4.9$ Hz, 1 H). ^{13}C NMR{ ^1H } (CDCl₃, 300 K, 126 MHz): δ (ppm) = 172.9, 138.4, 128.8, 127.9, 127.6, 43.7, 39.8, 36.6, 33.0, 23.7, 19.9, 19.8, 19.7, 18.7, 14.6, 14.5. IR (ATR): $\tilde{\nu}$ [cm⁻¹] = 3288 (w), 2956 (m), 2929 (w), 2871 (w), 1643 (s), 1547 (m), 1454 (m), 1329 (w), 1029 (w), 732 (m), 697 (s). HRMS (ESI): m/z : calcd for C₁₈H₂₇NO [M + Na]⁺: 296.1985; found: 296.1978.

N-Butyl-2-(2,2-dipropylcyclopropyl)acetamide (4cd). In accordance with the general procedure, enone **1c** (33.3 mg) and *n*-butylamine (0.10 mL, 73.1 mg) were converted to amide **4cd**. Flash chromatography (2 \times 20 cm, hexane/EtOAc = 2/1) led to 26.9 mg (0.11 mmol, 56%) of **4cd** which was isolated as a pale yellow oil. TLC: R_f = 0.56 (hexane/EtOAc = 1/1) [KMnO₄]. ^1H NMR (CDCl₃, 300 K, 500 MHz): δ (ppm) = 5.85 (br s, 1 H), 3.30–3.24 (m, 2 H), 2.40 (dd, $^2J = 16.5$ Hz, $^3J = 6.4$ Hz, 1 H), 2.14 (dd, $^2J = 16.5$ Hz, $^3J = 8.7$ Hz, 1 H), 1.49 (virt quint, $^3J \approx ^3J \approx 7.3$ Hz, 2 H), 1.43–1.28 (m, 8 H), 1.17–1.03 (m, 2 H), 0.93 (t, $^3J = 7.3$ Hz, 3 H), 0.91–0.85 (m, 6 H), 0.74 (virt tt, $^3J \approx ^3J \approx 8.5$ Hz, $^3J \approx ^3J \approx 5.8$ Hz, 1 H), 0.54 (dd, $^3J = 8.5$ Hz, $^2J = 4.3$ Hz, 1 H), 0.04 (virt t, $^2J \approx ^3J \approx 4.9$ Hz, 1 H). ^{13}C NMR{ ^1H } (CDCl₃, 300 K, 126 MHz): δ (ppm) = 173.0, 39.9, 39.3, 36.6, 33.1, 31.8, 23.7, 20.2, 20.0, 19.9, 19.7, 18.6, 14.6, 14.6, 13.9. IR (ATR): $\tilde{\nu}$ [cm⁻¹] = 3290 (w), 2957 (m), 2930 (m), 2872 (m), 1642 (s), 1552 (m), 1465 (m), 1458 (m), 1331 (w), 736 (w), 695 (w). HRMS (ESI): m/z : calcd for C₁₅H₂₉NO [M + Na]⁺: 262.2141; found: 262.2135.

N-(tert-Butyl)-2-(2,2-dipropylcyclopropyl)acetamide (4ce). In accordance with the general procedure, enone **1c** (33.3 mg) and *tert*-butylamine (0.10 mL, 73.1 mg) were converted to amide **4ce**. Flash chromatography (2 \times 20 cm, hexane/EtOAc = 4/1) led to 30.0 mg (0.13 mmol, 63%) of **4ce** which was isolated as a colorless solid. TLC: R_f = 0.28 (hexane/EtOAc = 4/1) [KMnO₄]. Mp = 51–54 °C. ^1H NMR (CDCl₃, 300 K, 500 MHz): δ (ppm) = 5.67 (br s, 1 H), 2.28 (dd, $^2J = 16.4$ Hz, $^3J = 6.7$ Hz, 1 H), 2.12 (dd, $^2J = 16.4$ Hz, $^3J = 8.5$ Hz, 1 H), 1.43–1.30 (m, 6 H), 1.36 (s, 9 H), 1.18–1.09 (m, 1 H), 1.08–1.00 (m, 1 H), 0.93–0.84 (m, 6 H), 0.73 (virt tdd, $^3J \approx ^3J \approx 8.5$ Hz, $^3J = 6.7$ Hz, $^3J = 5.4$ Hz, 1 H), 0.53 (dd, $^3J = 8.4$ Hz, $^2J = 4.3$ Hz, 1 H), 0.03 (virt t, $^2J \approx ^3J \approx 4.9$ Hz, 1 H). ^{13}C NMR{ ^1H } (CDCl₃, 300 K, 126 MHz): δ (ppm) = 172.8, 51.3, 39.9, 37.5, 33.1, 28.9, 23.7, 20.1, 20.0, 19.8, 18.6, 14.7, 14.6. IR (ATR): $\tilde{\nu}$ [cm⁻¹] = 3291 (w), 2961 (m), 2939 (m), 2869 (w), 1639 (s), 1557 (s), 1452 (m), 1360 (m), 1338 (m), 1225 (m), 1018 (w), 692 (m). HRMS (ESI): m/z : calcd for C₁₅H₂₉NO [M + Na]⁺: 262.2141; found: 262.2136.

2-(2,2-Dipropylcyclopropyl)-N-(2-methoxyethyl)acetamide (4cg). In accordance with the general procedure, enone **1c** (33.3 mg) and 2-methoxyethylamine (0.09 mL, 75.1 mg) were converted to amide **4cg**. Flash chromatography (2 \times 20 cm, hexane/EtOAc = 1/2) led to 30.1 mg (0.12 mmol, 62%) of **4cg** which was isolated as a pale yellow oil. TLC: R_f = 0.40 (EtOAc) [KMnO₄]. ^1H NMR (CDCl₃, 300

K, 500 MHz): δ (ppm) = 6.21 (br s, 1 H), 3.50–3.44 (m, 4 H), 3.36 (s, 3 H), 2.39 (dd, $^2J = 16.4$ Hz, $^3J = 6.7$ Hz, 1 H), 2.19 (dd, $^2J = 16.4$ Hz, $^3J = 8.3$ Hz, 1 H), 1.44–1.29 (m, 6 H), 1.17–1.01 (m, 2 H), 0.89 (t, $^3J = 7.0$ Hz, 3 H), 0.88 (t, $^3J = 7.0$ Hz, 3 H), 0.77 (virt tdd, $^3J \approx ^3J \approx 8.4$ Hz, $^2J = 6.7$ Hz, $^3J = 5.4$ Hz, 1 H), 0.54 (dd, $^2J = 8.4$ Hz, $^3J = 4.4$ Hz, 1 H), 0.05 (virt t, $^2J \approx ^3J \approx 4.9$ Hz, 1 H). ^{13}C NMR (^1H) (CDCl₃, 300 K, 126 MHz): δ (ppm) = 173.4, 71.4, 58.9, 39.3, 39.3, 36.6, 33.0, 23.7, 20.0, 19.7, 19.6, 18.6, 14.7, 14.6. IR (ATR): $\tilde{\nu}$ [cm⁻¹] = 3294 (w), 2956 (m), 2929 (m), 2872 (m), 1644 (s), 1547 (m), 1457 (m), 1197 (m), 1125 (s), 1097 (m), 1021 (w), 728 (w), 692 (w). HRMS (ESI): m/z : calcd for C₁₄H₂₇NO₂ [M + Na]⁺: 264.1934; found: 264.1928.

N-Benzyl-2-(spiro[2.4]heptan-1-yl)acetamide (4da). In accordance with the general procedure, enone **1d** (27.2 mg) and benzylamine (0.11 mL, 107 mg) were converted to amide **4da**. Flash chromatography (2 × 20 cm, hexane/EtOAc = 2/1) led to 34.9 mg (0.14 mmol, 72%) of **4da** which was isolated as a pale yellow solid. TLC: $R_f = 0.25$ (hexane/EtOAc = 2/1) [KMnO₄]. Mp = 73–75 °C. ^1H NMR (CDCl₃, 300 K, 500 MHz): δ (ppm) = 7.37–7.31 (m, 2 H), 7.31–7.27 (m, 3 H), 6.10 (br s, 1 H), 4.51 (dd, $^2J = 14.8$ Hz, $^3J = 5.8$ Hz, 1 H), 4.45 (dd, $^2J = 14.8$ Hz, $^3J = 5.6$ Hz, 1 H), 2.34 (dd, $^2J = 16.6$ Hz, $^3J = 6.8$ Hz, 1 H), 2.20 (dd, $^2J = 16.6$ Hz, $^3J = 7.9$ Hz, 1 H), 1.75–1.44 (m, 7 H), 1.42–1.34 (m, 1 H), 0.97 (virt tdd, $^3J \approx ^3J \approx 8.1$ Hz, $^3J = 6.8$ Hz, $^2J = 5.3$ Hz, 1 H), 0.74 (dd, $^2J = 8.4$ Hz, $^3J = 4.4$ Hz, 1 H), 0.22 (virt t, $^2J \approx ^3J \approx 4.8$ Hz, 1 H). ^{13}C NMR (^1H) (CDCl₃, 300 K, 126 MHz): δ (ppm) = 172.8, 138.5, 128.9, 127.8, 127.6, 43.6, 38.3, 37.4, 30.6, 27.0, 26.6, 26.3, 20.3, 19.1. IR (ATR): $\tilde{\nu}$ [cm⁻¹] = 3256 (w), 3068 (w), 2949 (m), 2930 (m), 2861 (w), 1639 (m), 1565 (m), 1496 (m), 1453 (m), 1345 (m), 1030 (m), 733 (m), 708 (s), 694 (s). HRMS (ESI): m/z : calcd for C₁₆H₂₁NO [M + Na]⁺: 266.1515; found: 266.1508.

N-Butyl-2-(spiro[2.4]heptan-1-yl)acetamide (4dd). In accordance with the general procedure, enone **1d** (27.2 mg) and *n*-butylamine (0.10 mL, 73.1 mg) were converted to amide **4dd**. Flash chromatography (2 × 20 cm, hexane/EtOAc = 2/1) led to 22.5 mg (0.11 mmol, 54%) of **4dd** which was isolated as a pale yellow oil. TLC: $R_f = 0.52$ (hexane/EtOAc = 1/1) [KMnO₄]. ^1H NMR (CDCl₃, 300 K, 500 MHz): δ (ppm) = 5.87 (br s, 1 H), 3.35–3.22 (m, 2 H), 2.32–2.25 (m, 1 H), 2.19–2.12 (m, 1 H), 1.78–1.56 (m, 6 H), 1.50 (virt quint, $^3J \approx ^3J \approx 7.3$ Hz, 2 H), 1.54–1.46 (m, 1 H), 1.42–1.32 (m, 3 H), 0.97–0.89 (m, 1 H), 0.93 (t, $^3J = 7.3$ Hz, 3 H), 0.75 (dd, $^3J = 8.4$ Hz, $^2J = 4.3$ Hz), 0.21 (virt t, $^2J \approx ^3J \approx 4.8$ Hz, 1 H). ^{13}C NMR (^1H) (CDCl₃, 300 K, 126 MHz): δ (ppm) = 173.1, 39.4, 38.1, 37.4, 31.8, 30.6, 27.0, 26.6, 26.4, 20.3, 20.2, 19.1, 13.9. IR (ATR): $\tilde{\nu}$ [cm⁻¹] = 3290 (w), 2954 (m), 2935 (m), 2865 (m), 1642 (s), 1549 (m), 1449 (w), 1377 (w), 1192 (w), 736 (w), 695 (w). HRMS (ESI): m/z : calcd for C₁₃H₂₃NO [M + Na]⁺: 232.1672; found: 232.1670.

N-(tert-Butyl)-2-(spiro[2.4]heptan-1-yl)acetamide (4de). In accordance with the general procedure, enone **1d** (27.2 mg) and *tert*-butylamine (0.10 mL, 73.1 mg) were converted to amide **4de**. Flash chromatography (2 × 15 cm, hexane/EtOAc = 4/1) led to 35.0 mg (0.17 mmol, 84%) of **4de** which was isolated as a colorless solid. TLC: $R_f = 0.62$ (hexane/EtOAc = 1/1) [KMnO₄]. Mp = 88–91 °C. ^1H NMR (CDCl₃, 300 K, 500 MHz): δ (ppm) = 5.68 (br s, 1 H), 2.18 (dd, $^2J = 16.0$ Hz, $^3J = 6.8$ Hz, 1 H), 2.14 (dd, $^2J = 16.0$ Hz, $^3J = 6.7$ Hz, 1 H), 1.79–1.57 (m, 6 H), 1.57–1.50 (m, 1 H), 1.45–1.34 (m, 1 H), 1.38 (s, 9 H), 0.97–0.90 (m, 1 H), 0.76 (dd, $^3J = 8.5$ Hz, $^2J = 4.2$ Hz, 1 H), 0.22 (virt t, $^2J \approx ^3J \approx 4.8$ Hz, 1 H). ^{13}C NMR (^1H) (CDCl₃, 300 K, 126 MHz): δ (ppm) = 172.2, 51.0, 39.4, 37.5, 30.5, 29.0, 26.9, 26.7, 26.4, 20.4, 19.4. IR (ATR): $\tilde{\nu}$ [cm⁻¹] = 3287 (w), 2958 (m), 2863 (w), 1638 (s), 1552 (s), 1449 (m), 1359 (m), 1226 (m), 686 (m). HRMS (ESI): m/z : calcd for C₁₃H₂₃NO [M + Na]⁺: 232.1672; found: 232.1667.

N-(2-Methoxyethyl)-2-(spiro[2.4]heptan-1-yl)acetamide (4dg). In accordance with the general procedure, enone **1d** (27.2 mg) and 2-methoxyethylamine (0.09 mL, 75.1 mg) were converted to amide **4dg**. Flash chromatography (2 × 15 cm, EtOAc) led to 30.1 mg (0.14 mmol, 71%) of **4dg** which was isolated as a pale yellow oil. TLC: $R_f = 0.31$ (EtOAc) [KMnO₄]. ^1H NMR (CDCl₃, 300 K, 500 MHz): δ (ppm) = 6.24 (br s, 1 H), 3.53–3.41 (m, 4 H), 3.36 (s, 3

H), 2.28–2.17 (m, 2 H), 1.78–1.57 (m, 6 H), 1.49 (ddd, $^2J = 14.4$ Hz, $^3J = 7.1$ Hz, $^3J = 3.6$ Hz, 1 H), 1.42–1.34 (m, 1 H), 1.00–0.91 (m, 1 H), 0.74 (dd, $^3J = 8.5$ Hz, $^2J = 4.3$ Hz, 1 H), 0.21 (virt t, $^2J \approx ^3J \approx 4.9$ Hz, 1 H). ^{13}C NMR (^1H) (CDCl₃, 300 K, 126 MHz): δ (ppm) = 173.1, 71.4, 58.9, 39.2, 38.2, 37.3, 30.5, 27.0, 26.6, 26.3, 20.3, 19.0. IR (ATR): $\tilde{\nu}$ [cm⁻¹] = 3296 (w), 2943 (m), 2865 (w), 1644 (s), 1543 (m), 1450 (m), 1197 (m), 1121 (s), 1093 (m), 1025 (w), 694 (w). HRMS (ESI): m/z : calcd for C₁₂H₂₁NO₂ [M + Na]⁺: 234.1464; found: 234.1460.

N-Benzyl-2-(spiro[2.5]octan-1-yl)acetamide (4ea). In accordance with the general procedure, enone **1e** (30.0 mg) and benzylamine (0.11 mL, 107 mg) were converted to amide **4ea**. Flash chromatography (2 × 20 cm, hexane/EtOAc = 4/1 → 1/1) led to 32.4 mg (0.13 mmol, 63%) of **4ea** which was isolated as a colorless solid. TLC: $R_f = 0.44$ (hexane/EtOAc = 1/1) [KMnO₄]. Mp = 60–62 °C. ^1H NMR (CDCl₃, 300 K, 500 MHz): δ (ppm) = 7.38–7.32 (m, 2 H), 7.31–7.26 (m, 3 H), 6.11 (br s, 1 H), 4.50 (dd, $^2J = 14.8$ Hz, $^3J = 5.7$ Hz, 1 H), 4.46 (dd, $^2J = 14.8$ Hz, $^3J = 5.6$ Hz, 1 H), 2.46 (dd, $^2J = 16.5$ Hz, $^3J = 6.5$ Hz, 1 H), 2.26 (dd, $^2J = 16.5$ Hz, $^3J = 8.4$ Hz, 1 H), 1.54–1.43 (m, 5 H), 1.41–1.34 (m, 2 H), 1.34–1.24 (m, 3 H), 0.77 (virt tdd, $^3J \approx ^3J \approx 8.4$ Hz, $^3J = 6.5$ Hz, $^3J = 5.3$ Hz, 1 H), 0.53 (dd, $^3J = 8.4$ Hz, $^2J = 4.3$ Hz, 1 H), 0.05 (virt t, $^2J \approx ^3J \approx 4.8$ Hz, 1 H). ^{13}C NMR (^1H) (CDCl₃, 300 K, 126 MHz): δ (ppm) = 173.0, 138.5, 128.9, 127.9, 127.6, 43.7, 37.7, 36.3, 30.9, 26.4, 25.7, 25.7, 23.4, 19.9, 18.3. IR (ATR): $\tilde{\nu}$ [cm⁻¹] = 3274 (w), 2919 (m), 2847 (m), 1643 (s), 1542 (s), 1495 (m), 1443 (m), 1250 (m), 1030 (m), 727 (s), 694 (s), 671 (m). HRMS (ESI): m/z : calcd for C₁₇H₂₃NO [M + Na]⁺: 280.1672; found: 280.1661.

N-Butyl-2-(spiro[2.5]octan-1-yl)acetamide (4ed). In accordance with the general procedure, enone **1e** (30.0 mg) and *n*-butylamine (0.10 mL, 73.1 mg) were converted to amide **4ed**. Flash chromatography (2 × 20 cm, hexane/EtOAc = 2/1) led to 22.1 mg (0.10 mmol, 49%) of **4ed** which was isolated as a pale yellow oil. TLC: $R_f = 0.23$ (hexane/EtOAc = 2/1) [KMnO₄]. ^1H NMR (CDCl₃, 300 K, 500 MHz): δ (ppm) = 5.81 (br s, 1 H), 3.35–3.21 (m, 2 H), 2.38 (dd, $^2J = 16.6$ Hz, $^3J = 6.6$ Hz, 1 H), 2.15 (dd, $^2J = 16.6$ Hz, $^3J = 8.3$ Hz, 1 H), 1.62–1.27 (m, 14 H), 0.94 (t, $^3J = 7.3$ Hz, 3 H), 0.74 (virt tdd, $^3J \approx ^3J \approx 8.3$ Hz, $^3J = 6.6$ Hz, $^3J = 5.3$ Hz, 1 H), 0.53 (dd, $^3J = 8.3$ Hz, $^2J = 4.3$ Hz, 1 H), 0.05 (virt t, $^2J \approx ^3J \approx 4.8$ Hz, 1 H). ^{13}C NMR (^1H) (CDCl₃, 300 K, 126 MHz): δ (ppm) = 173.0, 39.3, 37.8, 36.3, 31.9, 30.9, 26.5, 25.7, 25.7, 23.3, 20.3, 20.0, 18.2, 13.9. IR (ATR): $\tilde{\nu}$ [cm⁻¹] = 3289 (w), 2923 (s), 2851 (m), 1641 (s), 1551 (m), 1444 (m), 1227 (w), 1118 (w), 907 (w), 737 (w), 708 (w), 674 (w). HRMS (ESI): m/z : calcd for C₁₄H₂₅NO [M + Na]⁺: 246.1828; found: 246.1825.

N-(tert-Butyl)-2-(spiro[2.5]octan-1-yl)acetamide (4ee). In accordance with the general procedure, enone **1e** (30.0 mg) and *tert*-butylamine (0.10 mL, 73.1 mg) were converted to amide **4ee**. Flash chromatography (2 × 20 cm, hexane/EtOAc = 4/1) led to 31.0 mg (0.14 mmol, 69%) of **4ee** which was isolated as a colorless solid. TLC: $R_f = 0.69$ (hexane/EtOAc = 1/1) [KMnO₄]. Mp = 80–83 °C. ^1H NMR (CDCl₃, 300 K, 500 MHz): δ (ppm) = 5.66 (br s, 1 H), 2.24 (dd, $^2J = 16.5$ Hz, $^3J = 7.2$ Hz, 1 H), 2.13 (dd, $^2J = 16.5$ Hz, $^3J = 7.8$ Hz, 1 H), 1.64–1.38 (m, 7 H), 1.36 (s, 9 H), 1.35–1.14 (m, 3 H), 0.71 (virt qd, $^3J \approx ^3J \approx 7.7$ Hz, $^3J = 5.2$ Hz, 1 H), 0.52 (dd, $^3J = 8.3$ Hz, $^2J = 4.3$ Hz, 1 H), 0.03 (virt t, $^2J \approx ^3J \approx 4.8$ Hz, 1 H). ^{13}C NMR (^1H) (CDCl₃, 300 K, 126 MHz): δ (ppm) = 172.4, 51.0, 37.9, 37.4, 30.9, 29.0, 26.5, 25.7, 25.7, 23.3, 20.3, 18.2. IR (ATR): $\tilde{\nu}$ [cm⁻¹] = 3276 (w), 2923 (m), 2851 (m), 1640 (s), 1552 (s), 1447 (m), 1359 (m), 1226 (m), 931 (w), 698 (w), 664 (w). HRMS (ESI): m/z : calcd for C₁₄H₂₅NO [M + Na]⁺: 246.1828; found: 246.1818.

N-(2-Methoxyethyl)-2-(spiro[2.5]octan-1-yl)acetamide (4eg). In accordance with the general procedure, enone **1e** (30.0 mg) and 2-methoxyethylamine (0.09 mL, 75.1 mg) were converted to amide **4eg**. Flash chromatography (2 × 15 cm, hexane/EtOAc = 1/2) led to 32.9 mg (0.15 mmol, 73%) of **4eg** which was isolated as a pale yellow oil. TLC: $R_f = 0.16$ (hexane/EtOAc = 1/2) [KMnO₄]. ^1H NMR (CDCl₃, 300 K, 500 MHz): δ (ppm) = 6.22 (br s, 1 H), 3.54–3.41 (m, 4 H), 3.37 (s, 3 H), 2.35 (dd, $^2J = 16.6$ Hz, $^3J = 7.1$ Hz, 1 H), 2.21 (dd, $^2J = 16.6$ Hz, $^3J = 7.9$ Hz, 1 H), 1.57–1.34 (m, 8 H), 1.32–

1.24 (m, 1 H), 1.20–1.13 (m, 1 H), 0.80–0.72 (m, 1 H), 0.54 (dd, $^3J = 8.3$ Hz, $^2J = 4.4$ Hz, 1 H), 0.05 (virt t, $^2J \approx ^3J \approx 4.8$ Hz, 1 H). ^{13}C NMR{ ^1H } (CDCl₃, 300 K, 126 MHz): δ (ppm) = 173.1, 71.4, 58.9, 39.2, 37.7, 36.3, 30.8, 26.5, 25.7, 25.7, 23.3, 19.9, 18.2. IR (ATR): $\tilde{\nu}$ [cm⁻¹] = 3296 (w), 2923 (s), 2850 (m), 1644 (s), 1545 (m), 1445 (m), 1302 (w), 1197 (m), 1124 (s), 1097 (m), 1028 (m), 695 (w), 675 (w). HRMS (ESI): m/z : calcd for C₁₃H₂₃NO₂ [M + Na]⁺: 248.1621; found: 248.1616.

■ ASSOCIATED CONTENT

Supporting Information

The Supporting Information is available free of charge at <https://pubs.acs.org/doi/10.1021/acs.joc.2c01156>.

Data sheets of light sources; ^1H and $^{13}\text{C}\{^1\text{H}\}$ NMR spectra for compounds **1b-1e**, **4aa-4eg**; and spectroscopic and computational studies (PDF)

Cartesian coordinates of computationally optimized molecular structures (all calculated structures as part of the manuscript and the Supporting Information, e.g., minima in the ground and excited states, conical intersections and minimum energy intersystem crossing points, 33 in total) (XYZ)

FAIR data, including the primary NMR FID files, for compounds **1b-1e**, and **4aa-4eg** (ZIP)

■ AUTHOR INFORMATION

Corresponding Author

Thorsten Bach – School of Natural Sciences, Department of Chemistry and Catalysis Research Center (CRC), Technical University of Munich, 85747 Garching, Germany;
 ● orcid.org/0000-0002-1342-0202;
 Email: thorsten.bach@ch.tum.de

Authors

Noah Jeremias – School of Natural Sciences, Department of Chemistry and Catalysis Research Center (CRC), Technical University of Munich, 85747 Garching, Germany

Martin T. Peschel – Department Chemie, Ludwig-Maximilians-Universität München, 81377 München, Germany

Constantin Jaschke – Department Chemie, Ludwig-Maximilians-Universität München, 81377 München, Germany

Regina de Vivie-Riedle – Department Chemie, Ludwig-Maximilians-Universität München, 81377 München, Germany; ● orcid.org/0000-0002-7877-5979

Complete contact information is available at: <https://pubs.acs.org/doi/10.1021/acs.joc.2c01156>

Notes

The authors declare no competing financial interest.

■ ACKNOWLEDGMENTS

Financial support by the Deutsche Forschungsgemeinschaft (DFG, German Research Foundation), TRR 325 (B1, C5), 444632635 is gratefully acknowledged.

■ REFERENCES

(1) Reviews: (a) Baldwin, S. W. Synthetic Aspects of [2 + 2] Cycloadditions of α,β -Unsaturated Carbonyl Compounds. *Org. Photochem.* **1981**, *5*, 123–225. (b) Crimmins, M. T.; Reinhold, T. L. Enone Olefin [2 + 2] Photochemical Cycloadditions. *Org. React.* **1993**, *44*, 297–588. (c) Pete, J.-P. Asymmetric Photoreactions of

Conjugated Enones and Esters. *Adv. Photochem.* **1996**, *21*, 135–216. (d) Margaretha, P. Photocycloaddition of Cycloalk-2-enones to Alkenes. In *Synthetic Organic Photochemistry, Molecular and Supramolecular Photochemistry*, Vol. 12, Griesbeck, A. G.; Mattay, J., Eds.; Dekker: New York, 2005; pp 211–237. (e) Poplata, S.; Tröster, A.; Zou, Y.-Q.; Bach, T. Recent Advances in the Synthesis of Cyclobutanes by Olefin [2 + 2] Photocycloaddition Reactions. *Chem. Rev.* **2016**, *116*, 9748–9815.

(2) Early reports: (a) Ciamician, G.; Silber, P. Chemische Lichtwirkungen. *Ber. Dtsch. Chem. Ges.* **1908**, *41*, 1928–1935. (b) Büchi, G.; Goldman, I. M. Photochemical Reactions. VII. The Intramolecular Cyclization of Carvone to Carvonecamphor. *J. Am. Chem. Soc.* **1957**, *79*, 4741–4748. (c) Eaton, P. E. On the Mechanism of the Photodimerization of Cyclopentenone. *J. Am. Chem. Soc.* **1962**, *84*, 2454–2455. (d) De Mayo, P.; Takeshita, H.; Sattar, A. B. M. A. The Photochemical Synthesis of 1,5-Diketones and Their Cyclisation: a New Annulation Process. *Proc. Chem. Soc.* **1962**, 119. (e) Corey, E. J.; Mitra, R. B.; Uda, H. Total Synthesis of d,l-Caryophyllene and d,l-Isocaryophyllene. *J. Am. Chem. Soc.* **1963**, *85*, 362–363.

(3) (a) Schuster, D. I.; Dunn, D. A.; Heibel, G. E.; Brown, P. B.; Rao, J. M.; Woning, J.; Bonneau, R. Enone photochemistry. Dynamic properties of triplet excited states of cyclic conjugated enones as revealed by transient absorption spectroscopy. *J. Am. Chem. Soc.* **1991**, *113*, 6245–6255. (b) Schalk, O.; Schuurman, M. S.; Wu, G.; Lang, P.; Mucke, M.; Feifel, R.; Stolow, A. Internal Conversion versus Intersystem Crossing: What drives the Gas Phase Dynamics of Cyclic α,β -Enones? *J. Phys. Chem. A* **2014**, *118*, 2279–2287.

(4) García-Expósito, E.; Bearpark, M. J.; Ortuño, Branchadell, V.; Robb, M. A.; Wilsey, S. The T1 3($\pi-\pi^*$)/S0 Intersections and Triplet Lifetimes of Cyclic α,β -Enones. *J. Org. Chem.* **2001**, *66*, 8811–8814.

(5) Peschel, M. T.; Kabaciński, P.; Schwinger, D. P.; Thyraug, E.; Cerullo, G.; Bach, T.; Hauer, J.; de Vivie-Riedle, R. Activation of 2-Cyclohexenone by BF₃ Coordination: Mechanistic Insights from Theory and Experiment. *Angew. Chem., Int. Ed.* **2021**, *60*, 10155–10163. and refs cited therein.

(6) Nevesely, T.; Wienhold, M.; Molloy, J. J.; Gilmour, R. Advances in the E → Z Isomerization of Alkenes Using Small Molecule Photocatalysts. *Chem. Rev.* **2022**, *122*, 2650–2694.

(7) Schwinger, D. P.; Peschel, M. T.; Jaschke, C.; Jandl, C.; de Vivie-Riedle, R.; Bach, T. Diels–Alder Reaction of Photochemically Generated (E)-Cyclohept-2-enones: Diene Scope, Reaction Pathway, and Synthetic Application. *J. Org. Chem.* **2022**, *87*, 4838–4851. and refs cited therein

(8) Review: Schuster, D. I. Mechanistic Issues in [2 + 2]-Photocycloadditions of Cyclic Enones to Alkenes. In *CRC Handbook of Photochemistry and Photobiology*, 2nd ed.; Horspool, W. M., Lenci, F., Eds.; CRC Press: Boca Raton, 2004; pp 72/1–72/24.

(9) (a) Iriando-Alberdi, J.; Greaney, M. F. Photocycloaddition in Natural Product Synthesis. *Eur. J. Org. Chem.* **2007**, 4801–4815. (b) Hoffmann, N. Photochemical Reactions as Key Steps in Organic Synthesis. *Chem. Rev.* **2008**, *108*, 1052–1103. (c) Bach, T.; Hehn, J. P. Photochemical Reactions as Key Steps in Natural Product Synthesis. *Angew. Chem., Int. Ed.* **2011**, *50*, 1000–1045. (d) Karkas, M. D.; Porco, J. A.; Stephenson, C. R. J. Photochemical Approaches to Complex Chemotypes: Applications in Natural Product Synthesis. *Chem. Rev.* **2016**, *116*, 9683–9747. (e) Scignano, M.; Rodríguez, R. I.; Alemán, J. Recent Visible Light and Metal Free Strategies in [2 + 2] and [4 + 2] Photocycloadditions. *Eur. J. Org. Chem.* **2021**, 2021, 3303–3321.

(10) Recent reviews on the topic: (a) Genzink, M. J.; Kidd, J. B.; Swords, W. B.; Yoon, T. P. Chiral Photocatalyst Structures in Asymmetric Photochemical Synthesis. *Chem. Rev.* **2022**, *122*, 1654–1716. (b) Prentice, C.; Morrisson, J.; Smith, A. D.; Zysman-Colman, E. Recent developments in enantioselective photocatalysis. *Beilstein J. Org. Chem.* **2020**, *16*, 2363–2441. (c) Silvi, M.; Melchiorre, P. Enhancing the potential of enantioselective organocatalysis with light. *Nature* **2018**, *554*, 41–49.

(11) For contributions from our group to the field, see: (a) Brenninger, C.; Jolliffe, J. D.; Bach, T. Chromophore Activation

- of α,β -Unsaturated Carbonyl Compounds and Its Application to Enantioselective Photochemical Reactions. *Angew. Chem., Int. Ed.* **2018**, *57*, 14338–14349. (b) Schwinger, D. P.; Bach, T. Chiral 1,3,2-Oxazaborolidine Catalysts for Enantioselective Photochemical Reactions. *Acc. Chem. Res.* **2020**, *53*, 1933–1943.
- (12) Poplata, S.; Bach, T. Enantioselective Intermolecular [2 + 2] Photocycloaddition Reaction of Cyclic Enones and Its Application in a Synthesis of (–)-Grandisol. *J. Am. Chem. Soc.* **2018**, *140*, 3228–3231. and refs cited therein.
- (13) Leverenz, M.; Merten, C.; Dreuw, A.; Bach, T. Lewis Acid Catalyzed Enantioselective Photochemical Rearrangements on the Singlet Potential Energy Surface. *J. Am. Chem. Soc.* **2019**, *141*, 20053–20057.
- (14) (a) Agosta, W. C.; Smith, A. B., III; Kende, A. S.; Eilerman, R. G.; Benham, J. The intramolecular photorearrangement of cyclopentenones. *Tetrahedron Lett.* **1969**, *10*, 4517–4520. (b) Agosta, W. C.; Smith, A. B., III Photochemical Reactions of Simple Cyclopentenones. *J. Am. Chem. Soc.* **1971**, *93*, 5513–5520.
- (15) Interestingly, heteroanalogues (heteroatom at C4) of 5,5-dimethylcyclopent-2-enone do not undergo the rearrangement, see for example: Gebel, R.-C.; Margaretha, P. *Chem. Ber.* **1990**, *123*, 855–858 and refs cited therein.
- (16) For related rearrangement reactions of 4,4-dialkylcyclohex-2-enones, see: Margaretha, P. Photorearrangement Reactions of Cyclohex-2-enones. In *CRC Handbook of Photochemistry and Photobiology*, 2nd ed.; Horspool, W. M.; Lenci, F., Eds.; CRC Press: Boca Raton, 2004; pp 76/1–76/12.
- (17) (a) Cohen, S. G.; Baumgarten, R. J. Photoreduction of benzophenone by amines, alcohols, and hydrocarbons. Medium effects. Photochemical oxidative deamination. *J. Am. Chem. Soc.* **1967**, *89*, 3471–3475. (b) Bartholomew, R. F.; Davidson, R. S. The photosensitized oxidation of amines. *J. Chem. Soc. D* **1970**, 1174–1175. (c) Yates, S. F.; Schuster, G. B. Photoreduction of triplet thioxanthone by amines: charge transfer generates radicals that initiate polymerization of olefins. *J. Org. Chem.* **1984**, *49*, 3349–3356.
- (18) (a) Tanemura, K.; Suzuki, T.; Nishida, Y.; Satsumabayashi, K.; Horaguchi, T. A mild and efficient procedure for alpha-bromination of ketones using *N*-bromosuccinimide catalysed by ammonium acetate. *Chem. Commun.* **2004**, 470–471. (b) Hua, D. H.; Chen, Y.; Sin, H.-S.; Maroto, M. J.; Robinson, P. D.; Newell, S. W.; Perchellet, E. M.; Ladesich, J. B.; Freeman, J. A.; Perchellet, J.-P.; Chiang, P. K. A One-Pot Condensation of Pyrones and Enals. Synthesis of 1*H*,7*H*-5*a*,6,8,9-Tetrahydro-1-oxopyrano[4,3-*b*][1]benzopyrans. *J. Org. Chem.* **1997**, *62*, 6888–6896.
- (19) (a) Karpf, M.; Dreiding, A. S. Thermische Cyclisierung von α -Alkinonen zu 2-Cyclopentenonen. *Helv. Chim. Acta* **1979**, *62*, 852–865. (b) Srikrishna, A.; Praveen Kumar, P. Spiroannulation of a cyclopentane ring. Synthesis of spiro[4.*n*](*n*+5)alk-2-en-1-ones. *J. Indian Chem. Soc.* **1999**, *76*, 521–526.
- (20) Dormán, G.; Nakamura, H.; Pulsipher, A.; Prestwich, G. D. The Life of Pi Star: Exploring the Exciting and Forbidden Worlds of Pi the Benzophenone Photophore. *Chem. Rev.* **2016**, *116*, 15284–15398.
- (21) Cao, J.; Xie, Z.-Z. Internal conversion and intersystem crossing in α,β -enones: a combination of electronic structure calculations and dynamics simulations. *Phys. Chem. Chem. Phys.* **2016**, *18*, 6931–6945.
- (22) (a) Shiozaki, T.; Gyórfy, W.; Celani, P.; Werner, H.-J. Communication: Extended multi-state complete active space second-order perturbation theory: Energy and nuclear gradients. *J. Chem. Phys.* **2011**, *135*, 081106. As implemented in BAGEL, see: (b) Shiozaki, T. BAGEL: Brilliantly Advanced General Electronic-structure Library. *WIRE's Comput. Mol. Sci.* **2018**, *8*, No. e1331.
- (23) (a) Cui, Q.; Morokuma, K. Ab initio study of nonadiabatic interactions in the photodissociation of ketene. *J. Chem. Phys.* **1997**, *107*, 4951–4959. (b) Liu, Y.; Yu, J.-K.; Huang, X.-R.; Sun, C.-C. Theoretical study of photodissociation dynamics on the lowest-lying Rydberg state of ketene. *J. Chem. Phys.* **2006**, *125*, 044311.
- (24) Herkstroeter, W. G.; Lamola, A. A.; Hammond, G. S. Mechanisms of Photochemical Reactions in Solution. XXVIII. Values of Triplet Excitation Energies of Selected Sensitizers. *J. Am. Chem. Soc.* **1964**, *86*, 4537–4540.
- (25) (a) Lapouyade, R.; Koussini, R.; Bouas-Laurent, H. Primary and tertiary amines as catalysts of hydrogen transfer in the photocyclization of 1,1-diarylethylenes. *J. Am. Chem. Soc.* **1977**, *99*, 7374–7376. (b) Franz, J. F.; Kraus, W. B.; Zeitler, K. No photocatalyst required – versatile, visible light mediated transformations with polyhalomethanes. *Chem. Commun.* **2015**, *51*, 8280–8283. (c) Böhm, A.; Bach, T. Radical Reactions Induced by Visible Light in Dichloromethane Solutions of Hünig's Base: Synthetic Applications and Mechanistic Observations. *Chem.—Eur. J.* **2016**, *22*, 15921–15928.
- (26) (a) Rackl, D.; Kais, V.; Kreitmeier, P.; Reiser, O. Visible light photoredox-catalyzed deoxygenation of alcohols. *Beilstein J. Org. Chem.* **2014**, *10*, 2157–2165. (b) Lenhart, D.; Bauer, A.; Pöthig, A.; Bach, T. Enantioselective Visible-Light-Induced Radical-Addition Reactions to 3-Alkylidene Indolin-2-ones. *Chem.—Eur. J.* **2016**, *22*, 6519–6523.

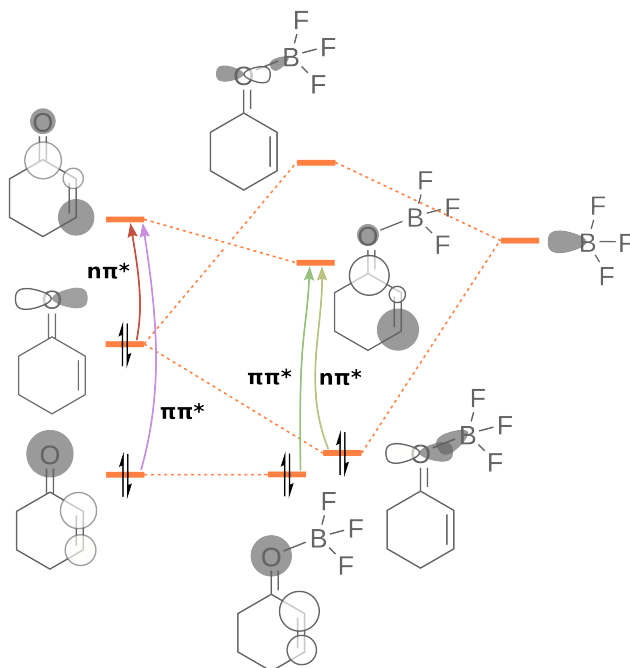
4. Excited State Dynamics and Spectroscopy of Lewis-Acid-Enone Complexes

2-Enones feature an electron-poor C=C double bond due to the $-M$ -effect of the carbonyl group. The conjugation with the carbonyl group lowers the π^* lowest unoccupied molecular orbital (LUMO) compared to other unsaturated compounds. Furthermore, the carbonyl group contains a high-lying non-bonded oxygen orbital that forms the highest occupied molecular orbital (HOMO) of the 2-enone. Accordingly, the lowest excited states of 2-enones are the $n\pi^*$ and $\pi\pi^*$ states which are discussed in detail in chapter 3.

How does the coordination to a Lewis acid change these orbitals and, consequently, these excited states? An orbital scheme illustrating the changes is displayed in scheme 6 for the example of cyclohex-2-enone- BF_3 . The Lewis acid forms a coordinate covalent bond with the enone by transferring electron density from the HOMO of the 2-enone into the LUMO of the Lewis acid. Thus, the n orbital of the 2-enone acquires bonding character and is significantly lowered in energy. The effect on the π^* orbital is more subtle. By decreasing electron density at the carbonyl oxygen, the Lewis acid increases the $-M$ -effect of the carbonyl group. This means that charge is more easily transferred from the C=C double bond to the carbonyl moiety during the excitation process.[184] This implies that the π^* LUMO is energetically lowered by the coordination of the Lewis acid. This effect is smaller than the lowering of the energy of the n orbital; thus, a significant blueshift is observed for the $n\pi^*$ states. Since the π orbital (HOMO-1) is not much affected, the bright $\pi\pi^*$ state experiences a redshift.[163] These shifts are more pronounced for stronger Lewis acids (see fig. 4.1). The redshift allows for selective excitation of the enone-Lewis acid complex even if free enone is simultaneously present in the solution. At the excitation wavelengths that are typically employed in experiments, which lie on the red edge of the absorption, the Lewis acid-enone complexes feature the strong redshifted $\pi\pi^*$ absorption while free enones only feature the weak $n\pi^*$ absorption.

In many cases, Lewis acids even alter the order of the excited states, such that the ${}^1\pi\pi^*$ state falls below the ${}^1n\pi^*$ state already in the FC region. This can especially be observed in enones where the C=C double bond is part of a larger conjugated system (and the $\pi\pi^*$ states are generally lower-lying) and can completely alter the photoreactivity of the 2-enone. Particularly striking examples of this are the [2+2] photocycloadditions of phenanthrene-carbaldehydes and naphthaldehydes where, instead of the usual Paternò-Büchi reactions, photocycloadditions to the aromatic system are observed (*ortho* photocycloaddition) if Lewis acids are added to the reaction mixture.[169, 185]

The features discussed above make Lewis acids attractive catalysts for the photoreactions of enones. The first recorded use of a Lewis acid in a [2+2] photocycloaddition was likely made in 1910 by Pratorius and Korn, who found that dimerization of diben-



Scheme 6: Orbital interaction scheme for the formation of the cyclohex-2-enone- BF_3 complex explaining the redshift of the $\pi\pi^*$ and blueshift of the $n\pi^*$ state.

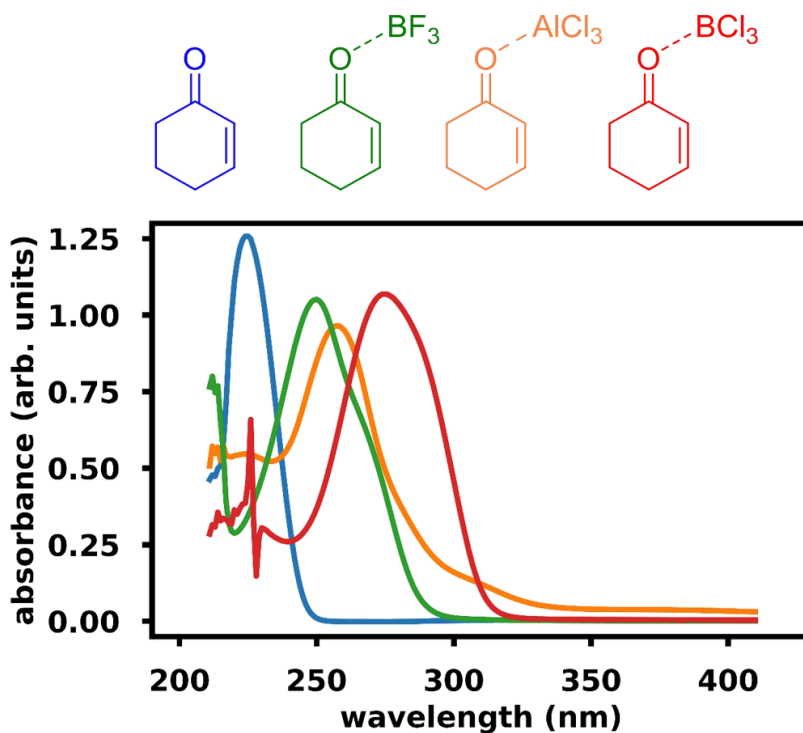


Figure 4.1.: UV-Vis spectra of complexes of cyclohex-2-enone with various Lewis acids. A redshift of the bright $\pi\pi^*$ absorption is observed, which is more pronounced when the Lewis acid is stronger. Spectra measured by *D. P. Schwinger*.

zylideneacetone in acetic acid could be achieved by adding uranium salts and exposing the mixture to sunlight.[39] Lewis acid photocatalysis of [2+2] photocycloadditions was further explored by Lewis *et al.* who extensively studied the photo-dimerizations and crossed [2+2] cycloadditions of a variety of compounds, such as coumarins,[186] cinnamic esters[187] and phenanthrene-9-carboxylates.[188] During the last fifteen years, the group of T. Bach discovered that the Lewis acids not only increase quantum yield and allow the reactions to proceed at longer wavelengths, but they can also be used to perform these reactions in an enantioselective fashion. In this way, chiral variants of the [2+2] cycloaddition were developed for a large variety of compounds (for example, coumarins,[189] dihydropyridones,[53], cyclohex-2-enones[42] and phenanthrene-9-carbaldehydes[185]) using different activated oxazaborolidines as the Lewis acid.[55]

First theoretical investigations of the electronic structure of Lewis acid-enone complexes were performed by Wang *et al.*[184] They discovered that for the complexes of oxazaborolidine-AlBr₃ with a dihydropyridinone derivative, the ¹ $\pi\pi^*$ state is so low in energy that conversion to the reactive ³ $\pi\pi^*$ triplet states takes place without the involvement of the $n\pi^*$ states and is instead mediated by increased SOC due to the presence of heavy atoms in the Lewis acid catalyst. In the next sections, the cyclohex-2-enone-BF₃ complex is discussed, which does not contain any heavy atoms. However, in this system, the $n\pi^*$ is also easily accessible as the transition dipole moment between it and the ground state significantly increases due to vibronic intensity borrowing from the bright $\pi\pi^*$ state and thus, coupling to ³ $\pi\pi^*$ is still efficient.[149] Wang *et al.* also uncovered that Lewis acids change the PES in the $\pi\pi^*$ states of coumarins, such that lower barriers and more accessible crossings might speed up [2+2] cycloadditions.[190] A similar observation was made by us in cyclohex-2-enone-BF₃, where an energetic lowering of CoIns with the ground state was observed.[2] However, these CoIns are unproductive. It appears that the $\pi\pi^*$ states obtain a flatter topography when a Lewis acid is coordinated, which, generally, speeds up both reactive and unreactive pathways.

The sections of this chapter deal with two specific enone-Lewis acid complexes, cyclohex-2-enone-BF₃, and benzaldehyde-BCl₃. The methodology used to treat both of these systems was similar. After an initial optimization of critical points at a high level of theory, TSH simulations of the system in the gas phase were performed at a lower level which was carefully benchmarked against the high-level calculations. Based on these simulations, ultrafast TA experiments were planned and executed to substantiate or refute the theoretical predictions. From global fits to the TA data, evolution associated decay spectra (EADS) were obtained. These were interpreted using high-level calculations such that a coherent picture of the ultrafast process emerged. Then, synthetic experiments exploiting that process were performed. This methodology is only possible due to collaboration between different fields within chemistry. The TA measurements were performed by P. Kabacinski in the group of G. Cerullo and interpreted by E. Thyraug in the group of J. Hauer, measurements of static spectra and organic synthesis were performed by D. P. Schwinger and T. Rigotti in the group of T. Bach.

Cyclohex-2-enone-BF₃ serves as a model to better understand the transformation of the electronic structure evoked by the Lewis acid in the Enone substrate and how it influences the short-time relaxation dynamics. Since these short-time dynamics dictate which states are populated, they are essential for a deep understanding of the photocatalytic mechanism. Hence, the first section of this chapter covers static calculations and dynamics in the gas phase as well as time-resolved spectroscopic measurements that

show how the reactive $\pi\pi^*$ state is populated. The second section covers dynamics in solution that were performed in collaboration with J. Kussmann from the group of C. Ochsenfeld. These dynamics show that interaction with the solvent cage plays a critical role in the relaxation of the complex.

In section 4.3 on benzaldehyde- BCl_3 , the topic of Lewis acid enone interaction is approached from a different angle. The original aim was to use a firm theoretical understanding of the ultrafast processes to find a possibility to enable [2+2] photocycloadditions in *ortho* position. Thus, calculations on the benzaldehyde- BCl_3 system were performed. However, these calculations revealed that the electronic structure of this complex does not allow for the desired *ortho* [2+2] photo-cycloaddition to take place. Instead, dissociative states in the singlet and triplet manifold (homolysis of B-Cl bond mediated via chlorine lone pairs) preclude a clean relaxation to bound triplet minima. However, this unknown reactivity opened up new possibilities. The chlorine radicals generated in the homolytic dissociation can be employed in a new C-C bond-forming hydroalkylation. A mechanistic exploration of this reaction concludes this chapter.

4.1. Relaxation to the Triplet States in Cyclohex-2-enone-BF₃

As discussed in chapter 3, triplet states play a crucial role in the photo-reactivity of enones. It is thus of great interest to determine how these states are populated in enone-Lewis acid complexes and how they are altered from the free enone. The cyclohex-2-enone BF₃ complex serves as a model for the interaction of a Lewis acid with a 2-enone. Simulating the photo-relaxation of the complex and comparing it to the relaxation of free cyclohex-2-enone will be the topic of this section and the following section 4.2.

The static calculations and the TSH simulation performed on cyclohex-2-enone both use the XMS-CASPT2 electronic structure method. This method offers a balanced description of a molecule's ground and excited states. We discovered that, with a triple-zeta basis set, XMS-CASPT2 reproduces the static spectra of free cyclohexenone and the complex almost quantitatively if the geometries for which excitation energy and transition dipoles are calculated are sampled from a Wigner distribution. Most importantly, no energetic shift is necessary, as is often employed in simulations using time-dependent density functional theory (TDDFT). Thus, XMS-CASPT2 can be used to assign spectral features confidently, even if they are relatively broad and unstructured, which is especially helpful for excited state absorption signals at ambient temperature in solution. For a description of the Wigner sampling approach to calculate optical spectra, see appendix A.

To elucidate the relaxation mechanism, static and dynamic simulations of the complex are complemented by ultrafast TA measurements. In brief, static calculations show three possible relaxation pathways; 1) heterolytic dissociation of the complex in S₁, leading to a loss of the Lewis acid, 2) relaxation to a shallow minimum in the S₁ with subsequent ISC to the triplet manifold, and 3) IC from S₁ to S₀ via conical intersections that become accessible through the coordination of the Lewis acid. Dynamic calculations of the complex were performed on the XMS-CASPT2/cc-pvdz level of theory for the singlet states in the gas phase. These simulations mainly showed dissociation and only a minor contribution of direct S₁ to S₀ relaxation. The dissociation occurs on an ultrafast timescale. Accordingly, in a subsequent, slower [2+2] cycloaddition, the Lewis acid would not be in proximity to the substrate. When larger, chiral Lewis acids are used to induce chirality during the [2+2] photocycloaddition step,^[42] the Lewis acid is obviously required to be attached to the substrate. Thus, dissociation can not be prominent in reality as in the simulation. Solvent effects might slow down dissociation enough for ISC to be a competitive process, or re-association of the Lewis acid might occur between the initial excitation event and the [2+2] cycloaddition. There might also be the possibility that BF₃ is not a good model for the larger, chiral complexes. Section 4.2 will deal with calculations investigating the influence of the solvent on the dissociation. This section (section 4.1) will discuss the results of TA experiments that further elucidate the relaxation process of cyclohex-2-enone-BF₃.

A global analysis of the TA data yielded four different time constants, shown in fig. 4.2 and the corresponding EADS. We calculated the corresponding ESA using the methodology presented in appendix A for the FC region, the ³ππ* minimum of the complex and the ³ππ* minimum of isolated cyclohex-2-enone. None of the measured EADS matched the latter, meaning that the Lewis acid is firmly attached when the ³ππ* is reached. Indeed, the 4 ps EADS shows the signatures of the ³ππ* minimum of

the complex. The 130 fs EADS also matches the calculated spectra of the complex in the FC region. Thus, we assign this smallest time constant to relaxation out of the FC region either towards (partial) dissociation or the shallow S_1 minimum. These processes are not easily differentiated based on their ESA. The 400 fs EADS is tentatively associated with ISC since the 4 ps EADS can be assigned to relaxation processes inside the triplet states with high confidence due to the excellent match of the calculated ESA. The largest time constant, which can not be resolved on the time scale of the experiment, is associated with a return to the ground state since no significant chemical changes were observed between excitation pulses.

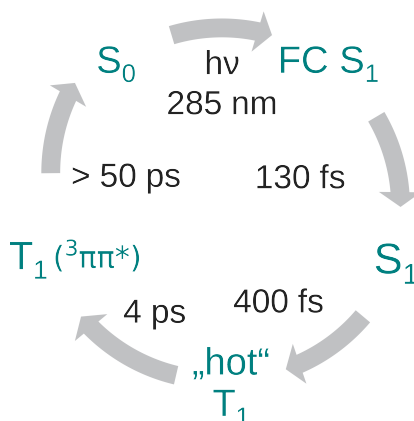


Figure 4.2.: Time constants extracted from TA measurements and assignment to the relaxation processes in the cyclohex-2-enone- BF_3 complex. For a detailed explanation, see the narrative.

The article “Activation of 2-Cyclohexenone by BF_3 Coordination: Mechanistic Insights from Theory and Experiment” was published in *Angewandte Chemie International Edition*. The following points provide a summary of the article.

- Upon addition of Lewis acid BF_3 to cyclohexenone, the absorption spectrum changes drastically. The almost dark $S_1(n\pi^*)$ is blueshifted from 335 nm to 266 nm and the bright $S_2(\pi\pi^*)$ is redshifted from 250 nm to 266 nm. This is accompanied by a large increase in absorbance for the S_1 state.
- XMS-CASPT2 calculations reproduce the shifts and changes in absorbance to high precision. Sampling from a Wigner distribution roughly reproduces the shape of the absorption bands. Thus, XMS-CASPT2 calculations can be used to study the dynamics of the system and to explain the results of the experiments.
- The blueshift of $S_1(n\pi^*)$ is caused by the coordination of the Lewis acid to the oxygen n orbital, significantly lowering its energy. The π^* orbital is also stabilized but to a lesser extent. The π orbital is largely unaffected by the Lewis acid coordination; thus, a redshift results for the $S_2(\pi\pi^*)$. Due to the spectral shift, S_1 and S_2 are energetically close in the complex, and a CoIn between these states was found in the FC region. The increase in absorbance of S_1 can thus be attributed to intensity borrowing via vibronic coupling to the bright S_2 .

- For cyclohexenone without Lewis acid, TSH simulations including triplet states show a relaxation from S₁ to T₁ with a time constant of 746 fs. This occurs through ISC near the S₁ minimum, where there is significant SOC. The transition occurs mainly from S₁(nπ*) to T₂(ππ*) in accordance with El Sayed’s rule.[149] However, geometrically close to the S₁ minimum there is a T₁T₂ CoIn which is passed diabatically within a few fs after ISC, leading to relaxation into a biradicaloid T₁(ππ*) minimum, where the H–C=C–H dihedral angle is twisted.
- Based on static calculations at critical points, the above relaxation pathway is also found to be accessible in the complex. However, in the complex additional relaxation pathways become available. These are ultrafast relaxation from S₁ to S₀ via two different CoIns and dissociation of the Lewis acid due to the weakening of the dative bond in the nπ* state. TSH simulations of the complex in these singlet states showed mainly dissociation of the complex. For trajectories started in S₁, ultrafast relaxation without dissociation is observed in 11% of the trajectories, dissociation in 89% of the trajectories.
- The dynamics of the complex can be followed using femtosecond TA spectroscopy. These spectra show the immediate formation of a broad band between 400 nm and 600 nm that decays on a 100 fs timescale, while a band in the UV is formed. After this, smaller changes in the UV band are observed on a picosecond timescale. A multiexponential signal fit yielded four time constants and their EADS. These time constants are: 0.13 ps, 0.4 ps, 4 ps, > 50 ps
- Comparison of EADS to calculated ESA spectra allowed assignment of the 0.13 ps EADS to the S₁ in the FC region and the 4 ps EADS to the T₁ close to the ππ* minimum, with the Lewis acid attached (see fig. 4.2).
- The following relaxation mechanism is proposed: Relaxation of the FC region (0.13 ps), ISC into triplets (0.4 ps), vibrational cooling in the triplets (4 ps) and relaxation to the ground state (> 50 ps).
- Since we do not observe a signal from cyclohexenone without a Lewis acid, we assume that the Lewis acid stays attached during the relaxation. We postulate that the dissociation observed in the TSH simulations is likely hindered by the solvent cage, so relaxation into the triplets with the attached Lewis acid can compete.
- In synthetic studies, BF₃ is active as a photocatalyst in the [2+2]-cycloaddition of isobutene to cyclohexenone upon a judicious choice of irradiation wavelength. Our study shows that the state from which these reactions occur is the T₁(ππ*) of the cyclohexenone-BF₃ complex.

Hereafter, The article “Activation of 2-Cyclohexenone by BF₃ Coordination: Mechanistic Insights from Theory and Experiment” published in *Angewandte Chemie International Edition* is reproduced. The supporting information is available online.

Activation of 2-Cyclohexenone by BF₃ Coordination: Mechanistic Insights from Theory and Experiment

Martin T. Peschel[†], Piotr Kabaciński[†], Daniel P. Schwinger, Erling Thyryhaug, Giulio Cerullo, Thorsten Bach, Jürgen Hauer* and Regina de Vivie-Riedle*

Abstract: Lewis acids have recently been recognized as catalysts enabling enantioselective photochemical transformations. Mechanistic studies on these systems are however rare, either due to their absorption at wavelengths shorter than 260 nm, or due to the limitations of theoretical dynamic studies for larger complexes. In this work, we overcome these challenges and employ sub-30-fs transient absorption in the UV, in combination with a highly accurate theoretical treatment on the XMS-CASPT2 level. We investigate 2-cyclohexenone and its complex to boron trifluoride and analyze the observed dynamics based on trajectory calculations including non-adiabatic coupling and intersystem crossing. This approach explains all ultrafast decay pathways observed in the complex. We show that the Lewis acid remains attached to the substrate in the triplet state, which in turn explains why chiral boron-based Lewis acids induce a high enantioselectivity in photocycloaddition reactions.

Introduction

Lewis acids modulate the photochemical behavior of carbonyl compounds by coordination to the Lewis-basic oxygen atom. Although the fact that Lewis acids can have a beneficial impact on the course of photochemical reactions has been known for more than a century,^[1] systematic studies of the interaction between a Lewis acid and a carbonyl

chromophore were first undertaken in the 1980s and 1990s. Among several notable contributions,^[2] the topic was most comprehensively investigated by the groups of Lewis and Fukuzumi. Lewis and co-workers explored the photochemistry of coumarins, quinolones, cinnamates and related compounds in a series of papers entitled „Lewis Acid Catalysis of Photochemical Reactions“.^[3] The group of Fukuzumi interrogated the influence of a Lewis acid on the photoredox properties of carbonyl compounds^[4] in the context of their general interest in the effect of Lewis acids on photoredox catalysis.^[5] In more recent years, the interest in Lewis acids and carbonyl compounds has been largely triggered by the desire to exploit chiral Lewis acids for the enantioselective catalysis of photochemical reactions.^[6] The [2+2] photocycloaddition attracted the most attention and several modes of action were shown to be operative, including (a) a stabilization of the excited state,^[7] (b) a more facile photoredox event,^[8] (c) a bathochromic absorption shift,^[9] (d) a lowering of the energy of the triplet state^[10] or combinations thereof.^[11] Apart from the enantioselectivity issue, Lewis acids have also been found to be useful to activate aromatic carbonyl compounds towards a reaction at the aromatic or heteroaromatic core.^[12] They may also allow for new reaction pathways, such that reactions can take place in a different spin state.^[13]

Several experimental studies were accompanied^[10,11,12a,13,14] or supported^[15] in separate papers by calculations which aided to understand the course of the reaction. However, despite the increasing number of synthetic studies, very little attention has been paid to the immediate influence of the Lewis acid on a carbonyl chromophore upon excitation. Despite early laser flash photolysis studies on relevant carbonyl compounds, e.g. cyclic α,β -unsaturated ketones (enones),^[16] an elemental picture of the fate of a typical photochemical substrate in the presence of a Lewis acid does not exist. Previous theoretical studies already addressed the nature of the excited states and reaction paths of simple enones^[17–19] and semiclassical dynamics gave insight into the singlet-triplet crossing mechanisms.^[20] The reaction paths in Lewis acid complexes have also been investigated computationally, but these studies were focused on different classes of enones (coumarines and 5,6-dihydro-4-pyridones), for which the order of the excited states is different.^[15]

Here we present a detailed mechanistic study on the effects of the addition of the Lewis acid BF₃ to the paradigmatic 2-cyclohexenone (**1**), to form the photocatalytic complex (**2**), (Scheme 1). The combination of state-of-the-art femtosecond transient absorption (TA) in the UV and high-

[*] M. T. Peschel,^[†] R. de Vivie-Riedle
Department Chemie, Ludwig-Maximilians-Universität München
81377 München (Germany)
E-Mail: regina.de_vivie@cup.uni-muenchen.de

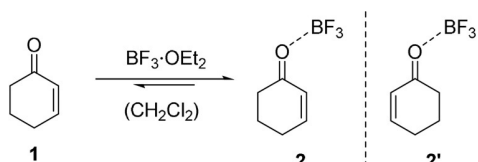
P. Kabaciński,^[†] G. Cerullo
IFN-CNR and Dipartimento di Fisica, Politecnico di Milano
20133 Milano (Italy)

D. P. Schwinger, E. Thyryhaug, T. Bach, J. Hauer
Department of Chemistry and Catalysis Research Center (CRC),
Technische Universität München
85747 Garching (Germany)
E-Mail: juergen.hauer@tum.de

[†] These authors contributed equally to this work.

Supporting information and the ORCID identification number(s) for the author(s) of this article can be found under:
<https://doi.org/10.1002/anie.202016653>.

© 2021 The Authors. *Angewandte Chemie* published by Wiley-VCH GmbH. This is an open access article under the terms of the Creative Commons Attribution Non-Commercial NoDerivs License, which permits use and distribution in any medium, provided the original work is properly cited, the use is non-commercial and no modifications or adaptations are made.



Scheme 1. 2-Cyclohexenone (**1**) as a model substrate to explore the photophysical properties of its Lewis acid complex **2** to boron trifluoride (Isomer **2'** with BF₃ coordinated away from the double bond).

level quantum dynamical and quantum chemical methods on the XMS-CASPT2 level of theory allows us to (a) highlight the effects of Lewis acid addition on both static and dynamic system properties, (b) identify and describe not only the reaction pathway towards the photocatalytically active low-lying triplet state T₁, but also an important loss channel, namely radiationless S₁→S₀ internal conversion via a conical intersection.

Results and Discussion

Vertical Excitation Energies and Calculated Absorption Spectra. The 2-cyclohexenone-BF₃ complex (**2**) was generated by treatment of 2-cyclohexenone (**1**) with an excess of BF₃·OEt₂ in dichloromethane solution. In previous work by Childs et al., complex **2** had been studied by NMR spectroscopy and was identified as a 1:1 complex.^[21] Addition of BF₃·OEt₂ to 2-cyclohexenone led to a bathochromic shift of the strong absorption band at λ = 224 nm (ε = 12.6 × 10⁻³ L mol⁻¹ cm⁻¹) to a new signal with a maximum at λ = 250 nm. Beyond 5.0 equiv. of BF₃·OEt₂, the absorbance did not increase further (Figure 1 b), indicating complete formation of complex **2** at this concentration. The isosbestic point at λ = 236 nm revealed that no other species was formed but the 1:1 complex. The weak absorption at λ = 330 nm observed in **1** (ε = 34 L mol⁻¹ cm⁻¹, see Figure 1 a) disappeared completely. Instead, a shoulder developed at λ = 266 nm (Figure 1 b).

The large red shift in the absorption spectra of the complex **2** compared to 2-cyclohexenone (**1**) can be explained by inspection of the calculated vertical excitation energies. Starting from the optimized ground state geometry, the excited state energies were calculated on XMS-CASPT2(6,5)/cc-pvtz level of theory for the singlets S₁, S₂ and the triplets T₁ and T₂. In both cases the agreement between theory and experiment is excellent (Table 1).

In the enone **1**, the S₁(nπ*) state is almost dark, only the S₂(ππ*) state exhibits a significant transition dipole moment of 4.53 D (Table 1). Complex **2** exists in two conformers (see Scheme 1 and Figure S7), in which the boron atom resides in the plane of the conjugated π-system and the BF₃ group is oriented either towards or away from the C=C double bond (structure **2**, respectively, **2'** in Scheme 1). Both conformers exhibit very similar energies and nearly identical absorption spectra. All frontier orbitals of **2** involved in the excitation process, π, n, and π*, shown in Figure 2 for one of the conformers, are stabilized with respect to **1**. The n-orbital representing a lone pair orbital of oxygen is most strongly

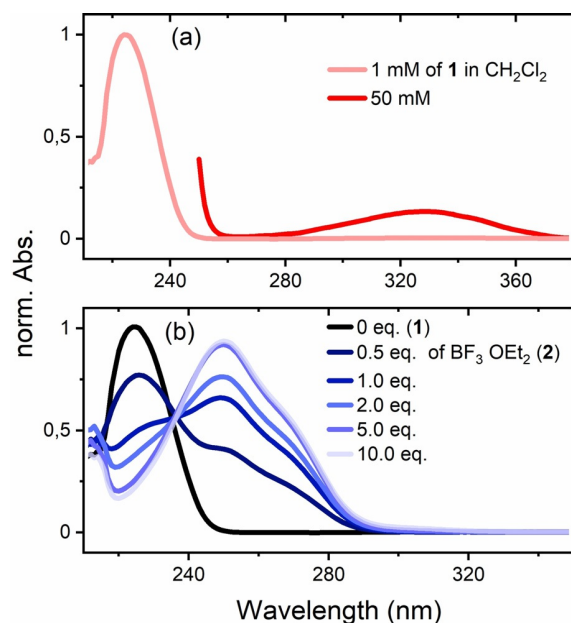


Figure 1. (a) UV/Vis absorption spectrum of 2-cyclohexenone (**1**, CH₂Cl₂, c = 1.0 mM, rose; c = 50 mM, red) and (b) its variation (c = 1.0 mM) upon addition of 0 equiv. (black), 0.5 equiv., 1.0 equiv., 2.0 equiv., 5.0 equiv. and 10.0 equiv. of BF₃·OEt₂ (formation of **2**, blue).

Table 1: Calculated absorption maxima and transition dipole moments for the lowest two singlet transitions in **1** and **2**. The two values for **2/2'** are for the two different conformers (see Scheme 1 and Figure S7). The absorption maxima of the experimental absorption bands and the shoulder observed in the complex **2** are given in parentheses.

| | Excited State | Transition Energy in eV | Transition Wavelength in nm | Transition Dipole in D |
|-------------|----------------------|-------------------------|-----------------------------|------------------------|
| 1 | S ₁ (nπ*) | 3.73 (3.76) | 333 (335) | 0.0695 |
| | S ₂ (ππ*) | 5.74 (5.54) | 216 (224) | 4.53 |
| 2/2' | S ₁ (nπ*) | 4.87/ 4.87 (4.66) | 255/ 255 (266) | 0.126/ 0.594 |
| | S ₂ (ππ*) | 5.08/ 5.15 (4.96) | 244/ 241 (250) | 4.93/ 5.06 |

affected as it participates in the σ-bond formation with the Lewis acid BF₃. The partial transfer of electron density from the oxygen to the boron atom lends some oscillator strength to the nπ* transition and causes a strong blue shift of the S₁(nπ*) absorption band from 333 nm to 255 nm. The π*-orbital is subject to an intermediate level of stabilization as it is not directly involved in the O–B bond but is localized close to the oxygen atom. The π-orbital is the least stabilized by complex formation, leading to an overall red shift of the S₂(ππ*) state in the complex.

The absorption spectra are computed as described in the Computational Methods section of the supporting information and are compared to the experimental spectra in Figure 3 a for **1** and Figure 3 b for **2**. In complex **2**, the S₂ and S₁ bands partly overlap such that the S₁ contribution can be assigned to the shoulder in the experimental spectrum (Figure 3 b). Complex formation affects singlet and triplet states in a similar manner. As the two triplet states lie very

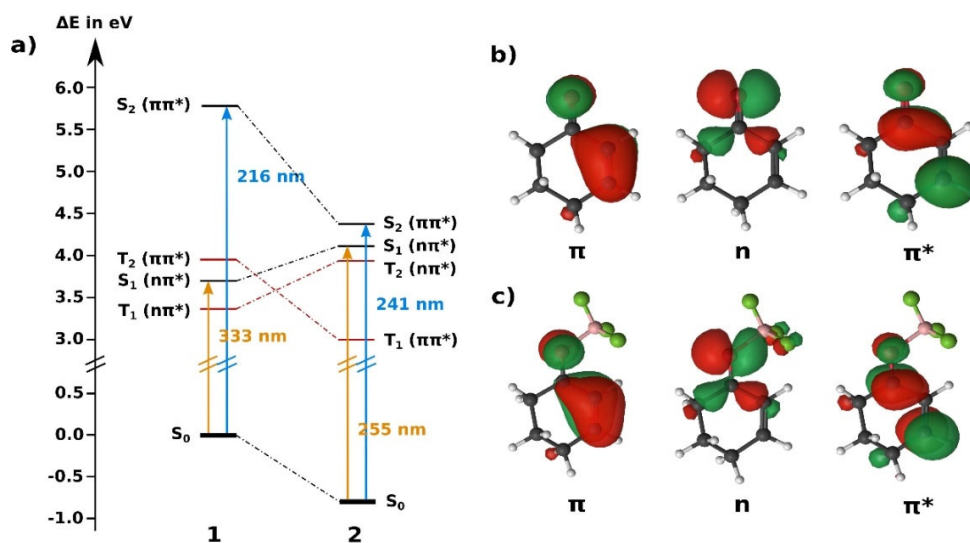


Figure 2. (a) Calculated relative energies of the three lowest singlet and two lowest triplet states at the Franck-Condon point of **1** and **2**. Excitation wavelengths corresponding to the transitions from the ground to the singlet excited states are indicated to allow a direct comparison with the experimental spectra. Orbitals with major contributions to the excitations of **1** and **2** are shown to the right in (b) and (c), respectively.

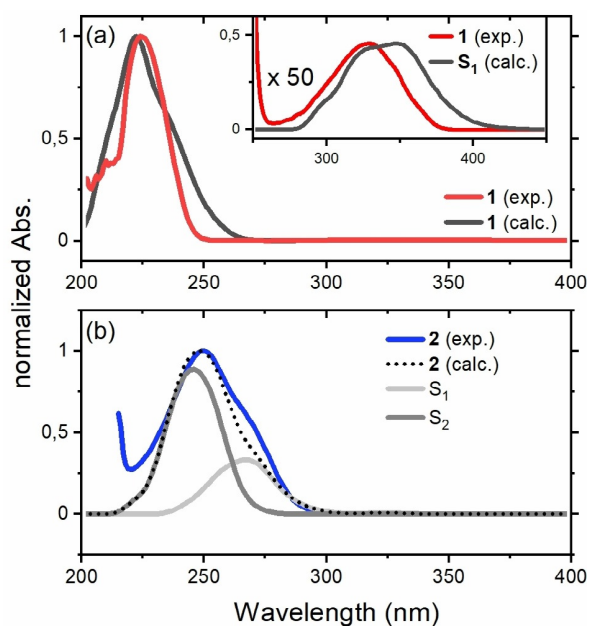


Figure 3. Comparison of the theoretical and experimental UV/Vis spectra. (a) Experimental spectrum of **1** (CH_2Cl_2 , $c=1.0$ mM, $c=50$ mM in the inset, red), calculated absorption (black) of the $S_1(\pi\pi^*)$ state (in the inset, multiplied by a factor of 50) and the $S_2(\pi\pi^*)$ state of **1**. (b) Experimental spectrum of **2** (CH_2Cl_2 , $c=1.0$ mM, blue), calculated absorption of the $S_1(\pi\pi^*)$ state (light grey), the $S_2(\pi\pi^*)$ state (dark grey) and total absorption (black, dotted) of **2**.

close in **1**, complexation leads to a change of character of the T_1 and T_2 states. In both isomers of the complex (**2/2'**) T_1 has now $^3(\pi\pi^*)$ character, while T_2 assumes $^3(n\pi^*)$ character. In **1**, the S_1 state is sandwiched between $T_1(n\pi^*)$ and $T_2(\pi\pi^*)$ while in the complex both triplets are located energetically below the S_1 state (see Figure 2a). Significant spin-orbit coupling

only occurs between $\pi\pi^*$ and $n\pi^*$ configurations in accordance with El Sayed's rule.^[22]

Reaction Path and Trajectory Calculations for Enone 1. Starting from the Franck-Condon (FC) geometry, the $^1(\pi\pi^*)$ electronic configuration is preserved along the reaction path in the S_1 state. A planar $S_1(\pi\pi^*)$ minimum could be located as well as two conical intersections (CoIn) with the ground state S_0 . At CoIn 1, the ring structure is twisted along the HC=CH dihedral and CoIn 2 is an open ring structure (Figure 4). CoIn 1 lies energetically at the same level as the FC geometry whereas CoIn 2 lies energetically above the FC point (Figure 4, see also Table S5). Hence, no significant transfer through these intersections is expected, instead relaxation might occur via the triplet states. Two minima are found in the adiabatic T_1 potential: the first is planar and of $n\pi^*$ configuration and lies in the FC region, while the second lower one is twisted and of $\pi\pi^*$ configuration (Figure 4). Both minima are connected via a CoIn (T_1T_2 CoIn) and a barrier in its close vicinity. Thus, along the reaction coordinate the $T_2(\pi\pi^*)$ state crosses the $S_1(\pi\pi^*)$ state. Between these states the spin orbit coupling of 37.96 cm^{-1} is large enough and the energy gap small enough to expect significant intersystem crossing (ISC) from $S_1(\pi\pi^*)$ to $T_2(\pi\pi^*)$. Thereafter, the $T_2(\pi\pi^*)$ population passes the T_1T_2 CoIn diabatically and becomes $T_1(\pi\pi^*)$, which is long-lived as its spin-orbit coupling to the ground state is small (5.73 cm^{-1}) and the energy gap is large (1.06 eV).

The expectations from the static calculations were verified by trajectory calculations at the XMS-CASPT2(8,7)/cc-pvdz level of theory including non-adiabatic and also spin-orbit coupling. For the dynamics, a smaller double-zeta basis set was employed, which leaves the energetic order of the involved states unaffected at critical points of the potential energy surface (see Tables S6 and S9).

13 Trajectories were started from the S_1 state, ten of which reached the final simulation time of 2 ps. For details see section 6.4 of the supporting information. This small sample

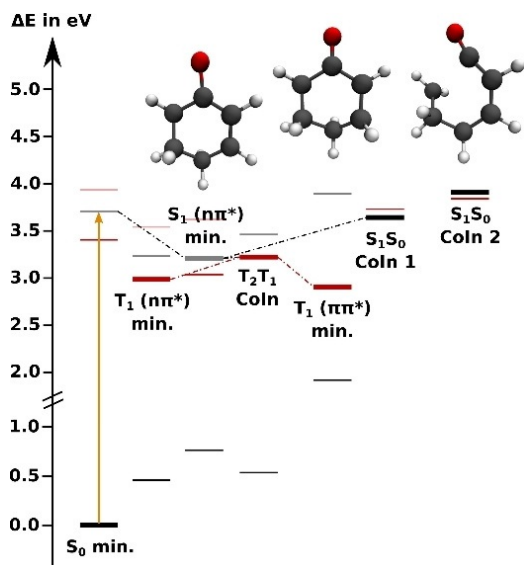


Figure 4. Energy levels of the adiabatic states of **1** at critical points relevant to the relaxation process evaluated on XMS-CASPT2(8,7)/cc-pvdz level of theory. S_0 is shown in black, S_1 in grey; T_1 is shown in red and T_2 in faint red. The thick horizontal lines indicate the energies of the optimized states, while the thin lines indicate the energies of all other states at the optimized geometries (see Tables S5–S10). The dotted lines suggest possible relaxation pathways. The molecular structures are the planar $S_1(n\pi^*)$ minimum (left, slightly elongated C–O bond), the twisted $T_1(\pi\pi^*)$ minimum (middle, torsion around the C–C double bond) and the ring-opening CoIn between S_1 and S_0 (right).

size at a high level of electronic structure theory should give a good picture of the major reaction pathways as all the surviving trajectories show a similar behavior. Only reaction channels of minor importance might be missed. No repopulation of the ground state via either S_1S_0 CoIn 1 or S_1S_0 CoIn 2 was observed, instead, the S_1 state decayed completely to the triplet states with a time constant of approximately 750 fs (Figure 5).

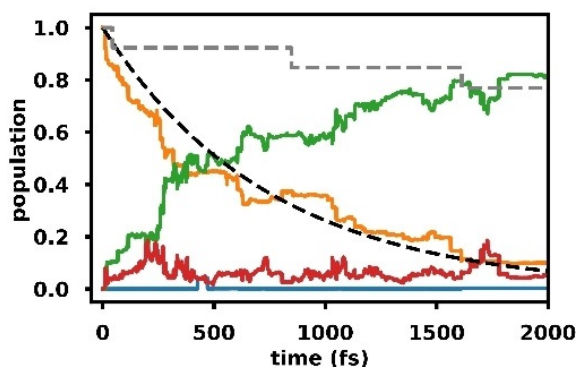


Figure 5. Adiabatic state populations based on quantum amplitudes for XMS-CASPT2(8,7)/cc-pvdz surface hopping trajectories started in the S_1 state of **1**; S_1 (orange), S_0 (blue), T_1 (green), T_2 (red), exponential fit of the singlet triplet population transfer with a time constant of 746 fs (black, dashed), fraction of active trajectories (grey, dashed).

This is in good agreement with previous experiments in which a triplet quantum yield close to unity was reported after excitation of 2-cyclohexenone (**1**) to the S_1 state.^[16] After subtraction of the backwards crossings, there were in total eleven hops from S_1 to T_2 and eleven hops from T_2 to T_1 . All transitions between S_1 and T_2 occurred at nearly planar geometries close to the S_1 minimum. These transitions were associated with a change in the character of the electronic wavefunction from $^1(n\pi^*)$ to $^3(\pi\pi^*)$. Since the T_2T_1 CoIn is also close to the planar geometry, the crossings from $S_1(n\pi^*)$ to $T_2(\pi\pi^*)$ were generally followed immediately by a hop from $T_2(\pi\pi^*)$ to $T_1(\pi\pi^*)$. Accordingly, Figure 5 does not show a significant build-up of population in T_2 . The T_1 state can subsequently relax to the $T_1(\pi\pi^*)$ minimum via a twist in the HC=CH dihedral angle. All trajectories that reached the final 2 ps showed some amount of twisting. As no cooling mechanisms were included, they can oscillate quite far away from the triplet minimum due to the large amount of kinetic energy gained along the relaxation path from the FC region which leads to occasional crossings back into T_2 .

Reaction Path and Trajectory Calculations for Complex 2.

The two conformers **2** and **2'** are energetically very similar with equivalent local and global minima on the potential energy surface. In the following, we will limit our discussion to conformer **2**. In **2**, the FC geometry (Figure 6) is close to a CoIn between S_2 and S_1 (S_2S_1 CoIn). Even an excitation to S_2 will relax very fast to S_1 via the S_2S_1 CoIn, which simultaneously acts as a branching point towards two different pathways.

Preserving the $\pi\pi^*$ character the system reaches a CoIn with the ground state (S_1S_0 CoIn 1) at a twisted geometry. Preserving the $n\pi^*$ character, the system can reach the $S_1(n\pi^*)$ minimum. At this geometry the BF_3 group is rotated out of the molecular plane and the oxygen-boron bond is elongated. This path can lead to heterolytic dissociation of the complex in the gas phase. In this direction another CoIn with the ground state (S_1S_0 CoIn 2) was found with an open ring structure. Thus, in contrast to enone **1** there are two energetically accessible CoIns, and internal conversion can act as a competing channel to ISC. During relaxation into the $S_1(n\pi^*)$ minimum the $T_2(\pi\pi^*)$ state crosses the S_1 state allowing for significant ISC with spin-orbit couplings around 25 cm^{-1} . As in **1**, the T_1 state of **2** displays two minima, one local of $n\pi^*$ - and one global of $\pi\pi^*$ -character, which are connected by the T_1T_2 CoIn. The $T_1(n\pi^*)$ minimum is geometrically close to the S_1 minimum with the BF_3 group rotated out of plane, while the $T_1(\pi\pi^*)$ minimum is geometrically close to the S_1S_0 CoIn 1 with a twist along the C=C double bond. Compared to the enone reaction path we observe two main differences: close lying and optically addressable S_1 and S_2 states and energetically accessible CoIns with the ground state.

To verify whether the proposed relaxation pathways actually take place in the excited complex **2**, we performed surface hopping calculations at the XMS-CASPT2(8,7)/cc-pvdz level of theory. Due to computational costs, triplet states and spin-orbit coupling could not be included. In addition, a smaller basis set was employed, which only had minor effects on the relative energies of the involved states at critical

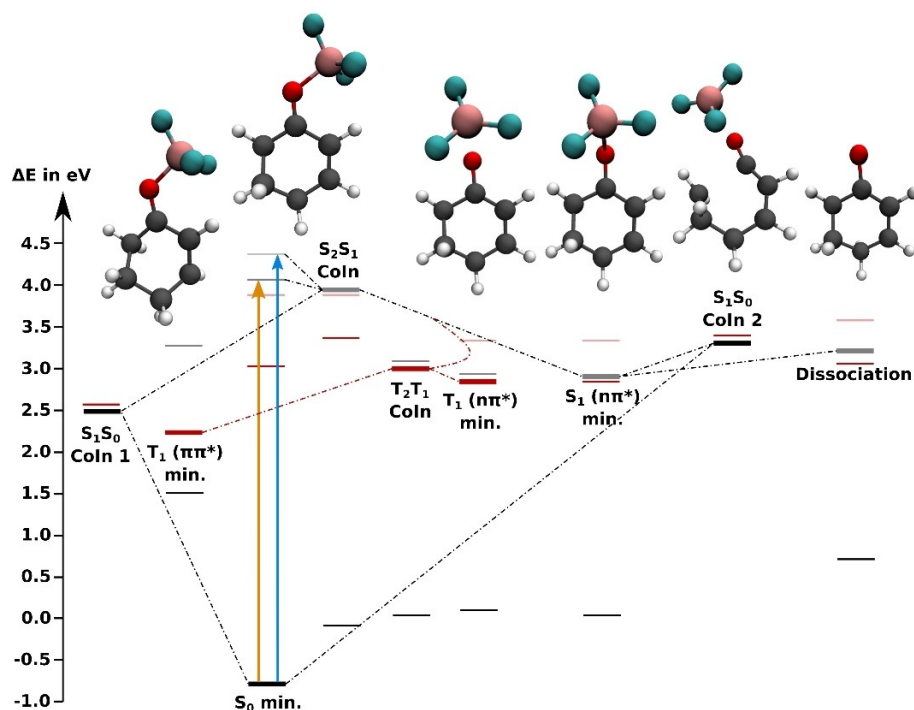


Figure 6. Energy levels of the adiabatic states of **2** at critical points relevant to the relaxation process evaluated at XMS-CASPT2(8,7)/cc-pvdz level of theory. S_0 is shown in black, S_1 in grey and S_2 in faint grey; T_1 is shown in red and T_2 in faint red. The thick horizontal lines indicate the energies of the optimized states, while the thin lines indicate the energies of all other states at the optimized geometries (see Tables S15–S20). The dotted lines suggest possible relaxation pathways. The molecular structures are (from left to right): The twisted $T_1(\pi\pi^*)$ minimum (torsion around the C–C double bond), the FC geometry, the $T_1(n\pi^*)$ and $S_1(\pi\pi^*)$ minima with the torsion around the C–O double bond and the elongated O–B bond, the ring opening CoIn between S_1 and S_0 and the S_1 minimum of free 2-cyclohexenone (**1**) that is reached by dissociation in the S_1 state.

points of the potential energy surface (see Tables S16 and S19). While dynamics in the singlet states can only provide a part of the picture, it was possible to investigate a larger number of trajectories. In total 50 trajectories per conformer and initial state were run. The results differed depending on whether the trajectories were started in the $S_1(n\pi^*)$ state or the $S_2(\pi\pi^*)$ state. Starting from S_1 , most trajectories led to dissociation, since by removing an electron from the n-orbital the oxygen-boron bond is weakened so that the energy gained by relaxation from the FC region is enough to break it. Eleven trajectories did not dissociate. All of them showed a hop from S_1 to S_0 early in the propagation. In total, we observed thirteen hops from S_1 to S_0 , of which eleven happened at a twisted structure (S_1S_0 CoIn 1) while two occurred at an open ring structure (S_1S_0 CoIn 2). Interestingly, there was a significant difference between the two conformers of the complex. When the BF_3 was on the same side as the double bond (**2**), the relaxation mainly proceeded through S_1S_0 CoIn 1. When the BF_3 pointed away from the double bond (**2'**), dissociation was more likely, and relaxation mainly proceeded through S_1S_0 CoIn 2. The population dynamics of the trajectories starting in S_2 is shown in Figure 7. In this case, the difference between the two conformers was small. All trajectories quickly relaxed to S_1 , but from there, different pathways were taken. 34 Trajectories relaxed to the S_0 state, 30 of them hopped at

a twisted structure similar to the S_1S_0 CoIn 1. In general, these trajectories did not show dissociation. They followed the electronic $\pi\pi^*$ character diabatically. The other four hops occurred at an open-ring structure similar to S_1S_0 CoIn 2 and contained a broken or very elongated oxygen-boron bond. Due to these accessible relaxation channels we see a re-population of the S_0 ground state on a time scale below 150 fs. The remaining 66 trajectories stayed in the S_1 . These trajectories follow the $n\pi^*$ character diabatically and mainly show dissociative behavior in the gas phase. In solution, caging effects could decelerate or even prevent the dissociation.^[23]

Transient Absorption Spectra. We experimentally addressed the photoinduced dynamics of compound **2** on time-scales commensurate with intramolecular electronic relaxation using femtosecond TA spectroscopy. We initiated excited-state dynamics by pulses centered at 285 nm, to predominantly excite the $S_0 \rightarrow S_1$ transition, and followed the time-evolution by UV and UV/Vis probe pulses. A

representative selection of TA spectra is shown in Figure 8, where the spectral evolution over the first several picoseconds after excitation is clearly illustrated.

Over the time-range displayed here, substantial changes were observed in particular in the visible: immediately on

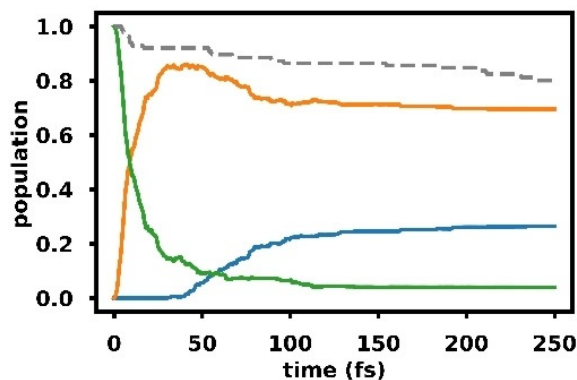


Figure 7. Adiabatic state populations based on Boltzmann averaged quantum amplitudes for XMS-CASPT2(8,7)/cc-pvdz surface hopping trajectories started in the S_2 state of **2** and **2'**; S_2 (green), S_1 (orange), S_0 (blue); Boltzmann weighted fraction of active trajectories of **2** and **2'** (grey, dashed).

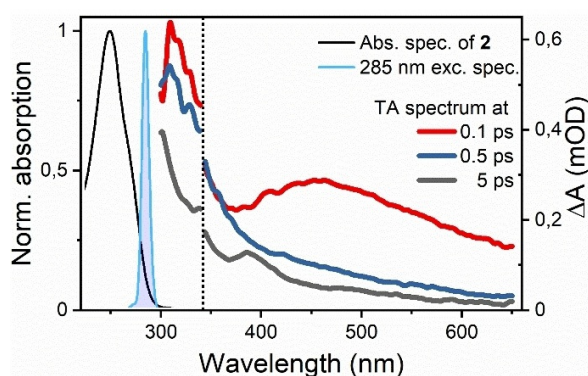


Figure 8. Normalized absorption (black line), excitation spectra (blue shaded area) and TA spectra of **2** at several time-delays (colored lines). TA spectra in the UV ($\lambda < 340$ nm) and Visible ($\lambda > 340$ nm) range were recorded in separate experiments.

excitation, a broad visible excited-state absorption (ESA) band covering 400–600 nm was formed. This band subsequently decayed on a timescale of a few hundred femtoseconds, revealing rapid population transfer out of the initially excited FC region. Following this initial process, subtler changes, as well as an overall loss of signal intensity, took place across the UV/Vis spectral range over the next several picoseconds. Figure 9 displays the (normalized) TA maps in two-dimensional detection wavelength vs. time-delay plots.

The initial ≈ 100 fs of the dynamics are dominated by the coherent artifact (CA), inhibiting detailed analysis within this range. After the CA, however, the spectra were well behaved

and revealed the relaxation dynamics on the excited state surface. Again, we saw a broad ESA feature characterizing the excited state at the FC point. This band rapidly decayed, leaving only a weak featureless ESA in the visible range as well as a more intense band in the UV. These bands decayed much more slowly, reaching a quasi-equilibrium state after a few picoseconds as demonstrated by the transients at UV and visible detection wavelengths in Figure 9b. TA spectra from experiments recorded using 260 nm excitation, displaying similar behavior, are shown in Figures S1 and S2. Note that long-lived oscillatory features were observed across the spectrum regardless of detection wavelength, but with highest amplitude at 340 nm as shown in Figure 9b. These oscillations are not related to intra-molecular dynamics of the studied complex but are rather impulsive stimulated Raman scattering features originating from the solvent (see Figure S4 for pure solvent spectra).

Kinetic Model and Data Analysis. We can extract quantitative information about the excited-state relaxation dynamics by simultaneously fitting the time-evolution of the signal at all detection wavelengths to a sum-of-exponentials decay model (sequential model, see below), using the time constants as global parameters. A purely sequential model ($A \rightarrow B \rightarrow C \dots$) is one of the simplest deactivation schemes, which is however also supported by the theoretical model in Figure 6. From a physical perspective, we expect a bifurcation of the S_1 population via $S_1 \rightarrow S_0$ and $S_1 \rightarrow T_1$. We do not expect to observe the former channel directly, that is, the formation of a vibrationally hot ground state, as the TA probing range does not cover the ground state bleach region (see Figure 9 in comparison to the absorption spectrum in Figure 8). For the remaining and spectrally observable reaction pathway, $S_1 \rightarrow$

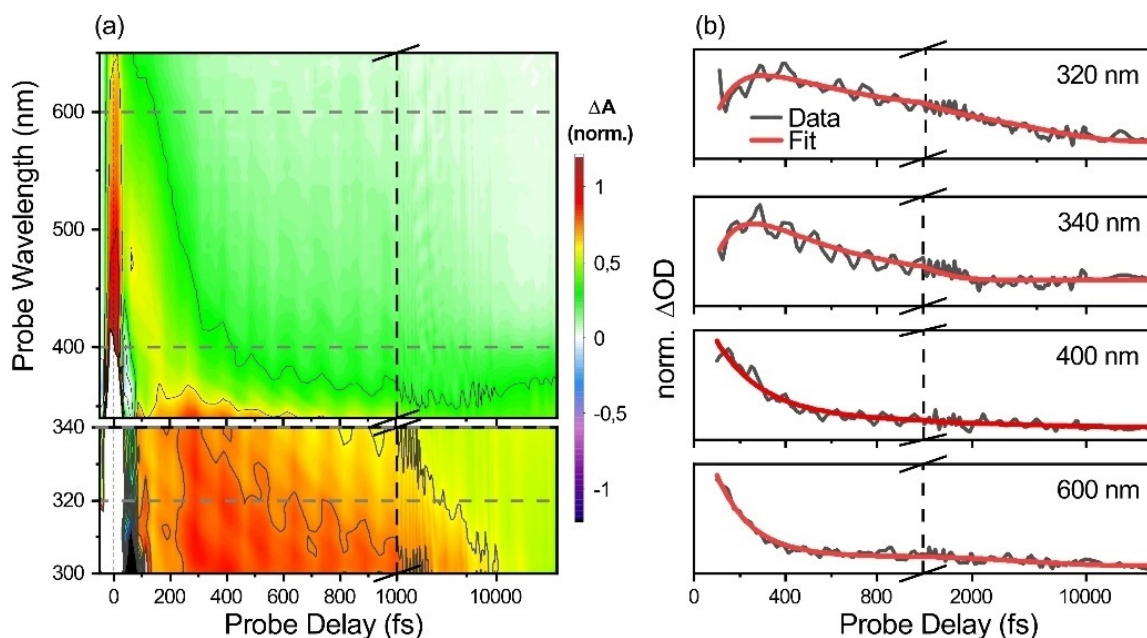


Figure 9. (a) Transient absorption maps for **2** DUV (bottom) and UV/Visible (top) probe range spectra after 285 nm excitation. Spectra are normalized to the signal maximum in the DUV experiment. Time-scale changed to logarithmic at 1 picosecond. (b) Transients at indicated detection wavelengths (dark grey) in comparison to fit results from global analysis (red). Spectra at each detection wavelength are normalized to their respective maximum.

T_1 , theory predicts a uni-directional relaxation, for which a purely sequential model is a good approximation. Singular value decomposition and inspection of the resulting fit residuals reveals that four time constants suffice to explain the photodynamics after 285 nm excitation. All time constants are collected in Table 2.

Table 2: Collected time constants extracted from global kinetic analysis of the transient absorption experiments. The longest living component (corresponding to the ground-state recovery) has a decay-time longer than the measurement time window.

| | Component | Lifetime in ps |
|-----------|-----------|----------------|
| DUV probe | τ_1 | 0.10 |
| | τ_2 | 0.45 |
| | τ_3 | 4.8 |
| | τ_4 | > 50 |
| VIS probe | τ_1 | 0.16 |
| | τ_2 | 0.30 |
| | τ_3 | 4.4 |
| | τ_4 | > 50 |

The fastest component in the TA data decays on a 100–150 fs timescale and is readily attributed to rapid decay of the initially excited FC state, while the ground-state recovery at long times proceeds on timescales longer than our probe window (i.e. > 50 ps). At intermediate times, the picture is less clear, at least before a comparison with the theoretical studies was made as given in the next section. We observe two components with sub-ps and few ps dynamics.

In addition to the time constants of the components in a multi-exponential decay fit, it is useful to represent also their amplitudes. A spectral representation of these reveals detailed information about the probe wavelengths at which a given process contributes. While a number of spectral representations are possible, we here show the *Evolution Associated Decay Spectra* (EADS)^[24] in Figure 10 (time constants and EADS from 260 nm excitation experiment shown in Figure S3). The physical model imposed on the data in this representation is a strictly sequential transfer between a set of „compartments“, where the EADS can be interpreted

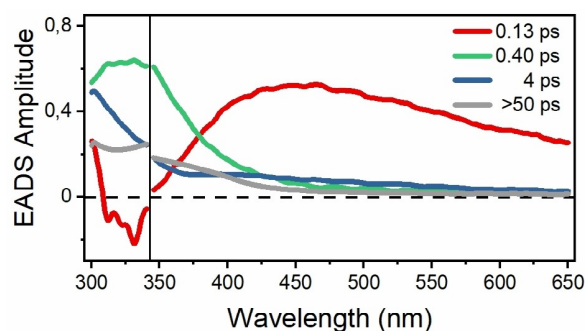


Figure 10. Evolution associated decay spectra extracted from global kinetic analysis of TA data after excitation at 285 nm. The time constants noted are approximate representations of parameters extracted from both UV and visible experiments—the actual time constants from a given dataset can be found in Table 2.

as the transient spectra of the individual compartments. As such, the population is initially found in „compartment 1“, whereafter it transfers to „compartment 2“, and so on.

The EADS in Figure 10 renders our qualitative observations quantitative regarding the raw data in Figure 9. The initially excited state displays a broad ESA across the visible spectrum. As it decays on a ≈ 130 fs time-scale, a spectrally distinct state—characterized largely by strong UV absorption—is formed. Subsequently, on timescales from several hundred fs to a few ps, we observe signal loss and small-scale spectral changes largely in the UV range between 300 and 400 nm.

Overall, these spectral dynamics are consistent with initial excitation, followed by rapid transfer into a manifold of states, where the electronic structure is substantially different. In the following section, these assignments are substantiated significantly by a theoretical analysis of excited state spectra.

Excited State Spectra—Experiment vs. Theory. The theoretical approaches discussed so far describe processes connected to the optical excitation (Figures 2 and 3), and the subsequent population relaxation processes including non-adiabatic coupling and ISC (Figures 4–7). As XMS-CASPT2 can also accurately capture higher lying excited states, it further provides a direct connection between populations and spectral observables through calculated ESA spectra (the calculation of the ESA spectra is described in the Computational Methods section of the supporting information). This in turn greatly facilitates the discussion of the experimental results, as the EADS in Figure 10 can now be assigned to specific excited states and molecular geometries by comparison with calculated ESA features. In Figure 11 we compare the calculated ESA spectra of S_1 in the FC region and T_1 in the

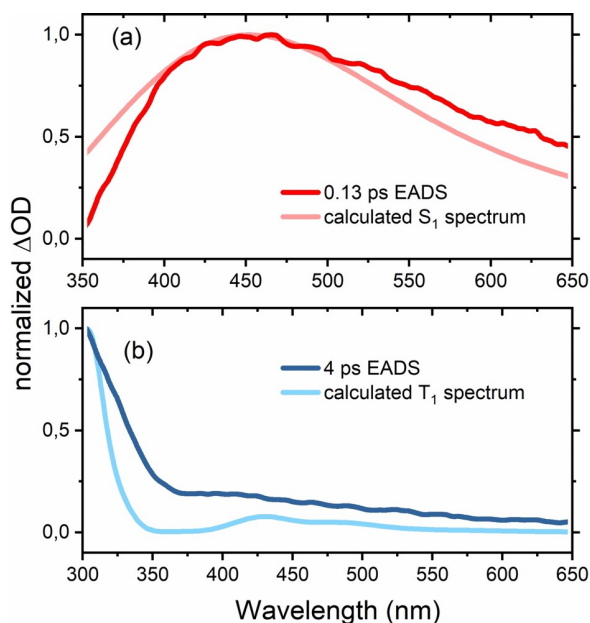


Figure 11. Comparison between selected EADS (full colors) and calculated ESA spectra (faint colors) of singlet state S_1 of $2/2'$ in the FC region (a) and triplet state T_1 thermalized in the $T_1(\pi\pi^*)$ minimum (b).

T₁($\pi\pi^*$) minimum to relevant EADS. Based on the fact that S₁ may deactivate both towards S₀ (see Figure 7 for population dynamics of **2**) and to the triplet states T₁ and T₂, we expect its overall lifetime to be short. Accordingly, comparison of the fastest decaying EADS component with a 0.13 ps lifetime (red curve in Figure 11(a)) with the calculated ESA spectrum of S₁ in the FC region (faint red curve) gives qualitatively excellent agreement. The calculated spectrum is the sum of three transitions, that is, S₁→S_{2,3,4}, where we depict their relative weights and the analogous decomposition of the T₁ ESA spectrum in Figures S11 and S10, respectively. The minor deviation between experiment and theory in Figure 11(a) in the spectral regions below 400 nm is readily explained by the pump pulse-related CA, still contributing significantly at such early delay times.^[25] Thus we can assign the fastest decay component to the relaxation of S₁ out of the FC region either to the ground-state S₀ through conical intersections or to the S₁($n\pi^*$) minimum.

The triplet state T₁ is the lowest lying excited state of **2** (see Figure 6). Hence, we compare the calculated ESA spectrum in the T₁($\pi\pi^*$) minimum (blue faint line in Figure 11(b)) to the component with a long lifetime—specifically the 4 ps EADS (blue line). Even though we retrieved a component with an even longer lifetime (see Figure 9), we chose to compare to the 4 ps EADS, as this component's lifetime is still reliable within the 50 ps delay window of the experiment. As for the S₁ case, the qualitative agreement between experiment and theory is remarkable (Figure 11(b)). We note that the results of global analysis, that is, EADS, relate to the entire TA-signal, while the theoretical predictions were made for ESA spectra only. The direct comparison of the calculated ESA-spectra to the retrieved EADS is only feasible thanks to the lack of ground state bleach contributions in the employed probing range of Figure 11 and to the weak stimulated signal for both S₁ and T₁. Comparison to theory hence allows us to assign the retrieved spectral species of Figure 9 to relaxation out of the FC region of S₁ (0.13 ps EADS), ISC to triplet states (0.4 ps), relaxation of hot triplet states (4 ps) and a long-lived residual (> 50 ps), which is attributable to the lowest lying triplet state T₁ and its relaxation back to the ground state. The excellent agreement of the calculated triplet spectrum and the 4 ps EADS strongly suggests that the dissociation that is predicted by surface hopping calculations in the gas phase is not a large contributor to the dynamics of **2** in solution. The triplet spectra of **1** which would result from dissociation, were also calculated and do not match the observed EADS but are instead much more red-shifted (see Figure S12).

Preliminary studies on photoreactivity. Our results indicate that it should be possible to involve enones in a photochemical Lewis acid-catalyzed reaction upon proper selection of the irradiation wavelength. While complexation opens up additional relaxation pathways which avoid the photochemically relevant triplet state, these additional decay routes are non-critical, as they lead back to the electronic ground state. Hence, there are no chemical by-products and the complex remains in solution for further photocatalytic cycles. By appropriate choice of the excitation wavelength, it should therefore be possible to compensate for the loss of

reactive excited state species by an increased absorption cross section.

In a preliminary study, we investigated whether the BF₃ complex **2** is productive in photocatalysis. 2-Cyclohexenone (**1**) was irradiated together with isobutene at a wavelength ($\lambda = 272$ nm) at which the compound is transparent (see Figure 1). There was no detectable conversion after six hours (see section 7 of the SI for details). When the same reaction was performed in the presence of BF₃·OEt₂ (50 mol %) a steady conversion could be detected (see Figure S13). In the absence of light there was no reaction. This preliminary work supports the fact that the triplet state of **2** is productive in photocatalysis and suggests Lewis acid catalyzed photochemical reactions to be possible upon judicious choice of the irradiation wavelength.

Conclusion

In summary, we have investigated the small enone Lewis acid complex **2** by highly accurate quantum chemical methods and by state-of-the art ultrafast transient absorption spectroscopy in the UV-range. The complex serves as a prototype to understand the influence of Lewis acid catalysts on the photochemistry of cyclic enones. The changes due to complexation were evaluated by comparison with the free enone **1**. Regarding absorption in the UV/Vis spectrum, the Lewis acid induces a significant blue shift of the S₁ state and increases its oscillator strength. The S₁ state is almost dark for enone **1** but becomes bright for complex **2**. The bright S₂ state of the enone is red-shifted by the Lewis acid and overlaps energetically with S₁. While the enone decays from S₁ completely to the triplet ($n\pi^*$) and ($\pi\pi^*$) states, the enone complex **2** passes conical intersections at which a decay to the ground state S₀ is feasible. An alternative pathway allows the enone complex to populate the triplet T₁($\pi\pi^*$) state. Both the S₁ and T₁ state of complex **2** could be detected by transient absorption spectroscopy and it was shown that coordination to the Lewis acid is retained in T₁. The latter observation is in line with the fact that chiral boron-based Lewis acids induce a high enantioselectivity in the [2+2] photocycloaddition reaction of 2-cyclohexenone.^[26] Population of T₁ occurs on a picosecond time scale which in turn suggests that this state is solely responsible for the photochemistry of the Lewis acid-enone complex. Further synthetic studies are warranted to identify novel reaction pathways for Lewis acid-enone complexes as compared to the known transformations of enones.

Acknowledgements

Financial support by the European Research Council under the European Union's Horizon 2020 research and innovation programme (grant agreement No 665951—ELICOS) is gratefully acknowledged. R.dVR and J.H. acknowledge funding by DFG under Germany's ExcellenceStrategy-EXC 2089/1–390776260. D.P.S. thanks *Studienstiftung des deutschen Volkes* for a Ph.D. fellowship, S. Breitenlechner (TUM) for fruitful discussions and J. Kudermann (TUM) for his help with GLC

analyses. Open access funding enabled and organized by Projekt DEAL.

Conflict of interest

The authors declare no conflict of interest.

Stichwörter: calculations · enones · lewis acids · photochemistry · time-resolved spectroscopy

- [1] a) P. Praetorius, F. Korn, *Ber. Dtsch. Chem. Ges.* **1910**, *43*, 2744–2746; b) F. H. Stobbe, E. Färber, *Ber. Dtsch. Chem. Ges.* **1925**, *58*, 1548–1553.
- [2] a) S. C. Shim, E. I. Kim, K. T. Lee, *Bull. Korean Chem. Soc.* **1987**, *8*, 140–144; b) T. Ogawa, Y. Masui, S. Ojima, H. Suzuki, *Bull. Chem. Soc. Jpn.* **1987**, *60*, 423–425; c) S. C. Shim, S. S. Lee, *Bull. Korean Chem. Soc.* **1989**, *10*, 324–326.
- [3] Most recent contributions from the series: a) F. D. Lewis, S. V. Baranczyk, E. L. Burch, *J. Am. Chem. Soc.* **1992**, *114*, 3866–3870; b) F. D. Lewis, G. D. Reddy, J. E. Elbert, B. E. Tillberg, J. A. Meltzer, M. Kojima, *J. Org. Chem.* **1991**, *56*, 5311–5318.
- [4] a) S. Fukuzumi, T. Okamoto, J. Otera, *J. Am. Chem. Soc.* **1994**, *116*, 5503–5504; b) S. Fukuzumi, N. Satoh, T. Okamoto, K. Yasui, T. Suenobu, Y. Seko, M. Fujitsuka, O. Ito, *J. Am. Chem. Soc.* **2001**, *123*, 7756–7766.
- [5] For a recent review, see: S. Fukuzumi, J. Jung, Y.-M. Lee, W. Nam, *Asian J. Org. Chem.* **2017**, *6*, 397–409.
- [6] Recent reviews: a) C. Prentice, J. Morrisson, A. D. Smith, E. Zysman-Colman, *Beilstein J. Org. Chem.* **2020**, *16*, 2363–2441; b) T. Rigotti, J. Alemán, *Chem. Commun.* **2020**, *56*, 11169–11190; c) C. Brenninger, J. Jolliffe, T. Bach, *Angew. Chem. Int. Ed.* **2018**, *57*, 14338–14349; *Angew. Chem.* **2018**, *130*, 14536–14547.
- [7] H. Guo, E. Herdtweck, T. Bach, *Angew. Chem. Int. Ed.* **2010**, *49*, 7782–7785; *Angew. Chem.* **2010**, *122*, 7948–7951.
- [8] J. Du, K. L. Skubi, D. M. Schultz, T. P. Yoon, *Science* **2014**, *344*, 392–396.
- [9] R. Brimiouille, T. Bach, *Science* **2013**, *342*, 840–843.
- [10] T. R. Blum, Z. D. Miller, D. M. Bates, I. A. Guzei, T. P. Yoon, *Science* **2016**, *354*, 1391–1395.
- [11] X. Huang, T. R. Quinn, K. Harms, R. D. Webster, L. Zhang, O. Wiest, E. Meggers, *J. Am. Chem. Soc.* **2017**, *139*, 9120–9123.
- [12] a) N. Hu, H. Jung, Y. Zheng, J. Lee, L. Zhang, Z. Ullah, X. Xie, K. Harms, M.-H. Baik, E. Meggers, *Angew. Chem. Int. Ed.* **2018**, *57*, 6242–6246; *Angew. Chem.* **2018**, *130*, 6350–6354; b) S. Stegbauer, C. Jandl, T. Bach, *Angew. Chem. Int. Ed.* **2018**, *57*, 14593–14596; *Angew. Chem.* **2018**, *130*, 14801–14805; c) S. Stegbauer, N. Jeremias, C. Jandl, T. Bach, *Chem. Sci.* **2019**, *10*, 8566–8570; d) J. Ma, F. Schäfers, C. Daniliuc, K. Bergander, C. A. Strassert, F. Glorius, *Angew. Chem. Int. Ed.* **2020**, *59*, 9639–9645; *Angew. Chem.* **2020**, *132*, 9726–9732.
- [13] M. Leverenz, C. Merten, A. Dreuw, T. Bach, *J. Am. Chem. Soc.* **2019**, *141*, 20053–20057.
- [14] S. Poplata, A. Bauer, G. Storch, T. Bach, *Chem. Eur. J.* **2019**, *25*, 8135–8148.
- [15] a) H. Wang, X. Cao, X. Chen, W. Fang, M. Dolg, *Angew. Chem. Int. Ed.* **2015**, *54*, 14295–14298; *Angew. Chem.* **2015**, *127*, 14503–14506; b) H. Wang, W.-H. Fang, X. Chen, *J. Org. Chem.* **2016**, *81*, 7093–7101.
- [16] D. I. Schuster, D. A. Dunn, G. E. Heibel, P. B. Brown, J. M. Rao, J. Woning, R. Bonneau, *J. Am. Chem. Soc.* **1991**, *113*, 6245–6255.
- [17] a) E. García-Expósito, M. J. Bearpark, R. M. Ortuño, V. Branchadell, M. A. Robb, S. Wilsey, *J. Org. Chem.* **2001**, *66*, 8811–8814; b) E. García-Expósito, M. J. Bearpark, R. M. Ortuño, M. A. Robb, V. Branchadell, *J. Org. Chem.* **2002**, *67*, 6070–6077.
- [18] A. M. D. Lee, J. D. Coe, S. Ullrich, M.-L. Ho, S.-J. Lee, R.-M. Cheng, M. Z. Zgierski, I.-C. Chen, T. J. Martinez, A. Stolow, *J. Phys. Chem. A* **2007**, *111*, 11948–11960.
- [19] O. Schalk, M. S. Schuurman, G. Wu, P. Lang, M. Mucke, R. Feifel, A. Stolow, *J. Phys. Chem. A* **2014**, *118*, 2279–2287.
- [20] J. Cao, Z.-Z. Xie, *Phys. Chem. Chem. Phys.* **2016**, *18*, 6931–6945.
- [21] R. F. Childs, D. L. Mulholland, A. Nixon, *Can. J. Chem.* **1982**, *60*, 801–808.
- [22] M. A. El-Sayed, *Acc. Chem. Res.* **1968**, *1*, 8–16.
- [23] S. Thallmair, M. Kowalewski, J. P. P. Zauleck, M. K. Roos, R. de Vivie-Riedle, *J. Phys. Chem. Lett.* **2014**, *5*, 3480–3485.
- [24] I. H. M. van Stokkum, D. S. Larsen, R. van Grondelle, *Biochim. Biophys. Acta Bioenerg.* **2004**, *1657*, 82–104.
- [25] V. Perlik, J. Hauer, F. Sanda, *J. Opt. Soc. Am. B* **2017**, *34*, 430–439.
- [26] S. Poplata, T. Bach, *J. Am. Chem. Soc.* **2018**, *140*, 3228–3231.

Manuskript erhalten: 15. Dezember 2020

Veränderte Fassung erhalten: 1. Februar 2021

Akzeptierte Fassung online: 17. Februar 2021

Endgültige Fassung online: 23. März 2021

4.2. Excited State Dynamics of Cyclohex-2-enone-BF₃ in Solution

As shown in section 4.1, there are two pathways in the excited state dynamics of the cyclohexenone-BF₃ complex; 1) the dissociation of the BF₃ group, which occurs in the $n\pi^*$ states due to a weakening of the coordinative O–B bond; 2) the crossing into the states of $\pi\pi^*$ character, which are more strongly bound and lead to a twist of the H–C=C–H dihedral. Dynamic calculations in the gas phase with only the singlet states establish that the first pathway dominates with these simulation parameters. However, neither the time-resolved spectra nor the synthetic studies show direct evidence for this dissociation. The observed dissociation in singlet state dynamics can be rationalized because the gradient at the FC point in the S₁ state, which is of $n\pi^*$ character, points towards O–B bond elongation. Furthermore, no stable $\pi\pi^*$ minimum exists in the singlet states that can be reached by the excitation energies used in the experiments. Instead, if crossing into the $\pi\pi^*$ singlet state would occur, rapid IC through a Con with the groundstate would lead to a loss of the excitation. Thus, crossing into the triplet states is necessary to explain the experimental observations in [2]. Relaxation towards the T₁($\pi\pi^*$) minimum would allow follow-up reactions, like the observed [2+2] cycloaddition, and would explain the enantioselectivity of this reaction in complexes with chiral Lewis acids.[42] The measured transient absorption signal matches the intact complex in the T₁($\pi\pi^*$) state.

In the free enone, for the ISC process, a time constant of 746 fs was observed in TSH simulations.[2] Although there is evidence that this process is faster in complexes with Lewis acids that contain heavy atoms,[184] there is no reason to expect such a speedup in cyclohexenone-BF₃. Thus, dissociation of the complex in the singlet states, occurring on a timescale of 200 fs to 300 fs, is expected to be faster than ISC in the gas phase. A reasonable mechanism explaining a slowdown of the dissociation would be a caging effect of the surrounding solvent. This slowdown would allow ISC to compete with dissociation in solution.

In this section, TSH simulations of the cyclohexenone-BF₃ complex in an explicit solvent environment are presented, which show that caging effects do indeed slow down the dissociation significantly and altogether prevent it in a large number of cases. Although these simulations only include singlet states, they cover a duration longer than the expected time necessary for ISC. Thus, since these simulations show significantly reduced dissociation, it is reasonable to expect ISC with the Lewis acid attached. The explicit inclusion of triplet states and the simulation of the entire time-dependent spectrum will be the subject of future study.

Simulating the singlet state dynamics of cyclohexenone-BF₃ in solution is a complex task. To adequately describe the slowdown of the dissociation, multiple shells of the solvent DCM need to be included in the simulation, which amounts to several hundred solvent molecules. Obtaining the excited state gradients for such an extensive system using a quantum mechanics (QM) model is prohibitively expensive. Since there is no evidence that excitation leaves the complex, a description of the solvent by classical molecular mechanics (MM) is sufficient. Hence, a QM/MM approach is chosen, where the cyclohexenone-BF₃ complex constitutes the central QM region and the DCM shells form the MM region around it. The OPLS/AA force field was chosen to describe the MM region. The OPLS/AA force field is specifically designed for the simulation of

organic liquids and describes the properties of DCM reasonably well.[191–193] For the QM region, a good choice would be XMS-CASPT2,[61, 62], which was used to describe the gas phase dynamics in the previous study.[2] However, this would be very costly, and since the dissociation takes place entirely in the S_1 state, a cheaper alternative is available in TDDFT. TDDFT requires that a suitable functional is chosen that reproduces the XMS-CASPT2 excited state gradients at the geometries encountered during the simulation.

Apart from the gradient ∇E_1 , two other parameters should be considered when choosing the density functional; 1) the S_0S_1 energy gap ΔE_{01} , relevant for the selection of initial geometries based on the calculated absorption spectrum and theoretically possible ultrafast relaxation processes to S_0 (although these are, in general, not adequately described by TDDFT[194]); 2) the S_1S_2 energy gap ΔE_{12} , which might become relevant because the S_1 and S_2 states are energetically close in the FC region and thus S_2 might be transiently populated even after an initial excitation to S_1 . A benchmark set was explicitly constructed for 2-cyclohexenone-BF₃. From the short gas-phase dynamics presented in [2], $N = 96$ geometries were randomly sampled. At these geometries, excitation energies and gradients were calculated at the XMS-CASPT2(8,7)/cc-pvqz level of theory (for details regarding the active space, see appendix C.1).

There is a large number of DFT functionals available in the library LibXC.[195] Nearly all of them were tested (93 in total; some were excluded for technical reasons, see table C.1 for a list of all tested functionals). Corrections due to dispersion (VV10[196], D3[135]) were also tested. Since the overall errors for energies and gradients in excited states are much larger than in the ground state, the resulting corrections were found to be negligible. Since the dynamics can be performed at most with a triple-zeta basis set due to computational costs, all DFT calculations were performed using the def2-TZVP basis set. The different functionals f were compared to the benchmark calculations on the three criteria of 1) S_1 gradients ∇E_1 , 2) S_1S_2 energy gap ΔE_{12} , 3) S_0S_1 energy gap ΔE_{01} . The root-mean-square deviation (RMSD) for each criterion x and each functional f were calculated according to

$$\text{RMSD}(x, f) = \sqrt{\frac{\sum_i^N |x_i^f - x_i^{\text{CASPT2}}|^2}{N}}. \quad (4.1)$$

The RMSD values for each criterion x were shifted and scaled to obtain normalized values NRMSD(x, f). This was done so that the best ten functionals for that criterion covered the range between 0 and 1.

Then, a combined measure of error M was calculated as

$$\begin{aligned} M(f) = & w_1 \cdot \text{NRMSD}(\nabla E_1, f) \\ & + w_2 \cdot \text{NRMSD}(\Delta E_{12}, f) \\ & + w_3 \cdot \text{NRMSD}(\Delta E_{01}, f) \end{aligned} \quad (4.2)$$

with weighting factors $\{w_i\}$ that sum to 1. These weighting factors encode the relative importance of the accurate description of each benchmarked criterion for the process under study. Different functionals perform best, depending on the choice of $\{w_i\}$. In fig. 4.3, the best-performing functionals (minimal M) are shown, depending on w_1 , w_2 and w_3 . For all functionals that are best performing at any choice of $\{w_i\}$, the RMSD values for each criterion are given in table 4.1, and the averages over all 93

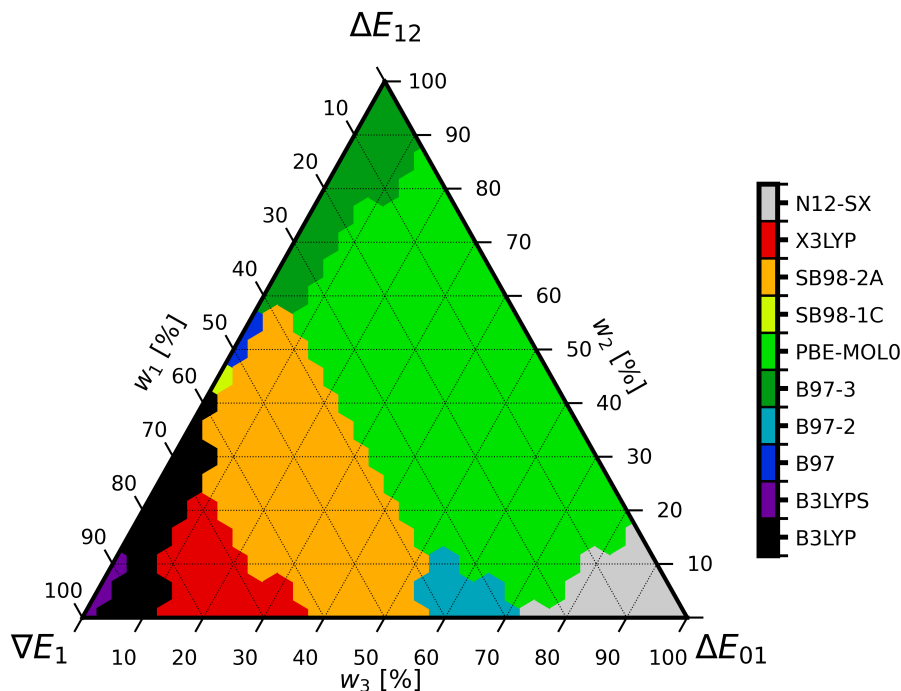


Figure 4.3.: Functionals with a minimal measure of error M according to eq. (4.2) for all different combinations of weights; weight w_1 for the gradient ∇E_1 , weight w_2 for the S_0S_1 energy gap ΔE_{01} , and weight w_3 for the S_1S_2 energy gap ΔE_{12}

tested functionals are shown in the last row. The exact RMSD values for all tested functionals can be found in the appendix (appendix C.2). The prediction of the S_1S_2 energy gap is the most difficult task with errors that are approximately a factor of three higher than for the S_0S_1 energy gap. The functionals PBE-MOL0[197] and B97-3[198] perform significantly better in the prediction of the S_1S_2 energy gap than all other functionals. Of these, PBE-MOL0 performs best for the S_0S_1 energy gap. Thus, the functional PBE-MOL0, a non-empirically improved version of PBE0 for molecular properties,[197] was chosen for the dynamics. It is the second-best for ΔE_{12} , the third-best for ΔE_{01} , and provides gradients significantly better than the average functional. We do not make generalizing conclusions about the performance of functionals in other circumstances (other properties, other molecules, or even different excited states of the same molecule) from our benchmark data. Even though our benchmark tests a lot of different functionals, it focuses on one specific excited state of a single molecule. Thus, significance for and transferability to other cases are exceedingly limited. However, a more general benchmark of TDDFT excited state gradients and couplings on a variety of small to medium-sized organic molecules (for example, Thiel’s benchmark set[199, 200]) away from the FC region might be a worthwhile undertaking in the future since existing benchmarks focus heavily on equilibrium geometries (for recent examples, see [201–203]).

| Functional | RMSD(∇E_1) [eV/Å] | RMSD(ΔE_{12}) [eV] | RMSD(ΔE_{01}) [eV] |
|------------|-----------------------------|------------------------------|------------------------------|
| N12-SX | 4.5786 | 0.1725 | 0.7267 |
| X3LYP | 4.3673 | 0.1773 | 0.7329 |
| SB98-2A | 4.4028 | 0.1753 | 0.7204 |
| SB98-1C | 4.3895 | 0.1953 | 0.7207 |
| PBE-MOL0 | 4.5141 | 0.1733 | 0.7096 |
| B97-3 | 4.5263 | 0.1811 | 0.7048 |
| B97-2 | 4.4534 | 0.1740 | 0.7214 |
| B97 | 4.3926 | 0.1939 | 0.7202 |
| B3LYP | 4.3367 | 0.1859 | 0.7325 |
| B3LYPS | 4.3186 | 0.2479 | 0.7509 |
| Average | 5.6960 | 0.3411 | 0.7873 |

Table 4.1.: Performace of selected functionals compared to XMS-CASPT2(8,7)/cc-pvqz. The last row shows the average for all 93 tested functionals.

There are now quite a few program interfaces that enable TSH simulations with QM/MM gradients.[204–206]. In this work, we want to leverage the speed of the FermiONs++ QM program for the simulation of the QM region.[58–60] Since, in the future, we aspire to simulate the dynamics of triplet states, it is interfaced with the TSH code SHARC[114–116], which handles the non-adiabatic dynamics and the coupling between states of every character. The MM part of the calculation is performed internally by FermiONs++ via an interface to the OpenMM library.[207] The current implementation follows the blueprint of the other SHARC interfaces and uses file-based communication between the primary SHARC executable (`sharc.x`) and the main script (`SHARC_FERMIONS.py`) to exchange information during each time-step of the simulation. This exchange during one time-step of a TSH simulation is depicted in fig. 4.4. First, SHARC writes a file named `QM.in`, which contains the molecular geometry at

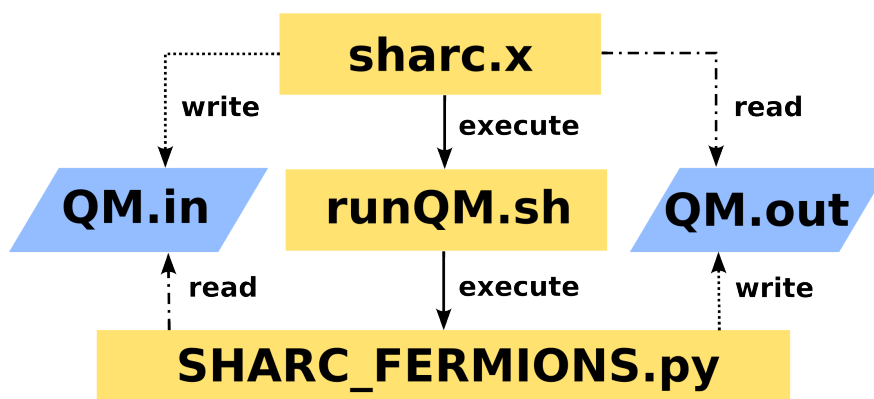


Figure 4.4.: General overview of program calls and file-based communication during one time-step of a TSH simulation.

the current time step and additional information that specifies quantities that need to be calculated. Then it executes a helper script `runQM.sh`, which runs the main script `SHARC_FERMIONS.py`. This script reads `QM.in`, calculates energies, gradients, dipole moments, and state overlaps and writes the results to the file `QM.out`. It then returns

control to `runQM.sh`, which returns control to `sharc.x`. Then, `sharc.x` reads `QM.out` and uses its information to propagate the system to the next time-step.

The communication between `SHARC_FERMIONS.py` and the main FermiONS++ program does not rely on file exchanges. It uses the Python interface of FermiONS++ to create a Python object representing the main FermiONS++ program and passes to it the molecular geometry. Other parameters, such as functional, basis set, and topology of the MM environment, must also be passed to FermiONS++. To do this, the user has to supply a file called `Fermions_config.py` containing a Python function that appropriately modifies the object. Then, ground state energies and gradients, the required excited state energies and gradients, and (transition) dipole moments are calculated. To perform the local diabaticization implemented in SHARC, overlaps between the different states are also required. An external module called `cis_nto.exe` written by Sapunar *et al.* is used for this task. It calculates these quantities very efficiently by expanding the wave functions of each state in terms of excitations between natural transition orbitals.[208] To interface with this program, we again rely on file exchanges. `cis_nto.exe` requires appropriately formatted files for the basis set, molecular orbital (MO) coefficients, configuration interaction (CI) coefficients and coordinates that can be generated from the information present in the FermiONS++ object. Since `cis_nto.exe` requires a configuration interaction singles (CIS)-like wavefunction, the TDDFT simulation has to be performed using the Tamm-Dancoff approximation (TDA) since TDA couplings can be calculated precisely using a CIS-style auxiliary many-electron wavefunction in the basis of the Kohn-Sham orbitals.[209]

Two equilibration steps were performed to set up the simulations. Firstly, a classical MD simulation with the OPLS/AA force field was carried out, followed by *ab initio* ground state MD at the QM/MM level. The first step aims to pre-equilibrate the solvent, such that long equilibration times in the *ab initio* MD can be avoided. The second step leads to full equilibration. No parameters are available for the interactions of BF₃ with cyclohexenone in OPLS/AA. Thus, in the first step of the equilibration, cyclohex-2-enone-BF₃ was replaced by the isoelectronic *N*-(trifluoromethyl)cyclohex-2-enimine for which MM parameters were obtained using LigParGen.[210] The molecule was placed in a cubic box with 511 molecules of DCM and equilibrated at 298 K and 1 atm. Then, the system was propagated for 50 ns in an NPT ensemble. From this simulation, 200 snapshots were taken. The procedure was repeated for both conformers of cyclohexenone-BF₃ (which are nearly isoenergetic (see scheme 1 in [2])) for a total of 400 snapshots.

For the second step, the 268 DCM molecules closest to the center mass of cyclohex-2-enone-BF₃ were retained, and the others were discarded. For each snapshot, the system was then confined inside a sphere with a radius of 20 Å, which keeps the density approximately equal to the equilibrium density of the classical MD simulation. C1 of cyclohex-2-enone-BF₃ was kept approximately stationary at its initial position by a weak harmonic constraint to keep the molecule of interest close to the center of the confining sphere. Then, *ab initio* ground state MD simulations were performed for 5 ps in an NVT ensemble to equilibrate the system. An exemplary result for one of the snapshots is shown in fig. 4.5. The cyclohex-2-enone-BF₃ complex can be seen in the center, surrounded by multiple shells of DCM.

Transition dipole moments for the lowest three excited states were calculated for each final geometry of the previous step. Systems were randomly transferred to the excited

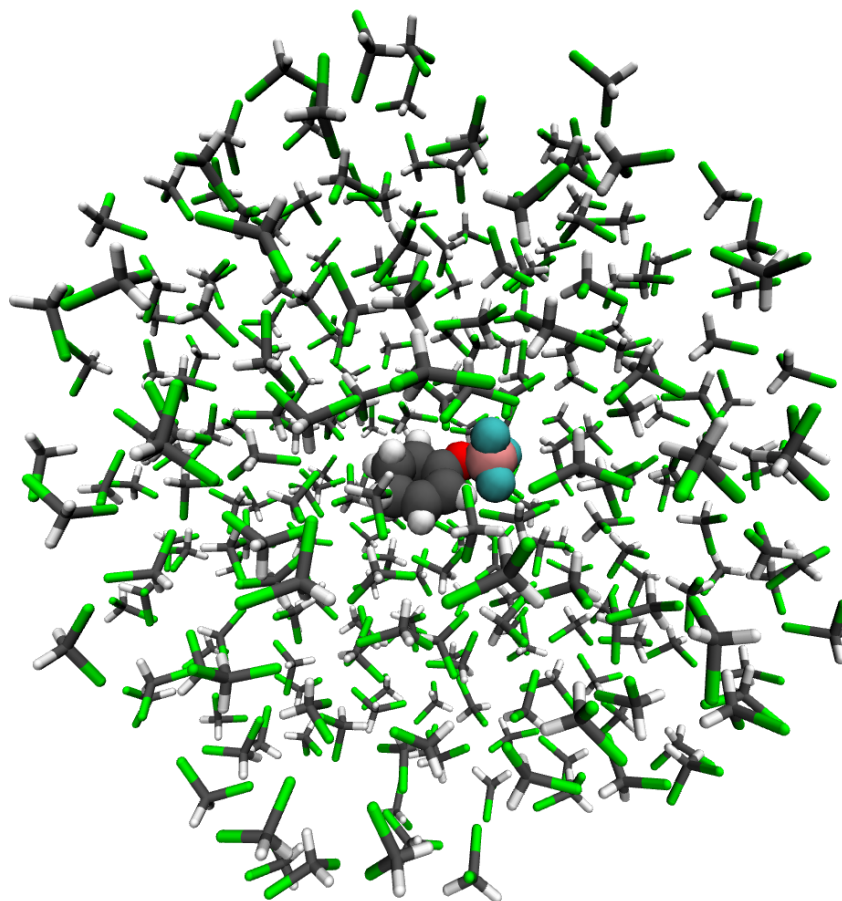


Figure 4.5.: Equilibrated cyclohex-2-enone-BF₃ complex in DCM.

state, with the total probability for each state proportional to its total oscillator strength in the range 0 eV to 5 eV. This resulted in 60 trajectories in S_1 and no trajectories in other excited states. Then, QM/MM TSH simulations were run for 1 ps. As a reference, 0.5 ps long gas-phase TSH simulations were also run for the same initial conditions.

In the TSH simulations, no hops were observed. This is not unexpected since the TSH simulation in [2] also showed only very few hops to other states, primarily to S_0 between 50 fs, and 100 fs. This slight discrepancy does not impede further analysis since the trajectories that relax are not relevant for the excited state reactivity. It can likely be attributed to a difference in initial conditions between the current simulation and the simulation in [2], that leads to less energy in the excited S_1 , such that an intersection with S_0 can not be reached. It can not be entirely excluded that the inability of TDDFT to capture adequately said intersection plays a role, but this is unlikely since in the current simulation, S_1 and S_0 are far apart at all times, and all geometries and the S_1S_0 energy gap is well described by the density functional due to extensive benchmarking.

Thus, we focus our analysis on the geometric changes and compare them between the molecule in the gas phase and the DCM solvent environment. Two internal coordinates are critical to the observed dynamics in the S_1 . The O-B bond distance captures the dissociation of the Lewis acid from the enone. The C-C=O-B dihedral angle is most

relevant for the relaxation in the S₁ towards the $n\pi^*$ minima, where the BF₃ group is rotated by 90° out of the molecular plane. These coordinates are depicted in fig. 4.6.

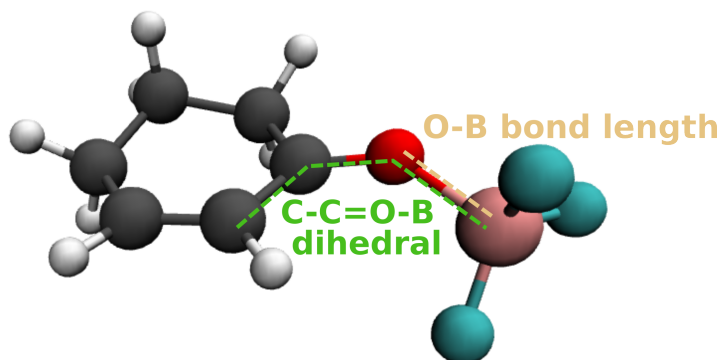


Figure 4.6.: Internal coordinates relevant for the relaxation of the complex in S₁.

The dynamics in these coordinates are extracted from the full-dimensional MD simulation and are displayed in fig. 4.7 a) for the gas-phase dynamics and in fig. 4.7 b) for the dynamics in solution. In the gas phase, all trajectories show a dissociation of the O-B bond based on a cutoff value of 2 Å. For the dihedral angle, the following can be observed; in the beginning, the geometries are clustered around 0° and 180° according to the two conformers of the complex in the ground state. As BF₃ leaves the complex, the C-C=O-B dihedral angle becomes randomly distributed, as the interaction between the enones and BF₃ at long separations is too weak to cause a preferred orientation. The situation is different in solution, where, based on a cutoff of 2 Å, only 20% of trajectories show dissociation. Even in these cases, the Lewis acid stays close to the enone with bond distances of 3-4 Å after 1 ps. Similar distances are reached at approximately 150 fs in the gas phase. It is also noteworthy that re-association of BF₃ to cyclohexenone occurs frequently, with 55% of those trajectories that are bound at the end of the simulation re-associating at some point during propagation. Following the relaxation in the S₁ via the dihedral angle reveals that starting from the initial dihedral angle of 0° or 180°, the angles change to cluster around 90° or -90°, indicating that the BF₃ group twists towards the S₁ minima above and below the molecular plane. This process takes around 400 fs and occurs in nearly all trajectories.

These results show how the embedding in the solvent hinders the dissociation of the complex although it is not prevented in all cases. Relaxation to the S₁ minimum is observed within a few hundred femtoseconds. From there, ISC to the triplet states will likely explain the signals observed in the time-resolved pump-probe spectrum. Thus, only three steps still need to be included to completely reproduce the experiment and fully understand the short-time dynamics of this Lewis acid-enone complex. Firstly, the SHARC-FermiONs++ interface has to be expanded to enable hopping to triplet states; this includes testing the FermiONs++ implementation of analytic TDDFT gradients. Then surface hopping simulations, including triplet states, need to be performed. Finally, a full transient absorption signal can be constructed from single point XMS-CASPT2 calculations at regular time intervals along the trajectories since TDDFT is not able to correctly capture the higher-lying excited states that are necessary to describe the ESA signal observed in the experiment.

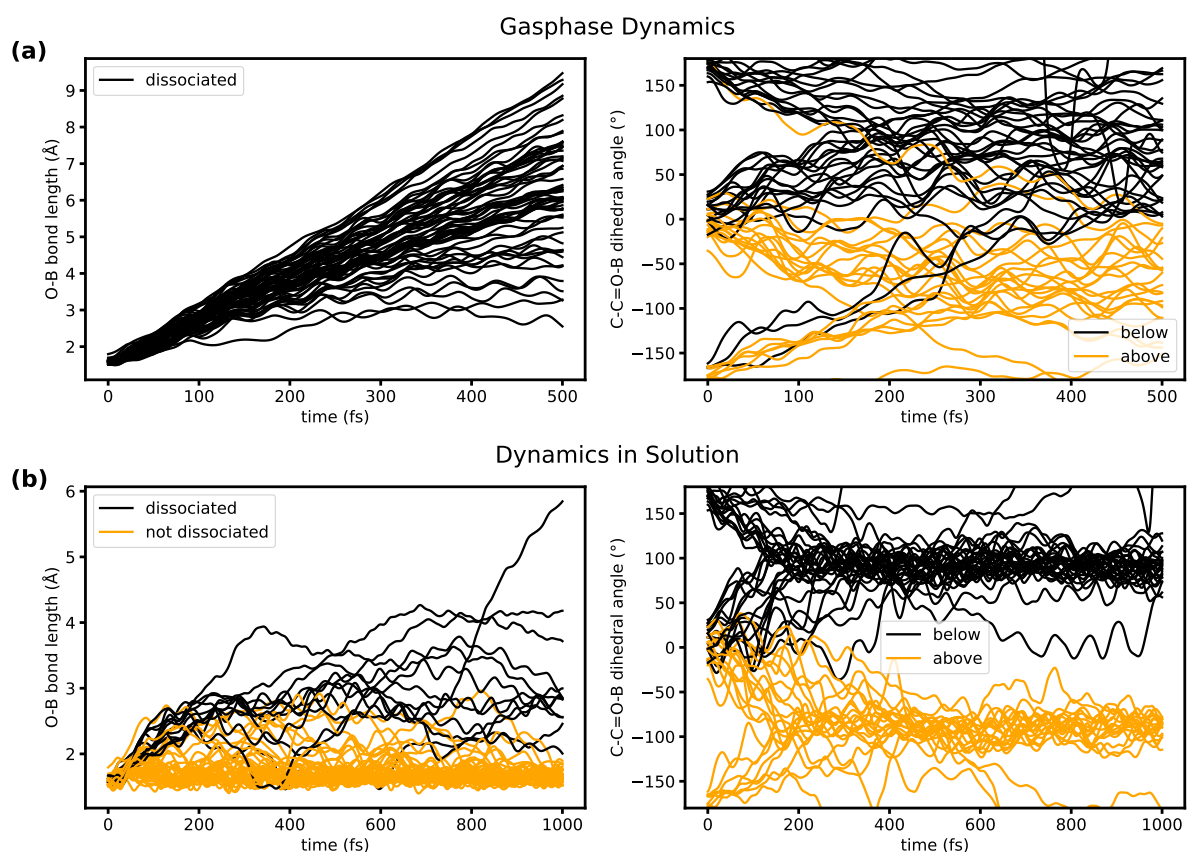


Figure 4.7.: Geometric changes during the dynamics for all trajectories in the gas phase (a) and in solution (b). (left) O–B bond lengths (right) C–C=O–B dihedral angle. For the bond length, trajectories are classified into dissociated (black) and not dissociated (yellow) based on a cutoff of 2 Å for the bond length at the end of the simulation. For the dihedral angle, trajectories are classified depending on whether the BF₃ group is below the molecular plane (black) or above the molecular plane (yellow) at the end of the simulation.

4.3. A Complex Excited State Electronic Structure Leads to Unexpected Reactivity: B–Cl Bond Fission in Benzaldehyde-BCl₃

As discussed in chapter 3, when benzaldehyde is irradiated in the presence of alkenes, a Paternò-Büchi reaction occurs in which the alkene adds to the C=O bond. The source of this reactivity is the low-lying $n\pi^*$ state of benzaldehyde. In more flexible enones, reactivity at the C=C double bond predominates since a rotation of the H–C=C–H dihedral can stabilize the $\pi\pi^*$ state. This rotation does not occur in benzaldehyde because the C=C double bond is embedded in the rigid aromatic ring system.

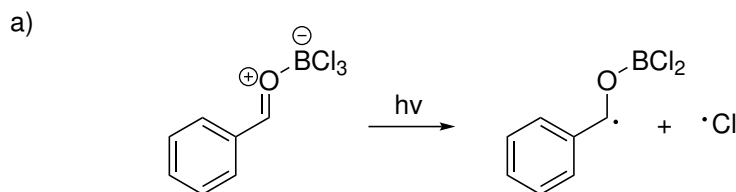
However, Lewis acids also stabilize the $\pi\pi^*$, independently from the flexibility of the 2-enone. Thus, *ortho* [2+2] photocycloaddition can be observed when polycyclic aromatic aldehydes are irradiated in the presence of alkenes and Lewis acids.[169, 185] Of course, this reaction disrupts conjugation in the aromatic system which is associated with a lower energetic penalty for larger polycyclic hydrocarbons.[211] Thus, it is reasonable to ask whether a similar reaction is possible in the monocyclic benzaldehyde. To investigate this, we performed calculations on the benzaldehyde-BCl₃ complex.

The complex turned out to have a very intricate excited state structure. The broad redshifted absorption band of the complex, which was assumed to be caused only by the two $\pi\pi^*$ states, contained several additional transitions. Most of these were attributed to charge transfer states, where electrons are transferred from the chlorine lone pairs of the Lewis acid into the lowest anti-bonding π^* orbital of the aromatic system. These diabatic charge transfer states interact strongly with the $\pi\pi^*$ states (if the interaction is symmetry allowed, which is not the case for all chlorine lone pairs). Thus, a mixed character is observed in the adiabatic description. A large number of states with excitations originating from many different orbitals made a simulation of the complex using XMS-CASPT2 computationally expensive and prevented the calculation of gradients at the XMS-CASPT2 level. Instead, TDDFT using the ω B97x-d3 functional[212] was used with a scaling factor to bring the TDDFT transition energies in line with XMS-CASPT2 results. With this electronic structure method, optimizations of critical points and surface hopping simulations could be performed.

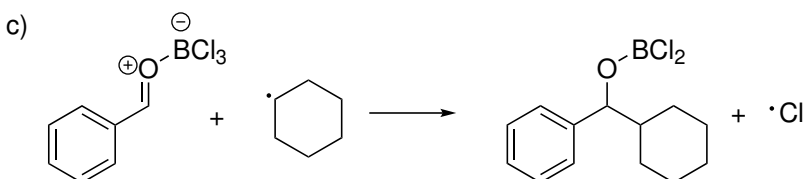
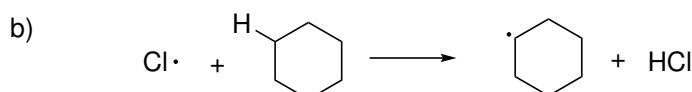
TSH simulations revealed that the charge transfer states influence the reactivity in a way that was not expected from previous static calculations. After crossing into these states, homolytic dissociation of the B–Cl bond is observed. A chlorine radical and a borylated ketyl radical are formed (see scheme 7 a). States with significant charge transfer character are populated either directly by the excitation or by nonadiabatic transitions in the first 50 fs of the simulation. They obtain substantial $\sigma\pi^*$ character upon a slight elongation of the B–Cl bond. In this way, an electron has been removed from the bonding orbital of the B–Cl bond, which leads to its dissociation.

We presumed that this borylated ketyl radical should be detectable in ultrafast TA experiments. Indeed, a strong ESA between 440 and 460 nm is observed that can be assigned to the radical species. Calculating the EADS for the radical species in thermal equilibrium is quite simple. It just corresponds to simulating a normal (static) spectrum of the radical. Since the electronic structure simplifies significantly when the chlorine radical leaves the complex, this can even be done using XMS-CASPT2 as the electronic structure method.

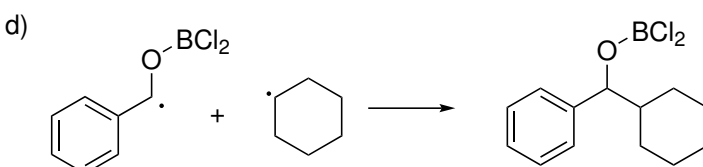
Initiation - Photolytic Bond Cleavage



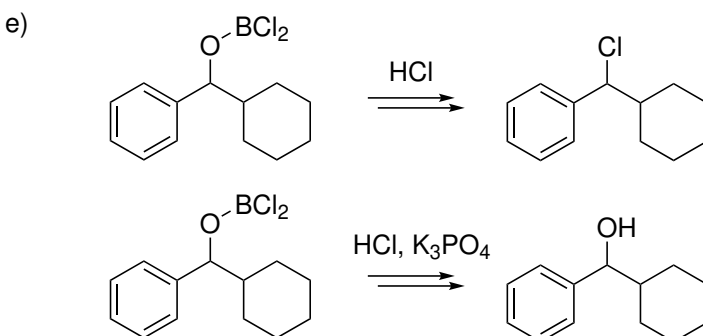
Radical Chain Propagation



Recombination



Follow-up Processes Leading to the Final Products



Scheme 7: Mechanistic steps for the photo-chemical addition of cyclohexane to benzaldehyde in the presence of BCl_3 : a) Generation of chlorine radicals and borylated ketyl radicals by photo-dissociation of the benzaldehyde- BCl_3 complex initiates the radical chain. b) Hydrogen abstraction from cyclohexane forms the first step of radical chain propagation. c) Attack of the cyclohexyl radical on the benzaldehyde- BCl_3 complex liberates chlorine radical, the second step of radical chain propagation. d) The borylated ketyl radical directly recombines with the cyclohexyl radical, one of the possible chain-termination events. Other recombination products have not been isolated. e) Follow-up steps yield the final isolated products.

The observed dissociation makes the benzaldehyde-BCl₃ complex unsuitable for *ortho* [2+2] photocycloadditions. However, the chlorine radical can be employed in other reactions. For example, it can abstract hydrogen from unsubstituted alkanes. This process is part of the catalytic cycle for light-induced C–C bond-forming reactions that use transition metal complexes as catalysts. The charge transfer process in the benzaldehyde-BCl₃ complex is in many ways similar to a dissociative ligand to metal charge transfer (LMCT) of a chloride ligand in a transition metal complex.[213, 214] In both cases, by the interaction of a bright state and a charge transfer state, the excitation removes electron density from the chlorine, which leads to a depopulation of the binding σ orbital. The difference is, of course, that boron is not a redox-active transition metal and does not act as the electron acceptor. Instead, a carbon-centered radical is formed that is stabilized by the aromatic system.

Thus, a C–C bond-forming reaction that leads to the addition of an unsubstituted alkane, such as cyclohexane, to the C=O bond of benzaldehyde can be envisioned. Indeed, when adding cyclohexane to the reaction mixture, the product of addition to benzaldehyde could be isolated after irradiation. Due to the surprisingly high quantum yield of the reaction, we reasoned that a radical chain (scheme 7 b and c) must be involved in the mechanism (in addition to direct recombination, scheme 7 d). It can be shown that step b) in scheme 7 is possible from known bond dissociation energies of the involved compounds.[215] Unrestricted DLPNO-CCSD(T)[216] calculations demonstrate that scheme 7 c is also feasible. Without additional additives, [chloro(cyclohexyl)methyl]benzene was isolated, while the addition of potassium phosphate led to the formation of the alcohol. Both products can be formed from the recombination product of the cyclohexyl radical and the borylated ketyl radical in follow-up steps under the respective conditions (scheme 7 e).

The article “Photoinduced B–Cl Bond Fission in Aldehyde-BCl₃ Complexes as a Mechanistic Scenario for C–H Bond Activation” was published in *Journal of the American Chemical Society*. The following points briefly summarize the article, focusing on the theoretical results.

- Just like in other enones,[2] the bright state of the aromatic benzaldehyde experiences a pronounced redshift upon coordination of the Lewis acid BCl₃. However, besides the blueshifted oxygen $n\pi^*$ and redshifted $\pi\pi^*$ states, the broad first absorption band contains several chlorine $n\pi^*$ states.
- TSH simulations show that after excitation into the first broad absorption band, the complex dissociates by releasing a chlorine radical. 81% of trajectories showed dissociation, mainly in the lowest triplet state.
- A relaxed scan of the B–Cl bond length revealed many crossings between bound and repulsive states close to the FC region. The S₁ is dissociative, and the bright S₂ becomes dissociative upon a slight elongation of the B–Cl bond. The two lowest triplets show minima that are well separated from the other states in the FC region and cross the dissociative singlet states at 2.5 Å.
- The following mechanism explains the observed dissociation: Higher lying singlet states relax to S₁ or S₂, and dissociation starts in these states. Early hops to $^3\pi\pi^*$ states lead to trapping in the FC region. All other trajectories dissociate and hop to the triplet states at a later point in time. All in all, the dissociation should occur on a timescale of a few hundred femtoseconds.

- Femtosecond TA spectroscopy is used to confirm the theoretical predictions. After excitation, two distinct spectral features are observed. The first feature appears with a time constant of approximately 150 fs and transforms into the second feature with a time constant of approximately 400 ps. With the help of XMS-CASPT2 calculations, the spectral signature of the first feature can be assigned to a borolated ketyl radical, which shows the elimination of a chlorine radical from the complex. The second feature can be tentatively assigned to a borolated ketyl cation, which might form from the radical by a Marcus-like electron transfer.[217]
- The generated chlorine radical can be used synthetically to abstract hydrogen from cyclohexane. The resulting alkyl radical attacks the benzaldehyde- BCl_3 complex, leading to C–C bond formation. Under these conditions, the isolated product is [chloro(cyclohexyl)methyl]benzene. Potassium phosphate, as an additive, leads to the formation of the corresponding alcohol. This hydroalkylation reaction succeeded for 19 examples with yields from 42%
- Quantum yield measurements reveal that the reaction rate decreases over time. The quantum yield at the beginning of the reaction is 1.06 ± 0.06 , which indicates that another mechanism produces chlorine radicals in addition to light-induced dissociation. Correspondingly, in a light-on-light-off experiment, residual reactivity is detected after the light is turned off.
- A radical chain mechanism is proposed, where an alkyl radical attacks the benzaldehyde- BCl_3 complex, leading to product formation and liberation of a chlorine radical, which can abstract hydrogen from the alkane and regenerate the alkyl radical. This mechanism was confirmed by unrestricted DLPNO-CCSD(T) calculations, which show that the proposed mechanism is exergonic and all involved barriers are small.

Hereafter, The article “Photoinduced B–Cl Bond Fission in Aldehyde- BCl_3 Complexes as a Mechanistic Scenario for C–H Bond Activation” published in *Journal of the American Chemical Society* is reproduced. Copyright 2022 American Chemical Society. The supporting information is available online.

Photoinduced B–Cl Bond Fission in Aldehyde-BCl₃ Complexes as a Mechanistic Scenario for C–H Bond Activation

Daniel P. Schwinger,[#] Martin T. Peschel,[#] Thomas Rigotti,[#] Piotr Kabaciński, Thomas Knoll, Erling Thyraug, Giulio Cerullo, Jürgen Hauer,^{*} Regina de Vivie-Riedle,^{*} and Thorsten Bach^{*}



Cite This: *J. Am. Chem. Soc.* 2022, 144, 18927–18937



Read Online

ACCESS |



Metrics & More

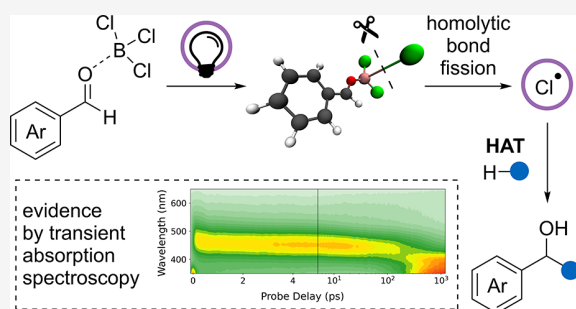


Article Recommendations



Supporting Information

ABSTRACT: In concert with carbonyl compounds, Lewis acids have been identified as a versatile class of photocatalysts. Thus far, research has focused on activation of the substrate, either by changing its photophysical properties or by modifying its photochemistry. In this work, we expand the established mode of action by demonstrating that UV photoexcitation of a Lewis acid–base complex can lead to homolytic cleavage of a covalent bond in the Lewis acid. In a study on the complex of benzaldehyde and the Lewis acid BCl₃, we found evidence for homolytic B–Cl bond cleavage leading to formation of a borylated ketyl radical and a free chlorine atom only hundreds of femtoseconds after excitation. Both time-dependent density functional theory and transient absorption experiments identify a benzaldehyde-BCl₂ cation as the dominant species formed on the nanosecond time scale. The experimentally validated B–Cl bond homolysis was synthetically exploited for a BCl₃-mediated hydroalkylation reaction of aromatic aldehydes (19 examples, 42–76% yield). It was found that hydrocarbons undergo addition to the C=O double bond via a radical pathway. The photogenerated chlorine radical abstracts a hydrogen atom from the alkane, and the resulting carbon-centered radical either recombines with the borylated ketyl radical or adds to the ground-state aldehyde-BCl₃ complex, releasing a chlorine atom. The existence of a radical chain was corroborated by quantum yield measurements and by theory. The photolytic mechanism described here is based on electron transfer between a bound chlorine and an aromatic π -system on the substrate. Thereby, it avoids the use of redox-active transition metals.



INTRODUCTION

Lewis acids represent the most frequently used class of catalysts in conventional (thermal) C–C bond forming reactions.¹ They act by coordination to a Lewis basic entity of the substrate, frequently the oxygen atom of a carbonyl group. In α,β -unsaturated carbonyl compounds the energy of the lowest unoccupied molecular orbital (LUMO) decreases upon Lewis acid coordination, rendering them more electrophilic. A major benefit of Lewis acid catalysis is the plethora of chiral Lewis acids available that enable enantioselective catalysis of a given reaction.² In contrast to the great success Lewis acids have encountered in thermal reactions, their influence on photochemical reactions has not been appreciated for many years. In the photochemical case, the stabilization of the LUMO also plays a key role, as it renders α,β -unsaturated carbonyl compounds more amenable to photoexcitation in the near UV. Thus, there has recently been an increased interest in chiral Lewis acids in the context of enantioselective photochemical reactions.³ Formation of an assembly with a Lewis acid alters the reactivity pattern of a substrate and opens up alternative reaction channels that are inaccessible by direct irradiation.⁴ The photochemical behavior of 2-naphthaldehyde (**1**) toward olefins

such as 2,3-dimethyl-2-butene serves as an illustrative example (Scheme 1).⁵

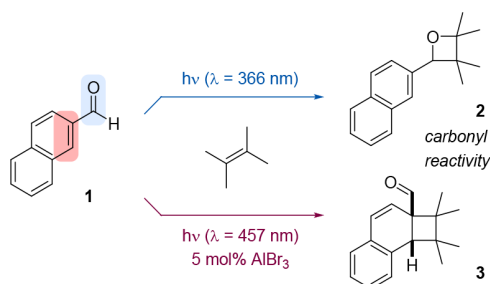
Direct irradiation of the compound at $\lambda = 366$ nm delivers exclusively products stemming from reactivity at the carbonyl group, for example oxetane **2** as the product of a Paternò–Büchi reaction. This reaction channel is inaccessible upon Lewis acid coordination, and instead a clean [2+2] photocycloaddition with 2,3-dimethyl-2-butene occurs at the aromatic double bond (*ortho* photocycloaddition) to obtain cyclobutane **3**.

In studies initially directed to a related *ortho* photocycloaddition⁶ of benzaldehyde and olefins, we have investigated the 1:1 complex of benzaldehyde and the Lewis acid boron trichloride. Although its ground-state properties had been investigated previously,⁷ there was no information on its excited-state properties. In earlier work, we had seen that excited-state calculations in combination with transient absorption spectroscopy

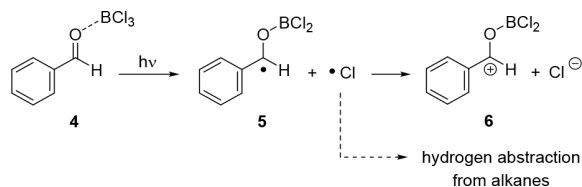
Received: June 25, 2022

Published: October 7, 2022



Scheme 1. Reactivity of 2-Naphthaldehyde (1) toward 2,3-Dimethylbutene in the Absence and in the Presence of AlBr₃ as a Lewis Acid

copy provide valuable insights into the nature of Lewis acid complexes in the excited state. We were able to assign excited-state absorptive signals of a 1:1 complex between cyclohex-2-enone and boron trifluoride and to elucidate the photophysical relaxation processes on the singlet and triplet hypersurface.⁸ Surprisingly, boron trichloride and benzaldehyde displayed a completely different and unexpected behavior (Scheme 2).

Scheme 2. A 1:1 Complex of Benzaldehyde and Boron Trichloride (4) Is Predicted to Cleave Homolytically after Irradiation and to Undergo a Subsequent Electron Transfer

Their 1:1 complex was predicted by theory to be unstable in the excited state, and many trajectories were found in which a homolytic cleavage to a chlorine atom and a boronated ketyl radical **5** occurred. In analogy to observations on benzhydryl radicals,⁹ a subsequent electron transfer was suggested, leading to cation **6** with a chloride counterion. Both predictions were corroborated in detailed transient absorption experiments on the fs and ns time scales. The initial step of this pathway is reminiscent of the visible-light-induced homolysis (VLIH) of earth-abundant metal complexes, which has found recently increased synthetic attention.^{10,11} It was thus attempted to employ the generated chlorine radical in metal-free C–H activation reactions (hydrogen abstraction), which finally culminated in a procedure for the Lewis acid-mediated addition of hydrocarbons on aromatic aldehydes. Our study establishes a detailed mechanistic picture behind the homolytic photocleavage reaction depicted in Scheme 2, based on a combination of theory and femtosecond UV-pump white-light-probe transient absorption spectroscopy. We tested and utilized the reaction mechanism in synthetic work, establishing a new method for the generation of halogen radicals from main group compounds and their application to the activation of C–H bonds. A coherent mechanistic picture evolved, which reaches beyond current knowledge of transition-metal-based VLIH processes.

The discussion in the following sections commences with a theoretical treatise of the benzaldehyde-BCl₃ complex and its predicted photochemical behavior, most notably the B–Cl bond fission. The second section describes the photochemical

dynamics of the complex by transient absorption spectroscopy experiments. It is linked to theory by comparison of calculated and experimentally obtained spectra of the transient intermediates. The final part takes up the results of theory and spectroscopy by devising a synthetic application of the B–Cl bond fission. The suggested reaction pathway involves a release of a chlorine atom upon attack of a carbon-centered radical on the benzaldehyde-BCl₃ complex, which in turn is supported by calculations.

RESULTS AND DISCUSSION

Vertical Excitation Energies and Static Absorption Spectra. The small aromatic carbonyl compound benzaldehyde is a relatively strong absorber in the mid- to deep-UV spectral range. Its UV absorption spectrum has been discussed extensively in the literature.¹² In CH₂Cl₂ solution, it features three partially overlapping absorption bands in the region from 400 to 220 nm (Figure 1).

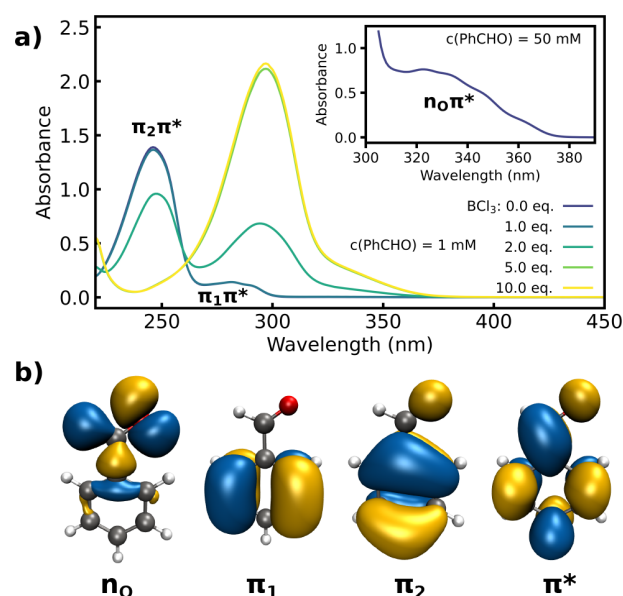


Figure 1. Panel a: UV–vis spectrum of benzaldehyde (dark blue) with varying amounts of BCl₃, showing formation of complex **4** (dark green-yellow). The bright $S_0 \rightarrow S_2(\pi_1\pi^*)$ and $S_0 \rightarrow S_3(\pi_2\pi^*)$ transitions are labeled. The inset shows the UV–vis spectrum of benzaldehyde at a higher concentration, revealing the symmetry-forbidden $S_0 \rightarrow S_1(n_O\pi^*)$ transition. Panel b: Natural transition orbitals (NTOs) for the respective transitions displayed in panel a, calculated using time-dependent ω b97x-D3/ZORA-def2-TZVP.

The first band at $\lambda \cong 330$ nm is very weak and attributed to the symmetry forbidden $S_0 \rightarrow S_1(n_O\pi^*)$ transition out of a lone-pair orbital at the carbonyl oxygen atom. The second (at $\lambda \cong 280$ nm) and third band (at $\lambda \cong 240$ nm) are caused by bright $S_0 \rightarrow S_2(\pi_1\pi^*)$ and $S_0 \rightarrow S_3(\pi_2\pi^*)$ transitions. The excitations originate from two different π -orbitals of the aromatic core. Upon addition of BCl₃, the absorption bands shifted and, after addition of five equivalents, no further changes were observed, indicating that complex formation was complete (see Figure 1). The observed spectral shifts are typical for carbonyl compounds on complexation with Lewis acids.^{4,13} The final spectrum of complex **4** displayed a single, broad band with an absorption maximum at $\lambda = 297$ nm including a red-shifted shoulder. The coordination of the Lewis acid strongly stabilizes the oxygen n-

orbital of benzaldehyde and weakly stabilizes its π^* -orbital (LUMO), leaving the π_1 - and π_2 -orbitals almost unchanged. Thus, we expected the absorption range of **4** to contain all three transitions ($n_{\text{O}}\pi^*$, $\pi_1\pi^*$, and $\pi_2\pi^*$) with the $n_{\text{O}}\pi^*$ transition blue-shifted and both $\pi\pi^*$ transitions red-shifted, as was observed in our earlier study of a cyclohexenone-BF₃ complex.⁸ Additionally, the chlorine lone pairs n_{Cl} in **4** are close in energy to the π -orbitals, and excitations from these orbitals into the π^* -orbital appear in the near to middle UV region as well. Each chlorine atom contributes two high-lying chlorine lone pairs, so an additional six $n_{\text{Cl}}\pi^*$ states have to be considered. This is in contrast to the previously investigated BF₃ complex,⁸ where transitions from the halogen lone pairs lie significantly below 200 nm and are not relevant for photochemical processes after UV excitation. In Figure 2a, the experimental absorption spectrum of **4** is displayed together with vertical lines indicating the calculated transition energies and oscillator strengths at the Franck–Condon (FC) point. The calculations were performed at the time-dependent (TD) ω B97X-D3/ZORA-def2-

TZVP^{14,15} level of theory. As this method was found to overestimate the excitation energy, we scaled the energies by a factor of 0.836. This factor is not universal, but was validated for complex **4** by benchmarking to match the experimental absorption spectrum and XMS-CASPT2¹⁶ benchmark calculations in the Franck–Condon region and beyond (see Figure S5 and tables on pages S14 and S15). From now on, we will refer to this as scaled time-dependent density functional theory (TDDFT), and we used it consistently in all TDDFT calculations on complex **4**. There are nine electronic states in the experimental absorption region between 360 and 240 nm, representing the expected six $n_{\text{Cl}}\pi^*$ and the three shifted benzaldehyde states $n_{\text{O}}\pi^*$, $\pi_1\pi^*$, and $\pi_2\pi^*$. The natural transition orbitals (NTOs) characterizing these states require further discussion, and a selection of NTOs is displayed in Figure 2b. The lowest lying singlet state is the S_1 [NTO₁(n_{Cl}) \rightarrow NTO₆(π^*)] state. Due to symmetry, it is a dark state and the NTO₁(n_{Cl}) orbital does not contain any contribution from orbitals at the aromatic core. The S_2 [NTO₂(π_1) \rightarrow NTO₆(π^*)] is the bright state that corresponds to the S_2 ($\pi_1\pi^*$) observed in free benzaldehyde. S_3 and S_4 are nearly degenerate at the FC point. S_3 is a bright state characterized as NTO₃(n_{Cl}) \rightarrow NTO₆(π^*), with NTO₃(n_{Cl}) being a linear combination of chlorine lone pairs and the π_2 -orbital of benzaldehyde. S_4 is a dark state characterized by a transition from an NTO that is a linear combination of the lone pairs of chlorine (n_{Cl}) and oxygen (n_{O}). The situation for the nearly degenerate states S_5 and S_6 is similar. While S_5 is a dark state characterized by a transition out of a linear combination of n_{Cl} -orbitals and n_{O} (NTO₄(n_{O})), S_6 has the largest oscillator strength with an NTO that is a linear combination of n_{Cl} -orbitals and π_2 (NTO₅(π_2)). The states S_7 – S_9 all have low oscillator strength. S_7 and S_8 are of $n_{\text{Cl}}\pi^*$ character, and S_9 contains contributions from σ -orbitals of the aromatic core.

Trajectory Calculations and Mechanism of Dissociation. All nine states contributing to the first absorption band overlap energetically (see Figure S6 in the Supporting Information). Excitation into this broad absorption band might cause nonadiabatic dynamics in a variety of states including additional dark triplet states. The energetic order of the lowest singlet and triplet states is given in the Supporting Information. To elucidate the fate of complex **4** after photoexcitation, we simulated nonadiabatic trajectories at the scaled TDDFT level of theory using the SHARC program.¹⁷ We started sampling trajectories in a spectral window reaching from 0 to 3.85 eV (322 nm), the red shoulder of the absorption spectrum, which is a typical excitation wavelength in photocatalytic applications. The sampling led to a total of 171 trajectories propagated for up to 350 fs and distributed over the states according to their transition dipole moment within the spectral window (for more detailed technical information see the Supporting Information). To our surprise, most of the trajectories led to the dissociation of a chlorine atom (Figure 3).

In all cases, only a single chlorine atom (out of three) dissociates and the mean B–Cl bond distance (shown in Figure 3a) was used to categorize the trajectories into “dissociated” and “not dissociated” based on a cutoff value of 2.15 Å. As the equilibrium B–Cl bond distance is 1.82 Å, this cutoff value roughly corresponds to an elongation of a single B–Cl bond to 2.80 Å. Based on this criterion, 81% of trajectories led to a dissociation. Dissociation occurs over the whole simulation time, although it becomes rarer as the simulation progresses and the most energetic trajectories are already dissociated. Figure 3b

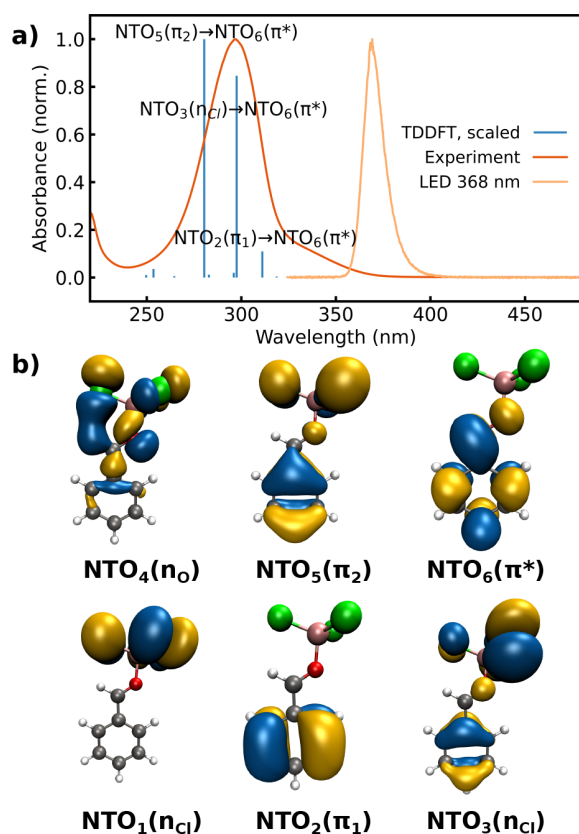


Figure 2. Panel a: UV–vis spectrum of benzaldehyde-BCl₃ complex **4** (red), excitation energies (transition wavelengths) and relative oscillator strengths at the FC point (calculated using scaled ω B97X-D3/ZORA-def2-TZVP), and emission spectrum (orange) of the LED used in synthetic and mechanistic studies (vide infra, $\lambda_{\text{max}} = 368$ nm). For the three brightest states, the natural transition orbitals (NTOs) that characterize these states are indicated. Panel b: NTOs of different excited states in complex **4**. All nine excited states that form the first absorption band are characterized by transitions into the NTO₆(π^*) orbital. For the three bright states, S_2 , S_3 , and S_6 , the excitations originate from NTO₂(π_1), NTO₃(n_{Cl}), and NTO₅(π_2), respectively. Excitation from NTO₁(n_{Cl}) belongs to the lowest singlet state S_1 ($n_{\text{Cl}}\pi^*$). NTO₄(n_{O}) has a large contribution from the n_{O} -orbital of benzaldehyde and forms the adiabatic state S_5 .

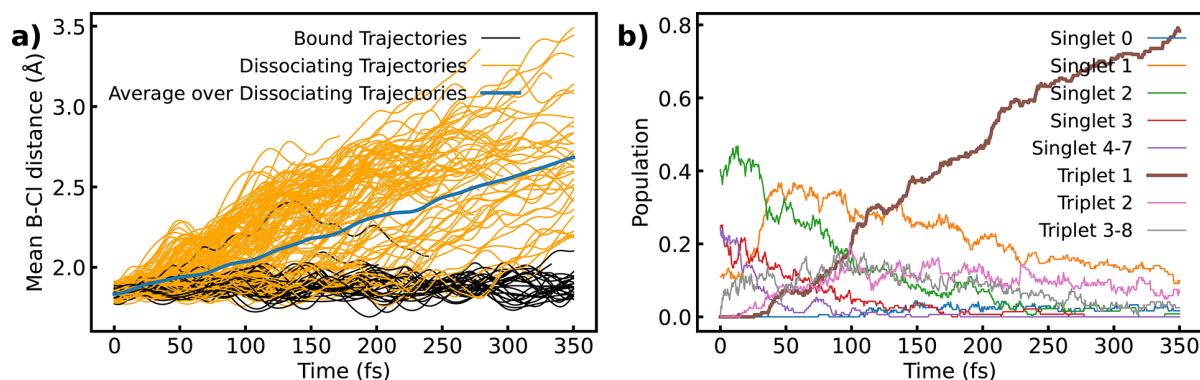


Figure 3. Results of semiclassical nonadiabatic molecular dynamics simulations. Panel a: Mean B–Cl bond distances of dissociating trajectories (orange) and nondissociating trajectories (black). The average bond distance over dissociating trajectories is marked in blue and was only calculated over trajectories that ran for the entire 350 fs simulation. Panel b: Adiabatic state populations.

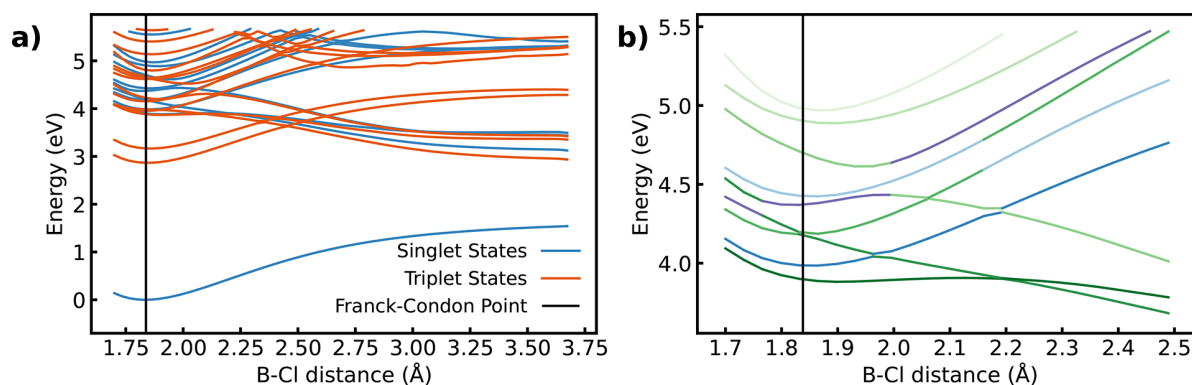


Figure 4. Adiabatic potential energy surfaces of **4** along a ground-state relaxed scan of the B–Cl bond of the chlorine atom in the molecular symmetry plane. The calculations were performed at the scaled TDDFT level of theory. Panel a: Singlet and triplet states. The lowest singlet states show mainly dissociative behavior. The lowest two triplet states are bound in the FC region but after a barrier at 2.50 Å, which is associated with a change from $\pi\pi^*$ to $n\pi^*$ character, become dissociative as well. Panel b: Zoom-in of the FC region, showing the lowest nine excited singlet states forming the first absorption band in the UV spectrum of **4**. The two states with the largest $\pi\pi^*$ contribution are shown in shades of blue, the state with the largest $n\pi^*$ contribution is shown in violet, and the other states, which have large contributions from different $n_{\text{Cl}}\pi^*$ -orbitals, are shown in shades of green.

shows that the initial excitation leads to the population of a multitude of different states, as expected from the broad absorption spectrum featuring many overlapping states. The largest population was found in the bright $S_2(\pi_1\pi^*)$ state. Leaving the FC region, trajectories quickly relax to S_1 , leading to a large rise in its population after around 40 fs. Then, population is more slowly transferred from S_1 to T_2 and to T_1 . More highly excited states also relax quickly. After 350 fs, most population ends up in the lowest three excited states with 78% in T_1 , 10% remaining in S_1 , 7% remaining in T_2 , and 5% in all other states. Dissociation occurs in all three states.

To explain the dissociation and relate it to the observed population dynamics of the adiabatic states, we performed a relaxed scan in the ground state of complex **4**, and we calculated excitation energies at each point along the scan to obtain the adiabatic potential energy surfaces (PESs). In Figure 4a, the singlet and triplet PESs are shown. The states lying within the experimental absorption band emerge densely packed between 3.8 and 5.2 eV, displaying repulsive and bound-state features and many crossings between states of the same and different multiplicity. Curve crossings between states of bound $\pi\pi^*$ - and dissociative $n_{\text{Cl}}\pi^*$ -character center around 2.1 and 2.5 Å (Figure 4a). Figure 4b highlights the complexity of the situation for the lowest nine excited singlet states. The change in color marks the change in electronic character. The process relevant contribu-

tions from the $n_{\text{Cl}}\pi^*$ -orbitals are shown in shades of green. The two well-separated triplet states $T_1(\pi_2\pi^*)$ and $T_2(\pi_1\pi^*)$ (Figure 4a) may act as trapping states for short bond distances.

Their relatively deep minima visible at 2.9 and 3.2 eV are close to the FC region (for the energy and geometry of the optimized T_1 minimum, see the Supporting Information). Trajectories with fairly low energy crossing into these triplets soon after excitation can become trapped in their minima, which explains the 19% of the trajectories that do not dissociate. All others pass the crossing region at around 2.5 Å, leading to dissociation, which is initiated by six low-lying $n_{\text{Cl}}\pi^*$ states (three of the singlet manifold and three of the triplet manifold). They cross with the states of $\pi\pi^*$ character including the bright S_2 state. Upon B–Cl bond elongation, the contributing $n_{\text{Cl}}\pi^*$ -orbitals transform into the three 3p-orbitals of the chlorine radical in accordance with the bond cleavage.

Taken together, the data led us to propose the following dissociation mechanism: Starting from the bright $S_2(\pi_1\pi^*)$ state, the dissociating trajectories can either (1) cross early into $S_1(n_{\text{Cl}}\pi^*)$ and dissociate nearly barrierless following the $n_{\text{Cl}}\pi^*$ character diabatically or (2) cross a small barrier at 2.0 Å associated with the change in character of S_2 from bound $\pi_1\pi^*$ to dissociative $n_{\text{Cl}}\pi^*$. These trajectories will continue to cross into the dissociative part of T_1 at a later point. In summary, the nonadiabatic dynamics predict efficient photoinduced cleavage

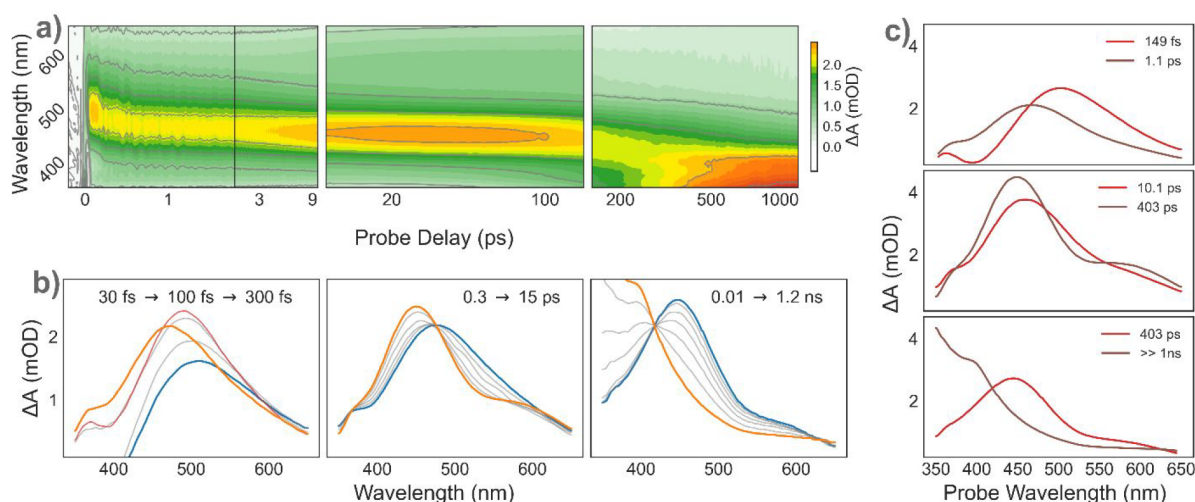


Figure 5. TA data acquired from benzaldehyde-BCl₃ complex **4** in CH₂Cl₂ solution at room temperature. Panel a: 2D representation vs time and detection wavelength of the TA spectra. Data from individual experiments are shown in separate panels. Note the change from linear to logarithmic time scale at 1.8 ps (black vertical line). Panel b: TA spectra at selected probe delays highlight the spectral evolution from early (blue) to late (orange) times at the different time scales. The spectrum at the intermediate time of 100 fs in the left panel is shown in red. Note the isosbestic points, suggesting state-to-state transitions at vastly differing time scales. Panel c: Evolution-associated spectra extracted from global kinetic fits to the data. Component lifetimes are denoted in the figure labels. See the narrative for details.

of **4** into a chlorine radical and the borylated ketyl radical **5** on a time scale of a few 100 fs. The bond cleavage is induced due to the prominent participation of the n_{Cl} lone pairs in the excited electronic wave functions. To provide data for direct comparison with transient absorption experiments, we calculated the absorption spectra for the borylated ketyl radical (**5**) and cation (**6**) using XMS-CASPT2^{16,18} (see the [Supporting Information](#) for details).

Time-Resolved Optical Properties and Photoinduced Dynamics. The computational work in the preceding section provided detailed predictions about the cascade of relaxation processes taking place within the benzaldehyde-BCl₃ complex (**4**) after absorption of a UV photon. Moreover, these predictions were associated with accessible experimental observables in the form of calculated optical spectra. As such, it was conceptually straightforward to validate the computational predictions by direct comparison to experiment, and we thus undertook a time-domain observation of the photochemical processes triggered by UV photoexcitation of complex **4**. To achieve a detailed picture of these ultrafast dynamics, we made use of ultrafast transient absorption (TA) spectroscopy, where interaction with an excitation (“pump”) pulse generates an excited-state wave packet, the fate of which can subsequently be followed by monitoring the time evolution of the probe transmission spectrum. Despite the inherent challenges in generating short pulses in the UV spectral range, this strategy has been proved highly valuable in elucidating light-induced dynamics in complex molecular systems.^{9,19} To initiate excited-state dynamics, we used 20 fs pulses with a central wavelength of 275 nm, while the pump-induced changes in optical absorption of the sample were interrogated using a white-light supercontinuum pulse with a spectrum spanning ~350–725 nm. The total experimental TA data are collected in [Figure 5a](#). Two general observations can be made immediately: (1) As both the excitation pulse and the lowest energy (S₀ → S₁) transition fall outside the range of the probe spectrum, we observe predominantly excited-state absorption (ESA) signals, and (2) the induced dynamics occur on time scales covering

several orders of magnitude. To reach sufficient fidelity at all scales, it was thus necessary to perform three individual experiments, each targeting a subsection of the total time range. In [Figure 5a](#), these results are shown in separate panels for clarity.

A qualitative overview over the dynamics can be gained from the two-dimensional spectra plotted vs detection wavelength and probe delay in [Figure 5a](#) and the extracted TA spectra in [Figure 5b](#): Immediately after excitation, we observed predominantly a broad ESA feature around 500 nm, in addition to negative-amplitude signals in the near-UV range associated with the so-called coherent artifact.²⁰ Within 200 fs, these negative-amplitude signals disappear, and the ESA feature shifts noticeably toward the blue, now being centered at approximately 460 nm. Subsequent to this initial ultrafast relaxation, the excited dynamics take place over two distinct time scales: from approximately 300 fs to 15 ps and from a few tens of picoseconds to nanoseconds.

In the range from approximately 300 fs to 15 ps (central panels of [Figure 5a,b](#)) two effects dominate the spectral dynamics: a further blue-shift of the ESA maximum to 440 nm and an overall narrowing of the spectral profile. As a result of this narrowing, a band associated with one or more ESA transitions becomes clearly distinguishable near 600 nm. The appearance of a clean isosbestic point at 480 nm suggests that the underlying dynamics are a transition between two distinct states, with no substantial, if any, contributions from competing decay pathways. In particular, both the few picosecond time scale of this process and the characteristic change in spectral shape from a broad, red-shifted feature toward a more well-defined shape in the blue are typical of vibrational cooling processes.²¹ This suggests that the initial ultrafast dynamics leave the system in a vibrationally “hot” electronic state, the excess energy of which dissipates to leave a “cool” product state well before further relaxation processes can take place. In the time interval subsequent to these femto- to picosecond processes, further substantial spectral changes take place. In particular, the spectrum of the “cooled” product state disappears concom-

itantly with the appearance of an intense absorption band in the UV. Again, we observe a clear isosbestic point, implying the existence of another state-to-state transfer process with insignificant losses or other competing relaxation pathways.

Kinetic Analysis and Comparison with Theory.

Quantitative characterization of the photoinduced dynamics in complex **4** requires careful analysis. Here we analyze the dynamics in the standard kinetic framework of singular-value decomposition followed by global kinetic fitting to a sum-of-exponential-decays model. The observed kinetics can then be imposed on a particular relaxation model to determine a full relaxation scheme. The transient absorption signals reported in Figure 5b show two clear isosbestic points, suggesting a simple sequential deactivation scheme ($A \rightarrow B \rightarrow C \dots$) as a natural starting point for kinetic analysis. This commonly implemented scheme is advantageous in that it contains the exact same number of transfer processes as observable time constants, and thus it allows detailed analysis of the spectral dynamics by extraction of the optical spectra of the individual compartments. These spectra are commonly referred to as evolutionary associated (decay) spectra (EAS).²² In many practical cases, this simple model is a good approximation to the actual excited-state dynamics of the physical system, in which case the “compartments” correspond to the electronic (or vibrational) states of the system, and the EAS are the spectra of these states. The results of our global kinetic analysis are summarized in Figure 5c. The quantitative fit corroborates our qualitative analysis: the initially observed transition, with a time constant of ~ 150 fs, occurs from a state absorbing at approximately 500 nm to a state assigned to vibrationally hot radical **5** with an absorption maximum at 460 nm. This is followed by a further slight blue-shift and spectral narrowing with time constants of ~ 1 and 10 ps, respectively, before a final transfer process into a UV-absorbing state takes place with a time constant of ~ 400 ps. The phenomenological kinetic model extracted from the experimental kinetics can be compared directly with the predictions from theory (for the calculation of ESA, see the Supporting Information). We show this comparison in Figure 6. In the top panel we observe that the experimental TA spectrum extracted at 15 ps pump–probe delay is in good qualitative agreement with the spectrum calculated for the borylated ketyl radical **5** (Scheme 2). This is consistent with our expectation, in that the radical was predicted to form on ultrafast time scales and that its subsequent decay takes place on much longer time scales. The calculated radical spectrum in the top panel of Figure 6 was calculated at the XMS-CASPT2/cc-pvtz level. Only contributions from the transitions $D_1 \rightarrow D_2$ and $D_1 \rightarrow D_3$ are shown. When including the $D_1 \rightarrow D_4$ transition (dashed line in Figure 6, top panel), a rise in absorption occurs in the blue region that is not observed in the experiment. We attribute this to spuriously large perturbative corrections in the treatment of the D_4 state shifting the $D_1 \rightarrow D_4$ transition to the red. This is confirmed by calculations at the bt-PNO-STEOM-CCSD/def2-SVP²³ level (see the Supporting Information), where the transition appears at much shorter wavelengths.

At longer time scales, TDDFT with a continuum solvation model predicts the pair of the benzaldehyde- BCl_2 cation and the chloride anion to be $113.5 \text{ kJ mol}^{-1}$ more stable than the radical pair. It should therefore form by electron transfer via a Marcus-like mechanism.⁹ The predicted spectrum of the benzaldehyde- BCl_2 cation features intense absorption bands predominantly in the UV spectral range. This is in good qualitative agreement with the experimental observation of UV absorption and near-

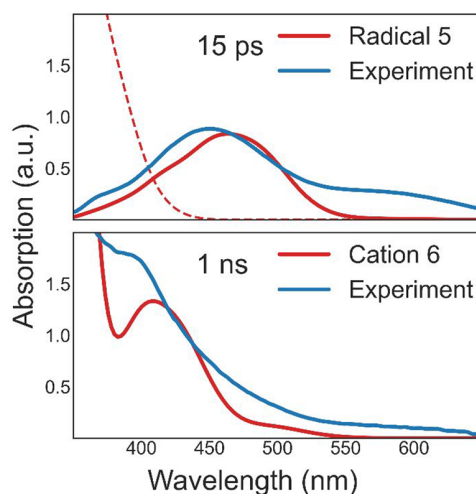
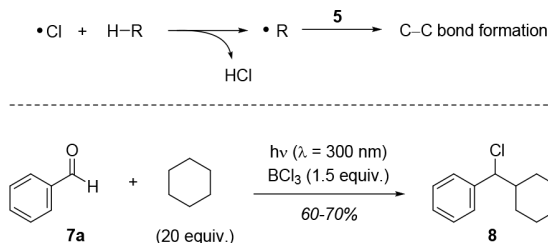


Figure 6. Comparison between calculated (red) and experimentally observed (blue) spectra. Top panel: calculated absorption spectrum of the borylated ketyl radical **5** and the experimental TA spectrum at 15 ps probe delay. The calculated spectrum for the radical only includes the $D_1 \rightarrow D_2$ and $D_1 \rightarrow D_3$ transitions. Including the $D_1 \rightarrow D_4$ transition (dashed line) leads to a rise in the UV that is discussed in the main text. Bottom panel: calculated spectrum of the benzaldehyde- BCl_2 cation **6** compared to the experimental TA spectrum at 1 ns probe delay.

negligible absorbance in the visible range at nanosecond pump–probe delays (Figure 6, bottom panel).

Addition Reaction of Hydrocarbons to Aromatic Aldehydes. With theory and transient absorption spectroscopy suggesting a homolytic B–Cl bond cleavage of complex **4**, it was attempted in synthetic studies to employ the putative chlorine radical for a hydrogen atom transfer (HAT) from an alkane H–R.²⁴ It was hypothesized that HAT would result in the formation of a carbon-centered radical, which would subsequently undergo C–C bond formation at the carbonyl carbon atom of the aldehyde (Scheme 3, top). The bond dissociation energy (BDE)

Scheme 3. Mechanistic Hypothesis for a Potential C–C Bond Formation (cf. Scheme 2) with a Hydrocarbon H–R and Preliminary Experiment on the UV-Mediated Reaction of Cyclohexane with Benzaldehyde in the Presence of Boron Trichloride

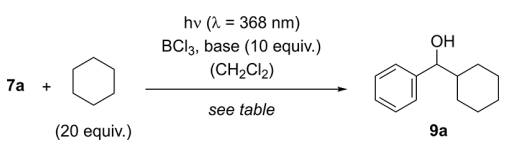


of HCl is sufficiently high ($\text{BDE} = 431 \text{ kJ mol}^{-1}$)²⁵ to render this process exothermic. Initially, cyclohexane ($\text{BDE} = 416 \text{ kJ mol}^{-1}$,²⁶ 20 equiv) was employed as the hydrocarbon that was irradiated together with benzaldehyde (**7a**) and BCl_3 (1.5 equiv) at $\lambda = 300 \text{ nm}$ in dichloromethane solution. The reaction was complete after 15 min, and a new product was isolated, which was identified as chloride **8** (Scheme 3, bottom).

The yields of the reaction were variable, and the isolation of the nonpolar product **8** from minor by-products was difficult.

There were indications that chloride **8** was formed from the respective alcohol by a thermal nucleophilic substitution reaction (*vide infra*). To support the assumption that the HCl developing in the HAT process was responsible for the formation of the chloride, the reaction was studied in the presence of a base. In addition, we employed for the optimization experiments an irradiation at longer wavelength ($\lambda = 368$ nm, cf. Figure 2a), which was found to also trigger the desired transformation. Gratifyingly, the addition of potassium phosphate (Table 1, entry 1) led to a suppression of the consecutive reaction, and alcohol **9a** was isolated in 53% yield.

Table 1. Optimization of the Reaction Conditions for the Light-Mediated Addition of Cyclohexane to Benzaldehyde in the Presence of Boron Trichloride



| entry ^a | equiv BCl ₃ | base | T [°C] | t ^b [min] | c [mM] | yield ^c [%] |
|--------------------|------------------------|---------------------------------|--------|----------------------|--------|------------------------|
| 1 | 1.5 | K ₃ PO ₄ | r.t. | 2.5 | 20 | 53 |
| 2 | 1.0 | K ₃ PO ₄ | r.t. | 10 | 20 | 51 |
| 3 | 0.5 | K ₃ PO ₄ | r.t. | 30 | 20 | 28 |
| 4 | 1.5 | K ₂ CO ₃ | r.t. | 2.5 | 20 | 45 |
| 5 | 1.5 | Cs ₂ CO ₃ | r.t. | 10 | 20 | 41 |
| 6 | 1.5 | K ₃ PO ₄ | r.t. | 2.5 | 40 | 51 |
| 7 | 1.5 | KH ₂ PO ₄ | r.t. | 5 | 40 | 40 |
| 8 | 1.5 | K ₃ PO ₄ | -78 | 90 | 40 | 53 |
| 9 | 1.5 | K ₃ PO ₄ | -40 | 15 | 40 | 65 |
| 10 | 1.5 | K ₃ PO ₄ | -10 | 10 | 40 | 67 |
| 11 | 1.5 | K ₃ PO ₄ | 0 | 10 | 40 | 65 |

^aA degassed solution of benzaldehyde (1.0 equiv), cyclohexane (20 equiv), boron trichloride, and base was irradiated by an LED with an emission maximum at $\lambda = 368$ nm (see the Supporting Information for details). ^bThe reaction was stopped once the reaction was complete based on TLC analysis. ^cYield of isolated product after column chromatography.

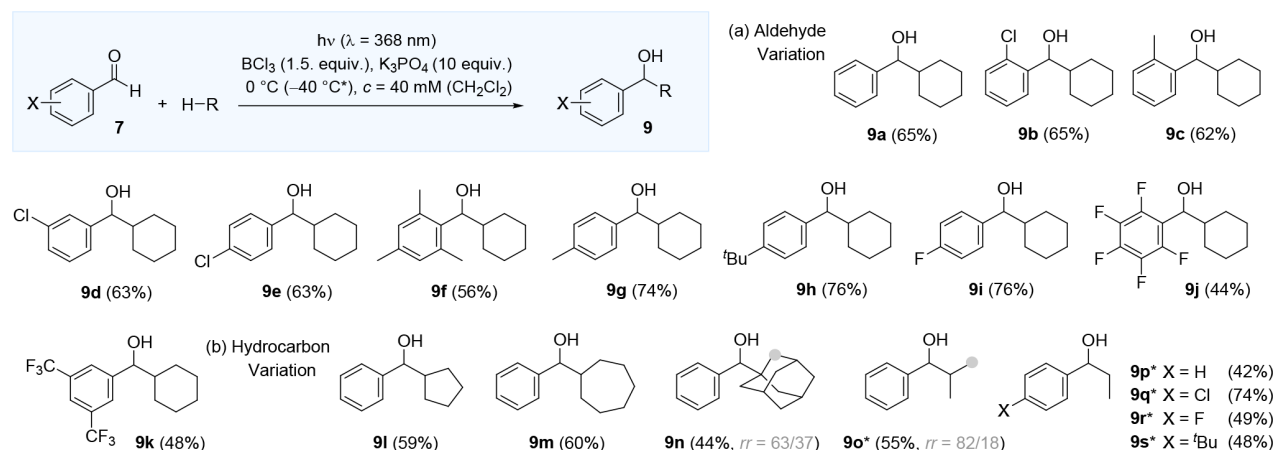
The reaction was complete in 150 s (2.5 min). A decrease of the Lewis acid concentration led to longer reaction times (entries 2, 3) and a lower yield. Other bases were less efficient as

acid scavengers (entries 4, 5, 7) compared to potassium phosphate. The influence of the substrate concentration was minimal (entry 6). Given that a lower amount of solvent facilitated the degassing procedure and allowed a more efficient stirring of the reaction mixture, the experiments at lower temperature were performed at $c = 40$ mM (entries 8–11). At -78 °C, the reaction rate decreased notably, and full conversion was achieved only after 90 min (entry 8). The situation improved at -40 °C (entry 9) and was best at -10 °C (entry 10). For practical reasons (ice bath), we also checked whether 0 °C was a suitable temperature, which turned out to be the case, and the conditions of entry 11 emerged as being optimal. Several modifications that are not listed in Table 1 did not lead to an improvement of the reaction yields (see the Supporting Information for details). Most notably, the use of other Lewis acids such as BBr₃ and AlBr₃ resulted in traces of product or no conversion, respectively. The scope of the reaction was first evaluated with regard to the aromatic aldehydes **7** (Scheme 4).

Tolerance toward functional groups such as chlorine (products **9b**, **9d**, **9e**), fluorine (products **9i**, **9j**), and trifluoromethyl (product **9k**) was established. The position of the chlorine substituent (*ortho*, *meta*, or *para*) had no influence on the reaction yield. The same observation was made for the methyl group (products **9c**, **9f**, **9g**), which was remarkably tolerated even in *ortho* position to the formyl group. Typically, *ortho*-methylbenzaldehydes undergo an intramolecular hydrogen abstraction to an *ortho*-quinodimethane intermediate.²⁷ This reaction was completely suppressed by the Lewis acid, confirming the absence of typical benzaldehyde reactivity emanating from the $n\pi^*$ triplet state. Other alkyl substituents like *tert*-butyl were well-tolerated (product **9h**). It was attempted to employ nonaromatic aldehydes in the reaction, but neither cinnamic aldehyde nor pivalaldehyde delivered the expected alcohol, even if the irradiation wavelength was altered.

Apart from cyclohexane, other alicyclic hydrocarbons such as cyclopentane (product **9l**) and cycloheptane (product **9m**) were successfully employed in the reaction. Adamantane gave a mixture of two regioisomeric products, the main isomer (product **9n**) of which was shown to display a quaternary carbon atom at the newly formed C–C junction. In a similar fashion, propane reacted preferably at the more highly substituted carbon atom, delivering mainly isopropyl ketone **9o**. Even light, short chain alkanes such as ethane could be

Scheme 4. Light-Mediated Addition of Hydrocarbons (H–R) to Aromatic Aldehydes **7** in the Presence of Boron Trichloride: Formation of Secondary Alcohols **9**

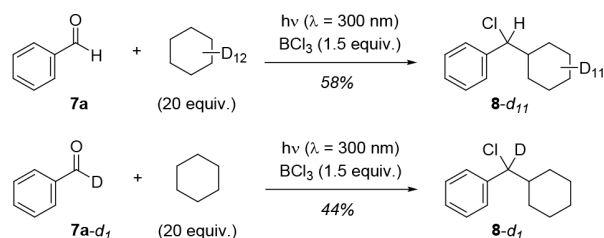


involved in the BCl_3 -mediated hydroalkylation reaction. Like for ketone **9o**, ethyl ketones **9p–9s** were obtained by irradiating a saturated solution of the hydrocarbon in CH_2Cl_2 at -40°C instead of 0°C . The other parameters remained unchanged compared to the optimized conditions. The reactions are amenable to scale-up, which was shown by performing the transformation **7a** ($X = \text{H}$) \rightarrow **9a** on a scale of 1.0 mmol. The desired product was obtained in 61% yield (117 mg).

Mechanistic Studies and Calculations on the Reaction Pathway. Mechanistic studies were undertaken to elucidate the individual steps responsible for the formation of products **8** and **9**. In a first set of experiments, alcohol **9a** was subjected to typical Lewis acid conditions in the absence of base and light (1.5 equiv of BCl_3 in CH_2Cl_2 at ambient temperature). The reaction occurred smoothly and showed the features of an $\text{S}_{\text{N}}1$ -type substitution; that is, a racemization of an enantioenriched alcohol was observed (see the [Supporting Information](#) for details). It is therefore reasonable to assume that alcohols **9** or their borylated analogues are the primary products of the reaction and chloride **8** is a consecutive product of **9a**. Similar observations were made by Kabalka et al., who studied the formation of secondary alcohols by addition of alkylboron chlorides to aromatic aldehydes.²⁸ In the absence of base, they also observed the formation of the respective benzylic chlorides, which likely derived from the primary C–C addition products.

Experiments with deuterated starting materials revealed that deuterium labeling was completely retained and no scrambling occurred ([Scheme 5](#)).

Scheme 5. Deuteration Experiments Performed with Fully Deuterated Cyclohexane- d_{12} (Top) and with Monodeuterated Benzaldehyde (7a-d₁**, Bottom)**



The reaction with cyclohexane- d_{12} delivered exclusively product **8-d₁₁** with no deuterium incorporated at the former benzaldehyde fragment. Vice versa, the monodeuterated benzaldehyde **7a-d₁** delivered product **8a-d₁** with exclusive deuterium incorporation at the alcohol carbon atom. In intermolecular competition experiments between nondeuterated cyclohexane (10 equiv) and cyclohexane- d_{12} (10 equiv), products **8** and **8-d₁₁** were isolated in equal amounts (see the [Supporting Information](#) for details), suggesting no significant kinetic isotope effect (KIE).²⁹ This is in line with previous work that found only marginal KIEs of approximately 1.1 for the H/D abstraction by a chlorine radical from cyclohexane.³⁰

Quantum yield measurements revealed that the reaction rate was not constant during the reaction but decreased over time (see the [Supporting Information](#) for details). We determined the quantum yield at the beginning of the reaction **7a** \rightarrow **8** by calculating the numerical quotient of benzaldehyde conversion over photon absorption ($\lambda = 368 \text{ nm}$). An average value for the quantum yield Φ was obtained from three individual runs resulting in $\Phi = 1.04 (\pm 0.06)$. The reaction rate increased if the concentration of cyclohexane was increased. Substrate con-

version scaled linearly with light intensity. The nonlinear behavior of the quantum yield was corroborated by monitoring the conversion in a light on–light off experiment at $\lambda = 368 \text{ nm}$ ([Figure 7](#)).

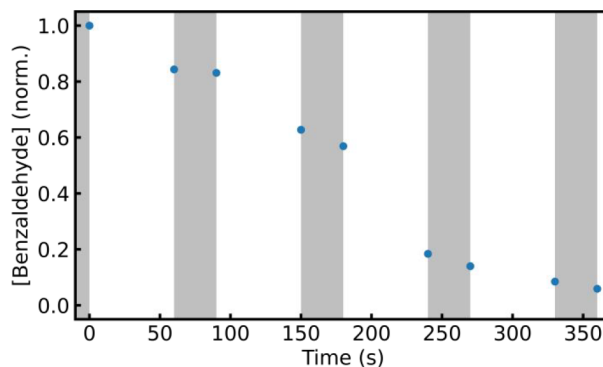


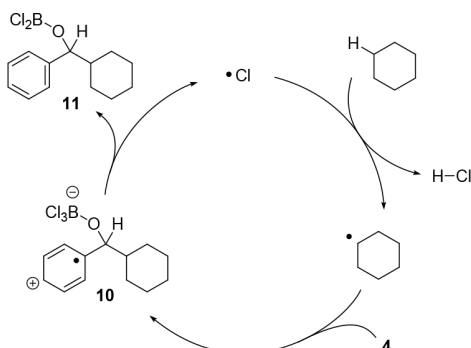
Figure 7. Kinetic profile of the reaction **7a** \rightarrow **8** under conditions of UV irradiation (cf. [Scheme 3](#): $\lambda = 368 \text{ nm}$, CH_2Cl_2 , 1.5 equiv of BCl_3 , 50 equiv of cyclohexane) depicted as a concentration decrease of **7a**. The light beam of the LED was blocked in the gray time intervals.

The reaction progressed even in time periods in which there was no exposure to light (gray bars). Together with the fact that the quantum yield exceeds unity and the cyclohexane concentration leverages the reaction rate, the result suggests that a radical chain process is involved in product formation. A mechanistic scenario often invoked for VLIH involves a chlorine radical that abstracts a hydrogen atom from a hydrocarbon with the resulting radical then entering a closed catalytic cycle. The BCl_3 -mediated alkylation occurs—at least partially—along a different reaction channel that leads to the formation of more than one product molecule per absorbed photon. While a recombination of the cyclohexyl radical with borylated ketyl radical **5** is feasible (cf. [Scheme 3](#)), a second reaction pathway appears to be competitive, which is responsible for the relatively high quantum yield. We suggest this process to be a radical chain that is mediated by the chlorine radical and that involves addition of the cyclohexyl radical to the benzaldehyde- BCl_3 complex (**4**). The addition is expected to occur at the carbonyl carbon atom, leading to putative intermediate **10**, from which a chlorine atom can dissociate and enter the radical chain ([Scheme 6](#)). The chain process can be terminated through radical–radical recombination, e.g., by a productive reaction of a cyclohexyl radical with borylated ketyl radical **5**.

Despite the fact that the addition of a nucleophilic cyclohexyl radical at the electrophilic carbon atom of **4** makes sense, it was not clear whether the proposed bond formation would be favorable, given that intermediate **10** displays a phenyl radical cation. To shed light on this issue, calculations were performed at the unrestricted DLPNO-CCSD(T)³¹/CBS(3/4,cc)// ω b97x-D3/def2-TZVP level of theory. It was found that the addition reaction is indeed feasible via a low-lying transition state **TS1** ([Figure 8](#)).

The postulated intermediate **10** was identified as an energy minimum on the reaction hypersurface (**Min2**), lying 17.4 kJ mol^{-1} below the energy of a complex **Min1** of the two starting components (cyclohexyl radical and **4**). Remarkably, the calculations also corroborated the subsequent step, i.e., the dissociation of the chlorine radical. This reaction proceeds again via a readily accessible transition state in which one B–Cl bond

Scheme 6. Mechanistic Pathway for a Potential Radical Chain by Addition of a Cyclohexyl Radical to the Benzaldehyde-BCl₃ Complex (4) and Subsequent Homolytic Cleavage of the B–Cl Bond within Intermediate 10



is elongated so that the chlorine atom eventually ends up as a π -complex (**Min3**) with the arene part of intermediate **11**. Although the ensuing reaction pathway was not further analyzed, it is reasonable to assume that the chlorine atom is available for another HAT so that the radical chain is continued. The results of the synthetic study thus correlate well with the predictions made by theory and with the experimental results obtained by transient absorption spectroscopy. They serve to substantiate the existence of the borylated ketyl radical **5** as a key intermediate in this chemistry, and the calculations support the existence of a radical chain as a reaction channel competing with a radical–radical recombination.

It was probed in some preliminary experiments whether there is synthetic evidence for cation **6** as the product of a consecutive electron transfer from radical **5** (Scheme 2). Trapping was attempted by using benzene as a potential nucleophile which would not be amenable to a premature HAT (BDE = 472 kJ mol⁻¹).²⁶ In the absence of light, the components did not show formation of a product that resulted from aromatic substitution at the benzene core. Upon irradiation, a sluggish conversion was observed and benzhydryl chloride (1,1-diphenylchloromethane) was detectable in low quantities by GLC-MS. However,

the product could not be isolated, and the yield was very low, which may be due to the low reactivity of the two components and/or a rapid recombination of cation **6** with the chloride anion to complex **4**.

CONCLUSION

We have used a combination of nonadiabatic dynamics simulations and femtosecond transient absorption spectroscopy to elucidate the key process occurring upon irradiation of the complex between an aromatic aldehyde and BCl₃. Rather than activating the aldehyde for a photochemical transformation, the Lewis acid is activated by the aldehyde toward a photoinduced homolytic bond cleavage. The borylated ketyl radical **5** was identified by both experiment and theory as the main intermediate of this process. It is conceivable that related processes are also responsible for homolytic bond cleavage reactions involving Lewis acid–base complexes of other Lewis acids such as TiCl₄.^{4b,32} A hydroalkylation of aromatic aldehydes was achieved, which was shown to involve a radical chain process. The key step is similar to the observed homolytic M–Cl cleavage occurring in transition metal complexes by ligand-to-metal charge transfer (LMCT) that has been exploited to unlock photochemical HAT-mediated transformations through the generation of a chlorine radical. In our case, no redox-active transition metal is required. Instead, an electron is directly transferred from the bound chlorine atom into the aromatic π -system of the substrate, thereby weakening the B–Cl bond. This Lewis acid–base activation mode may prove to be valuable for future applications that involve the cleavage of other bonds between boron and a given heteroatom.

ASSOCIATED CONTENT

Supporting Information

The Supporting Information is available free of charge at <https://pubs.acs.org/doi/10.1021/jacs.2c06683>.

Detailed information on experimental setups, light sources, procedures, and analytical data; characterization data including NMR spectra for new compounds; applied computational methods, calculated orbitals, and energies; further mechanistic studies (PDF)

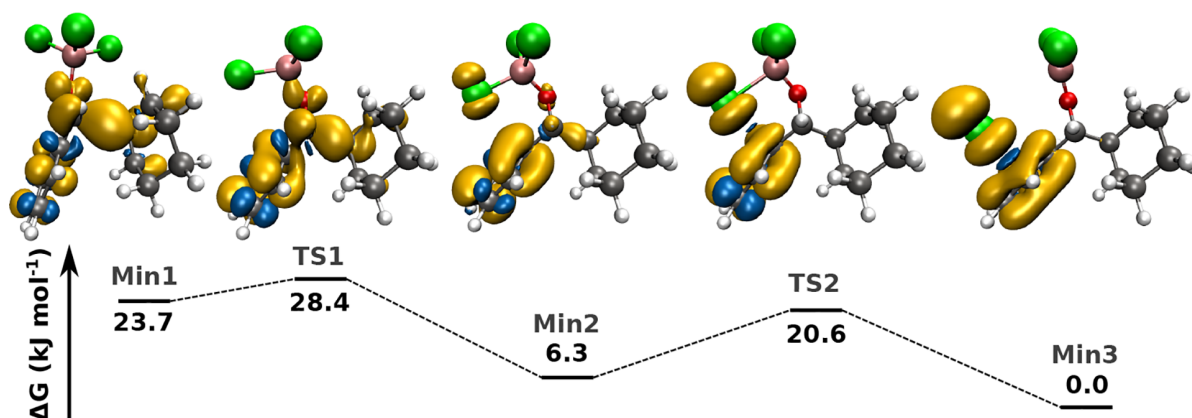


Figure 8. Attack of the cyclohexyl radical on the benzaldehyde-BCl₃ complex (**4**). On the top, structures of critical points along the reaction coordinate are displayed with the alpha spin density in yellow and the beta spin density in blue (isovalue = 0.002). At the bottom the relative Gibbs free energies of these structures are indicated. The structures were optimized at the unrestricted ω b97x-D3/def2-TZVP+CPCM (CH₂Cl₂) level of theory, and spin densities and entropic corrections were evaluated at the optimized points. The electronic contribution to the free energy was refined at the unrestricted DLPNO-CCSD(T)/CBS(3/4,cc) level. An intermediate **Min2** was identified that corresponds to structure **10** in Scheme 6. The free chlorine radical resides on the aromatic π -system (**Min3**) before being released as a free chlorine radical.

NMR data: Primary NMR data of new compounds, including FID files and acquisition data (ZIP)

Geometries and energies: Optimized geometries of the molecules in the computational study as an XYZ file; energies and geometries for the scan presented in Figure 4 as a CSV and XYZ file, respectively (ZIP)

AUTHOR INFORMATION

Corresponding Authors

Jürgen Hauer – Department Chemie and Catalysis Research Center (CRC) School of Natural Sciences, Technische Universität München, D-85747 Garching, Germany; orcid.org/0000-0002-6874-6138; Email: juergen.hauer@tum.de

Regina de Vivie-Riedle – Department of Chemistry, Ludwig-Maximilians-Universität München, D-81377 München, Germany; orcid.org/0000-0002-7877-5979; Email: regina.de_vivie@cup.uni-muenchen.de

Thorsten Bach – Department Chemie and Catalysis Research Center (CRC) School of Natural Sciences, Technische Universität München, D-85747 Garching, Germany; orcid.org/0000-0002-1342-0202; Email: thorsten.bach@ch.tum.de

Authors

Daniel P. Schwinger – Department Chemie and Catalysis Research Center (CRC) School of Natural Sciences, Technische Universität München, D-85747 Garching, Germany; orcid.org/0000-0002-3144-462X

Martin T. Peschel – Department of Chemistry, Ludwig-Maximilians-Universität München, D-81377 München, Germany

Thomas Rigotti – Department Chemie and Catalysis Research Center (CRC) School of Natural Sciences, Technische Universität München, D-85747 Garching, Germany

Piotr Kabaciński – IFN-CNR and Dipartimento di Fisica, Politecnico di Milano, I-20133 Milano, Italy; orcid.org/0000-0003-4591-5100

Thomas Knoll – Department of Chemistry, Ludwig-Maximilians-Universität München, D-81377 München, Germany; orcid.org/0000-0002-8509-571X

Erling Thyrhaug – Department Chemie and Catalysis Research Center (CRC) School of Natural Sciences, Technische Universität München, D-85747 Garching, Germany

Giulio Cerullo – IFN-CNR and Dipartimento di Fisica, Politecnico di Milano, I-20133 Milano, Italy; orcid.org/0000-0002-9534-2702

Complete contact information is available at: <https://pubs.acs.org/10.1021/jacs.2c06683>

Author Contributions

[#]D.P.S., M.T.P., and T.R. contributed equally. The manuscript was written through contributions by all authors.

Notes

The authors declare no competing financial interest.

ACKNOWLEDGMENTS

Financial support by the Deutsche Forschungsgemeinschaft (DFG, German Research Foundation), TRR 325 (projects B1, B8, C5) and 444632635, is gratefully acknowledged. D.P.S. thanks the Studienstiftung des Deutschen Volkes for a Ph.D. fellowship, J. Kudermann (TUM) for help with GC analyses,

and S. Breitenlechner (TUM) for fruitful discussions regarding the mechanism.

REFERENCES

- (1) (a) *Lewis Acids in Organic Synthesis*; Yamamoto, H., Ed.; Wiley-VCH: Weinheim, 2000. (b) *Lewis Acids and Selectivity in Organic Synthesis*; Santelli, M.; Pons, J.-M., Eds.; CRC Press: Boca Raton, 1996.
- (2) (a) *Chiral Lewis Acids in Organic Synthesis*; Mlynarski, J., Ed.; Wiley-VCH: Weinheim, 2017. (b) Sha, Q.; Deng, Y.; Doyle, M. P. The Future of Catalysis by Chiral Lewis Acids. *Top. Organomet. Chem.* **2015**, *62*, 1–26.
- (3) Recent reviews: (a) Genzink, M. J.; Kidd, J. B.; Swords, W. B.; Yoon, T. P. Chiral Photocatalyst Structures in Asymmetric Photochemical Synthesis. *Chem. Rev.* **2022**, *122*, 1654–1716. (b) Prentice, C.; Morrisson, J.; Smith, A. D.; Zysman-Colman, E. Recent developments in enantioselective photocatalysis. *Beilstein J. Org. Chem.* **2020**, *16*, 2363–2441. (c) Schwinger, D. P.; Bach, T. Chiral 1,3,2-Oxazaborolidine Catalysts for Enantioselective Photochemical Reactions. *Acc. Chem. Res.* **2020**, *53*, 1933–1943. (d) Silvi, M.; Melchiorre, P. Enhancing the potential of enantioselective organocatalysis with light. *Nature* **2018**, *554*, 41–49.
- (4) For pioneering studies, see: (a) Griffiths, J.; Hart, H. A new general photochemical reaction of 2,4-cyclohexadienones. *J. Am. Chem. Soc.* **1968**, *90*, 5296–5298. (b) Sato, T.; Yoshiie, S.; Imamura, T.; Hasegawa, K.; Miyahara, M.; Yamamura, S.; Ito, O. Metal-catalyzed Organic Photoreactions. Photoreactions of Compounds Containing a Carbon-oxygen or Carbon-nitrogen Multiple Bond with Alcohols in the Presence of Titanium(IV) Chloride or Uranyl Chloride. *Bull. Chem. Soc. Jpn.* **1977**, *50*, 2714–2730. (c) Lewis, F. D.; Howard, D. K.; Oxman, J. D. Lewis acid catalysis of coumarin photodimerization. *J. Am. Chem. Soc.* **1983**, *105*, 3344–3345. (d) Lewis, F. D.; Baranczyk, S. V.; Burch, E. L. Conformations, Spectroscopy, and Photochemistry of Methyl Phenanthrene-9-carboxylate, Phenanthrene-9-carboxamides, and Their Lewis Acid Complexes. *J. Am. Chem. Soc.* **1992**, *114*, 3866–3870. (e) Fukuzumi, S.; Okamoto, T.; Otera, J. Addition of Organosilanes with Aromatic Carbonyl Compounds via Photoinduced Electron Transfer in the Presence of Magnesium Perchlorate. *J. Am. Chem. Soc.* **1994**, *116*, 5503–5504. (f) Ischay, M. A.; Anzovino, M. E.; Du, J.; Yoon, T. P. Efficient Visible Light Photocatalysis of [2 + 2] Enone Cycloadditions. *J. Am. Chem. Soc.* **2008**, *130*, 12886–12887.
- (5) Stegbauer, S.; Jeremias, N.; Jandl, C.; Bach, T. Reversal of reaction type selectivity by Lewis acid coordination: the *ortho* photocycloaddition of 1- and 2-naphthaldehyde. *Chem. Sci.* **2019**, *10*, 8566–8570.
- (6) For reviews on the *ortho* photocycloaddition reaction, see: (a) Remy, R.; Bochet, C. Arene-Alkene Cycloaddition. *Chem. Rev.* **2016**, *116*, 9816–9849. (b) Hoffmann, N. Photochemical reactions of aromatic compounds and the concept of the photon as a traceless reagent. *Photochem. Photobiol. Sci.* **2012**, *11*, 1613–1641. (c) Wagner, P. J. Photoinduced *Ortho* [2 + 2] Cycloaddition of Double Bonds to Triplet Benzenes. *Acc. Chem. Res.* **2001**, *34*, 1–17.
- (7) Mayr, H.; Gorath, G. Kinetics of the Reactions of Carboxonium Ions and Aldehyde Boron Trihalide Complexes with Alkenes and Allylsilanes. *J. Am. Chem. Soc.* **1995**, *117*, 7862–7868.
- (8) Peschel, M. T.; Kabaciński, P.; Schwinger, D. P.; Thyrhaug, E.; Cerullo, G.; Bach, T.; Hauer, J.; de Vivie-Riedle, R. Activation of 2-Cyclohexenone by BF₃ Coordination: Mechanistic Insights from Theory and Experiment. *Angew. Chem., Int. Ed.* **2021**, *60*, 10155–10163.
- (9) Sailer, C. F.; Thallmair, S.; Fingerhut, B. P.; Nolte, C.; Ammer, J.; Mayr, H.; Pugliesi, I.; de Vivie-Riedle, R.; Riedle, E. A Comprehensive Microscopic Picture of the Benzhydryl Radical and Cation Photogeneration and Interconversion through Electron Transfer. *ChemPhysChem* **2013**, *14*, 1423–1437.
- (10) Recent review: Abderrazak, Y.; Bhattacharyya, A.; Reiser, O. Visible-Light-Induced Homolysis of Earth-Abundant Metal-Substrate Complexes: A Complementary Activation Strategy in Photoredox Catalysis. *Angew. Chem., Int. Ed.* **2021**, *60*, 21100–21115.

- (11) For selected contributions, see: (a) Kochi, J. K. Photolyses of Metal Compounds: Cupric Chloride in Organic Media. *J. Am. Chem. Soc.* **1962**, *84*, 2121–2127. (b) Shields, B. J.; Doyle, A. G. Direct C(sp³)-H Cross Coupling Enabled by Catalytic Generation of Chlorine Radicals. *J. Am. Chem. Soc.* **2016**, *138*, 12719–12722. (c) Ackerman, L. K. G.; Martinez Alvarado, J. I.; Doyle, A. G. Direct C-C Bond Formation from Alkanes Using Ni-Photoredox Catalysis. *J. Am. Chem. Soc.* **2018**, *140*, 14059–14063. (d) Hu, A.; Guo, J.-J.; Pan, H.; Zuo, Z. Selective functionalization of methane, ethane, and higher alkanes by cerium photocatalysis. *Science* **2018**, *361*, 668–672. (e) Treacy, S. M.; Rovis, T. Copper Catalyzed C(sp³)-H Bond Alkylation via Photo-induced Ligand-to-Metal Charge Transfer. *J. Am. Chem. Soc.* **2021**, *143*, 2729–2735. (f) Kang, Y. C.; Treacy, S. M.; Rovis, T. Iron-Catalyzed Photoinduced LMCT: A 1° C-H Abstraction Enables Skeletal Rearrangements and C(sp³)-H Alkylation. *ACS Catal.* **2021**, *11*, 7442–7449. (g) Jin, Y.; Zhang, Q.; Wang, L.; Wang, X.; Meng, C.; Duan, C. Convenient C(sp³)-H Bond Functionalisation of Light Alkanes and other Compounds by Iron Photocatalysis. *Green Chem.* **2021**, *23*, 6984–6989. (h) Yang, Q.; Wang, Y.-H.; Qiao, Y.; Gau, M.; Carroll, P. J.; Walsh, P. J.; Schelter, E. J. Photocatalytic C-H Activation and the Subtle Role of Chlorine Radical Complexation in Reactivity. *Science* **2021**, *372*, 847–852.
- (12) (a) Silva, C. R.; Reilly, J. P. Theoretical Calculations on Excited Electronic States of Benzaldehyde and Observation of the S₂←S₀ Jet-Cooled Spectrum. *J. Phys. Chem.* **1996**, *100*, 17111–17123. (b) Molina, V.; Merchán, M. Theoretical Analysis of the Electronic Spectra of Benzaldehyde. *J. Phys. Chem. A* **2001**, *15*, 3745–3751. (c) Cui, G.; Lu, Y.; Thiel, W. Electronic excitation energies, three-state intersections, and photodissociation mechanisms of benzaldehyde and acetophenone. *Chem. Phys. Lett.* **2012**, *537*, 21–26. (d) Ou, Q.; Subotnik, J. E. Electronic Relaxation in Benzaldehyde Evaluated via TD-DFT and Localized Diabatization: Intersystem Crossings, Conical Intersections, and Phosphorescence. *J. Phys. Chem. C* **2013**, *117*, 19839–19849.
- (13) For examples in the context of enantioselective photocatalysis, see: (a) Brimiouille, R.; Bauer, A.; Bach, T. Enantioselective Lewis Acid Catalysis in Intramolecular [2 + 2] Photocycloaddition Reactions: A Mechanistic Comparison between Representative Coumarin and Enone Substrates. *J. Am. Chem. Soc.* **2015**, *137*, 5170–5176. (b) Huang, X.; Quinn, T. R.; Harms, K.; Webster, R. D.; Zhang, L.; Wiest, O.; Meggers, E. Direct Visible-Light-Excited Asymmetric Lewis Acid Catalysis of Intermolecular [2 + 2] Photocycloadditions. *J. Am. Chem. Soc.* **2017**, *139*, 9120–9123. (c) Stegbauer, S.; Jandl, C.; Bach, T. Enantioselective Lewis Acid Catalyzed *ortho* Photocycloaddition of Olefins to Phenanthrene-9-carboxaldehydes. *Angew. Chem., Int. Ed.* **2018**, *75*, 14593–14596. (d) Yu, H.; Dong, S.; Yao, Q.; Chen, L.; Zhang, D.; Liu, X.; Feng, X. Enantioselective [2 + 2] Photocycloaddition Reactions of Enones and Olefins with Visible Light Mediated by N,N'-Dioxide-Metal Complexes. *Chem.—Eur. J.* **2018**, *24*, 19361–19367.
- (14) For the density functional: (a) Chai, J.-D.; Head-Gordon, M. Long-range corrected hybrid density functionals with damped atom-atom dispersion corrections. *Phys. Chem. Chem. Phys.* **2008**, *10*, 6615–6620. Dispersion correction: (b) Grimme, S.; Antony, J.; Ehrlich, S.; Krieg, H. A consistent and accurate ab initio parametrization of density functional dispersion correction (DFT-D) for the 94 elements H–Pu. *J. Chem. Phys.* **2010**, *132*, 154104.
- (15) For the ORCA program, see: Neese, F.; Wennmohs, F.; Becker, U.; Riplinger, C. The ORCA quantum chemistry program package. *J. Chem. Phys.* **2020**, *152*, 224108.
- (16) (a) Granovsky, A. A. Extended multi-configuration quasi-degenerate perturbation theory: The new approach to multi-state multi-reference perturbation theory. *J. Chem. Phys.* **2011**, *134*, 214113. (b) Shiozaki, T.; Györfly, W.; Celani, P.; Werner, H.-J. Communication: Extended multi-state complete active space second-order perturbation theory: Energy and nuclear gradients. *J. Chem. Phys.* **2011**, *135*, 081106.
- (17) Mai, S.; Marquetand, P.; González, L. Nonadiabatic dynamics: The SHARC approach. *Wiley Interdiscip. Rev.: Comput. Mol. Sci.* **2018**, *8*(6), No. e1370.
- (18) (c) For the BAGEL program, see BAGEL, Brilliantly Advanced General Electronic-structure Library. <http://www.nubakery.org> under the GNU General Public License. (d) Shiozaki, T. BAGEL: Brilliantly Advanced General Electronic-structure Library. *Wiley Interdiscip. Rev.: Comput. Mol. Sci.* **2018**, *8*, No. e1331.
- (19) (a) Cannizzo, A. Ultrafast UV spectroscopy: from a local to a global view of dynamical processes in macromolecules. *Phys. Chem. Chem. Phys.* **2012**, *14*, 11205–11223. (b) Bauer, B.; Sharma, R.; Chergui, M.; Oppermann, M. Exciton decay mechanism in DNA single strands: back-electron transfer and ultrafast base motions. *Chem. Sci.* **2022**, *13*, 5230–5242. (c) Riedle, E.; Roos, M. K.; Thalmair, S.; Sailer, C. F.; Krebs, N.; Fingerhut, B. P.; de Vivie-Riedle, R. Ultrafast photochemistry with two product channels: wavepacket motion through two distinct conical intersections. *Chem. Phys. Lett.* **2017**, *683*, 128–134. (d) Fingerhut, B. P.; Sailer, C. F.; Ammer, J.; Riedle, E.; de Vivie-Riedle, R. Build-up and Decay of the Optical Absorption in the Ultrafast Photo-Generation and Reaction of Benzhydryl Cations in Solution. *J. Phys. Chem. A* **2012**, *116*, 11064–11074.
- (20) Dobryakov, A. L.; Kovalenko, S. A.; Ernsting, N. P. Electronic and vibrational coherence effects in broadband transient absorption spectroscopy with chirped supercontinuum probing. *J. Chem. Phys.* **2003**, *119*, 988–1002.
- (21) Balevičius, V.; Pour, A. G.; Savolainen, J.; Lincoln, C. N.; Lukes, V.; Riedle, E.; Valkunas, L.; Abramavicius, D.; Hauer, J. Vibronic energy relaxation approach highlighting deactivation pathways in carotenoids. *Phys. Chem. Chem. Phys.* **2015**, *17*, 19491–19499.
- (22) van Stokkum, I. H. M.; Larsen, D. S.; van Grondelle, R. Global and target analysis of time-resolved spectra. *Biochim. Biophys. Acta* **2004**, *1657*, 82–104.
- (23) Dutta, A. K.; Nooijen, M.; Neese, F.; Izsák, R. Exploring the Accuracy of a Low Scaling Similarity Transformed Equation of Motion for Vertical Excitation Energies. *J. Chem. Theory Comput.* **2018**, *14*, 72–91.
- (24) (a) Capaldo, L.; Ravelli, D.; Fagnoni, M. Direct Photocatalyzed Hydrogen Atom Transfer (HAT) for Aliphatic C-H Bonds Elaboration. *Chem. Rev.* **2022**, *122*, 1875–1924. (b) Cao, H.; Tang, X.; Tang, H.; Yuan, Y.; Wu, J. Photoinduced intermolecular hydrogen atom transfer reactions in organic synthesis. *Chem. Catal.* **2021**, *1*, 523–598.
- (25) Luo, Y.-R. *Comprehensive Handbook of Chemical Bond Energies*; CRC Press, 2007.
- (26) Luo, Y.-R. *Handbook of Bond Dissociation Energies in Organic Compounds*; CRC Press, 2003.
- (27) (a) Klán, P.; Wirz, J.; Gudmundsdottir, A. D. Photoenolization and Its Applications. In *CRC Handbook of Organic Photochemistry and Photobiology*, 3rd ed.; Griesbeck, A.; Oelgemöller, M.; Ghetti, F., Eds.; CRC Press, 2012. (b) Yang, N. C.; Rivas, C. A New Photochemical Primary Process, the Photochemical Enolization of *o*-Substituted Benzophenones. *J. Am. Chem. Soc.* **1961**, *83*, 2213–2213.
- (28) Kabalka, G. W.; Wu, Z.; Ju, Y. Alkylation of aromatic aldehydes with alkylboron chloride derivatives. *Tetrahedron* **2001**, *57*, 1663–1670.
- (29) Simmons, E. M.; Hartwig, J. F. On the Interpretation of Deuterium Kinetic Isotope Effects in C-H Bond Functionalizations by Transition-Metal Complexes. *Angew. Chem., Int. Ed.* **2012**, *51*, 3066–3072.
- (30) Li, Z.; Pirasteh, A. Kinetic study of the reactions of atomic chlorine with several volatile organic compounds at 240–340 K. *Int. J. Chem. Kinet.* **2006**, *38*, 386–398.
- (31) Guo, Y.; Riplinger, C.; Liakos, D. G.; Becker, U.; Saitow, M.; Neese, F. Linear scaling perturbative triples correction approximation for open-shell domain-based local pair natural orbital coupled cluster singles and doubles theory [DLPNO-CCSD(T₀/T)]. *J. Chem. Phys.* **2020**, *152*, 024116.
- (32) Yamane, M.; Kanzaki, Y.; Mitsunuma, H.; Kanai, M. Titanium(IV) Chloride-Catalyzed Photoalkylation via C(sp³)-H Bond Activation of Alkanes. *Org. Lett.* **2022**, *24*, 1486–1490.

5. Summary

The first chapter of this thesis focused on theoretical methods able to describe the relaxation of a solvated molecule in an explicit solvent environment. We presented two new approaches which enable coupling between a quantum-dynamical nuclear wavepacket on a grid and a classical environment. The first approach is based on Ehrenfest dynamics and couples our in-house code QDng to the MD code GROMACS. We presented the dissociation of ICN in liquid argon and the photo relaxation of uracil in water as an example system and examined the decoherence in our simulations of the ICN system. While our approach is relatively general, it does not capture all correlation effects between the system and its environment. It does not describe vibrational energy redistribution correctly in the long time limit as the system approaches thermal equilibrium with its environment. The description is accurate for short timescales, especially for the initial collisions of the solvated system with the solvent cage in a dissociation reaction. More extended simulations could be achieved with a multiconfigurational approach. The MCEv2 approach was developed, implemented, and adapted to the coupling between the vibrational modes of a quantum system and a classical environment. The approach was tested on the dynamics of a 7-dimensional model of an I_2Kr_{18} cluster. The method reproduced the numerically exact MCTDH dynamics well and was able to correctly treat the decoherence induced in the system in the initial collision with the solvent cage. However, to significantly increase the time span for which MCE is able to describe the energy redistribution, a large number of coupled Ehrenfest trajectories are required, which increases computational cost. In the last section of the first chapter, TSH was reviewed, since, as a part of this thesis, three extensions to the program SHARC were implemented, which allow for 1) adaptive time-stepping, 2) spin-orbit coupling in simulations with analytical XMS-CASPT2 gradients and 3) the usage of the fast electronic structure code FermiONs++ for QM/MM TSH simulations.

In the second chapter of this thesis, simulations of the IR spectrum of methylsulfonylmethane ($DMSO_2$) in water were presented. The IR spectrum was calculated via the traditional harmonic approximation and the Fourier-transformed dipole autocorrelation function obtained from *ab initio* MD. These simulations were then put into the context by a sub-femtosecond electric field measurement in field-resolved spectroscopy performed by Theresa Buberl in the group of Ioachim Pupeza at Max Planck institute of quantum optics. A measure of coherent energy transfer from field to matter was established, and the dynamics of this quantity were analyzed. We observed that energy is transferred from the field to the sample with each half-cycle and that an additional series of stimulated emission and absorption events occur when a chirped pulse is used in the excitation. The signal yields a coherent sample-specific spectroscopic fingerprint carrying dephasing information due to molecular motion in varying environments. In the future, the ratio of the coherently transferred optical energy to the excitation energy could be used as an indicator of the required spectroscopic detection sensitivity.

The third chapter of this thesis focused on the excited states of 2-enones and their complex photochemistry. Examples for reactions from the $\pi\pi^*$ and $n\pi^*$ states were given.

Special attention was paid to two reaction sequences, the *Z/E* isomerization of cyclohept-2-enone followed by a Diels-Alder reaction and the formation of a cyclopropyl ketene from 5,5-Dimethylcyclopent-2-enone, with subsequent nucleophilic addition of a primary amine. In both cases, critical points on the excited state PES were explored, and in the end, the reaction was found to be possible both in the singlet and triplet manifold. For the Diels-Alder reaction, if cyclic dienes were employed, a notable exo/endo selectivity was recorded, mostly in favor of the exo-isomer, that could be predicted from DLPNO-CCSD(T)/CBS(3/4, cc) calculations.

The fourth chapter illuminated the influence of Lewis acid coordination on the electronic states of enones. The changes to the orbitals induced by the coordination and how they affect the UV-Vis spectrum were discussed in detail. As a direct effect of the coordination to the n orbital, the $n\pi^*$ state is blue-shifted. An increase in the electron-withdrawing effect of the carbonyl group could explain the redshift of the $\pi\pi^*$ state. The dynamics of the cyclohex-2-enone- BF_3 complex were investigated by TSH simulations at the XMS-CASPT2 level and compared to free cyclohex-2-enone, which showed that, in the gas phase, dissociation of the complex occurs and that conical intersections that are inaccessible in the free enone become accessible. In contrast, the free enone shows clean relaxation to the $^3\pi\pi^*$ state, typically associated with follow-up reactions like [2+2] photocycloaddition. State-of-the-art ultrafast transient absorption measurements on the complex showed that, in solution, an alternative pathway allows the enone complex to also populate this state on an ultrafast timescale without cleavage of the bond to the Lewis acid. This was supported by QM/MM TSH simulations at the TDDFT level performed with the help of a new SHARC-FermiONS++ interface. They showed that embedding in the solvent hinders the dissociation and leads to relaxation to the S_1 minimum within a few hundred femtoseconds. Since triplets are still missing from these simulations, adding triplet states will be the subject of future work to explain the observed transient absorption signal fully. Finally, we investigated the benzaldehyde- BCl_3 complex using the same combination of techniques (TSH simulations and ultrafast TA in the UV) as for the cyclohex-2-enone- BF_3 complex. In both theory and experiment, the formation of a borolated ketyl radical was observed, which means that rather than activating the aldehyde for a photochemical transformation, the Lewis acid is activated by the aldehyde toward a photoinduced homolytic bond cleavage of the B-Cl bond. This process could be rationalized by the interaction of the chlorine lone pair states with the bright states in the FC region. The resulting chlorine atom could be used as a hydrogen atom transfer reagent, and a hydroalkylation of aromatic aldehydes was achieved, which was shown to involve a radical chain process.

In summary, this thesis presented both new and well-known techniques to describe the initial relaxation processes of molecular systems computationally. Especially their interaction with an explicit solvation environment was described at different quantum/classical levels. Additionally, modeling spectroscopic observables was also in focus, ranging from applications in the IR to TA in the UV. For 2-enones and their Lewis acid complexes, a deep understanding of their photochemical properties was developed through the application of high-level electronic structure methods and dynamic simulations. That such a wide variety of systems could be treated successfully exemplifies the broad range of applicability of modern quantum chemistry and its ever-increasing predictive power.

A. The Semi-Classical Wigner Sampling Approach to Calculate Optical Spectra

The most straightforward method for calculating UV-Vis absorption spectra involves determining the vertical excitation energies and transition dipole moments of electronically excited states at the FC geometry. Adopting this static approach significantly reduces the computational effort since the molecule's motion is ignored. However, even with high-level electronic structure methods, the position of the absorption lines in these static stick spectra can deviate significantly from the maxima of the experimental absorption bands. In these cases, one should account for vibrational effects.[218–220]

The Wigner distribution is a mathematical tool used to represent a quantum mechanical system in phase space. It is a quasi-probability distribution similar to a distribution in classical phase space but can yield negative values, indicating interference and quantum coherence effects. However, there are no negative values for the ground state of a harmonic oscillator.[64, 221] Thus, by drawing samples from the Wigner distribution, the vibrational ground state of a molecule can be represented by a classical distribution (an ensemble) of geometries. This sampling approach gives access to the vibrational broadening of optical line shapes in a semi-classical fashion.[33, 222, 223]

Vertical excitation wavelengths and transition dipole moments are calculated for each geometry in the ensemble, and the resulting stick spectra are first broadened with an empirical lineshape to remove statistical noise and then averaged.[222] With this approach, one misses out on features that are due to the vibrational quantization of the excited state. Instead, one captures anharmonic effects and vibronic coupling in both the ground and excited states. Many methods that describe the vibrational fine structure fail to do this, as they mostly rely on a description of the excited states of the molecule as independent harmonic oscillators.[224, 225] It is, of course, possible to build parametrized fully coupled inharmonic models of the excited states of small molecules and obtain the resulting vibrational states using methods such as MCTDH,[226] VPT2[227] or other methods.[228] However, this requires significant effort and care from the model builder and might place high demands on their computational infrastructure due to the steep scaling of some of these methods. Thus, it is far from standard practice. So, when are spectra obtained from a Wigner distribution a good approximation? If, during the excitation process, mainly high-lying vibrational states are populated that behave essentially classically. According to the FC principle, this is the case if the minima in the ground state and the excited state are geometrically far apart, i. e. if there is large amplitude motion after excitation[34] or if the excited state is dissociative. In this way, sampling a Wigner distribution is complementary to the methods based on the harmonic approximation that work best for rigid molecules with small amplitude motion in the excited state.

After this initial discussion of static spectra, we will proceed with a discussion of transient spectra and dynamics. On the theoretical side, we use TSH to simulate the dynamics of a molecule, the theory of which is described in section 1.3. On the experimental side, the dynamics can be observed using ultrafast TA spectroscopy. TA spectroscopy can essentially be seen as time-resolved UV-Vis. A pump pulse (usually at a fixed wavelength corresponding to one of the molecular electronic transitions) excites the sample to measure a transient absorption spectrum. After a time delay, a white-light pulse interrogates the resulting dynamics. The static spectrum (without the pump pulse) is subtracted from the spectrum at the time delay. The full TA data is then composed of all these difference spectra at variable time delays. Thus, in principle, a TA signal consists of three components; 1) ground state bleach, a negative signal at the same frequencies as the static spectrum, caused by the decrease in ground state population due to the pump pulse; 2) stimulated emission, a negative signal caused by population in the excited state being dumped back into the ground state by the probe pulse and 3) ESA a positive signal caused by the excited state population absorbing the probe pulse to reach even higher excited states.[125]

Since, for the observations discussed in this work, ground state bleach lies outside the observed spectral range and stimulated emission is negligible, we focus our discussion on the calculation of ESA. In the same way as ground state absorption and consistent with the semi-classical Wigner sampling approach, the full ESA can, in principle, be calculated from an ensemble of classical trajectories evolving on the excited state PES that are propagated using TSH. For examples using this protocol, see [34, 229]. This work follows a slightly different, less computationally demanding approach. Using global fitting techniques, the TA signal can be decomposed into a series of spectral signatures called EADS. These correspond to the spectra of intermediates in the relaxation process between which conversion takes place with first-order kinetics. In some instances, these EADS can be calculated without referencing the actual dynamics. At $t = 0$, the system has not yet left the FC region, and the EADS can be calculated from the Wigner distribution of the ground state minimum. In a static spectrum, the absorbance of each $S_0 \rightarrow S_n$ transition is proportional to the square of the transition dipole moment. In contrast, in the EADS, the absorption of the $S_m \rightarrow S_n$ transition is proportional to the product of the squares of the transition dipole moments of the $S_0 \rightarrow S_m$ and the $S_m \rightarrow S_n$ transition, with S_m being the state to which the pump pulse promotes the system. This treatment neglects electronic coherence between S_0 and S_m induced by the pump pulse. After a certain time, the vibrational modes of the system will have reached approximate thermal equilibrium with its environment, while the electronic modes might still be excited. From this point onward, the EADS become the spectra of the system at minima of the PES. These can be calculated just like static spectra by sampling a Wigner distribution using the normal modes of the respective minimum and calculating transition dipole moments and wavelengths to higher excited states.

B. Supporting Information for Chapter 2

B.1. Susceptibility and Absorbance

The susceptibility χ is related to the absorption coefficient α as

$$\alpha = \frac{-k\text{Im}(\chi)}{\sqrt{\text{Re}(\chi) + 1}} \quad (\text{B.1})$$

for weakly absorbing media with $|\text{Im}(\chi)| \ll |1 + \chi|$ and as

$$\alpha = 2k\sqrt{-\text{Im}(\chi)/2} \quad (\text{B.2})$$

for strongly absorbing media with $|\text{Im}(\chi)| \gg |1 + \chi|$. k is the wavevector ($k = \frac{\omega}{c}$) of a monochromatic wave of frequency ω . The absorbance A is related to the absorption coefficient by the Beer-Lambert law

$$A = \ln \left(\frac{I_{ref}}{I_{sample}} \right) = \alpha d, \quad (\text{B.3})$$

where d is the thickness of the cuvette and I_{ref} and I_{sample} are the transmitted intensities through a reference solution of pure solvent and the (dilute) sample solution.

B.2. Sub-Cycle Dynamics and Coherent Transients Explained in Terms of the Evolution of the Coherence

In the article presented in the main part of this thesis,[4] we quantify coherent absorption and emission as

$$CET(t) = c\epsilon_0 \int_0^t |\mathcal{E}_{ref}(t)|^2 - |\mathcal{E}_{sample}|^2 dt_1 \quad (\text{B.4})$$

which we term coherent energy transfer $CET(t)$. \mathcal{E}_{ref} is the time-dependent electric field after passing through a reference (pure solvent), and \mathcal{E}_{sample} is the electric field after passing through the sample solution. It represents a running total of the energy coherently absorbed and emitted by the solvated DMSO₂ molecules. Accordingly, a decrease in $CET(t)$ marks stimulated emission, while an increase in $CET(t)$ marks absorption. Two main observations are made: 1) During the vibrational excitation of DMSO₂ by a few-fs pulse, alternating absorption and stimulated emission can be observed with each half-cycle of the electric field (sub-cycle dynamics). 2) On a femtosecond to picosecond timescale, another series of absorption and emission events can be observed when a chirped laser field is used (coherent transients). In this appendix, we will explain how the shape of these signals arises. The explanation combines insights from [230–233].

To explain these phenomena, it is instructive to look at the coherence ρ_{0k} between the ground state and a vibrational level k in a time-dependent picture. To explain the observed structure of $CET(t)$ qualitatively, it is sufficient to model the system as a two-level system with only one mode. In the short time limit ($t \ll \Gamma_k$) and low excitation power limit (leading to $|\rho_{0k}| \ll 1$), $CET(t)$ is proportional to the squared absolute value of the coherence

$$CET(t) \propto |\rho_{0k}|^2. \quad (\text{B.5})$$

Coherence can be calculated as

$$\rho_{0k}^{(1)}(t) = \frac{i}{\hbar} \mu_{0k} \int_0^\infty \mathcal{E}(t-t_1) e^{i\omega_k t_1} e^{-\Gamma_k t_1} dt_1 \quad (\text{B.6})$$

to first order using time-dependent perturbation theory, where $\mathcal{E}(t)$ is the impinging electric field.[125, 230] The electric field for a linearly chirped pulse can be represented as

$$\mathcal{E}(t) = 2\mathcal{E}_0(t) \cos((\omega_0 + ct)t) = \mathcal{E}_0(t) (e^{-i(\omega_0+ct)t} + e^{+i(\omega_0+ct)t}) \quad (\text{B.7})$$

with the amplitude $\mathcal{E}_0(t)$, the frequency ω_0 and the chirp c . Inserting into eq. (B.6) for zero chirp ($c = 0$) yields

$$\begin{aligned} \rho_{0k}^{(1)}(t) = & \frac{i}{\hbar} \mu_{0k} (e^{+i\omega_0 t} \int_0^\infty e^{i(\omega_0 - \omega_k)t_1} \mathcal{E}_0(t-t_1) e^{-\Gamma_k t_1} dt_1 \\ & + e^{-i\omega_0 t} \int_0^\infty e^{i(\omega_0 + \omega_k)t_1} \mathcal{E}_0(t-t_1) e^{-\Gamma_k t_1} dt_1). \end{aligned} \quad (\text{B.8})$$

There are two frequency-dependent integrals contributing to the coherence, one containing $e^{i(\omega_0 - \omega_k)t_1}$ and one containing $e^{i(\omega_0 + \omega_k)t_1}$. Close to resonance $\omega_0 \approx \omega_k$ $e^{i(\omega_0 - \omega_k)t_1}$ is constant. Thus, the magnitude of the coherence generated by this term is only limited by $\mathcal{E}_0(t-t_1)$ and $e^{-\Gamma_k t_1}$ as the upper bound of integration approaches infinity. The second term oscillates with approximately double the field frequency. Thus, the integral will be

close to zero when integrated over one cycle of the field and will stay much smaller than the first term when integrated over the whole range of integration. Accordingly, the first term will dominate the dynamics for times that are long enough, and the second term is often neglected, which is known as the RWA. However, the second term will cause modulations of the coherence on a timescale of $\frac{\pi}{\omega_0}$. These are the origin of the observed sub-cycle dynamics. When viewed in the complex plane, these modulations correspond to a cycloid structure imprinted on the general shape of the coherence.

The coherent transients happen on a much longer timescale and are much larger in magnitude. Thus, we can safely employ the RWA to explain the absorption and emission due to the chirp. We assume that the chirp is small enough such that $\omega_0 + ct \approx \omega_k$ for all t . We obtain

$$\tilde{\rho}_{0k}^{(1)}(t) = \frac{i}{\hbar} \int_0^\infty \mathcal{E}_0(t - t_1) e^{-\Gamma_k t_1} e^{i\omega_0 c(t-t_1)^2} dt_1, \quad (\text{B.9})$$

where we have introduced the coherence in the rotating frame $\tilde{\rho}_{0k}^{(1)}(t) = \rho_{0k}^{(1)}(t) e^{-i\omega_0 t}$. Then, the real and imaginary parts of the coherence in the rotating frame are separated which yields

$$\begin{pmatrix} \text{Re}(\tilde{\rho}_{0k}^{(1)}(t)) \\ \text{Im}(\tilde{\rho}_{0k}^{(1)}(t)) \end{pmatrix} = \frac{i}{\hbar} \int_0^\infty \mathcal{E}_0(t - t_1) e^{-\Gamma_k t_1} \begin{pmatrix} \cos(c(t - t_1)^2) \\ \sin(c(t - t_1)^2) \end{pmatrix} dt_1. \quad (\text{B.10})$$

If $\mathcal{E}_0(t)$ is approximately constant and $\Gamma_k \approx 0$, this is the parametric equation for an Euler spiral, with one of the focal points at the origin. This explains the observed coherent transients. At first, the coherence spirals around the origin of the complex plane, without increasing in magnitude. This does not lead to absorption and emission. Then as the pulse passes through the resonance, the coherence passes through the central section of the Euler spiral, significantly increasing in magnitude, which goes along with absorption. Then, the coherence spirals around the second focus of the Euler spiral, causing it to periodically increase and decrease in magnitude. This is correlated with the observed additional absorption and emission events. A finite duration of $\mathcal{E}_0(t)$ leads to a spiraling out of the origin at the beginning of the pulse, which manifest as a more gradual increase in absorption than would be expected for a continuous field. It also leads to a spiraling into the second focal point at the end of the pulse, thus dampening the coherent transients. A small, but nonzero Γ_k dampens the transients even more and leads to a gradual return of the coherence towards the origin of the complex plane.

C. Supporting Information for Section 4.2

C.1. Details of CASPT2 Calculations on Cyclohex-2-enone-BF₃

All XMS-CASPT2 calculations were performed using an (8,7) active space containing two π -orbitals (π_1 , π_2), two π^* -orbitals (π_1^* , π_2^*), the oxygen lone pair n and the σ - and σ^* -orbitals of the α -C-C bond (see fig. C.1). The calculations employed state averaging over three states (S_0 , S_1 , S_2), the single-state-single-reference flavor of multistate CASPT2 and an imaginary shift of 0.2. The cc-pvqz basis set was used with the resolution of the identity approximation and the cc-pvqz-jkfit auxiliary basis.

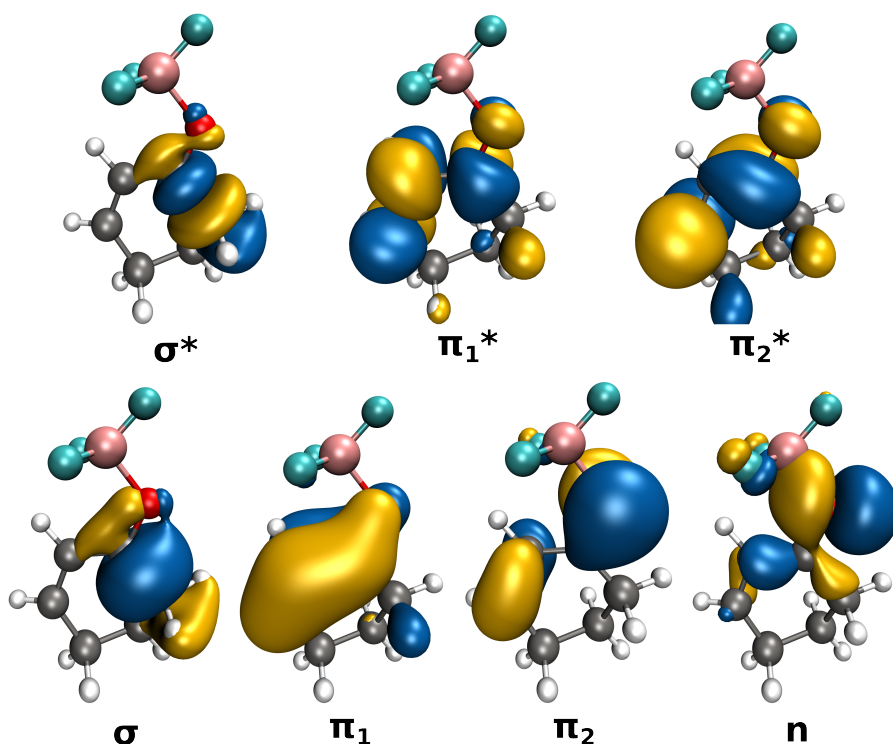


Figure C.1.: Orbitals in the (8,7) active space of cyclohexenone-BF₃ (isovalue: 0.02).

C.2. Results of the TDDFT Benchmark

Table C.1: Performance of all tested functionals compared to XMS-CASPT2(8,7)/cc-pvqz.

| Functional | RMSD(∇E_1) | RMSD(ΔE_{12}) | RMSD(ΔE_{01}) |
|--------------|----------------------|-------------------------|-------------------------|
| APBE0 | 4.5314 | 0.1736 | 0.7109 |
| APF | 4.5197 | 0.1771 | 0.7158 |
| B1LYP | 4.4076 | 0.1796 | 0.7298 |
| B1PW91 | 4.5500 | 0.1749 | 0.7122 |
| B1WC | 4.5950 | 0.2606 | 0.7463 |
| B3LYP | 4.3367 | 0.1859 | 0.7325 |
| B3LYP3 | 4.3377 | 0.1862 | 0.7326 |
| B3LYP5 | 4.3377 | 0.1862 | 0.7326 |
| B3LYP-MCM1 | 4.3878 | 0.1959 | 0.7433 |
| B3LYP-MCM2 | 4.5538 | 0.1739 | 0.7389 |
| B3LYPS | 4.3186 | 0.2479 | 0.7509 |
| B3P86 | 4.4419 | 0.1928 | 0.7285 |
| B3P86-NWCHEM | 4.4528 | 0.1900 | 0.7286 |
| B3PW91 | 4.4380 | 0.1932 | 0.7196 |
| B5050LYP | 5.7086 | 0.5538 | 0.8677 |
| B97 | 4.3926 | 0.1939 | 0.7202 |
| B97-1 | 4.4052 | 0.1837 | 0.7200 |
| B97-1P | 4.3759 | 0.2388 | 0.7333 |
| B97-2 | 4.4534 | 0.1740 | 0.7214 |
| B97-3 | 4.5263 | 0.1811 | 0.7048 |
| B97-K | 4.9029 | 0.3616 | 0.7495 |
| BHANDH | 6.3031 | 0.4925 | 0.8426 |
| BHANDHLYP | 5.6400 | 0.5575 | 0.8718 |
| BLYP35 | 4.7566 | 0.2983 | 0.7586 |
| CAM-B3LYP | 5.0122 | 0.3252 | 0.7657 |
| CAMH-B3LYP | 4.6893 | 0.2438 | 0.7420 |
| CAM-O3LYP | 37.1717 | 1.1106 | 1.5859 |
| CAM-PBEH | 5.4353 | 0.3216 | 0.7875 |
| CAM-QTP-00 | 6.9839 | 0.8142 | 1.0334 |
| CAM-QTP-01 | 5.9665 | 0.5240 | 0.8520 |
| CAM-QTP-02 | 6.3773 | 0.6135 | 0.8985 |
| CAP0 | 4.6025 | 0.1752 | 0.7108 |
| CASE21 | 4.5052 | 0.1736 | 0.7134 |

Continued on next page

Table C.1: Performance of all tested functionals compared to XMS-CASPT2(8,7)/cc-pvqz. (Continued)

| Functional | RMSD(∇E_1) | RMSD(ΔE_{12}) | RMSD(ΔE_{01}) |
|----------------|----------------------|-------------------------|-------------------------|
| EDF2 | 4.4099 | 0.2186 | 0.7493 |
| HAPBE | 4.4381 | 0.1976 | 0.7186 |
| HFLYP | 10.1031 | 1.4713 | 1.5253 |
| HPBEINT | 4.5996 | 0.2533 | 0.7376 |
| HSE03 | 4.5382 | 0.1735 | 0.7154 |
| HSE06 | 4.5395 | 0.1747 | 0.7161 |
| HSE12 | 4.7516 | 0.2059 | 0.7203 |
| HSE12S | 4.9283 | 0.2487 | 0.7291 |
| HSE-SOL | 4.8391 | 0.1822 | 0.7210 |
| KMLYP | 6.6171 | 0.6222 | 0.9019 |
| LB07 | 6.8732 | 0.5454 | 0.8063 |
| LC-BLYP | 5.4560 | 0.3400 | 0.7741 |
| LC-BLYP-EA | 5.2215 | 0.2804 | 0.7669 |
| LC-BLYPR | 5.4216 | 0.3436 | 0.7634 |
| LC-BOP | 6.5177 | 0.6070 | 0.8533 |
| LC-PBEOP | 5.4328 | 0.3346 | 0.7544 |
| LC-QTP | 6.5925 | 0.6135 | 0.8695 |
| LC-VV10 | 6.3408 | 0.5627 | 0.8051 |
| LC-WPBE | 5.9596 | 0.4686 | 0.7656 |
| LC-WPBE08-WHS | 6.3408 | 0.5627 | 0.8051 |
| LC-WPBEH-WHS | 6.7500 | 0.6758 | 0.8871 |
| LC-WPBESOL-WHS | 7.4771 | 0.8027 | 0.9645 |
| LC-WPBE-WHS | 5.9605 | 0.4694 | 0.7640 |
| LRC-WPBE | 5.1949 | 0.2690 | 0.7181 |
| LRC-WPBEH | 5.0020 | 0.2578 | 0.7334 |
| MB3LYP-RC04 | 4.3698 | 0.1810 | 0.7319 |
| MCAM-B3LYP | 4.4916 | 0.1926 | 0.7303 |
| MPW1K | 5.4188 | 0.4027 | 0.7760 |
| MPW1LYP | 4.4127 | 0.1794 | 0.7342 |
| MPW1PBE | 4.5795 | 0.1748 | 0.7146 |
| MPW1PW | 4.5643 | 0.1749 | 0.7153 |
| MPW3LYP | 4.3686 | 0.1776 | 0.7357 |
| MPW3PW | 4.4494 | 0.1938 | 0.7233 |
| MPWLYP1M | 4.5101 | 0.4322 | 0.8801 |
| O3LYP | 4.3838 | 0.2905 | 0.7542 |

Continued on next page

Table C.1: Performance of all tested functionals compared to XMS-CASPT2(8,7)/cc-pvqz. (Continued)

| Functional | RMSD(∇E_1) | RMSD(ΔE_{12}) | RMSD(ΔE_{01}) |
|------------|----------------------|-------------------------|-------------------------|
| PBE0-13 | 4.9022 | 0.2436 | 0.7268 |
| PBE-2X | 6.3504 | 0.6247 | 0.8828 |
| PBE38 | 5.1115 | 0.3056 | 0.7421 |
| PBE50 | 5.9021 | 0.5183 | 0.8256 |
| PBEB0 | 4.5604 | 0.1754 | 0.7195 |
| PBEH | 4.5878 | 0.1745 | 0.7148 |
| PBE-MOL0 | 4.5141 | 0.1733 | 0.7096 |
| PBE-MOLB0 | 4.4977 | 0.1749 | 0.7151 |
| PBE-SOLO | 4.8204 | 0.1777 | 0.7262 |
| QTP17 | 7.0301 | 0.7262 | 0.9695 |
| RCAM-B3LYP | 6.2604 | 0.5920 | 0.8841 |
| SB98-1A | 4.6156 | 0.1770 | 0.7458 |
| SB98-1B | 4.4934 | 0.1921 | 0.7208 |
| SB98-1C | 4.3895 | 0.1953 | 0.7207 |
| SB98-2A | 4.4028 | 0.1753 | 0.7204 |
| SB98-2B | 4.4724 | 0.1763 | 0.7263 |
| SB98-2C | 4.4288 | 0.1778 | 0.7236 |
| WB97 | 5.8680 | 0.5234 | 0.8285 |
| WB97X | 5.5078 | 0.4394 | 0.7998 |
| WC04 | 10.4154 | 0.8560 | 1.0653 |
| WHPBE0 | 20.3441 | 0.4801 | 0.8160 |
| WP04 | 6.0977 | 0.1899 | 0.7554 |
| X3LYP | 4.3673 | 0.1773 | 0.7329 |
| N12-SX | 4.5786 | 0.1725 | 0.7267 |
| SOGGA11-X | 4.9354 | 0.3666 | 0.7592 |

Bibliography

- [1] J. P. P. Zauleck, M. T. Peschel, F. Rott, S. Thallmair, and R. de Vivie-Riedle, “Ultrafast Reactive Quantum Dynamics Coupled to Classical Solvent Dynamics Using an Ehrenfest Approach”, *Journal of Physical Chemistry A* **122**, 2849–2857 (2018).
- [2] M. T. Peschel, P. Kabaciński, D. P. Schwinger, E. Thyryhaug, G. Cerullo, T. Bach, J. Hauer, and R. de Vivie-Riedle, “Activation of 2-Cyclohexenone by BF_3 Coordination: Mechanistic Insights from Theory and Experiment”, *Angewandte Chemie International Edition* **60**, 10155–10163 (2021).
- [3] D. P. Schwinger, M. T. Peschel, C. Jaschke, C. Jandl, R. de Vivie-Riedle, and T. Bach, “Diels-Alder Reaction of Photochemically Generated (*E*)-Cyclohept-2-enones: Diene Scope, Reaction Pathway, and Synthetic Application”, *Journal of Organic Chemistry* **87**, 4838–4851 (2022).
- [4] M. T. Peschel, T. Buberl, M. Högner, R. de Vivie-Riedle, and I. Pupeza, “Sub-optical-cycle light-matter energy transfer in molecular vibrational spectroscopy”, *Nature Communications* **13:5897**, 1–8 (2022).
- [5] D. P. Schwinger, M. T. Peschel, T. Rigotti, P. Kabaciński, T. Knoll, E. Thyryhaug, G. Cerullo, J. Hauer, R. de Vivie-Riedle, and T. Bach, “Photoinduced B–Cl Bond Fission in Aldehyde- BCl_3 Complexes as a Mechanistic Scenario for C–H Bond Activation”, *Journal of the American Chemical Society* **144**, 18927–18937 (2022).
- [6] N. Jeremias, M. T. Peschel, C. Jaschke, R. de Vivie-Riedle, and T. Bach, “Photochemical Ring Contraction of 5,5-Dialkylcyclopent-2-enones and *in situ* Trapping by Primary Amines”, *Journal of Organic Chemistry* **88**, 6294–6303 (2023).
- [7] R. Mundil, S. Hermanová, M. Peschel, A. Lederer, and J. Merna, “On the topology of highly branched polyethylenes prepared by amine-imine nickel and palladium complexes: the effect of *ortho*-aryl substituents”, *Polymer International* **67**, 946–956 (2018).
- [8] T. Buberl, M. Peschel, M. Högner, R. de Vivie-Riedle, and I. Pupeza, “Sub-Optical-Cycle Light-Matter Energy Transfer Dynamics in Molecular Vibrational Spectroscopy”, in *2021 Conference on Lasers and Electro-Optics Europe & European Quantum Electronics Conference (CLEO/Europe-EQEC)* (June 2021).
- [9] D. Ravelli, D. Dondi, M. Fagnoni, and A. Albini, “Photocatalysis. a multi-faceted concept for green chemistry”, *Chemical Society Reviews* **38**, 1999–2011 (2009).
- [10] M. Oelgemöller, C. Jung, and J. Mattay, “Green photochemistry: production of fine chemicals with sunlight”, *Pure and Applied Chemistry* **79**, 1939–1947 (2007).
- [11] T. P. Yoon, M. A. Ischay, and J. Du, “Visible light photocatalysis as a greener approach to photochemical synthesis”, *Nature Chemistry* **2**, 527–532 (2010).

- [12] S. Protti and M. Fagnoni, “The sunny side of chemistry: green synthesis by solar light”, *Photochemical and Photobiological Sciences* **8**, 1499–1516 (2009).
- [13] M. Born and R. Oppenheimer, “Zur Quantentheorie der Molekeln”, *Annalen der Physik* **389**, 457–484 (1927).
- [14] H. Köppel, W. Domcke, and L. S. Cederbaum, “Multimode Molecular Dynamics Beyond the Born-Oppenheimer Approximation”, in *Advances in chemical physics* (John Wiley & Sons, 1984), pp. 59–246.
- [15] B. K. Kendrick, C. Alden Mead, and D. G. Truhlar, “Properties of nonadiabatic couplings and the generalized Born-Oppenheimer approximation”, *Chemical Physics* **277**, 31–41 (2002).
- [16] M. Persico and G. Granucci, *Photochemistry: a modern theoretical perspective* (Springer, 2018).
- [17] S. Mai and L. González, “Molecular Photochemistry: Recent Developments in Theory”, *Angewandte Chemie International Edition* **59**, 16832–16846 (2020).
- [18] F. Schüppel, M. K. Roos, and R. de Vivie-Riedle, “Ultrafast non-adiabatic dynamics of excited diphenylmethyl bromide elucidated by quantum dynamics and semi-classical on-the-fly dynamics”, *Physical Chemistry Chemical Physics* **20**, 22753–22761 (2018).
- [19] S. Thallmair, M. Kowalewski, J. P. P. Zauleck, M. K. Roos, and R. de Vivie-Riedle, “Quantum Dynamics of a Photochemical Bond Cleavage Influenced by the Solvent Environment: A Dynamic Continuum Approach”, *The Journal of Physical Chemistry Letters* **5**, 3480–3485 (2014).
- [20] P. Ehrenfest, “Bemerkung über die angenäherte Gültigkeit der klassischen Mechanik innerhalb der Quantenmechanik”, *Zeitschrift für Physik* **45**, 455–457 (1927).
- [21] J. C. Tully, “Mixed quantum-classical dynamics”, *Faraday Discussions* **110**, 407–419 (1998).
- [22] X. Li, J. C. Tully, H. B. Schlegel, and M. J. Frisch, “*Ab initio* Ehrenfest dynamics”, *Journal of Chemical Physics* **123**, 084106 (2005).
- [23] A. Kirrander and M. Vacher, “Ehrenfest Methods for Electron and Nuclear Dynamics”, in *Quantum chemistry and dynamics of excited states* (John Wiley & Sons, 2020), pp. 469–497.
- [24] D. V. Shalashilin, “Quantum mechanics with the basis set guided by Ehrenfest trajectories: Theory and application to spin-boson model”, *Journal of Chemical Physics* **130**, 244101 (2009).
- [25] D. V. Shalashilin, “Nonadiabatic dynamics with the help of multiconfigurational Ehrenfest method: Improved theory and fully quantum 24D simulation of pyrazine”, *Journal of Chemical Physics* **130**, 244101 (2010).
- [26] K. Saita and D. V. Shalashilin, “On-the-fly *ab initio* molecular dynamics with multiconfigurational Ehrenfest method”, *Journal of Chemical Physics* **137**, 22A506 (2012).

-
- [27] D. V. Makhov, C. Symonds, S. Fernandez-Alberti, and D. V. Shalashilin, “*Ab initio* quantum direct dynamics simulations of ultrafast photochemistry with Multiconfigurational Ehrenfest approach”, *Chemical Physics* **493**, 200–218 (2017).
- [28] C. Symonds, J. A. Kattirtzi, and D. V. Shalashilin, “The effect of sampling techniques used in the multiconfigurational Ehrenfest method”, *Journal of Chemical Physics* **148**, 184113 (2018).
- [29] J. C. Tully, “Molecular dynamics with electronic transitions”, *Journal of Chemical Physics* **93**, 1061–1071 (1990).
- [30] L. Wang, A. Akimov, and O. V. Prezhdo, “Recent Progress in Surface Hopping: 2011-2015”, *Journal of Physical Chemistry Letters* **7**, 2100–2112 (2016).
- [31] M. J. Rosker, M. Dantus, and A. H. Zewail, “Femtosecond Clocking of the Chemical Bond”, *Science* **241**, 1200–1202 (1988).
- [32] A. H. Zewail, “Laser Femtochemistry”, *Science* **242**, 1645–1653 (1988).
- [33] M. Barbatti and K. Sen, “Effects of different initial condition samplings on photo-dynamics and spectrum of pyrrole”, *International Journal of Quantum Chemistry* **116**, 762–771 (2016).
- [34] M. F. Gelin, X. Huang, W. Xie, L. Chen, N. Došlić, and W. Domcke, “Ab Initio Surface-Hopping Simulation of Femtosecond Transient-Absorption Pump-Probe Signals of Nonadiabatic Excited-State Dynamics Using the Doorway-Window Representation”, *Journal of Chemical Theory and Computation* **17**, 2394–2408 (2021).
- [35] I. Pupeza, M. Huber, M. Trubetskov, W. Schweinberger, S. A. Hussain, C. Hofer, K. Fritsch, M. Poetzlberger, L. Vamos, E. Fill, T. Amotchkina, K. V. Kepesidis, A. Apolonski, N. Karpowicz, V. Pervak, O. Pronin, F. Fleischmann, A. Azzeer, M. Igman, and F. Krausz, “Field-resolved infrared spectroscopy of biological systems”, *Nature* **577**, 52–59 (2020).
- [36] P. E. Eaton, “Photochemical reactions of simple alicyclic enones”, *Accounts of Chemical Research* **1**, 50–57 (1968).
- [37] W. C. Agosta and A. B. Smith, “Photochemical reactions of simple cyclopentenones”, *Journal of the American Chemical Society* **93**, 5513–5520 (1971).
- [38] A. C. Chan and D. I. Schuster, “Photochemistry of ketones in solution. 76. stereospecific photoreduction of polycyclic α,β -unsaturated ketones”, *Journal of the American Chemical Society* **108**, 4561–4567 (1986).
- [39] P. Praetorius and F. Korn, “Belichtung ungesättigter Ketone bei Gegenwart von Uranylsalzen”, *Berichte der deutschen chemischen Gesellschaft* **43**, 2744–2747 (1910).
- [40] G. Ciamician and P. Silber, “Chemische Lichtwirkungen”, *Berichte der deutschen chemischen Gesellschaft* **41**, 1928–1935 (1908).
- [41] S. Poplata, A. Tröster, Y.-Q. Zou, and T. Bach, “Recent Advances in the Synthesis of Cyclobutanes by Olefin [2+2] Photocycloaddition Reactions”, *Chemical Reviews* **116**, 9748–9815 (2016).

- [42] S. Poplata and T. Bach, “Enantioselective Intermolecular [2+2] Photocycloaddition Reaction of Cyclic Enones and Its Application in a Synthesis of (-)-Grandisol”, *Journal of the American Chemical Society* **140**, 3228–3231 (2018).
- [43] E. J. Corey, M. Tada, R. LaMahieu, and L. Libit, “*trans*-2-Cycloheptenone”, *Journal of the American Chemical Society* **87**, 2051–2052 (1965).
- [44] P. E. Eaton and K. Lin, “*trans*-2-Cycloheptenone¹”, *Journal of the American Chemical Society* **87**, 2052–2054 (1965).
- [45] O. Schalk, M. S. Schuurman, G. Wu, P. Lang, M. Mucke, R. Feifel, and A. Stolow, “Internal conversion versus intersystem crossing: What drives the gas phase dynamics of cyclic α,β -enones?”, *Journal of Physical Chemistry A* **118**, 2279–2287 (2014).
- [46] E. García-Expósito, M. J. Bearpark, R. M. Ortuño, V. Branchadell, M. A. Robb, and S. Wilsey, “The $T_1^3(\pi-\pi^*)/S_0$ intersections and triplet lifetimes of cyclic α,β -enones”, *Journal of Organic Chemistry* **66**, 8811–8814 (2001).
- [47] L. Marzo, S. K. Pagire, O. Reiser, and B. König, “Visible-Light Photocatalysis: Does It Make a Difference in Organic Synthesis?”, *Angewandte Chemie International Edition* **57**, 10034–10072 (2018).
- [48] A. Vega-Peñalosa, J. Mateos, X. Companyó, M. Escudero-Casao, and L. Dell’Amico, “A Rational Approach to Organo-Photocatalysis: Novel Designs and Structure-Property Relationships”, *Angewandte Chemie International Edition* **60**, 1082–1097 (2021).
- [49] F. Strieth-Kalthoff, M. J. James, M. Teders, L. Pitzer, and F. Glorius, “Energy transfer catalysis mediated by visible light: principles, applications, directions”, *Chemical Society Reviews* **47**, 7190–7202 (2018).
- [50] D. P. Hari and B. König, “Synthetic applications of eosin Y in photoredox catalysis”, *Chemical Communications* **50**, 6688–6699 (2014).
- [51] R. Foja, A. Walter, C. Jandl, E. Thyraug, J. Hauer, and G. Storch, “Reduced Molecular Flavins as Single-Electron Reductants after Photoexcitation”, *Journal of the American Chemical Society* **144**, 4721–4726 (2022).
- [52] I. Ghosh, T. Ghosh, J. I. Bardagi, and B. König, “Reduction of aryl halides by consecutive visible light-induced electron transfer processes”, *Science* **346**, 725–728 (2014).
- [53] R. Brimiouille and T. Bach, “Enantioselective Lewis acid catalysis of intramolecular enone [2+2] photocycloaddition reactions”, *Science* **342**, 840–843 (2013).
- [54] S. Poplata, A. Bauer, G. Storch, and T. Bach, “Intramolecular [2+2] Photocycloaddition of Cyclic Enones: Selectivity Control by Lewis Acids and Mechanistic Implications”, *Chemistry – A European Journal* **25**, 8135–8148 (2019).
- [55] D. P. Schwinger and T. Bach, “Chiral 1,3,2-Oxazaborolidine Catalysts for Enantioselective Photochemical Reactions”, *Accounts of Chemical Research* **53**, 1933–1943 (2020).
- [56] M. Thomas, M. Brehm, R. Fligg, P. Vöhringer, and B. Kirchner, “Computing vibrational spectra from *ab initio* molecular dynamics”, *Physical Chemistry Chemical Physics* **15**, 6608–6622 (2013).

-
- [57] M. Thomas, M. Brehm, and B. Kirchner, “Voronoi dipole moments for the simulation of bulk phase vibrational spectra”, *Physical Chemistry Chemical Physics* **17**, 3207–3213 (2015).
- [58] J. Kussmann and C. Ochsenfeld, “Pre-selective screening for matrix elements in linear-scaling exact exchange calculations”, *Journal of Chemical Physics* **138**, 134114 (2013).
- [59] J. Kussmann and C. Ochsenfeld, “Preselective Screening for Linear-Scaling Exact Exchange-Gradient Calculations for Graphics Processing Units and General Strong-Scaling Massively Parallel Calculations”, *Journal of Chemical Theory and Computation* **11**, 918–922 (2015).
- [60] L. D. M. Peters, J. Kussmann, and C. Ochsenfeld, “Nonadiabatic molecular dynamics on graphics processing units: performance and application to rotary molecular motors”, *Journal of Chemical Theory and Computation* **15**, 6647–6659 (2019).
- [61] A. A. Granovsky, “Extended multi-configuration quasi-degenerate perturbation theory: The new approach to multi-state multi-reference perturbation theory”, *Journal of Chemical Physics* **134**, 214113 (2011).
- [62] T. Shiozaki, W. Győrffy, P. Celani, and H.-J. Werner, “Communication: Extended multi-state complete active space second-order perturbation theory: Energy and nuclear gradients”, *Journal of Chemical Physics* **135**, 081106 (2011).
- [63] E. Schrödinger, “Quantisierung als Eigenwertproblem”, *Annalen der Physik* **386**, 109–139 (1926).
- [64] D. J. Tannor, *Introduction to Quantum Mechanics: A Time-Dependent Perspective* (University Science Books, 2007).
- [65] R. B. Gerber, V. Buch, and M. A. Ratner, “Time-dependent self-consistent field approximation for intramolecular energy transfer. I. Formulation and application to dissociation of van der Waals molecules”, *Journal of Chemical Physics* **77**, 3022–3030 (1982).
- [66] R. Gerber, M. Ratner, and V. Buch, “Simplified time-dependent self-consistent field approximation for intramolecular dynamics”, *Chemical Physics Letters* **91**, 173–177 (1982).
- [67] R. B. Gerber and M. A. Ratner, “Mean-field models for molecular states and dynamics: new developments”, *Journal of Physical Chemistry* **92**, 3252–3260 (1988).
- [68] L. Wang and A. B. McCoy, “Time-dependent studies of reaction dynamics: a test of mixed quantum/classical time-dependent self-consistent field approximations”, *Physical Chemistry Chemical Physics* **1**, 1227–1235 (1999).
- [69] G. S. Whittier and J. C. Light, “Quantum/classical time-dependent self-consistent field treatment of Ar+HCO inelastic and dissociative scattering”, *Journal of Chemical Physics* **110**, 4280–4290 (1999).
- [70] D. A. Micha, “A selfconsistent eikonal treatment of electronic transitions in molecular collisions”, *Journal of Chemical Physics* **78**, 7138–7145 (1983).
- [71] M. Giebel, S. Knapek, G. Zumbusch, and A. Caglar, *Numerische Simulationen in der Moleküldynamik* (Springer, 2004), pp. 21–25.

- [72] M. T. Peschel, “Dynamic Solvent Effects Treated with a Quantum/Classical TD-SCF Approach”, Master’s thesis (LMU München, 2016).
- [73] M. J. Abraham, T. Murtola, R. Schulz, S. Páll, J. C. Smith, B. Hess, and E. Lindahl, “GROMACS: High performance molecular simulations through multi-level parallelism from laptops to supercomputers”, *SoftwareX* **1-2**, 19–25 (2015).
- [74] F. Santoro, V. Barone, T. Gustavsson, and R. Improta, “Solvent Effect on the Singlet Excited-State Lifetimes of Nucleic Acid Bases: A Computational Study of 5-Fluorouracil and Uracil in Acetonitrile and Water”, *Journal of the American Chemical Society* **128**, 16312–16322 (2006).
- [75] A. Yoshikawa and S. Matsika, “Excited electronic states and photophysics of uracil-water complexes”, *Chemical Physics* **347**, 393–404 (2008).
- [76] P. Chakraborty, T. N. Karsili, B. Marchetti, and S. Matsika, “Mechanistic insights into photoinduced damage of DNA and RNA nucleobases in the gas phase and in bulk solution”, *Faraday Discussions* **207**, 329–350 (2018).
- [77] J. A. Green, S. Gómez, G. Worth, F. Santoro, and R. Improta, “Solvent Effects on Ultrafast Charge Transfer Population: Insights from the Quantum Dynamics of Guanine-Cytosine in Chloroform”, *Chemistry – A European Journal* **28**, e202201731 (2022).
- [78] P. M. Hare, C. E. Crespo-Hernández, and B. Kohler, “Solvent-Dependent Photophysics of 1-Cyclohexyluracil: Ultrafast Branching in the Initial Bright State Leads Nonradiatively to the Electronic Ground State and a Long-Lived $^1n\pi^*$ State”, *Journal of Physical Chemistry B* **110**, 18641–18650 (2006).
- [79] C. Canuel, M. Mons, F. Piuzzi, B. Tardivel, I. Dimicoli, and M. Elhanine, “Excited states dynamics of DNA and RNA bases: Characterization of a stepwise deactivation pathway in the gas phase”, *Journal of Chemical Physics* **122**, 074316 (2005).
- [80] P. V. Parandekar and J. C. Tully, “Mixed quantum-classical equilibrium”, *Journal of Chemical Physics* **122**, 094102 (2005).
- [81] P. V. Parandekar and J. C. Tully, “Detailed Balance in Ehrenfest Mixed Quantum-Classical Dynamics”, *Journal of Chemical Theory and Computation* **2**, 229–235 (2006).
- [82] A. Jain and J. E. Subotnik, “Vibrational Energy Relaxation: A Benchmark for Mixed Quantum-Classical Methods”, *Journal of Physical Chemistry A* **122**, 16–27 (2018).
- [83] H.-D. Meyer, U. Manthe, and L. Cederbaum, “The multi-configurational time-dependent Hartree approach”, *Chemical Physics Letters* **165**, 73–78 (1990).
- [84] M. Beck, “The multiconfiguration time-dependent Hartree (MCTDH) method: a highly efficient algorithm for propagating wavepackets”, *Physics Reports* **324**, 1–105 (2000).
- [85] H.-D. Meyer, “Studying molecular quantum dynamics with the multiconfiguration time-dependent Hartree method”, *Wiley Interdisciplinary Reviews: Computational Molecular Science* **2**, 351–374 (2012).

-
- [86] M. Bonfanti, G. A. Worth, and I. Burghardt, “Multi-Configuration Time-Dependent Hartree Methods: From Quantum to Semiclassical and Quantum-Classical”, in *Quantum chemistry and dynamics of excited states* (John Wiley & Sons, 2020), pp. 383–411.
- [87] E. J. Heller, “Frozen Gaussians: A very simple semiclassical approximation”, *Journal of Chemical Physics* **75**, 2923–2931 (1981).
- [88] J. C. Light and T. Carrington, “Discrete-variable representations and their utilization”, *Advances in Chemical Physics* **114**, 263–310 (2007).
- [89] J. R. Cash and A. H. Karp, “A variable order Runge-Kutta method for initial value problems with rapidly varying right-hand sides”, *ACM Transactions on Mathematical Software* **16**, 201–222 (1990).
- [90] M. Calvo, J. Montijano, and L. Randez, “A fifth-order interpolant for the Dormand and Prince Runge-Kutta method”, *Journal of Computational and Applied Mathematics* **29**, 91–100 (1990).
- [91] D. Picconi, J. A. Cina, and I. Burghardt, “Quantum dynamics and spectroscopy of dihalogens in solid matrices. I. Efficient simulation of the photodynamics of the embedded I_2Kr_{18} cluster using the G-MCTDH method”, *Journal of Chemical Physics* **150**, 064111 (2019).
- [92] D. Picconi, J. A. Cina, and I. Burghardt, “Quantum dynamics and spectroscopy of dihalogens in solid matrices. II. Theoretical aspects and G-MCTDH simulations of time-resolved coherent Raman spectra of Schrödinger cat states of the embedded I_2Kr_{18} cluster”, *Journal of Chemical Physics* **150**, 064112 (2019).
- [93] M. F. Herman and E. Kluk, “A semiclassical justification for the use of non-spreading wavepackets in dynamics calculations”, *Chemical Physics* **91**, 27–34 (1984).
- [94] M. Buchholz, F. Grossmann, and M. Ceotto, “Mixed semiclassical initial value representation time-averaging propagator for spectroscopic calculations”, *Journal of Chemical Physics* **144**, 094102 (2016).
- [95] J. C. Burant and V. S. Batista, “Real time path integrals using the Herman-Kluk propagator”, *Journal of Chemical Physics* **116**, 2748–2756 (2002).
- [96] S. C. Althorpe, “Path-integral approximations to quantum dynamics”, *The European Physical Journal B* **94**, 155 (2021).
- [97] G. Käb, “Fewest Switches Adiabatic Surface Hopping As Applied to Vibrational Energy Relaxation”, *Journal of Physical Chemistry A* **110**, 3197–3215 (2006).
- [98] J. C. Arce and M. F. Herman, “Semiclassical surface-hopping approximations for the calculation of solvent-induced vibrational-relaxation rate constants”, *Journal of Chemical Physics* **101**, 7520–7527 (1994).
- [99] S. Hammes-Schiffer and J. C. Tully, “Proton transfer in solution: Molecular dynamics with quantum transitions”, *Journal of Chemical Physics* **101**, 4657–4667 (1994).
- [100] G. Granucci, M. Persico, and A. Toniolo, “Direct semiclassical simulation of photochemical processes with semiempirical wave functions”, *Journal of Chemical Physics* **114**, 10608–10615 (2001).

- [101] F. Plasser, G. Granucci, J. Pittner, M. Barbatti, M. Persico, and H. Lischka, “Surface hopping dynamics using a locally diabatic formalism: Charge transfer in the ethylene dimer cation and excited state dynamics in the 2-pyridone dimer”, *Journal of Chemical Physics* **137**, 22A514 (2012).
- [102] D. F. Coker and L. Xiao, “Methods for molecular dynamics with nonadiabatic transitions”, *Journal of Chemical Physics* **102**, 496–510 (1995).
- [103] M. Barbatti, “Velocity Adjustment in Surface Hopping: Ethylene as a Case Study of the Maximum Error Caused by Direction Choice”, *Journal of Chemical Theory and Computation* **17**, 3010–3018 (2021).
- [104] A. W. Jasper and D. G. Truhlar, “Improved treatment of momentum at classically forbidden electronic transitions in trajectory surface hopping calculations”, *Chemical Physics Letters* **369**, 60–67 (2003).
- [105] A. E. Sifain, L. Wang, and O. V. Prezhdo, “Communication: Proper treatment of classically forbidden electronic transitions significantly improves detailed balance in surface hopping”, *Journal of Chemical Physics* **144**, 211102 (2016).
- [106] J. R. Schmidt, P. V. Parandekar, and J. C. Tully, “Mixed quantum-classical equilibrium: Surface hopping”, *Journal of Chemical Physics* **129**, 044104 (2008).
- [107] O. V. Prezhdo and P. J. Rossky, “Evaluation of quantum transition rates from quantum-classical molecular dynamics simulations”, *Journal of Chemical Physics* **107**, 5863–5878 (1997).
- [108] J. E. Subotnik and N. Shenvi, “Decoherence and surface hopping: When can averaging over initial conditions help capture the effects of wave packet separation?”, *Journal of Chemical Physics* **134**, 244114 (2011).
- [109] J. E. Subotnik, A. Jain, B. Landry, A. Petit, W. Ouyang, and N. Bellonzi, “Understanding the Surface Hopping View of Electronic Transitions and Decoherence”, *Annual Review of Physical Chemistry* **67**, 387–417 (2016).
- [110] G. Granucci, M. Persico, and A. Zocante, “Including quantum decoherence in surface hopping”, *Journal of Chemical Physics* **133**, 134111 (2010).
- [111] A. Jain, E. Alguire, and J. E. Subotnik, “An Efficient, Augmented Surface Hopping Algorithm That Includes Decoherence for Use in Large-Scale Simulations”, *Journal of Chemical Theory and Computation* **12**, 5256–5268 (2016).
- [112] G. Granucci and M. Persico, “Critical appraisal of the fewest switches algorithm for surface hopping”, *Journal of Chemical Physics* **126**, 134114 (2007).
- [113] J. E. Subotnik, W. Ouyang, and B. R. Landry, “Can we derive Tully’s surface-hopping algorithm from the semiclassical quantum Liouville equation? Almost, but only with decoherence”, *Journal of Chemical Physics* **139**, 214107 (2013).
- [114] M. Richter, P. Marquetand, J. González-Vázquez, I. Sola, and L. González, “SHARC: ab Initio Molecular Dynamics with Surface Hopping in the Adiabatic Representation Including Arbitrary Couplings”, *Journal of Chemical Theory and Computation* **7**, 1253–1258 (2011).
- [115] S. Mai, P. Marquetand, and L. González, “A general method to describe inter-system crossing dynamics in trajectory surface hopping”, *International Journal of Quantum Chemistry* **115**, 1215–1231 (2015).

-
- [116] S. Mai, P. Marquetand, and L. González, “Nonadiabatic dynamics: The SHARC approach”, *Wiley Interdisciplinary Reviews: Computational Molecular Science* **8**, e1370 (2018).
- [117] R. Kapral, “Surface hopping from the perspective of quantumclassical Liouville dynamics”, *Chemical Physics* **481**, 77–83 (2016).
- [118] A. Abedi, F. Agostini, Y. Suzuki, and E. K. U. Gross, “Dynamical Steps that Bridge Piecewise Adiabatic Shapes in the Exact Time-Dependent Potential Energy Surface”, *Physical Review Letters* **110**, 263001 (2013).
- [119] T. Fiedlschuster, J. Handt, E. K. U. Gross, and R. Schmidt, “Surface hopping in laser-driven molecular dynamics”, *Physical Review A* **95**, 063424 (2017).
- [120] S. Mai, M. Richter, M. Heindl, M. F. S. J. Menger, A. Atkins, M. Ruckebauer, F. Plasser, L. M. Ibele, S. Kropf, M. Oppel, P. Marquetand, and L. González, *SHARC2.1: Surface Hopping Including Arbitrary Couplings—Program Package for Non-Adiabatic Dynamics*, sharc-md.org, 2019.
- [121] L. Spörkel and W. Thiel, “Adaptive time steps in trajectory surface hopping simulations”, *Journal of Chemical Physics* **144**, 194108 (2016).
- [122] J. Finley, P.-Å. Malmqvist, B. O. Roos, and L. Serrano-Andrés, “The multi-state CASPT2 method”, *Chemical Physics Letters* **288**, 299–306 (1998).
- [123] T. Shiozaki, “BAGEL: Brilliantly Advanced General Electronic-structure Library”, *Wiley Interdisciplinary Reviews: Computational Molecular Science* **8**, e1331 (2018).
- [124] F. Aquilante, J. Autschbach, A. Baiardi, S. Battaglia, V. A. Borin, L. F. Chibotaru, I. Conti, L. De Vico, M. Delcey, I. F. Galván, N. Ferré, L. Freitag, M. Garavelli, X. Gong, S. Knecht, E. D. Larsson, R. Lindh, M. Lundberg, P. Å. Malmqvist, A. Nenov, J. Norell, M. Odellius, M. Olivucci, T. B. Pedersen, L. Pedraza-González, Q. M. Phung, K. Pierloot, M. Reiher, I. Schapiro, J. Segarra-Martí, F. Segatta, L. Seijo, S. Sen, D. C. Sergentu, C. J. Stein, L. Ungur, M. Vacher, A. Valentini, and V. Veryazov, “Modern quantum chemistry with [Open]Molcas”, *Journal of Chemical Physics* **152**, 214117 (2020).
- [125] S. Mukamel, *Principles of Nonlinear Optical Spectroscopy* (Oxford University Press, 1995).
- [126] J. Dupont-Roc and G. Grynberg, *Photons and Atoms: Introduction to Quantum Electrodynamics* (Wiley, 1997).
- [127] M.-X. Wang, S.-G. Chen, H. Liang, and L.-Y. Peng, “Review on non-dipole effects in ionization and harmonic generation of atoms and molecules*”, *Chinese Physics B* **29**, 013302 (2020).
- [128] A. D. Bandrauk, F. Fillion-Gourdeau, and E. Lorin, “Atoms and molecules in intense laser fields: gauge invariance of theory and models”, *Journal of Physics B: Atomic, Molecular and Optical Physics* **46**, 153001 (2013).
- [129] M. Huber, M. Trubetskov, S. A. Hussain, W. Schweinberger, C. Hofer, and I. Pupeza, “Optimum Sample Thickness for Trace Analyte Detection with Field-Resolved Infrared Spectroscopy”, *Analytical Chemistry* **92**, 7508–7514 (2020).

- [130] P. Sulzer, M. Högner, A.-K. Raab, L. Fürst, E. Fill, D. Gerz, C. Hofer, L. Voronina, and I. Pupeza, “Cavity-enhanced field-resolved spectroscopy”, *Nature Photonics* **16**, 692–697 (2022).
- [131] M. Brehm, M. Thomas, S. Gehrke, and B. Kirchner, “TRAVIS – A free analyzer for trajectories from molecular simulation”, *Journal of Chemical Physics* **152**, 164105 (2020).
- [132] T. D. Kühne, M. Iannuzzi, M. Del Ben, V. V. Rybkin, P. Seewald, F. Stein, T. Laino, R. Z. Khaliullin, O. Schütt, F. Schiffmann, D. Golze, J. Wilhelm, S. Chulkov, M. H. Bani-Hashemian, V. Weber, U. Borštnik, M. TAILLEFUMIER, A. S. Jakobovits, A. Lazzaro, H. Pabst, T. Müller, R. Schade, M. Guidon, S. Andermatt, N. Holmberg, G. K. Schenter, A. Hehn, A. Bussy, F. Belleflamme, G. Tabacchi, A. Glöß, M. Lass, I. Bethune, C. J. Mundy, C. Plessl, M. Watkins, J. VandeVondele, M. Krack, and J. Hutter, “CP2K: An electronic structure and molecular dynamics software package - Quickstep: Efficient and accurate electronic structure calculations”, *Journal of Chemical Physics* **152**, 194103 (2020).
- [133] A. D. Becke, “Density-functional exchange-energy approximation with correct asymptotic behavior”, *Physical Review A* **38**, 3098–3100 (1988).
- [134] C. Lee, W. Yang, and R. G. Parr, “Development of the Colle-Salvetti correlation-energy formula into a functional of the electron density”, *Physical Review B* **37**, 785–789 (1988).
- [135] S. Grimme, J. Antony, S. Ehrlich, and H. Krieg, “A consistent and accurate *ab initio* parametrization of density functional dispersion correction (DFT-D) for the 94 elements H-Pu”, *Journal of Chemical Physics* **132**, 154104 (2010).
- [136] J. P. Perdew and K. Schmidt, “Jacob’s ladder of density functional approximations for the exchange-correlation energy”, in *AIP Conference Proceedings* (2001), pp. 1–20.
- [137] Y. Zhao and D. G. Truhlar, “The M06 suite of density functionals for main group thermochemistry, thermochemical kinetics, noncovalent interactions, excited states, and transition elements: Two new functionals and systematic testing of four M06-class functionals and 12 other function”, *Theoretical Chemistry Accounts* **120**, 215–241 (2008).
- [138] B. Mennucci, “Polarizable continuum model”, *Wiley Interdisciplinary Reviews: Computational Molecular Science* **2**, 386–404 (2012).
- [139] A. S. Perera, J. Thomas, M. R. Poopari, and Y. Xu, “The Clusters-in-a-Liquid Approach for Solvation: New Insights from the Conformer Specific Gas Phase Spectroscopy and Vibrational Optical Activity Spectroscopy”, *Frontiers in Chemistry* **4**, 9 (2016).
- [140] S. Li, J. R. Schmidt, S. A. Corcelli, C. P. Lawrence, and J. L. Skinner, “Approaches for the calculation of vibrational frequencies in liquids: Comparison to benchmarks for azide/water clusters”, *Journal of Chemical Physics* **124**, 204110 (2006).
- [141] T. la Cour Jansen and W. M. Ruszel, “Motional narrowing in the time-averaging approximation for simulating two-dimensional nonlinear infrared spectra”, *Journal of Chemical Physics* **128**, 214501 (2008).
- [142] S. Patai and Z. Rappoport, eds., *Enones: Vol. 1* (John Wiley & Sons, 1989).

-
- [143] S. Patai and Z. Rappoport, eds., *Enones: Vol. 2* (John Wiley & Sons, 1989).
- [144] E. Paternò and G. Chieffi, “Sintesi in chimica organica per mezzo della luce. Nota II. Composti degli idrocarburi non saturi con aldeidi e chetoni”, *Gazzetta Chimica Italiana* **39**, 341–361 (1909).
- [145] A. M. Lee, J. D. Coe, S. Ullrich, M.-L. Ho, S.-J. Lee, B. M. Cheng, M. Z. Zgierski, I.-C. Chen, T. J. Martinez, and A. Stolow, “Substituent effects on dynamics at conical intersections: α,β -enones”, *Journal of Physical Chemistry A* **111**, 11948–11960 (2007).
- [146] M. O. McAnally, K. L. Zabronsky, D. J. Stupca, K. Phillipson, N. R. Pillsbury, and S. Drucker, “Lowest triplet (n,π^*) state of 2-cyclohexen-1-one: Characterization by cavity ringdown spectroscopy and quantum-chemical calculations”, *Journal of Chemical Physics* **139**, 214311 (2013).
- [147] J. Cao and Z.-Z. Xie, “Internal conversion and intersystem crossing in α,β -enones: A combination of electronic structure calculations and dynamics simulations”, *Physical Chemistry Chemical Physics* **18**, 6931–6945 (2016).
- [148] E. García-Expósito, M. J. Bearpark, R. M. Ortuño, M. A. Robb, and V. Branchadell, “Theoretical study of the photochemical [2+2]-cycloadditions of cyclic and acyclic α,β -unsaturated carbonyl compounds to ethylene”, *Journal of Organic Chemistry* **67**, 6070–6077 (2002).
- [149] M. A. El-Sayed, “Triplet state. Its radiative and nonradiative properties”, *Accounts of Chemical Research* **1**, 8–16 (1968).
- [150] O. D. Saltmarsh and R. G. W. Norrish, “98. Primary photochemical reactions. Part VI. The photochemical decomposition of certain cyclic ketones”, *Journal of the Chemical Society (Resumed)*, 455–459 (1935).
- [151] R. G. W. Norrish and M. E. S. Appleyard, “191. Primary photochemical reactions. Part IV. Decomposition of methyl ethyl ketone and methyl butyl ketone”, *Journal of the Chemical Society (Resumed)*, 874–880 (1934).
- [152] W. C. Agosta, A. B. Smith III, A. S. Kende, R. G. Eilerman, and J. Benham, “The intramolecular photorearrangement of cyclopentones”, *Tetrahedron Letters* **10**, 4517–4520 (1969).
- [153] G. Büchi, C. G. Inman, and E. S. Lipinsky, “Light-catalyzed Organic Reactions. I. The Reaction of Carbonyl Compounds with 2-Methyl-2-butene in the Presence of Ultraviolet Light”, *Journal of the American Chemical Society* **76**, 4327–4331 (1954).
- [154] T. Bach, “Stereoselective Intermolecular [2+2]-Photocycloaddition Reactions and Their Application in Synthesis”, *Synthesis* **1998**, 683–703 (1998).
- [155] M. Fréneau and N. Hoffmann, “The Paternò-Büchi reaction – Mechanisms and application to organic synthesis”, *Journal of Photochemistry and Photobiology C: Photochemistry Reviews* **33**, 83–108 (2017).
- [156] M. D’Auria and S. Stoia, *The Paternò-Büchi Reaction* (Cambridge Scholars Publishing, 2019).
- [157] R. Bonneau, “Transient species in photochemistry of enones. The orthogonal triplet state revealed by laser photolysis”, *Journal of the American Chemical Society* **102**, 3816–3822 (1980).

- [158] S. Yamauchi, N. Hirota, and J. Higuchi, "Direct observation of twisted excited triplet states of monocyclic conjugated enones by time-resolved electron paramagnetic resonance", *Journal of Physical Chemistry* **92**, 2129–2133 (1988).
- [159] D. I. Schuster, D. A. Dunn, G. E. Heibel, P. B. Brown, J. M. Rao, J. Woning, and R. Bonneau, "Enone photochemistry. Dynamic properties of triplet excited states of cyclic conjugated enones as revealed by transient absorption spectroscopy", *Journal of the American Chemical Society* **113**, 6245–6255 (1991).
- [160] J. Olmsted and M. El-Sayed, "Phosphorescence spectrum and mechanisms of benzaldehyde in methyl-cyclohexane at 4.2°K", *Journal of Molecular Spectroscopy* **40**, 71–83 (1971).
- [161] H. Gorner and H. J. Kuhn, "Laser flash photolysis study of the effects of substituents, solvents, and quenchers on the triplet state of benzaldehydes. Hydrogen/deuterium exchange following quenching by water- d_2 ", *Journal of Physical Chemistry* **90**, 5946–5955 (1986).
- [162] R. B. Woodward and R. Hoffmann, "The Conservation of Orbital Symmetry", *Angewandte Chemie International Edition* **8**, 781–853 (1969).
- [163] C. Brenninger, J. D. Jolliffe, and T. Bach, "Chromophore Activation of α,β -Unsaturated Carbonyl Compounds and Its Application to Enantioselective Photochemical Reactions", *Angewandte Chemie International Edition* **57**, 14338–14349 (2018).
- [164] C. R. Silva and J. P. Reilly, "Theoretical Calculations on Excited Electronic States of Benzaldehyde and Observation of the $S_2 \leftarrow S_0$ Jet-Cooled Spectrum", *Journal of Physical Chemistry* **100**, 17111–17123 (1996).
- [165] V. Molina and M. Merchán, "Theoretical Analysis of the Electronic Spectra of Benzaldehyde", *Journal of Physical Chemistry A* **105**, 3745–3751 (2001).
- [166] G. Cui, Y. Lu, and W. Thiel, "Electronic excitation energies, three-state intersections, and photodissociation mechanisms of benzaldehyde and acetophenone", *Chemical Physics Letters* **537**, 21–26 (2012).
- [167] Q. Ou and J. E. Subotnik, "Electronic Relaxation in Benzaldehyde Evaluated via TD-DFT and Localized Diabatization: Intersystem Crossings, Conical Intersections, and Phosphorescence", *Journal of Physical Chemistry C* **117**, 19839–19849 (2013).
- [168] K. Fletcher, U. H. F. Bunz, and A. Dreuw, "Fluorescence Quenching of Benzaldehyde in Water by Hydrogen Atom Abstraction", *ChemPhysChem* **17**, 2650–2653 (2016).
- [169] S. Stegbauer, N. Jeremias, C. Jandl, and T. Bach, "Reversal of reaction type selectivity by Lewis acid coordination: the *ortho* photocycloaddition of 1- and 2-naphthaldehyde", *Chemical Science* **10**, 8566–8570 (2019).
- [170] H. Shinozaki, S. Arai, and M. Tada, "The Photo-induced Diels-Alder Reaction of 2-Cycloocten-1-one and 2-Cyclohepten-1-one", *Bulletin of the Chemical Society of Japan* **49**, 821–822 (1976).
- [171] H. Dorr and V. H. Rawal, "The Intramolecular Diels-Alder Reactions of Photochemically Generated *trans*-Cycloalkenones", *Journal of the American Chemical Society* **121**, 10229–10230 (1999).

-
- [172] S. Ghosh and S. Saha, "Photo-Induced Diels-Alder reaction. A novel route to *trans* fused benzobicyclo-[5.3.0]decanes and [5.4.0]undecanes", *Tetrahedron Letters* **26**, 5325–5326 (1985).
- [173] J. Nikolai, Ø. Loe, P. M. Dominiak, O. O. Gerlitz, J. Autschbach, and H. M. L. Davies, "Mechanistic Studies of UV Assisted [4+2] Cycloadditions in Synthetic Efforts toward Vibsanin E", *Journal of the American Chemical Society* **129**, 10763–10772 (2007).
- [174] R.-B. Wang, S.-G. Ma, C. S. Jamieson, R.-M. Gao, Y.-B. Liu, Y. Li, X.-J. Wang, Y.-H. Li, K. N. Houk, J. Qu, and S.-S. Yu, "Library construction of stereochemically diverse isomers of spirooliganin: their total synthesis and antiviral activity", *Chemical Science* **12**, 7003–7011 (2021).
- [175] D. H. Ess, G. O. Jones, and K. N. Houk, "Conceptual, Qualitative, and Quantitative Theories of 1,3-Dipolar and Diels-Alder Cycloadditions Used in Synthesis", *Advanced Synthesis & Catalysis* **348**, 2337–2361 (2006).
- [176] K. N. Houk, F. Liu, Z. Yang, and J. I. Seeman, "Evolution of the Diels-Alder Reaction Mechanism since the 1930s: Woodward, Houk with Woodward, and the Influence of Computational Chemistry on Understanding Cycloadditions", *Angewandte Chemie International Edition* **60**, 12660–12681 (2021).
- [177] R. S. Paton, S. Kim, A. G. Ross, S. J. Danishefsky, and K. N. Houk, "Experimental Diels-Alder Reactivities of Cycloalkenones and Cyclic Dienes Explained through Transition-State Distortion Energies", *Angewandte Chemie International Edition* **50**, 10366–10368 (2011).
- [178] C. Jaschke, "Quantenchemische Untersuchung von Cycloheptenon bezüglich seiner Relaxationsmechanismen und konsekutiver Diels-Alder-Reaktionen", Bachelor's thesis (LMU München, 2021).
- [179] H.-J. Liu, W.-L. Yeh, and E. N. Browne, "Activated cycloheptenone dienophiles. A versatile approach to 6,7-fused ring targets", *Canadian Journal of Chemistry* **73**, 1135–1147 (1995).
- [180] F. M. Bickelhaupt and K. N. Houk, "Analyzing Reaction Rates with the Distortion/Interaction-Activation Strain Model", *Angewandte Chemie International Edition* **56**, 10070–10086 (2017).
- [181] G. S. Hammond, "A Correlation of Reaction Rates", *Journal of the American Chemical Society* **77**, 334–338 (1955).
- [182] J. E. Leffler, "Parameters for the Description of Transition States", *Science* **117**, 340–341 (1953).
- [183] H. Xiao, S. Maeda, and K. Morokuma, "CASPT2 Study of Photodissociation Pathways of Ketene", *Journal of Physical Chemistry A* **117**, 7001–7008 (2013).
- [184] H. Wang, X. Cao, X. Chen, W. Fang, and M. Dolg, "Regulatory Mechanism of the Enantioselective Intramolecular Enone [2+2] Photocycloaddition Reaction Mediated by a Chiral Lewis Acid Catalyst Containing Heavy Atoms", *Angewandte Chemie International Edition* **57**, 14593–14596 (2015).
- [185] S. Stegbauer, C. Jandl, and T. Bach, "Enantioselective Lewis Acid Catalyzed *ortho* Photocycloaddition of Olefins to Phenanthrene-9-carboxaldehydes", *Angewandte Chemie International Edition* **57**, 14593–14596 (2018).

- [186] F. D. Lewis and S. V. Barancyk, “Lewis acid catalysis of photochemical reactions. 8. Photodimerization and cross-cycloaddition of coumarin”, *Journal of the American Chemical Society* **111**, 8653–8661 (1989).
- [187] F. D. Lewis, S. L. Quillen, P. D. Hale, and J. D. Oxman, “Lewis acid catalysis of photochemical reactions. 7. Photodimerization and cross-cycloaddition of cinnamic esters”, *Journal of the American Chemical Society* **110**, 1261–1267 (1988).
- [188] F. D. Lewis, S. V. Barancyk, and E. L. Burch, “Lewis acid catalysis of photochemical reactions. 11. Conformations, spectroscopy, and photochemistry of methyl phenanthrene-9-carboxylate, and phenanthrene-9-carboxamides, and their Lewis acid complexes”, *Journal of the American Chemical Society* **114**, 3866–3870 (1992).
- [189] R. Brimiouille, H. Guo, and T. Bach, “Enantioselective Intramolecular [2+2] Photocycloaddition Reactions of 4-Substituted Coumarins Catalyzed by a Chiral Lewis Acid”, *Chemistry – A European Journal* **25**, 8135–8148 (2012).
- [190] H. Wang, W.-H. Fang, and X. Chen, “Mechanism of the Enantioselective Intramolecular [2+2] Photocycloaddition Reaction of Coumarin Catalyzed by a Chiral Lewis Acid: Comparison with Enone Substrates”, *Journal of Organic Chemistry* **81**, 7093–7101 (2016).
- [191] W. L. Jorgensen, D. S. Maxwell, and J. Tirado-Rives, “Development and Testing of the OPLS All-Atom Force Field on Conformational Energetics and Properties of Organic Liquids”, *Journal of the American Chemical Society* **118**, 11225–11236 (1996).
- [192] W. L. Jorgensen and J. Tirado-Rives, “Potential energy functions for atomic-level simulations of water and organic and biomolecular systems”, *Proceedings of the National Academy of Sciences* **102**, 6665–6670 (2005).
- [193] C. Caleman, P. J. van Maaren, M. Hong, J. S. Hub, L. T. Costa, and D. van der Spoel, “Force Field Benchmark of Organic Liquids: Density, Enthalpy of Vaporization, Heat Capacities, Surface Tension, Isothermal Compressibility, Volumetric Expansion Coefficient, and Dielectric Constant”, *Journal of Chemical Theory and Computation* **8**, 61–74 (2012).
- [194] B. G. Levine, C. Ko, J. Quenneville, and T. J. Martínez, “Conical intersections and double excitations in time-dependent density functional theory”, *Molecular Physics* **104**, 1039–1051 (2006).
- [195] S. Lehtola, C. Steigemann, M. J. Oliveira, and M. A. Marques, “Recent developments in libxc – A comprehensive library of functionals for density functional theory”, *SoftwareX* **7**, 1–5 (2018).
- [196] O. A. Vydrov and T. Van Voorhis, “Nonlocal van der Waals density functional: The simpler the better”, *Journal of Chemical Physics* **133**, 244103 (2010).
- [197] J. M. del Campo, J. L. Gázquez, S. B. Trickey, and A. Vela, “Non-empirical improvement of PBE and its hybrid PBE0 for general description of molecular properties”, *Journal of Chemical Physics* **136**, 104108 (2012).
- [198] T. W. Keal and D. J. Tozer, “Semiempirical hybrid functional with improved performance in an extensive chemical assessment”, *Journal of Chemical Physics* **123**, 121103 (2005).

-
- [199] M. Schreiber, M. R. Silva-Junior, S. P. A. Sauer, and W. Thiel, “Benchmarks for electronically excited states: CASPT2, CC2, CCSD, and CC3”, *Journal of Chemical Physics* **128**, 134110 (2008).
- [200] M. R. Silva-Junior, M. Schreiber, S. P. A. Sauer, and W. Thiel, “Benchmarks for electronically excited states: Time-dependent density functional theory and density functional theory based multireference configuration interaction”, *Journal of Chemical Physics* **129**, 104103 (2008).
- [201] J. Wang and B. Durbeej, “How accurate are TDDFT excited-state geometries compared to DFT ground-state geometries?”, *Journal of Computational Chemistry* **41**, 1718–1729 (2020).
- [202] A. Ali, M. I. Rafiq, Z. Zhang, J. Cao, R. Geng, B. Zhou, and W. Tang, “TD-DFT benchmark for UV-visible spectra of fused-ring electron acceptors using global and range-separated hybrids”, *Physical Chemistry Chemical Physics* **22**, 7864–7874 (2020).
- [203] R. Sarkar, M. Boggio-Pasqua, P.-F. Loos, and D. Jacquemin, “Benchmarking TD-DFT and Wave Function Methods for Oscillator Strengths and Excited-State Dipole Moments”, *Journal of Chemical Theory and Computation* **17**, 1117–1132 (2021).
- [204] D. Avagliano, M. Bonfanti, M. Garavelli, and L. González, “QM/MM Nonadiabatic Dynamics: the SHARC/COBRAMM Approach”, *Journal of Chemical Theory and Computation* **17**, 4639–4647 (2021).
- [205] D. A. Tracy, S. Fernandez-Alberti, S. Tretiak, and A. E. Roitberg, “Adiabatic Excited-State Molecular Dynamics with an Explicit Solvent: NEXMD-SANDER Implementation”, *Journal of Chemical Theory and Computation* **18**, 5213–5220 (2022).
- [206] D. V. Cofer-Shabica, M. F. S. J. Menger, Q. Ou, Y. Shao, J. E. Subotnik, and S. Faraji, “INAQS, a Generic Interface for Nonadiabatic QM/MM Dynamics: Design, Implementation, and Validation for GROMACS/Q-CHEM simulations”, *Journal of Chemical Theory and Computation* **18**, 4601–4614 (2022).
- [207] P. Eastman, J. Swails, J. D. Chodera, R. T. McGibbon, Y. Zhao, K. A. Beauchamp, L.-P. Wang, A. C. Simmonett, M. P. Harrigan, C. D. Stern, R. P. Wiewiora, B. R. Brooks, and V. S. Pande, “OpenMM 7: Rapid development of high performance algorithms for molecular dynamics”, *PLOS Computational Biology* **13**, e1005659 (2017).
- [208] M. Sapunar, T. Piteša, D. Davidović, and N. Došlić, “Highly Efficient Algorithms for CIS Type Excited State Wave Function Overlaps”, *Journal of Chemical Theory and Computation* **15**, 3461–3469 (2019).
- [209] I. Tavernelli, B. F. E. Curchod, A. Laktionov, and U. Rothlisberger, “Nonadiabatic coupling vectors for excited states within time-dependent density functional theory in the Tamm-Dancoff approximation and beyond”, *Journal of Chemical Physics* **133**, 194104 (2010).
- [210] L. S. Dodda, I. Cabeza de Vaca, J. Tirado-Rives, and W. L. Jorgensen, “LigPar-Gen web server: an automatic OPLS-AA parameter generator for organic ligands”, *Nucleic Acids Research* **45**, W331–W336 (2017).

- [211] E. Anslyn and D. Dougherty, *Modern physical organic chemistry* (University Science Books, 2004), pp. 116–119.
- [212] Y.-S. Lin, G.-D. Li, S.-P. Mao, and J.-D. Chai, “Long-Range Corrected Hybrid Density Functionals with Improved Dispersion Corrections”, *Journal of Chemical Theory and Computation* **9**, 263–272 (2013).
- [213] Y. Abderrazak, A. Bhattacharyya, and O. Reiser, “Visible-Light-Induced Homolysis of Earth-Abundant Metal-Substrate Complexes: A Complementary Activation Strategy in Photoredox Catalysis”, *Angewandte Chemie International Edition* **60**, 21100–21115 (2021).
- [214] M. Yamane, Y. Kanzaki, H. Mitsunuma, and M. Kanai, “Titanium(IV) Chloride-Catalyzed Photoalkylation via C(sp³)-H Bond Activation of Alkanes”, *Organic Letters* **24**, 1486–1490 (2022).
- [215] Y.-R. Luo, *Handbook of Bond Dissociation Energies in Organic Compounds* (CRC Press, 2002).
- [216] Y. Guo, C. Riplinger, D. G. Liakos, U. Becker, M. Saitow, and F. Neese, “Linear scaling perturbative triples correction approximations for open-shell domain-based local pair natural orbital coupled cluster singles and doubles theory [DLPNO-CCSD(T₀/T)]”, *Journal of Chemical Physics* **152**, 10.1063/1.5127550 (2020).
- [217] C. F. Sailer, S. Thallmair, B. P. Fingerhut, C. Nolte, J. Ammer, H. Mayr, I. Pugliesi, R. de Vivie-Riedle, and E. Riedle, “A Comprehensive Microscopic Picture of the Benzhydryl Radical and Cation Photogeneration and Interconversion through Electron Transfer”, *ChemPhysChem* **14**, 1423–1437 (2013).
- [218] J. P. Zobel, J. J. Nogueira, and L. González, “Quenching of Charge Transfer in Nitrobenzene Induced by Vibrational Motion”, *Journal of Physical Chemistry Letters* **6**, 3006–3011 (2015).
- [219] J. J. Nogueira, F. Plasser, and L. González, “Electronic delocalization, charge transfer and hypochromism in the UV absorption spectrum of polyadenine unravelled by multiscale computations and quantitative wavefunction analysis”, *Chemical Science* **8**, 5682–5691 (2017).
- [220] J. P. Zobel, M. Heindl, J. J. Nogueira, and L. González, “Vibrational Sampling and Solvent Effects on the Electronic Structure of the Absorption Spectrum of 2-Nitronaphthalene”, *Journal of Chemical Theory and Computation* **14**, 3205–3217 (2018).
- [221] E. Wigner, “On the quantum correction for thermodynamic equilibrium”, *Physical Review* **40**, 749–759 (1932).
- [222] M. Barbatti, A. J. A. Aquino, and H. Lischka, “The UV absorption of nucleobases: semi-classical *ab initio* spectra simulations”, *Physical Chemistry Chemical Physics* **12**, 4959 (2010).
- [223] D. S. Tikhonov and Y. V. Vishnevskiy, “Describing nuclear quantum effects in vibrational properties using molecular dynamics with Wigner sampling”, *Physical Chemistry Chemical Physics* **25**, 18406–18423 (2023).

- [224] W. Domcke, L. Cederbaum, H. Köppel, and W. von Niessen, “A comparison of different approaches to the calculation of Franck-Condon factors for polyatomic molecules”, *Molecular Physics* **34**, 1759–1770 (1977).
- [225] F. J. Avila Ferrer and F. Santoro, “Comparison of vertical and adiabatic harmonic approaches for the calculation of the vibrational structure of electronic spectra”, *Physical Chemistry Chemical Physics* **14**, 13549 (2012).
- [226] Q. Meng and H.-D. Meyer, “A full-dimensional multilayer multiconfiguration time-dependent Hartree study on the ultraviolet absorption spectrum of formaldehyde oxide”, *Journal of Chemical Physics* **141**, 124309 (2014).
- [227] F. Egidi, D. B. Williams-Young, A. Baiardi, J. Bloino, G. Scalmani, M. J. Frisch, X. Li, and V. Barone, “Effective Inclusion of Mechanical and Electrical Anharmonicity in Excited Electronic States: VPT2-TDDFT Route”, *Journal of Chemical Theory and Computation* **13**, 2789–2803 (2017).
- [228] A. Hazra, H. H. Chang, and M. Nooijen, “First principles simulation of the UV absorption spectrum of ethylene using the vertical Franck-Condon approach”, *Journal of Chemical Physics* **121**, 2125–2136 (2004).
- [229] F. Rott, M. Reduzzi, T. Schnappinger, Y. Kobayashi, K. F. Chang, H. Timmers, D. M. Neumark, R. de Vivie-Riedle, and S. R. Leone, “Ultrafast strong-field dissociation of vinyl bromide: An attosecond transient absorption spectroscopy and non-adiabatic molecular dynamics study”, *Structural Dynamics* **8**, 034104 (2021).
- [230] P. Hamm, “Principles of Nonlinear Optical Spectroscopy: A Practical Approach or Mukamel for Dummies”, Lecture script (Universität Zürich, 2005).
- [231] S. Zamith, J. Degert, S. Stock, B. de Beauvoir, V. Blanchet, M. Aziz Bouchene, and B. Girard, “Observation of Coherent Transients in Ultrashort Chirped Excitation of an Undamped Two-Level System”, *Physical Review Letters* **87**, 033001 (2001).
- [232] A. Monmayrant, B. Chatel, and B. Girard, “Quantum State Measurement Using Coherent Transients”, *Physical Review Letters* **96**, 103002 (2006).
- [233] S. N. Andreev, A. V. Mikhailov, V. N. Ochkin, N. V. Pestovskiy, and S. Y. Savinov, “Self-radiation of an absorbing medium induced by a fast frequency-tuning laser”, *Laser Physics* **25**, 025701 (2015).

Acronyms

BO Born-Oppenheimer. 1, 6, 30

CASPT2 complete active space perturbation theory. 4, 32, 45, 50, 67, 83, 84, 96, 101, 103, 106, 120, 126–129, 149

CI configuration interaction. 99

CIS configuration interaction singles. 99

CoIn conical intersection. 30, 45, 81, 84, 85, 95

DCM dichloromethane. 4, 95, 96, 99, 100

DFT density functional theory. 35, 96

DMSO₂ methylsulfonylmethane. 3, 34, 35, 119

DVR discrete variable representation. 19, 20

EADS evolution associated decay spectra. 81, 83–85, 103, 122

ESA excited state absorption. 2, 83–85, 101, 103, 122

FC Franck-Condon. 21, 24, 45, 50, 79, 83–85, 95–97, 105, 120–122

HOMO highest occupied molecular orbital. 79

IC internal conversion. 46, 47, 49, 83, 95

ICN cyanogen iodide. 3, 7

IR infrared. 3, 120

ISC intersystem crossing. 45, 47–49, 51, 67, 83–85, 95, 101

LMCT ligand to metal charge transfer. 105

LUMO lowest unoccupied molecular orbital. 79

MCE multi-configurational Ehrenfest. 2, 5, 18, 20–24, 26–28

MCH molecular Coulomb Hamiltonian. 31, 32

MCTDH multi-configuration time-dependent Hartree. 18, 21, 24, 27, 28, 121

- MD** molecular dynamics. 3, 7, 34, 35, 99, 101, 119
- MM** molecular mechanics. 95, 98, 99
- MO** molecular orbital. 99
- PES** potential energy surface. 1, 2, 7, 18, 46, 81, 120, 122
- QD** quantum dynamics. 3, 7
- QM** quantum mechanics. 95, 98
- QM/MM** quantum mechanics/molecular mechanics. 4, 95, 98–100, 119, 120
- RMSD** root-mean-square deviation. 96, 97
- RWA** rotating wave approximation. 35, 125
- SHARC** surface hopping with arbitrary couplings. 32, 98, 99
- SOC** spin-orbit coupling. 32, 45, 50, 68, 81, 85
- TA** transient absorption. 2, 4, 48, 81, 83–85, 103, 106, 120, 122
- TDA** Tamm-Dancoff approximation. 99
- TDDFT** time-dependent density functional theory. 83, 96, 97, 99, 100, 103, 120
- TDH** time-dependent Hartree. 6, 24, 27
- TDSCF** time-dependent self-consistent field. 6, 18
- TDSE** time-dependent Schrödinger equation. 5, 6, 18, 29, 30
- TSH** trajectory surface hopping. 2, 3, 5, 7, 29–32, 81, 83, 85, 95, 98, 100, 103, 105, 119, 120, 122
- UV** ultraviolet. 45–47, 50, 80, 120–122
- Vis** visible. 80, 121, 122
- XMS-CASPT2** extended multi-state CASPT2. 4, 32, 45, 50, 67, 83, 84, 96, 101, 103, 106, 120, 126–129

Danksagung

Auf den letzten beiden Seiten dieser Arbeit möchte ich mich bei all jenen Bedanken, die in den vielen Jahren meiner Promotion zum Gelingen dieser Doktorarbeit beigetragen haben.

Zuallererst gilt mein Dank all meinen experimentellen Kooperationspartnern, ohne die diese Arbeit nicht möglich gewesen wäre. Erst die Kooperation mit Experimentatoren macht die Arbeit des Theoretikers richtig interessant. Hier möchte ich mich bei Daniel P. Schwinger, Maximilian Högner, Erling Thyrhaug, Theresa Buberl, Noah Jeremias und Thomas Rigotti bedanken. Wir hatten viele intensive Zoom-Calls um die Publikationen in dieser Arbeit zu planen, durchzuführen und abzurunden. Für die spannenden Themen, wertvollen Vorschläge und exzellente Zusammenarbeit bedanke ich mich außerdem bei Jürgen Hauer, Giulio Cerullo, Thorsten Bach und Ioachim Pupeza. Mein besonderer Dank gilt auch Piotr Kabaciński (und nochmals Daniel P. Schwinger), für das Durchführen der TA Messungen.

Aus der Theorie möchte ich mich bei Jörg Kussmann und Christian Ochsenfeld bedanken. Fermions ist schon echt flott unterwegs. Außerdem bedanke ich mich bei Irene Burghardt, Matteo Bonfanti und David Picconi für die Einführung in die Welt der multi-konfigurationellen Methoden und ihren Input, der wesentlich zum ersten Kapitel dieser Arbeit beigetragen hat.

Als nächstes natürlich vielen Dank an meine aktuellen und ehemaligen Kollegen im Arbeitskreis. Vielen Dank Florian Rott, Sebastian Reiter, Ferdinand Kiss, Lena Bäuml, Franziska Schüppel, Thomas Schnappinger, Daniel Keefer, Matthias Roos, Sven Oesterling, Robert Siemering, Patrick Kölle und Julius Zauleck. Ihr habt immer mit angeregten Diskussionen für eine angenehme Atmosphäre gesorgt, habt meine vielen (im Nachhinein teilweise recht trivialen) Fragen beantwortet und mir bei vielen kleinen und großen Dingen geholfen. Ganz besonders hervorheben möchte ich hier Flo, für seine unermühtlichen Einsatz an Cluster und Compiler-Maschine, Sebastian für den Upkeep von VPN, Backup-System und Wiki und Ferdi für das erste Korrekturlesen dieser Arbeit.

Diese Arbeit wäre auch nicht möglich gewesen ohne die Beiträge von Constantin Jaschke, Danke für das Vergnügen deine Bachelorarbeit betreuen zu dürfen und die große Hilfe die du als Hiwi bist. Mein Dank geht auch an meine anderen Masteranden, F-Praktikanten und Hiwi's: Thomas Knoll, Maximilian Lloyd Ach und Jan Kruse.

Ganz herzlichen Dank auch an für Marianne Fleuti für ihre Liebe, Unterstützung, Korrekturen und einen Schreibtisch in der schönen Stadt Prag. Außerdem Danke an meine Eltern für das Fördern meiner Interessen, ihr offenes Ohr und ihre immerwährende Unterstützung.

An letzter –und wichtigster– Stelle geht mein Dank an meine Doktormutter und Chefin Regina de Vivie-Riedle, die mich in Ihre Gruppe aufgenommen und umfassend unterstützt hat. Ihr wissenschaftlicher Input, die vielen Denkanstöße und Ihre Betreuung sind etwas ganz besonderes. Ganz explizit möchte ich mich auch für die Finanzierung bedanken und dafür, dass Sie die vielen Kooperationen zu Stande gebracht und mitgetragen haben. Außerdem bedanke ich mich für die Konferenzen und Workshops auf denen ich meine Ergebnisse präsentieren durfte und die Möglichkeit im CRC325 mitwirken zu können.

Vielen Dank!

```
.#####.  
.# Happy landing! #.  
.#####.
```